Microstructure Analysis of Polymer amended Fluid Fine Tailings Using Fiji-ImageJ Image Analysis Software

By

Nadine Sallam

A thesis submitted to the Faculty of Graduate and Postdoctoral Affairs in partial fulfillment of the requirements for the degree of

Master of Applied Science

in

Civil and Environmental Engineering

Carleton University
Ottawa, Ontario

Abstract

Optimizing the flocculation process is crucial for improving the long-term dewatering behaviour of oil sands tailings. Using optical microscopy, the objective of this research is to assess the long-term dewatering behaviour and consolidation properties of the polymer amended Fluid Fine Tailings (FFTs) from reliable key indicators at an early stage of the production process. The experiments include processing optical microscope images using an image analysis software, "Fiji-Image J", to generate quantitative metrics of floc morphology. Particle size distributions derived from the Image J based analysis show replicability, when multiple images from the same sample are analyzed. Preliminary correlations between image metrics and consolidation characteristics show some explanatory power, though further advanced statistical analyses will be required to properly assess the predictive power of the image-derived information.

Dedication

This thesis is dedicated to my parents, siblings & my little niece.

To my husband, Mido, I wouldn't have done it without you. Thank you for having my back and supporting me every step of the way.

Acknowledgments

I would like to thank my supervisor, Prof. Paul Simms for his time and guidance throughout the whole research. Thank you for giving me the opportunity and for supporting me in every way possible.

I would also like to thank my NRCan team, Dr. Felix Kwamena & Andrew Lackey for all their support and understanding throughout my Co-op term. Thank you for taking a bet on me and for providing me with the opportunity to be part of the team, I am forever grateful.

Table of Contents

ABSTRACT II

DEDICATION III

ACKNOWLEDGMENTS IV

LIST OF TABLES VIII

LIST OF FIGURES IX

LIST OF ABBREVIATIONS XVII

CHAPTER 1: INTRODUCTION 1

1.1 OBJECTIVES OF THE RESEARCH 3

1.2 NOVELTY OF RESEARCH 4

CHAPTER 2: LITERATURE REVIEW 7

2.1 ALBERTA'S OIL SANDS DEPOSITS 7

2.1.1 CONSOLIDATION BEHAVIOR OF HISTORICAL FFT 10

2.1.2 IMPLICATIONS AND CHALLENGES OF POOR DEWATERABILITY: 11

2.2 CONSOLIDATION 12

2.3 FLOCCULATION 17

2.4 METHODS TO EVALUATE FLOCCULATION STATE 19

2.5 DIGITAL IMAGE PROCESSING OF SOIL MICROSTRUCTURE IMAGES 21

2.5.1 LASER DIFFRACTION METHOD 22

2.5.2 SCAN ELECTRON MICROSCOPY (SEM) 23

2.5.3 X-RAY COMPUTED TOMOGRAPHY (CT) TECHNIQUE 26

2.5.4 FLOC CHARACTERIZATION USING VARIOUS MICROSCOPY TECHNIQUES 28

2.5.5 DIGITAL IMAGE PROCESSING TECHNIQUE USING OPTICAL MICROSCOPY 29

CHAPTER 3: MATERIALS AND METHODS 32

3.1 OIL SAND FLUID FINE TAILINGS 32

3.2 BASIC MINING AND GEOTECHNICAL PARAMETERS 33

3.3 POLYMER STOCK SOLUTION 34

3.4 PREPARATION METHOD FOR FLOCCULATED FFT (FFFT) 34

3.4.2 ASSESSING THE EFFECTS OF DIFFERENT MIXING DURATIONS ON SYNCRUDE TAILINGS 37

3.4.3 PIPELINE TRANSPORT SHEAR MODELLING ON FLOCCULATED TAILINGS 37

3.5 KAOLINITE PREPARATION METHOD 40

3.6 METHODS 40

3.6.1 OPTICAL MICROSCOPE DIGITAL IMAGE PROCESSING METHODS: 41

3.6.3 OSCILLATORY RHEOMETER 56

3.6.4 CAPILLARY SUCTION TIME (CST) TEST: 59

3.6.5 ESTIMATING CONSOLIDATION PROPERTIES: 60

CHAPTER 4: RESULTS AND DISCUSSIONS 64

4.1.1 CHARACTERIZATION TESTS 75

4.2 POLYMER OPTIMIZATION OF FLOCCULATED FFT: 82

4.3 PIPELINE TRANSPORT SHEAR MODELLING ON FLOCCULATED TAILINGS 98

4.5 OPTICAL MICROSCOPY APPLICATIONS IN QUANTIFYING THE MICROSTRUCTURE OF KAOLINITE 113

4.6 QUANTITATIVE CORRELATIONS OF MICROSCOPE IMAGE METRICS TO CONSOLIDATION PROPERTIES 126

4.6.1 ALL FLOCCULATED FFT SAMPLES 127

4.6.2 KAOLINITE 132

CHAPTER 5: CONCLUSION AND RECOMMENDATIONS 136

5.1 CONCLUSIONS 136

5.2 RECOMMENDATIONS FOR FUTURE WORK 138

REFERENCES 139

APPENDIX A **147**

List of Tables

Table 1. Properties of bounding functions

Table 2. Description of the different flocculation protocols

Table 3: Physical properties of the raw fluid fine tailings parameters

Table 4: summarizes the calculated shear rates, pipe diameters and flow rate at which the material follows through the pipe.

Table 5: Rotational speed for a modeled transport distance of 1000 m and their corresponding pipeline transport time.

Table 6: Summarized tests, tailing type, mixing method and tests performed in each test.

Table 7: Performance indicator tests

List of Figures

Figure 2.1: Location Map of oil sands reserves in Canada

Figure 2.2: Total volume of fluid fine tailings produced over time (Canadian Association of Petroleum Producers, 2019).

Figure 2.3: Tailings storage facility (https://www.oilsandsmagazine.com/technical/mining/tailings-ponds#:~:text=Tailings%20ponds%20are%20massive%20earth,when%20no%20longer%20in%20use).

Figure 2.4: The relationship between the hydraulic conductivity, void ratio and effective stress for oil sand tailings (Babaoglu, Y., 2020).

Figure 2.5 (A&B): Hydraulic conductivity-void ratio-effective stress treated oil sands tailings (Babaoglu, 2020)

Figure 2.6: Distribution of void ratio with an initial elevation in a 100 m deposit of oil sand tailings

Figure 2.7: Compressibility function- Fitting lower bound: $e= 3\sigma'^{-0.3}$ and upper bound $e=3\sigma'^{-0.13}$

Figure 2.8: Flocculation process through charge neutralization

Figure 2.9: Flocculation process through bridging

Figure 2.10: Torque development during flocculation and during pipeline transport modeling

Figure 2.11: SEM microscopy and SEM image formation (Lawson, K., 2020)

Figure 2.12: Environmental Scanning electron Microscope (https://www.azom.com/article.aspx?ArticleID=1556)

Figure 2.13: Example of Scanning Electron Microscope image of Leda clay

Figure 2.14: X-ray computed tomography (CT) technique (Asante , S., 2015).

Figure 2.15: Synopsis of Fiji-ImageJ software

Figure 3.1: Flocculation mixing protocol using a Couette rheometer

Figure 3.2: Couette rheometer geometry

Figure 3.3: Optical microscope (Nikon model eclipse Ti: NIS Elements AR3.2)

Figure 3.4: Optical microscope image for fFFT – Magnification 200x

Figure 3.5: Enhancing the contrast and brightness on the raw images for better visualizations

Figure 3.6 (A-D): Maxima function for particle segmentation

Figure 3.7 (A&B): Trainable Weka segmentation – Particles vs Void Classification

Figure 3.8: Generated Probability map & Thresholded Image

Figure 3.9: Combining two segmentation techniques to produce a final binary image

Figure 3.10 (A-C): Quantitative Image Analysis of particles using "Analyze Particle" tool

Figure 3.11: Workflow chart for Image processing and Quantitative analysis of Optical microscope images

Figure 3.12: Oscillatory sweep test illustrating increasing shear stress with each oscillation at a constant oscillation frequency (Modified from Muhammad (2020)).

Figure 3.13: Amplitude sweep tests performed on fFFT showing the linear viscoelastic regions for three different frequencies (-10 Hz, -5 Hz, amd -1.6 Hz). (from Mizani et al. 2017)

Figure 3.14: Oscillatory rheometer HAAKE Viscotester iQ

Figure 3.15: Triton Type 319 Multi-purpose CST machine

Figure 3.16 (A-F): Methodology for estimating consolidation properties

Figure 4.1: Developed Torque over time during flocculation

4.2 (A&B): Raw Optical microscope image & Binary Image after processing using ImageJ - Trial 1 for “Peak torque + 3 secs”

Figure 4.3 (A&B): Raw Optical microscope image and Binary Image after processing using ImageJ - Trial 2 for “Peak torque + 3 secs”

Figure 4.4 (A&B): Raw Optical microscope image and Binary Image after processing using ImageJ - Trial 3 for “Peak torque + 3 secs”

Figure 4.5 (A&B): Particle size distribution for “Peak torque + 3 secs” normal & log scales.

Figure 4.6 (A&B): Raw Optical microscope image and Binary Image trial 1 for “Peak torque + 10 secs”

Figure 4.7 (A&B): Raw optical microscope image and Binary Image - Trial 2 for “Peak torque + 10 secs”

Figure 4.8 (A&B): Particle size distribution for “Peak torque + 10 secs”

Figure 4.9: Particle size distribution curve comparing “Peak torque + 3 secs” with “Peak torque + 10 secs” samples on the same scale.

Figure 4.10: The average total particle area for “Peak torque + 3 secs” in comparison with “Peak torque + 10 secs”.

Figure 4.11: Shearing effect on the CST values

Figure 4.12 (A&B): Oscillatory Rheometer data for peak torque + 3 seconds , peak torque +10 seconds samples

Figure 4.13: Void ratio vs Elevation for (A) “Peak torque + 3 secs” and (B) “Peak torque + 10 secs”

Figure 4.14: Compressibility function for “Peak torque + 3 secs” and “Peak torque + 10 secs”

Figure 4.15: Settlement over time comparing “Peak torque + 3 seconds” vs “Peak torque + 10 seconds”

Figure 4.16: The k-e relationship comparing “Peak torque + 3 seconds” with “Peak torque + 10 seconds”.

Figure 4.17: Effect of particle size distribution on the hydraulic conductivity (Sikandar, P., & Christen, E. W. (2012))

Figure 4.18: Maximum developed torque corresponding to various polymer dosages.

Figure 4.19 (A&B): Raw optical microscope image and Binary Image - Trial 1 for 400 ppm polymer dosage

Figure 4.20 (A&B): Raw optical microscope image and Binary Image - Trial 2 for 400 ppm polymer dosage

Figure 4.21 (A&B): Particle size distribution for 400 ppm polymer dosage

Figure 4.22 (A&B): Raw optical microscope image and Binary Image - Trial 1 for 600 ppm polymer dosage

Figure 4.23 (A&B): Raw optical microscope image and Binary Image - Trial 2 for 600 ppm polymer dosage

Figure 4.24 (A&B): Particle size distribution for 600 ppm polymer dosage.

Figure 4.25 (A&B): Raw optical microscope image and Binary Image - Trial 1 for 800 ppm polymer dosage

Figure 4.26 (A&B): Raw optical microscope image and Binary Image - Trial 2 for 800 ppm polymer dosage

Figure 4.27 (A&B): Particle size distribution for 800 ppm polymer dosage

Figure 4.28 (A&B): Raw optical microscope images for 1000 ppm polymer dosage

Figure 4.29 (A&B): The average total particle area for all polymer dosages (400ppm, 600ppm, 800ppm).

Figure 4.30: The Capillary Suction time for the different polymer dosages.

Figure 4.31 (A&B): Oscillatory Rheometer data for 400ppm polymer dosed samples.

Figure 4.32 (A&B): Oscillatory Rheometer data for 600ppm polymer dosed samples.

Figure 4.33(A&B): Oscillatory Rheometer data for 800ppm polymer dosed samples.

Figure 4.34 (A&B): Oscillatory Rheometer data for 1000ppm polymer dosed samples.

Figure 4.35: Settlement rate over time comparing different polymer dosages (400 ppm, 600 ppm, 800 ppm & 1000 ppm).

Figure 4.36: The k-e relationship between all polymer dosages

Figure 4.37 (A&B): Raw optical microscope image and Binary Image - Trial 1 for 4.23 s^{-1} shearing rate

Figure 4.38 (A&B): Raw optical microscope image and Binary Image - Trial 2 for 4.23 s^{-1} shearing rate

Figure 4.39 (A&B): Particle size distribution for 4.23 s^{-1} shearing rate

Figure 4.40 (A&B): Raw optical microscope image and Binary Image - Trial 1 for 8.27 s^{-1}

Figure 4.41 (A&B): Raw optical microscope image and Binary Image - Trial 2 for 8.27 s^{-1} shearing rate

Figure 4.42 (A&B): Particle size distribution for 8.27 s^{-1} shearing rate

Figure 4.43 (A&B): Raw optical microscope image and Binary Image - Trial 1 for 16.93 s^{-1} shearing rate

Figure 4.44 (A&B): Raw optical microscope image and Binary Image - Trial 2 for 16.93 s^{-1} shearing rate

Figure 4.45 (A&B): Particle size distribution for 16.93 s^{-1} shearing rate

Figure 4.46 (A&B): Raw optical microscope image and Binary Image - Trial 1 for 33.1 s^{-1} shearing rate

Figure 4.47 (A&B): Particle size distribution for 33.1 s^{-1} shearing rate

Figure 4.48: Oscillatory Rheometer data for 4.23 s^{-1} sheared samples

Figure 4.49: Oscillatory Rheometer data for 8.27 s^{-1} sheared samples

Figure 4.50: Oscillatory Rheometer data for 16.93 s^{-1} sheared samples

Figure 4.51: Settlement rate over time comparing the different shear rates

Figure 4.52 (A-D): Void ratio vs Elevation for shear rates: (A) 4.23 s^{-1} (B) 8.27 s^{-1} (C) 16.93 s^{-1} (D) 33 s^{-1}

Figure 4.53: Compressibility function for all shear rates

Figure 4.54: k-e relationships all shear rates

Figure 4.55 (A&B): Raw optical microscope image and Binary Image for flocculated Kaolinite at 100% - Trial 1

Figure 4.56 (A&B): Raw optical microscope image and Binary Image for flocculated Kaolinite at 100% - Trial 2

Figure 4.57 (A&B): Particle size distribution for flocculated Kaolinite at 100%

Figure 4.58(A&B): Raw optical microscope image and Binary Image for flocculated Kaolinite at 500% - Trial 1

Figure 4.59 (A&B): Raw optical microscope image and Binary Image for flocculated Kaolinite at 500% - Trial 2

Figure 4.60 (A&B): Particle size distribution for flocculated Kaolinite at 500%

Figure 4.61 (A&B): Raw optical microscope image and Binary Image for flocculated Kaolinite at 1000% - Trial 1

Figure 4.62 (A&B): Raw optical microscope image and Binary Image for flocculated Kaolinite at 1000% - Trial 2

Figure 4.63 (A&B): Particle size distribution for flocculated Kaolinite at 1000%

Figure 4.64 (A&B): Raw optical microscope image and Binary Image for flocculated Kaolinite

Figure 4.65 (A&B): Raw optical microscope image and Binary Image for flocculated Kaolinite at 2000% - Trial 2

Figure 4.66: Particle size distribution for flocculated Kaolinite at 2000%

Figure 4.67: Settlement over time for flocculated Kaolinite at different water contents

Figure 4.68 (A-D): Void ratio vs Elevation for water contents 100%, 500%, 1000% and 2000%

Figure 4.69: The k-e relationship between all flocculated Kaolinite samples at different water contents

Figure 4.70: The compressibility function all flocculated Kaolinite samples at different water contents

Figure 4.71: Average particle diameter for all flocculated FFT correlations with C parameter – Small particles 0-20 μm^2

Figure 4.72: Average particle diameter for all flocculated FFT correlations with C parameter – Large particles 3000 to > 5000 μm^2

Figure 4.73: Average particle diameter for all flocculated FFT correlations with B parameter – Small particles 0-20 μm^2

Figure 4.74: Average particle diameter for all flocculated FFT correlations with B parameter – Large particles 3000 to > 5000 μm^2

Figure 4.75: Average particle diameter for all flocculated FFT correlations with A parameter – Small particles 0-20 μm^2

Figure 4.76: Average particle diameter for all flocculated FFT correlations with A parameter – Large particles 3000 to > 5000 μm^2

Figure 4.77: Average particle diameter for all flocculated FFT correlations with A parameter – Small particles 0-20 μm^2

Figure 4.78: Average particle diameter for all flocculated FFT correlations with A parameter – Large particles 3000 to > 5000 μm^2

Figure 4.79: Average particle diameter for all flocculated FFT correlations with B parameter – Small particles 0-20 μm^2

Figure 4.80: Average particle diameter for all flocculated FFT correlations with B parameter – Large particles 3000 to > 5000 μm^2

Figure 4.81: Average particle diameter for all flocculated FFT correlations with C parameter – Small particles 0-20 μm^2

Figure 4.82: Average particle diameter for all flocculated FFT correlations with C parameter – Large particles 3000 to > 5000 μm^2

List of Abbreviations

AER	Alberta Energy Regulator
CHEW	Clark Hot Water Extraction
COSIA	Canadian oil sands alliance
CST	Capillary Suction Time
DIP	Digital Image Processing
FFT	Fluid Fine Tailings
fFFT	Flocculated Fluid Fine Tailings
GWC	Gravimetric water content
GHG	Green house gases
LL	Liquid limit
OM	Optical Microscope
PI	Plasticity Index
PL	Plastic Limit
SEM	Scanning Electron Microscope
μm	micrometer

e	Void ratio
k	Hydraulic conductivity

Chapter 1: Introduction

The oil sands industry is one of the major driving forces to Canada's economy. Over the next two decades, the industry is expected to contribute about $4 trillion towards Canada's economy (Canadian Association of Petroleum Producers, 2019). In 2020, Canadian oil and natural gas provided $105 billion to Canada's GDP (Gross Domestic Product) (CAPP, 2019). Canada has one of the largest oil reserves worldwide, with 165 billion barrels in oil sands (Alberta Energy and Utilities Board 2005). However, substantial environmental challenges exist, probably the most challenging environmental issue is Greenhouse Gas (GHG) emissions. Oil Sands operations produce approximately 70 Megatonnes (Mt) per year of greenhouse gas emissions. In order to achieve Canada's initiatives towards the 2030 climate goals, Alberta is transitioning to an output-based allocation approach for carbon pricing per tonne. In addition, GHG emissions produced from oil sands will have a new legislative on emission limits. A new initiative has been created by leading companies to collectively work to achieve net zero GHG emissions by 2050 (Oil Sands Pathways, 2021).

Second in priority is the issue of tailings reclamation. Oil Sands are composed of bitumen, sand, clay and water; in order to extract the bitumen a water-based extraction technique is used. The separation process creates a by-product material referred to as oil sand tailings. These tailings are then transported to large impoundment facilities known as tailings ponds. The sand fraction of the tailings settles out quickly, leaving suspensions of finer particles with very high water content and low density. The footprint occupied by the tailing ponds in the Oil Sands in the vicinity of Fort McMurray are substantial, estimated to be ~ 300 km^2 , holding more than 1,200 million m^3 of Fluid Fine Tailings (FFT) (Alberta Energy Regulator, 2019). FFT has very high water contents , $w > 200\%$ (FTFC,1995) and poor consolidation behaviour/ solid settling rate,

hence this results in huge volumes of tailings that consolidate very slowly. This challenges reclamation, as FFT is expected to remain too weak to be used in terrestrial reclamation (COSIA, 2012) for hundreds to thousands of years.

Industry standard of care, however, presumes that FFT must be treated to improve its geotechnical performance. This is reflected in the Alberta Energy Regulator (AER) Directive 085, which states that stored FFT must be converted to tailings that are suitable for reclamation over the course of expected mine life of the current oil sands operations. For the tailings to be successfully and safely deposited, they must achieve a strong enough strength. This strength requires a solids content of around 70% (Mckenna et al. 2016). In addition, specific targets must be met in order to make sure the restoration plan is satisfied by ten years after the end of mining (AER, 2019).

Many treatments designed to improve the geotechnical performance of FFT use flocculation, as the poor consolidation properties of FFT arise from the dispersed state of clays native to the oil sands formation. The dispersed state is induced by the extraction process, which uses NaOH to separate bitumen from the soil. Flocculation intends to reverse this process, to aggregate clay particles to increase permeability and strength. Flocculation is typically achieved with a polymer, sometimes with additional coagulants, in conjunction with processes such as centrifugation, tank thickening or in-line thickening (Beier et al., 2013). The polymer binds to the raw FFT allowing the clay particles to form larger flocs, increasing the solids content in the short-term.

However, optimizing this flocculation process is quite challenging and involves many key performance indicator parameters (Sobkowicz, 2013; Beier et al., 2013; Lyn et al., 1992). Finding the optimum polymer dose, mixing protocol (time & speed) as well as the effect pipeline

transport are crucial for improving the long-term dewatering behaviour of the oil-sand tailings. Raw FFTs naturally have very low consolidation rate. This behaviour is governed by the low hydraulic conductivity because the clay particles distribution is very sparse. In addition, tailings deposits show thixotropic and creep behaviours during long term consolidation processes in FFT these time-dependent processes appear to slow the build up of effective stress (N. Suthaker & Scott, 1994).

Assessment of the effect of flocculation on hydraulic conductivity is, unfortunately, time consuming, as conventional methods such as large strain consolidation tests can take months to evaluate. Therefore, data that can be obtained in the short term but correlated to long term behaviour, is potentially very valuable, if such data can be used to predict long term behaviour. This research investigates one potential predictor, namely, the microstructure and morphology of the flocculated polymer amended FFT, as characterized using high powered optical microscopy. The research therefore compares non-biased parameters on microscopy images to the consolidation and other properties of the tailings.

1.1 Objectives of the research

Specific objectives of the research are:

i. Assessing the microstructural behaviour & evaluating the long-term dewatering behaviour of the polymer amended FFTs from reliable key indicators at an early stage of the production process using optical microscopy images

ii. Examining correlations between such images and consolidation properties from polymer-flocculated tailings (fFFT) and from more ideal soils (such as Kaolinite)

iii. Establishing a methodology to obtain useful information from optical microscope images of the same sample showing replicability and repeatability.

1.2 Novelty of Research

Digital Image processing techniques applied to the optical microscope images obtained from the samples are unique to this research and have been developed to enhance the quantitative fabric analysis. The state of art of this thesis is the innovative method used to analyze the optical microscope images limiting the dependence on the user's input and reducing bias by producing repeatable results while illustrating both visually and quantitatively the variations between the different samples. This technique will help obtain representative results from optical microscope images for a given sample showing replicability in a non-biased way. The novelty of this research is to recognize the best preforming methodology using Fiji-ImageJ, to obtain valuable key metrics related to the morphology and fabric of the samples and validate them with tailings performance indicators (Capillary Suction Time (CST) test, Oscillatory Rheometer and Consolidation properties).

To the author's knowledge, the only previous work that assessed the microstructural level of tailings using optical microscope analysis in combination with Fiji-ImageJ was done by Khattak (2018).The software was previously highly dependent on the user's input making the process more time consuming and subjected to variability from one trial to another. Hence, this study is based on enhancing and building on the methodology used in Khattak (2018) by producing repeatable results, limiting user's input through the use of the machine learning algorithms in ImageJ software in a time efficient manner.

1.3 Outline of thesis

The thesis includes the following sections:

Chapter 2:

- Literature review and brief background of the research topic
- Slurry behaviour including tailings (flocculation, sedimentation, consolidation)
- Overview of Alberta oil sands and the fluid fine tailings production after the extraction of bitumen.
- Description of flocculation, and consolidation processes.
- Techniques to directly quantify fabric appropriate for fluid fine tailings and similar geomaterials (for example laser diffraction, x-ray, scan electron microscopy and optical microscopy)

Chapter 3:

- Description of the materials preparation, the methods and techniques used in preparing the polymer amended tailings for Optical microscope analysis.
- Preparation of Tailings and polymer stock solution as well as the flocculation protocols and mixing methods used.
- Methods used in obtaining Optical Microscope Images and the Digital Image processing procedure using Fiji-ImageJ.

Chapter 5: Results and Discussion

- Summarizes the research findings from four different tests including:
    - Assessing the effects of different mixing durations on polymer amended FFT;
    - Polymer dose Optimization of flocculated FFT;
    - Pipeline transport shear modelling on flocculated tailings;

- Optical microscopy applications in quantifying the microstructure of Kaolinite

Chapter 6: Conclusion, limitations, and recommendations.

- Presenting recommendations for future research on tailings short and long behaviours.

Chapter 2: Literature Review

This chapter provides:

i. Brief background information on oil sands and Alberta oil sands tailings, their geotechnical behaviour and their poor consolidation and dewatering properties

ii. Different digital Image processing techniques for soils and other clay materials.

iii. A review of optical microscopy applications in quantifying the fabric of fFFT and other clays such as Kaolinite. This method is adopted to have a direct measurement of floc characteristics while validating results with the laboratory tests.

2.1 Alberta's oil sands deposits

Alberta's oil sands deposits have a total of 170 billion barrels in reserves with 34 billion recoverable barrels through mining (ERCB 2010d). Bitumen is extracted using the Clark Hot Water Extraction (CHWE) process. This process mixes hot water (35-80 degrees Celsius) with the crushed ore and sodium hydroxide to separate the bitumen as it floats to the top. Fine particles (particle size < 44 microns) are suspended within the water that surrounds the grains of sand. These fine particles separate from the ore in the CHWE process and gets mixed in the waste slurry that is sent to the tailings ponds or Dedicated Disposal Areas (DDA). Oil sand deposits are present in three locations in the Northeastern region of Alberta: Athabasca region, Cold lake region and Peace River region (Figure 2.1).

Figure 2.1: Location Map of oil sands reserves in Canada

(https://en.wikipedia.org/wiki/Athabasca_oil_sands)

The typical composition of the oil sands is 85% solids (sand, silts, clays), 5% water and 10% bitumen, the most prominent clays are kaolinite and illite.

Oil sand operations have a large contribution to Canada's national economy (Canadian Association of Petroleum Producers, 2019). However, the battle remains in the millions of tons of tailings increasing on an annual basis (Figure 2.2).

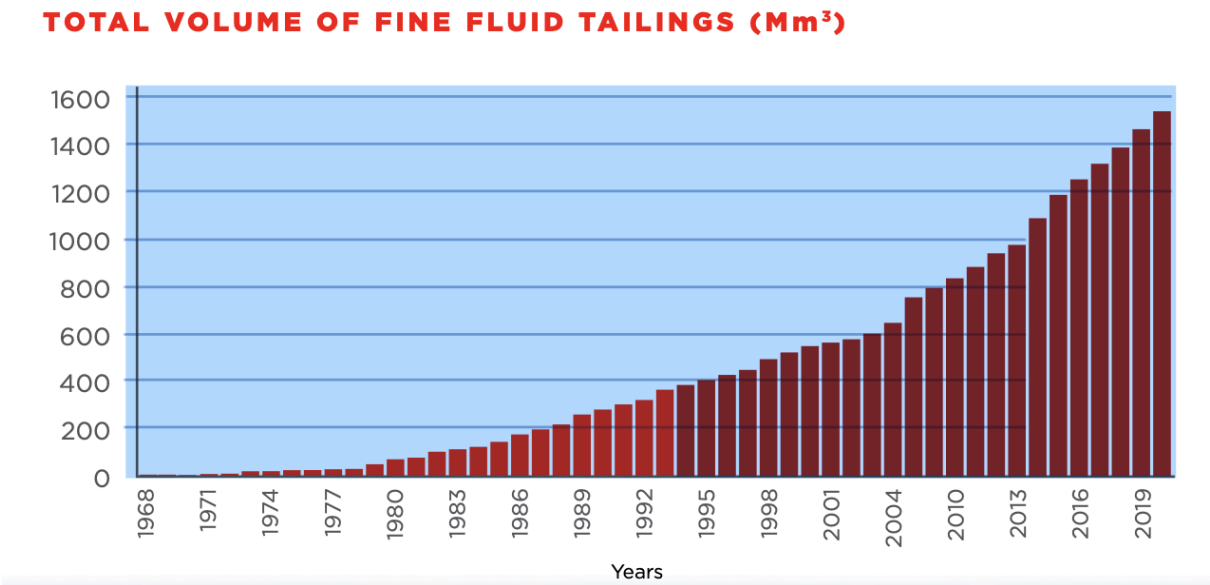

Figure 2.2: Total volume of fluid fine tailings produced over time (Canadian Association of Petroleum Producers, 2019).

In the primary flotation process, the bitumen is segregated from the ore, it floats on top of the vessel allowing it to be skimmed off. The solids settle to the bottom while the mixture of bitumen and water remain in the middle. The small clay particles (< 44 micrometers), i.e Fluid Fine Tailings (FFTs), remain while the coarser sand fraction settles quickly at the bottom forming beaches and dykes that contain the fluid tailings (Chalaturnyk et al., 2002).

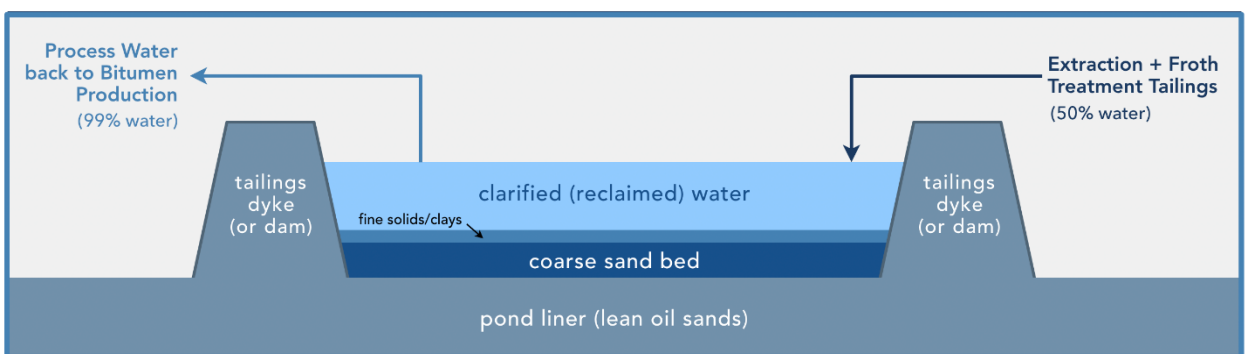

Figure 2.3: Tailings storage facility (https://www.oilsandsmagazine.com/technical/mining/tailings-ponds#:~:text=Tailings%20ponds%20are%20massive%20earth,when%20no%20longer%20in%20use).

2.1.1 Consolidation behavior of historical FFT

One of the most complex behaviours of oil sands tailings is their dewatering capabilities. FFT have poor dewaterability, typically achieving a natural water content about 200% (a solids content of ~ 35%), and not changing even after several decades and in deposits of large depth (> 100 m) (Hyndman and Sobkowicz, 2010). The key process responsible for the poor consolidation properties is the bitumen extraction process, which uses NaOH to promote dissociation of bitumen from the solids: the addition of NaOH also creates a pore-water chemistry that promotes a dispersed state in the clays, leading to smaller particles, lower pore-size, and hence very low hydraulic conductivity.

Typical k-e curve for untreated FFT is presented in Figure 2.4. It is possible to use this information to understand the slow consolidation rate in a simplified way. Using the k value for the void ratio corresponding at 35% solids, and taking the average gradient expected during consolidation, one can roughly estimate the average flux from the tailings. For the k-e relationship shown in Figure 2.4, a k value of 1×10^{-8} m/s at a void ratio of 4, and a hydraulic gradient of 0.1, is used to calculate the flux to be 0.0315m per year. Considering the depth of these impoundments (>100 m), even ignoring other processes, it can be seen that dewatering under these conditions is extremely slow. It is also understood that time-dependent processes (creep, thixotropy) in FFT are known to inhibit the development of effective stress

(Jeerrivapoolvarn 2009).

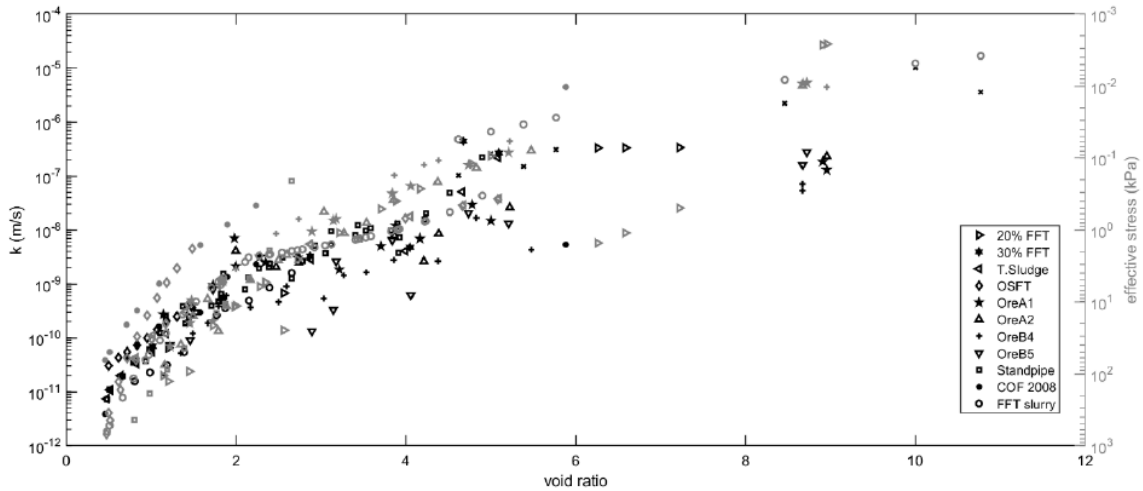

Figure 2.4: The relationship between the hydraulic conductivity, void ratio and effective stress for oil sand tailings (Babaoglu, Y., 2020).

To better consider the problem, consider that the Liquid Limit and Plastic Limit of FFT are between 40- 75% and 10-20 % respectively (BGC Engineering, 2010). To achieve sufficient strength and stiffness for the tailings to be used in reclamation, it is known that the tailings need to be dewatered to near their Plastic Limit. Therefore, the tailings must be dewatered from gravimetric water content of w=200% to around 40%. This is the context that drives the need for technology development that accelerates dewatering of the tailings.

2.1.2 Implications and Challenges of poor dewaterability:

To address this fundamental problem, several technologies have been developed that utilize the use of a polymer to induce flocculation of clays in tailings. The two widely used methods for adding polymers to the raw FFT are: a) in-line flocculation, b) physical-mechanical methods. A

polymer flocculant is introduced to the tailings stream to help the clay particles bind together creating larger flocs. The goal is to aggregate the small fine particles so they can settle faster. Physical-mechanical methods include thickening of tailings in a conventional gravity thickener and centrifugation. After the bitumen extraction from the CHWE process, the fine tailings from the cyclones enters the thickener as a cyclone overflow. The polymer is then added in order to facilitate the settling of the fine particles.

Some challenges are involved in the implementation of an in-line flocculation approach, these include finding the optimal polymer dosage as well as optimizing the mixing protocol (level, duration of mixing). The optimal polymer dose is dependent on the solids content of the tailings material, this is a crucial step in enhancing the treatment performance. In addition, excessive dosage results in making this treatment not feasible and expensive. The optimization of the mixing protocol ensures the polymer is well mixed with the tailings material creating larger flocs without applying additional shear stresses (as a result of prolonged mixing). The polymer is usually injected directly into the pipeline carrying the raw FFT at a distance several hundred meters from the deposition point. In this technique, the goal is to increase the solids content and enhance the dewatering behaviour for deposition.

2.2 Consolidation

Consolidation of saturated soils is defined as the process by which there's a reduction in the soil's volume and dissipation of excess pore water pressure (under applied stress) over time (Terzaghi,1943). Consolidation is a time-dependent process that plays an important role in tailings deposition as it allows the FFT to gain strength and reduce the void area between the particles through compression. Sedimentation and consolidation are interrelated but

unpredictable since the void ratio at which the effective stress initiates changes as the initial water content does.

The consolidation process was first introduced by K. Terzaghi (1943) and was defined as "a decrease of the water content of a saturated soil without the replacement of water by air". In the consolidation process, the excess pore water pressure dissipates while the effective stress of the soil increases. The one-dimensional consolidation theory is represented by the following equation:

$$Cv = \frac{\partial^2 u}{\partial z^2} = \frac{\partial u}{\partial t} \qquad \text{…..(2.1)}$$

Where Cv is the coefficient of consolidation, z is the one-dimensional vertical coordinate, u is the excess pore water pressure and t is the time. This theory assumes that the hydraulic conductivity (k) is constant, and the effective stress-void ratio relationship is linear. In addition, it assumes that the soil is homogenous and compression, small strains are negligible. Hence, the infinitesimal strain theory initially introduced is not representative to oil sand tailings since the void ratio changes during consolidation. Therefore, the compressibility and hydraulic conductivity also vary with the void ratio (Jeeravipolvaram,2010).

Fox and Berles (1997) proposed a piecewise linear solution where changes in volume are neglected over a small period of time, and as such, within a a small time-step and a small element, volume change can be neglected. This "piecewise linear" solution has been show to given identical results to conventional finite strain models. Recently, Qi et al (2017, 2020) extended this method to couple elasto-plastic unsaturated soil theory to large strain

consolidation. Qi et al. (2020) presented an analytical argument on the equivalence of piecewise linear predictions of large strain consolidation and direct solutions of Gibson's equation.

More important to understanding the dewatering behaviour is the understanding the material specific properties used in such models and how they influence both the rate of consolidation and the final expected distribution of density after consolidation. The materials parameters that control consolidation are the compressibility function and the *k-e* function. Both the compressibility function and the *k-e* functions are typically expressed in power or modified power form (Carrier and Freeman (2018). Equations 2.2 and 2.3 shown below are the simpler power form of these two functions:

$$e = A\,\sigma v'^{B} \qquad \ldots(2.2)$$

$$k = C\,e^{D} \qquad \ldots(2.3)$$

where e is the void ratio and $\sigma v'$ is the effective stress. Typical curves for treated oil sands tailings as well as the compressibility and k-e functions that bound the measured data are shown in Figures 2.5(A &B). These 4 curves are summarized in Table 1.

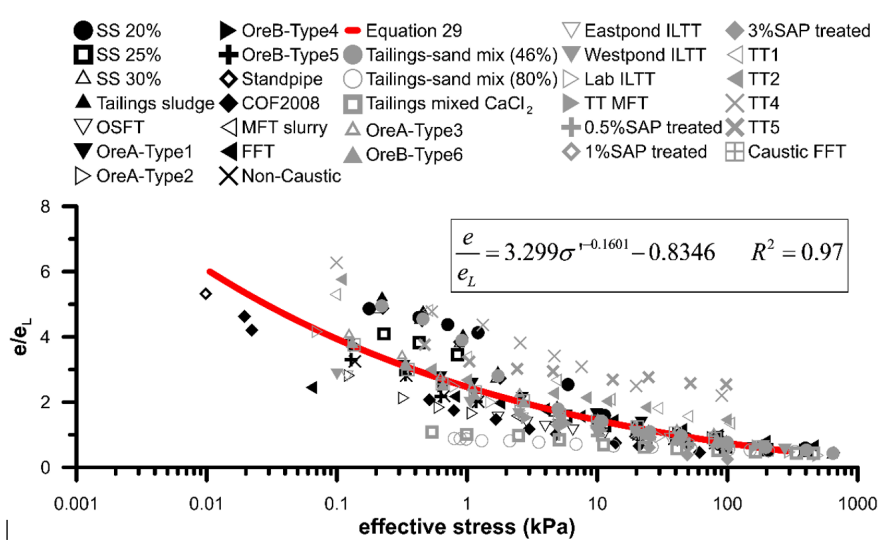

(A)

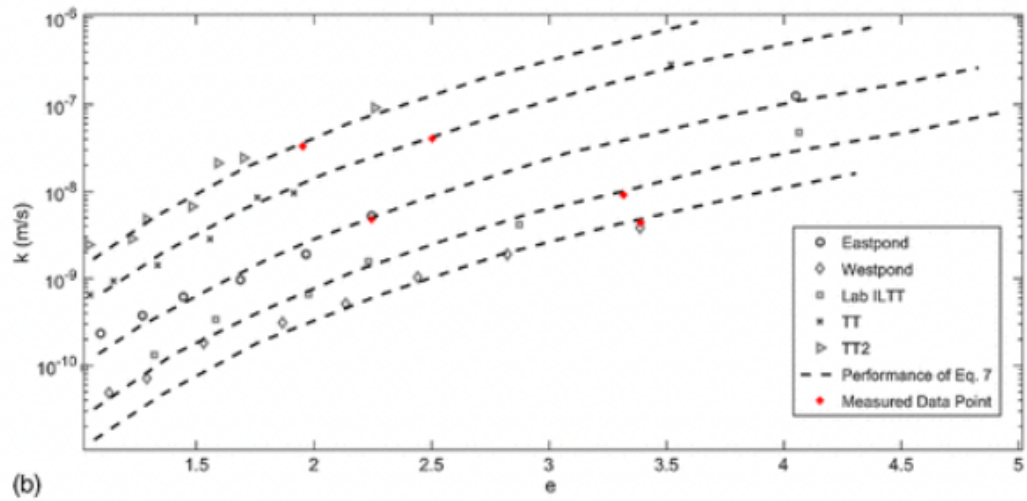

(B)

Figure 2.5 (A&B): Hydraulic conductivity-void ratio-effective stress treated oil sands tailings (Babaoglu, 2020)

The top and bottom curves correspond to $k = 7.62 \times 10^{-9}\ e^5$ and $k = 1.52 \times 10^{-10}\ e^5$ respectively.

Table 1: Properties of bounding functions shown in Figure 2.5

Function	**A**	**B**	**C**	**D**
***k-e* 1**	N/A	N/A	7.62×10^{-9}	5
***k-e* 2**	N/A	N/A	1.52×10^{-10}	5
Compressibility 1	3	-0.3	N/A	N/A
Compressibility 2	4.5	-0.22	N/A	N/A

The compressibility curve can be used to directly predict the expected variation in void ratio with depth at the end of consolidation, using direct analytical methods such as Qi and Simms 2019 or similar methods such as the Carrier and Freeman (2018) method.

As an example, the distribution of void ratio with an initial elevation in a 100 m deposit of oil sand tailings with specific gravity of 2.2 (typical for FFT) and an initial void ratio of 5 is shown in Figure 2.6.

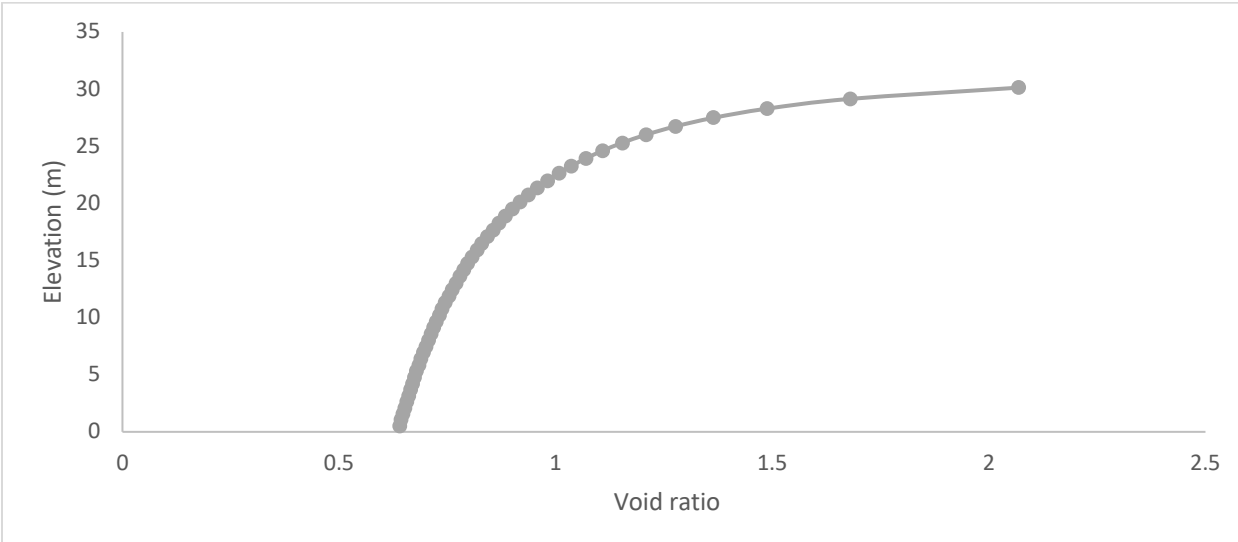

Figure 2.6: Distribution of void ratio with an initial elevation in a 100 m deposit of oil sand tailings

Numerical model results can be interpolated and expanded by some methods, including which can be simplified using interpolation of model results such as Carrier et al. (1983), or taking advantage of properties of predicted settlement curves as presented in Qi and Simms (2019), Qi et al (2020). However, the settlement time can be crudely estimated as follows: the flux at the surface is given by the hydraulic conductivity of the initial void ratio and the average hydraulic gradient during consolidation (q=KI). The average gradient during consolidation can be approximately estimated from the average of the initial gradient and 0, and can be predicted according to the method of Pane and Schiffman (1997):

$$I = \frac{Gs-1}{1+e} \qquad \ldots(2.4)$$

The influence of k-e can be explored and an estimate of the rate of consolidation can be estimated given the initial void ratio and hydraulic conductivity at the surface. The sensitivity of tailings dewatering and time to reclamation, are profoundly affected by k-e.

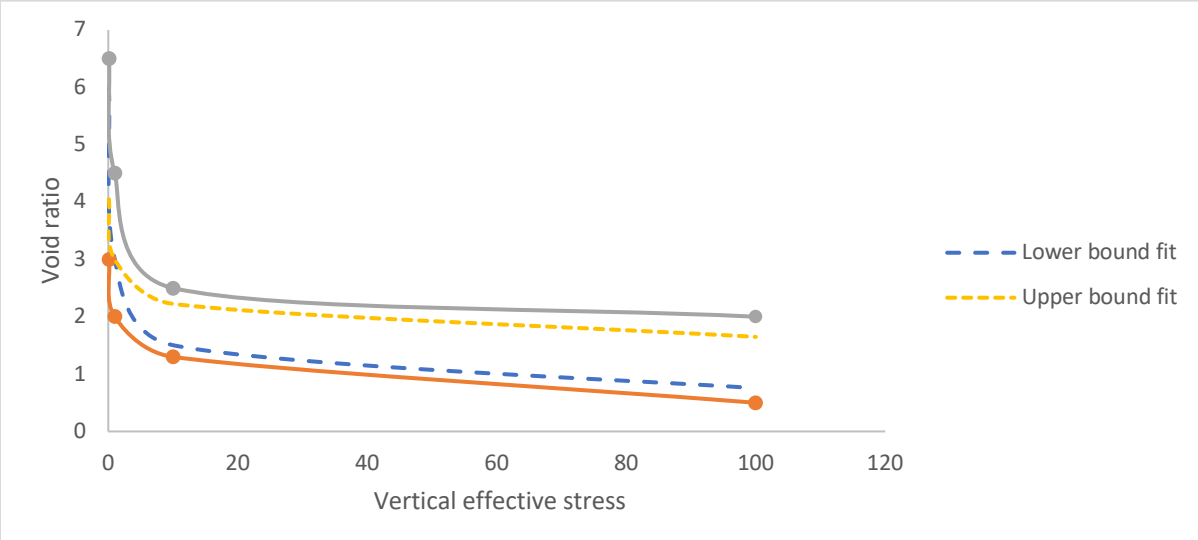

Figure 2.7: Compressibility function- Fitting lower bound: e= 3 $\sigma'^{-0.3}$ and upper bound e=3$\sigma'^{-0.13}$

Using the k-e curves and the compressibility functions, the time to consolidation will take around 120 years for the lower bound curve and 9 years for the upper bound curve, which is quite a substantial difference.

2.3 Flocculation

Flocculation is defined as the process by which a high molecular weight polymer binds with small fine particles to help with aggregation in creating larger flocs through charge neutralization (Figure 2.8) or bridging (Figure 2.9) (Vajihinejad et al., 2019). The flocculation process accelerates the dewatering and settling behaviour of the raw fluid fine tailings by creating larger particles that settle faster.

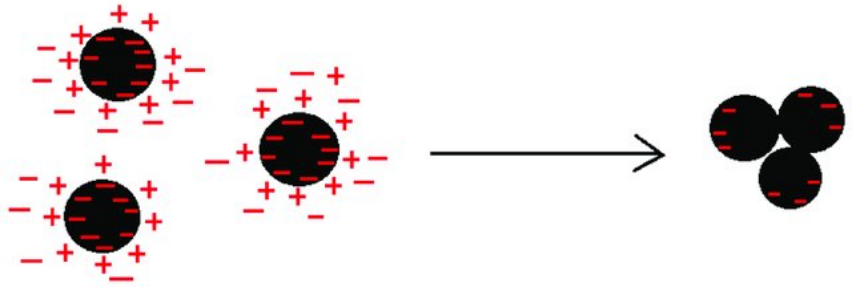

Figure 2.8: Flocculation process through charge neutralization

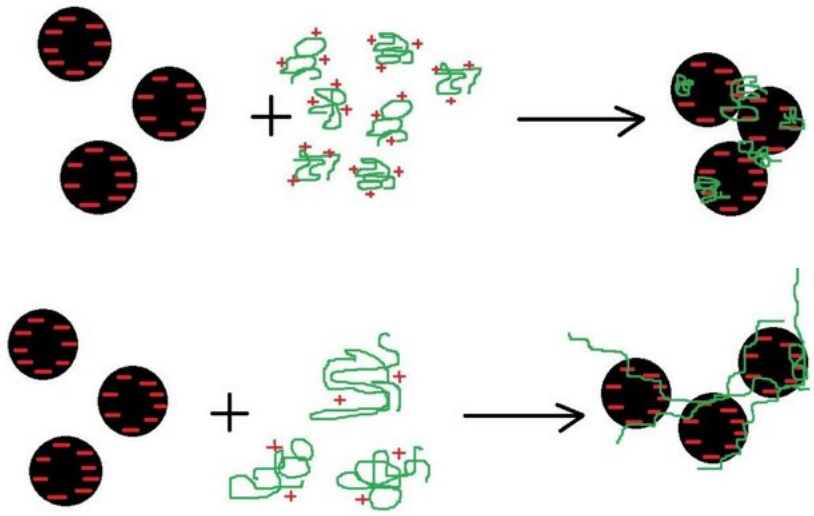

Figure 2.9: Flocculation process through bridging

In the charge neutralization mechanism, the charges on the colloidal particles are neutralized via the adsorption of flocculants. In return, the repulsion forces between the adjacent particles are reduced which causes the particles to aggregate by developing van der Waal forces. While in the bridging mechanism, high molecular weight flocculants adsorb on particles. Since the particles size are large, flocculants bridge particles and hence generate large flocs (Figure 2.9).

The polymer used in the flocculation process is usually a high molecular weight anionic polyacrylamide (PAM). In order to enhance the dewatering performance, finding the optimum polymer dosage must be studied. If the polymer is used in high dosages (above the optimal dose), the polymer particles will not have enough particle surfaces to adhere to. This will reduce the

efficacy of the flocculation process through bridging (Hogg, 1999). On the other hand, if an inadequate polymer dose is used, insufficient bridging links between the particles could result in dispersion (Tripathy and De, 2006). However, it is now understood that part of the flocculation process in the presence of anionic polymers, is charge neutralization is mediated by the presence of cations in the pore-water. Therefore, the pore-water chemistry of the a given tailings will influence flocculation with anionic polymers, independent of other characteristics such as clay content (Miller, 2010).

2.4 Methods to evaluate flocculation state

A range of parameters can be controlled to influence flocculation state, such as polymer type and dose, mixing rate or mixing energy, solids content of FFT at mixing, and the use of additional coagulants. To determine an optimal flocculation environment, several methods are used to assess flocculation state or performance in oil sands tailings, many of them adopted from wastewater. These include CST, torque feedback from mixers, rheology and short-term dewatering of grab samples.

Muhammad (2020), Aladeef (2020) and Aldaeef et al. (2021) investigated various flocculation methods and their impacts on short-term dewatering behaviour and the fabric of the sample. One of the most widely used treatment technologies is in-line flocculation, the flocculant is mixed in with the FFT during transport to the disposal area. This technique aims to enhance the immediate dewaterability, and fine particle aggregation creating larger flocs and increasing the overall strength. Finding optimal mixing conditions can be quite challenging such as the optimum flocculant dosage, optimum mixing rate and speed as well as the optimum mixing duration. Hence, optimizing these conditions in real-time during inline flocculation is very difficult which

in return produces oversheared or undersheared material. Many previous studies, such as Demoz and Mikula (2011) and Bara et al. (2013), evaluated the impacts of excessive mixing on the dewatering and settling behaviours of the fFFT. The study conducted by Aldaeef and Simms (2019 & 2020) evaluates using a torque feedback technique for regulating the flocculation process. In this study it was found that peak torque often corresponds to the largest floc formation, optimal immediate dewatering and settling behaviours.

Aldaeef et al. (2021) investigated four different protocols where anionic polymer A3888 was used at a polymer dose of 800 ppm for all trials. A description of the flocculation protocols is summarized in Table 2 below:

Table 2. Description of the different flocculation protocols

Protocol	**Pro#1**	**Pro#2**	**Pro#3**	**Pro#4**
	Fixed mixing time	Torque feedback		Fixed mixing time
Mixing vessel	20-L Pail	5-L Pail	Couette rheometer	Couette rheometer
Vessel Dia. (mm)	270	200	118	118
Impeller fixture	4-bladed vane; Dia. 160 mm and height of 10 mm.		Couette bobbin; Dia. 76 mm and height of 110 mm.	
Gap Ratio	0.80	0.59	0.66	0.66
Sample Size (ml)	2000	5000	1000	1000
Sample height (mm)	80	90	100	100
Polymer addition	One-shot	Regulated		Regulated

Rotational Speed (RPM)	320	20	250	250	35
Mixing time (Sec)	10	10	varies	20	1560

The developed torque exerted by the material during flocculation was recorded, it is defined by the difference between the torque feedback before and after polymer addition (Aldaeef and Simms, 2019).

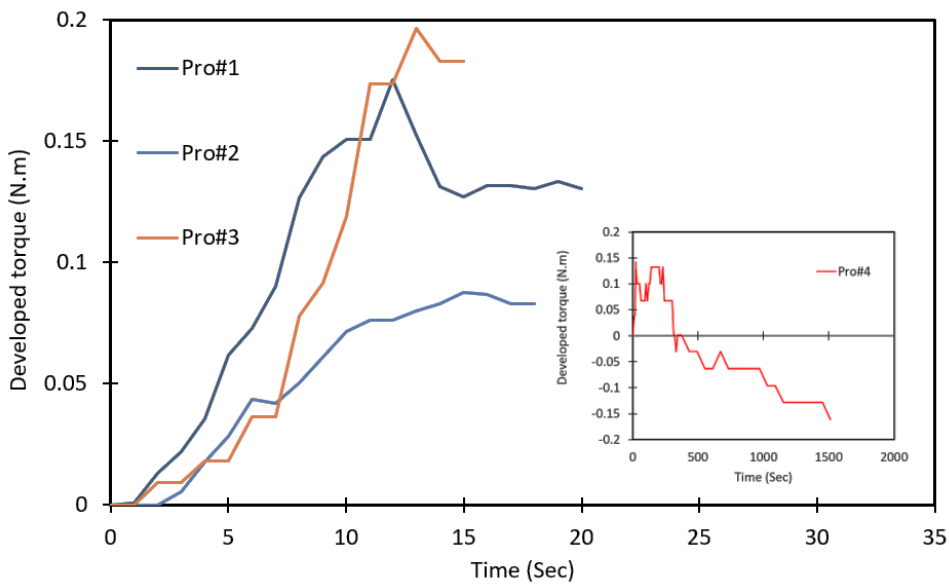

Figure 2.10: Torque development during flocculation and during pipeline transport modeling

Optical microscope images were used as a key indicator in this study to assess the flocculation behaviour. The microscope images showed that the largest floc size particles were obtained in Protocols 2 and 3 where the optimized torque technique was used.

2.5 Digital Image processing of soil microstructure images

Image analysis of optical microscope images are used in this thesis. While the only previous work of using optical microscopy to understand morphology in tailings or even soft clays has been Khattak (2018), considerable work has been done on interpretation of SEM images using imaging processing software. Khattak's (2018) work is reviewed at the end of the chapter, here follows a review of image analysis of SEM images in clays.

Assessing particle size distribution is one of the fundamental physical properties for oil sand tailings. It allows for classifying the fabric and texture of the tailings which is an essential factor affecting the hydraulic conductivity and dewatering properties.

In order to quantify the microstructure of soils, different techniques have been used in the literature such as Optical microscopy, Scan electron microscopy, X-ray computed tomography, Laser diffraction techniques and Ultrasonics.

2.5.1 Laser Diffraction Method

The laser diffraction technique has been increasingly used for the quantitative analysis of soil particle size distribution. Particle size analysis was initially developed in 1970s but has not been applied in soil science until the 1980s (Ma et al., 2000; Zer et al., 2010). In laser diffraction, the particle size is calculated based on the light intensity data collected through the detector. Laser diffraction technology uses Fraunhofer diffraction theory of light scattering for particle size analysis. Laser Diffraction Method (LDM) measures the particle size by comparing the scattered light measured with a calibrated version of an equivalent sphere (Jonasz, 1991; Di Stefano et al., 2010). The particle diameters of the spheres are derived from an equivalent sphere with the same cross-sectional area (Gee and Or, 2002). Limitations with this technique include: 1. Lasers can be used to measure particle sizes up to a limit of 600 microns. 2. If the weight of the sample is too large the sample's distribution becomes challenging for the laser technique as the change in

geometry decreases. 3. Key parameters such as refractive index and adsorption value are not standardized which could skew the particle size distribution data obtained (Yang, Wang, Wendroth, 2019). 4. A more critical issue is the fact that all particles are assumed to be spherical which contradicts the non-spherical shape of natural clay particles (Yang, Wang, Wendroth, 2019).

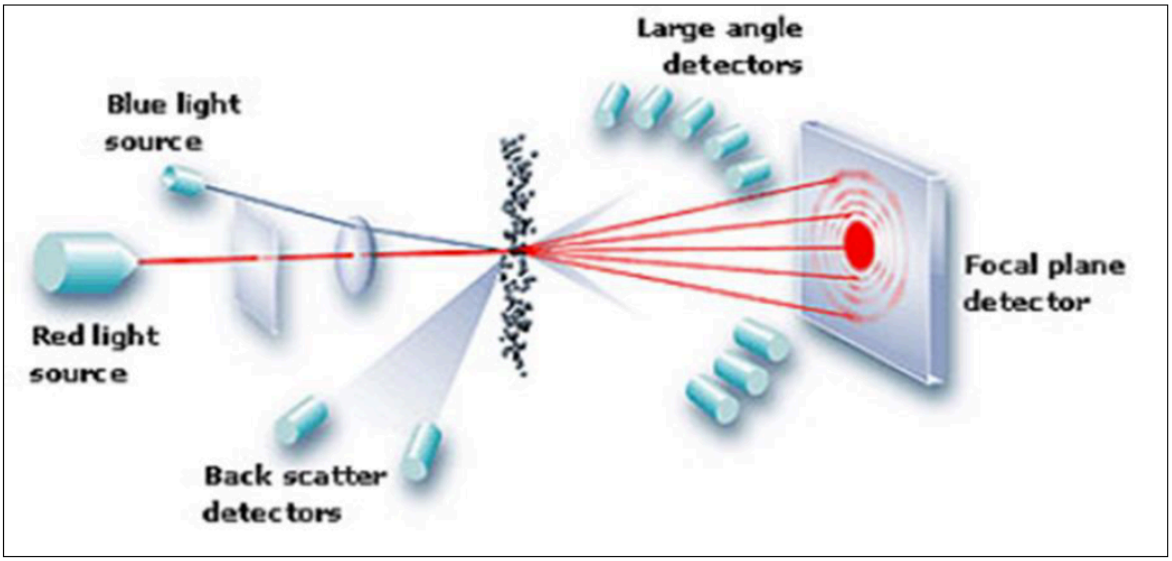

Figure 2.10: Laser diffraction technique (Asante , S., 2015).

2.5.2 Scan Electron Microscopy (SEM)

The SEM is a type of electron microscope that produces images of the sample by using a beam of high energy electrons to scan the surface. The electrons interact with the sample creating signals that contain information about the sample composition, texture/ morphology and topography (Khattak, 2018). A scan electron microscope consists of an electron gun with an electron column (creates the beam of high energy electrons), a sample chamber and an electron detector, which records and monitors the signals produced.

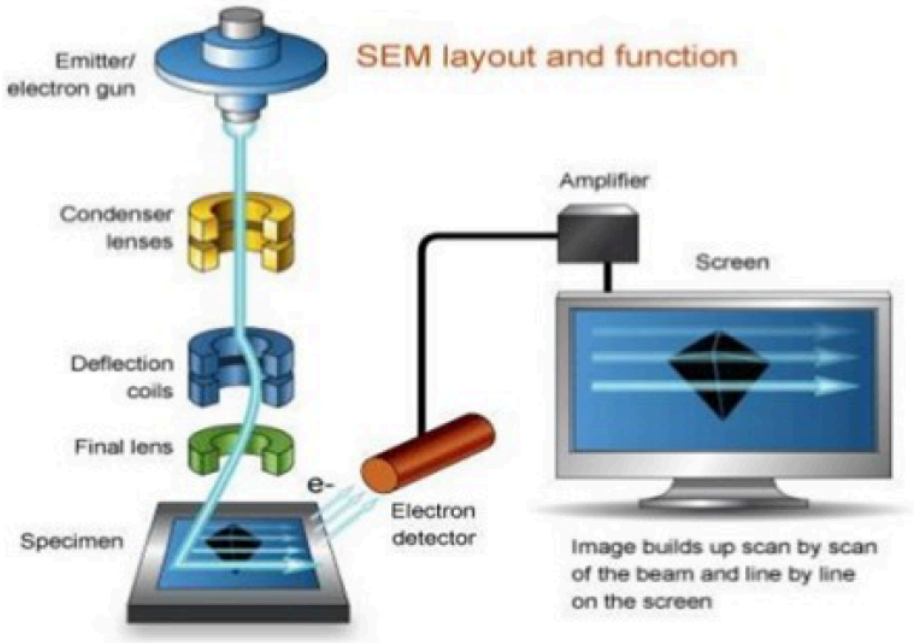

Figure 2.11: SEM microscopy and SEM image formation (Lawson, K., 2020)

Cryo Scanning electron microscopy (CyroSEM) is one of the SEM types used to evaluate the microstructure of oil sands. Hong et al. (2011) used a Cyro-electron microscopy (ZEISS/SUPRA40-FEG module OXFORD CT1500) by using the retrodiffused electron mode. Initially, the samples were frozen at a temperature of -200 °C into slush nitrogen before being used in the microscope. The goal is to preserve the microstructure of the saturated soils and rocks, hence the freezing process is done quickly to avoid water volume loss (Gillott 1973; Tovey and Wong 1973; Delage and Pellerin 1984). One of the limitations of this method is the frozen samples must be fractured and must be regulated under consistent lab conditions at very low temperatures. In some circumstances, shrinkage occurs during the freezing process which can change the fabric of the sample.

The most commonly used SEM techniques are Environmental SEM (ESEM) and Regular SEM. The ESEM can analyze samples with different moisture levels under various pressures and temperatures. On the other hand, the Regular SEM technique requires high vacuum and can only observe dehydrated/ dry or frozen and on electrically conductive samples. Therefore, the electron micrograph may not be an accurate representation of the shape and size of the particles in their natural state. The technique used in SEM and ESEM is similar where a beam of electrons releases electrons upon contact with the sample which is then detected and scanned. The energy-dispersive spectrometry detector provides information on the potential composition of the clay particles/ geo-materials being analyzed. (Jeeravipoolvarn, 2010).

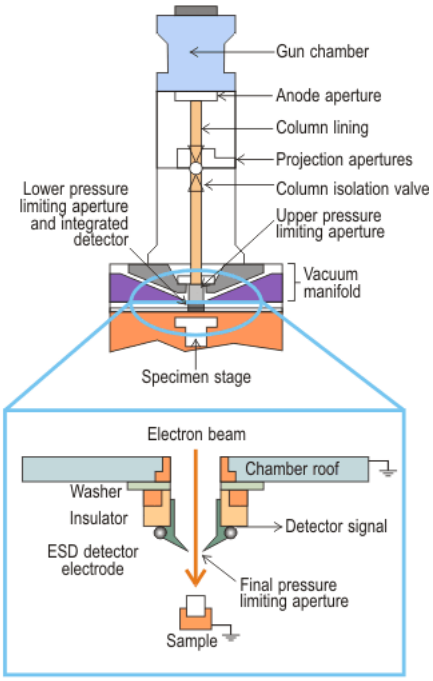

Figure 2.12: Environmental Scanning electron Microscope

(https://www.azom.com/article.aspx?ArticleID=1556)

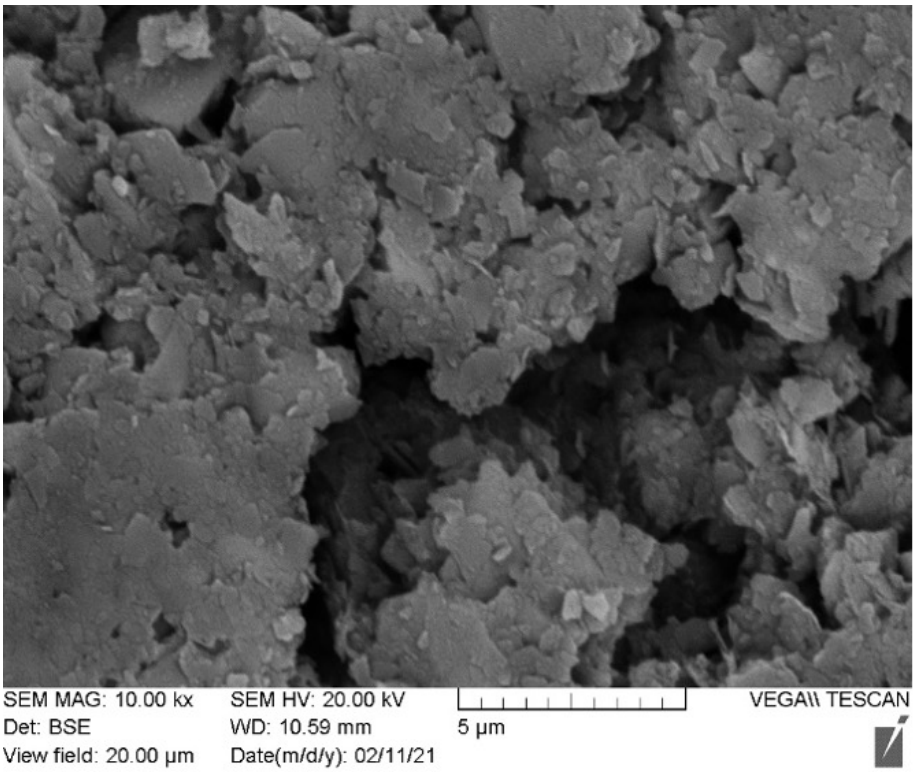

Figure 2.13: Example of Scanning Electron Microscope image of Leda clay

2.5.3 X-ray computed tomography (CT) technique

The X-ray CT technique is used to provide an insight about the soil configuration and micromorphology through digital image processing (DIP). The X-ray CT provides a visualization of the soil interior structure to assess pore topological properties and structure. (Vaz et al. 1999). The first commercial computed tomography scanner was introduced in 1972 by Godfrey Hounsfiled. (Hounsfiled, 1973). In soil mechanics, the technology was recognized by (Petrovic et al. 1982; Hainsworth and Aylmore 1983; Crestana et al.1985). More recently, advancements in imaging techniques in soil science were presented by Helliwell et al. 2013, and Cnudde and Bonne 2013. A comprehensive search was performed on scientific publication databases revealed that there are more than 400 papers on X-ray CT applications in soil science (Vaz et al. 2013).

In CT imagery, each data point is a function of X-ray attenuation, represented as an expression of relative density value named Hounsfield Unit (HU) (Huonsfield, 1973). X-rays are high-energy electromagnetic waves that can penetrate through different materials. A digital camera photographs the absorption pattern as the x-ray passes through the sample. Two factors have a huge impact on the resolution of the CT scans: 1. The quality of the phosphor screen (responsible for converting the x-ray absorption pattern to visible light) and 2. The location of the digital camera capturing the images as the visible light travels through the lens. Advantages of the x-ray technique include the visualization of the internal structure of the sample is achieved without disturbing its microstructure. For the x-ray technique to be successful, the transmission through the material must be sufficient in order to analyze the sample. Though, factors that affect the transmission of x-ray include: thickness, density, energy of photons and the atomic number of the material. The image spatial resolution is relatively low, which limits the ability to characterize and quantify the spatial distribution of pores and grains.

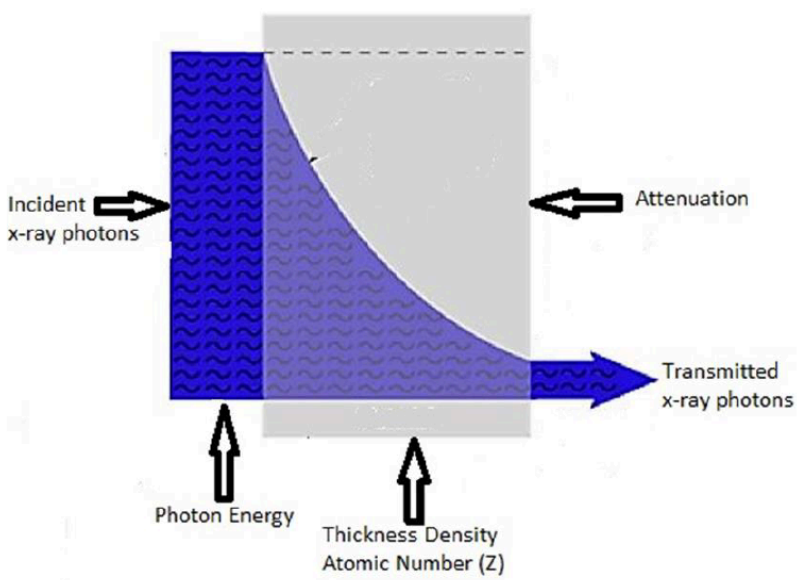

Figure 2.14: X-ray computed tomography (CT) technique (Asante , S., 2015).

2.5.4 Floc characterization using various microscopy techniques

Many researchers investigated the performance of flocculation in wastewater. There are similarities between FFT in oil sands and sludge in wastewater treatment in their fine particle content and the presence of organic matter. In both industries, dewatering remains one of the major challenges the industries are facing to date. Many factors affect the dewatering performance and polymer optimization is variable and difficult.

Historically, the techniques used did not provide valuable information regarding the floc characterizations (such as diameter, shape, size & density). The concept of ballasted flocculation is widely used in water & wastewater treatments, which typically involves the injection of a ballasting agent to aggregate the smaller floc particles into larger denser particles. However, the characteristics of the flocs are quite challenging to define in terms of their density & size. Lapointe and Barbeau (2016) used an optical microscope (Olympus DP70) to capture floc images to determine some of the floc characteristics. The floc and microsand dimensions were measured, and the floc count was recorded from 3 different sites on the cell to ensure acceptable floc distribution representation. Overall, the microscopy method provided information on the floc characteristics which allowed for optimizing the process while providing repeatable results for evaluating floc size, density & shape. . A similar approach is used in this research through using an anionic polyacrylamide (PAM) flocculant to treat the raw FFT, analyzing the floc characteristics using optical microscopy.

Wheatland et al (2020) investigated the application of combining two imaging methods by using X-ray tomography & electron microscopy to use 2D and 3D information in order to understand the floc structures with different materials. This technique enabled the authors to characterize

and quantify natural suspended sediment flocs while looking at their detailed composition on a scale from mm to nm.

2.5.5 Digital image processing technique using Optical microscopy

Digital image processing (DIP) in optical microscope enables the quantitative analysis of the tailings particle morphology. This technique was adapted by Heck and Elliot (2007) by using an optical microscopy to evaluate the microstructure of a Soil sample from Ontario by analyzing the pore-grain distribution and porosity of the soil.

The process involves the use of digital images created and an image processing software to analyze those images. Optical microscopy was performed on the flocculated polymer amended FFT samples immediately after mixing. The porosity of the soil, shape, size, arrangement of particles and permeability all affect the structure and the behaviour of the material. The porosity measures the void area in the material, while permeability measures the ability of the material to transmit fluids. The goal is to get a closer look at the microstructural level through visible light and the magnification lens in the optical microscope. The newer optical microscopes produce a high-resolution live image of the sample when connected to the computer. One of the major limitations to older optical microscope devices is the low resolution, usually only few hundred nanometers due to light diffraction limit (Khattak, 2018). High powered optical microscopes are designed to enable capturing the smallest features by using a system of lenses and backlighting. The optical microscope used throughout this research is the Nikon model NIS Elements AR 3.2 at a magnification of 200x view filed 650 um across width.

Unlike the Scanning electron microscope, the optical microscope keeps the integrity of the samples in their natural state without dehydration or freezing. This is crucial in assessing the

particle size distribution, which is an indicator for the dewatering, settlement, hydraulic conductivity behaviours of the oil sand tailings.

One of the limitations of using optical microscopy in the analysis of flocculated polymer amended oil sand tailings is the sample opaqueness and density. Optical microscope technique allows the light to penetrate through the sample to obtain the images, however, after 48 hours the polymer amended FFT become denser, hence it is challenging to analyze.

Khattak (2018) studied the use of optical microscope images for the quantification of the fFFT fabric and morphology. The raw images were then processed using image analysis software Fiji-ImageJ to enhance the images by treating the images with filters and adjusting the contrast and brightness to distinguish between the flocs and the voids. This is key in order to obtain reliable statistical data on the particle size distribution, and void area which is compared with other key performance indicators (CST, Rheology, Settlement). In this study, the software was highly dependent on the user's input when classifying the inputs under the segmentation step (discussed in detail in Chapter 4). This resulted in the process being more time consuming and subjected to variation from one trial to another. Hence, this study is based on enhancing and building on the methodology used in Khattak (2018) by producing repeatable results, limiting user's input through the use of the machine learning algorithms in ImageJ software in a time efficient manner.

An image processing software named "Fiji-Image J" is used to analyze the images obtained from the optical microscope. It is used to investigate the morphology and fabric behaviour of the tailings while quantitively analyzing important key indicators such as particle size distribution, number of pores, porosity as well as the changes in floc size after shearing.

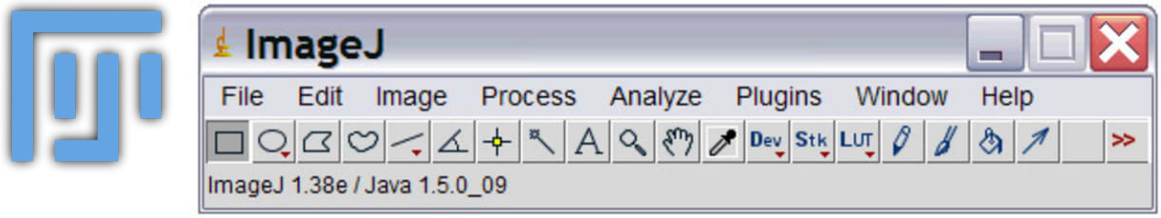

Figure 2.15: Synopsis of Fiji-ImageJ software

Chapter 3: Materials and Methods

This chapter describes the materials used, their geotechnical parameters, the sample preparation techniques and experimental method.

The chapter includes:

i. The properties of oil sand fluid fine tailings.

ii. The preparation procedure of the polymer stock solution and the polymer amended tailings.

iii. Preparation method for Kaolinite samples and the flocculating agent.

iv. Discussion on key performance indicators such as CST, Rheometer and Settlement columns to assess flocculation.

v. Description of the procedure for obtaining and enhancing the optical microscope images using Fiji-ImageJ.

3.1 Oil Sand Fluid Fine Tailings

Oil sands tailings samples were collected from a tailings pond in Northern Alberta, Canada, and shipped to Carleton University in Ottawa, Canada. In order for the fluid fine tailings to regain their initial solids content, the tailings were mixed continuously for 24 hours at 129 rpm using a drum mixer (Model number: DLM150VGD, Mixer direct). For a homogenous mixing, the rotating blades were switched between mixing in clockwise and anti-clockwise direction every two hours.

The characteristics of the tailings were identified through the different tests (chemical and physical) in the lab. The properties of raw FFT such as solids content, specific gravity, liquid limit, plastic limit, void ratio and gravimetric water content were all measured in the lab.

3.2 Basic Mining and geotechnical parameters

The raw FFT has an initial solids content of 31%, a Plastic Limit of 27% and a Liquid Limit of 60%. Other tailings' characteristics were recorded, the sands to fine ratio (SFR) was 0.25, the clay content obtained from the Methylene Blue Index (MBI) analysis ranged from 28% to 32%. The results from the X-ray diffraction (XRD) results show the composition of the clay fraction was 68-72% Kaolinite and 28-32% Illite. In addition, the Total Dissolved Solids (TDS) in the pore water collected from the raw fluid fine tailings (rFFT) was 1050 mg/L, and the electrical conductivity was 1590 mico-S/cm, while the dominant cations were sodium at concentration of 340 mg/L.

The typical physical properties of the tailings used are listed below in Table 3.

Table 3: Physical properties of the raw fluid fine tailings parameters

Properties	**Average value**
Initial solids content (%)	31
Initial water content (%)	220
Hydrocarbon content (%)	1.4
Initial wet density (g/cm3)	1.20
Initial void ratio	5.1
Specific gravity	2.12
Liquid limit (%)	60.0
Plastic limit (%)	27.0
Plasticity index (%)	33.0

3.3 Polymer stock solution

In this work an anionic polyacrylamide (PAM) flocculant is used to treat the raw FFT. This polymer has been used in commercial scale applications of tailings technologies in the oil sands. Polymer A3338 is a version of PAM commercially available through SNF, which has a molecular weight of 18 x 10^6 g/mol. Four grams of A3338 polymer were weighed in a plastic dish to create a 0.4% stock solution. The polymer was weighed using an analytical balance (Fisher Scientific, Sartorius AG Germany, LE225D) and decanted into a 1500 mL glass beaker to be mixed with 1000 mL of deionized water. The polymer solutions were stirred using a jar tester (Phipps and Bird, USA) at 250 rpm for 5 minutes and at 125 rpm for the following 55 minutes. The polymer solution was then mixed for 10 seconds using a hand blender and left for maturation for 1 hour prior to flocculation.

3.4 Preparation method for flocculated FFT (fFFT)

Various methods have been used to attempt to control flocculation in the laboratory (Chryss et al. , 2019 ; Webster et al., 2016 ; Salam et al., 2017 & 2018 ; Salam, 2020; AlAdaeef et al., 2022). These include specific mixing times and mixing speeds, some using mixing speed, some use two subsequent mixing speeds, the second lower mixing speed used for conditioning. An alternative means to regulate flocculation is by monitoring the torque from the mixer (Patent on syncrude, Derakhshandeh et al., 2016). Recently, Aldaeef et al. (2022) and Aldaeef and Simms (2019) proposed a mixing protocol that uses peak torque feedback in a modified couette rheometer to optimize or control flocculation. This technique is based on observing the relationship between the developed torque during the flocculation process. The samples are flocculated and the initial torque value is observed, then the polymer stock solution is injected and the subsequent

developed torque over time is recorded. The polymer is injected using a peristaltic pump that allows the polymer addition at a flow rate of 10 ml/s via two 0.5 mm-diameter tubes.

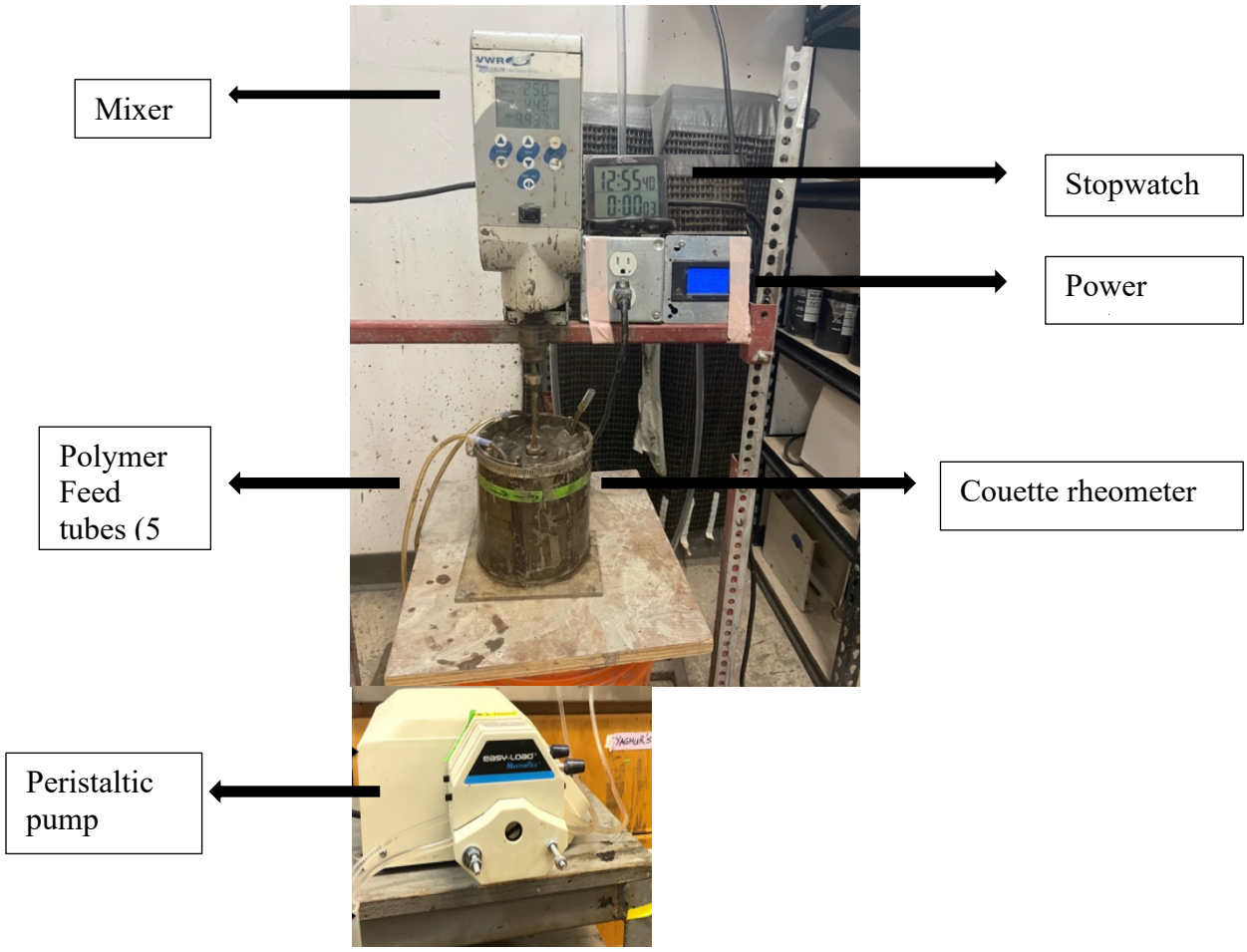

Figure 3.1: Flocculation mixing protocol using a Couette rheometer

Aldaeef et al. (2022) found that torque at the termination of flocculation or conditioning strongly correlated with indicators of sample dewaterability, most prominently the capillary suction time (CST), as well indicators of strength (such as small-strain shear modulus measured by oscillatory rheometry). The peak torque behavior is explained in literature based on the concept of elastic floc network (Langer at al. 1994).

The torque values reported in this thesis are calculated as follows:

$$T = \frac{\mathrm{P}}{0.105 * \mathrm{N_B}} \qquad \text{…. (3.1)}$$

where T is torque (N.m), P is the Power (joule/sec) utilized by motor turning the inner bobbin in the couette rheometer, and N_B is the rotational speed (rpm).

3.4.1 Apparatus

The Couette rheometer used in this study consists of an inner cylinder (bobbin) embedded with an outer stationary cylinder (cup). The height of the inner cylinder and the outer cylinder are 110 mm and 150 mm respectively. To minimize the wall slip and ensure a uniform shear force, the inside surface of the cup and outside surface of the bobbin were baffled with acrylic strips along their shafts (Figure 3.2).

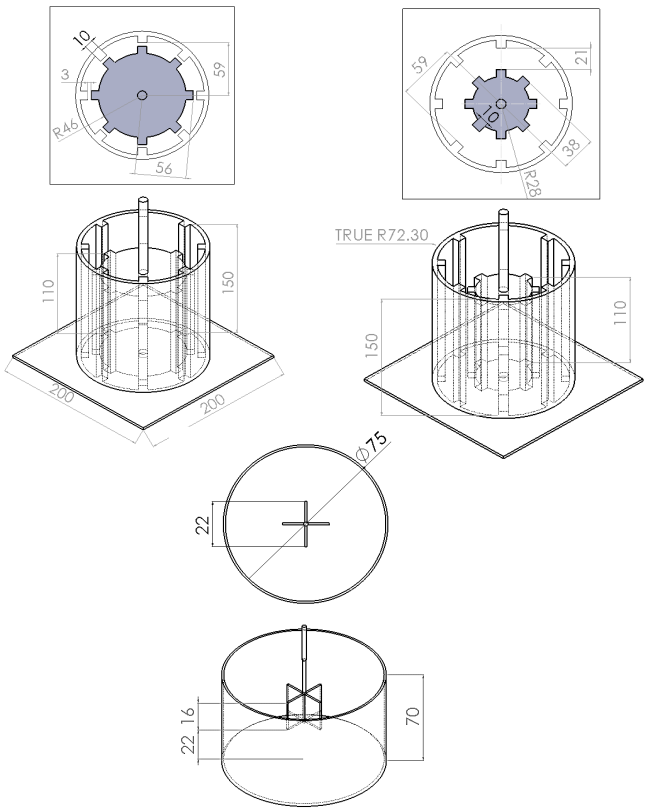

Figure 3.2: Couette rheometer geometry

The baffles cross sectional dimensions are 10 mm long and 8 mm wide. They are spaced at a radial distance of 46.3mm on the inner surface of the cup and 43.2 mm (wide-gaped) on the outer surface of the bobbin. Deng et al. (2010) showed that 8 vertical baffles would minimize the turbulence in the Couette rheometer.

3.4.2 Assessing the effects of different mixing durations on Syncrude tailings

The raw FFT samples were flocculated in the wide-gaped Couette rheometer using torque-based technique protocol. Samples were obtained to evaluate the microstructure using optical microscopy and the immediate dewaterability using Capillary Suction Time (CST). To evaluate the effects of pipeline transport, the raw FFT was flocculated at a mixing velocity of 250 RPM using a polymer dose of 600ppm. The flocculated samples were sheared for various shearing times by mixing the samples for longer durations (beyond the peak torque). The optimum mixing duration was determined based on the time that corresponded to the maximum developed torque during flocculation. To simulate and evaluate the effect of shearing on the flocculated samples, the samples were mixed for additional 3 seconds and 10 seconds after the peak torque is reached.

3.4.3 Pipeline transport shear modelling on flocculated tailings

A Couette rheometer is used for the flocculation of the polymer amended FFT, using an optimum predetermined polymer dosage of 800 ppm (Section 5.2). Four scenarios were modelled and examined in the Couette rheometer using the torque based technique. The shear rates were calculated as follows:

$$\dot{\gamma} = \frac{8U}{D} \quad \ldots(3.2)$$

where U is the flow velocity (m/s) and D is the pipe internal diameter (m).

This calculation only stands true if the flow is laminar and the fluid is Newtonian, hence the Reyonlds number is calculated to confirm this condition.

For the shear stress and shear rate in a concentric cylinder Couette rheometer to be accurate, the gap size has to finite. This means that the ratio between the inner cylinder radius and the outer cylinder radius should be greater than or equal to 0.99 (Krieger and Maron, 1952). In cases where this condition is not satisfied, a mathematical correction for shear stress and shear rate in the wide-gapped Couette rheometers is carried out to account for the wide gap effects (Chryss et al. 2019).

Krieger and Maron (1954) presented a method for correcting the measured shear stress and shear rate for power-law fluids in wide gap Couette rheometer by using the following formula:

$$\tau = \frac{T}{2.\pi.h.R_b^2} \quad (\ldots3.3)$$

$$\dot{\gamma} = \frac{2\omega}{n\left(1-b^{2/n}\right)} \quad (\ldots3.4)$$

where $\dot{\gamma}$ is the shear rate (s^{-1}), τ is the shear stress (Pa), T is the applied torque (N.m), h is the height of the cylinder (m) ω is the radial velocity (rad/s), $b = R_{bobbin}/R_{cup}$, and n is the slope determined by plotting T versus ω on a double-logarithmic basis.

The shearing duration was simulated for a pipeline transport distance of 1000m, the corresponding rotational speeds are presented in table 5. The couette rheometer evaluated consisted of a cup (outer cylinder) and a bobbin (inner cylinder) which is rotating at controlled rotational speed. The height of the cup and the bobbin ate 150mm and 110 mm respectively. To study the effects of the pipeline transport, the flocculated samples were exposed to the calculated

shear rates of 4.23 s^{-1} , 8.27 s^{-1} , 16.93 s^{-1} and 33.1 s^{-1} by applying the corresponding rational speeds in the Couette.

Table 4 summarizes the calculated shear rates, pipe diameters and flow rate at which the material follows through the pipe.

Flow Rate (Q) m^3/hr	**Pipe Diameter (D) inch**	**Cross Section Area (m^2)**	**Velocity m/sec**	**Shear rate s^{-1}**	**Reynolds number**
662	30	0.456	0.403	4.23	351
662	24	0.292	0.630	8.27	439
2648	30	0.456	1.614	16.93	1406
2648	24	0.292	2.521	33.1	1756

Table 5. Rotational speed for a modeled transport distance of 1000 m and their corresponding pipeline transport time.

Shear rate ($\dot{\gamma}$) s^{-1}	**Rotational speed (N_B) RPM**	**Transport time min.**
4.23	18	41
8.27	35	26
16.92	72	10
33.1	141	6

3.5 Kaolinite preparation method

EPK kaolinite used in this study was purchased and shipped from Edgar Minerals in Florida. The kaolinite powder is moisture free and has a distinct white color. The Kaolinite is the main mineral (99-99.9%) with silica quartz representing the remaining fraction. The pH was determined to be 5.8, the liquid limit and plastic limit were measured using ASTM D4318-10 to be 44 and 26, respectively (http://edgarmineralsinc.com/EPK-Clay.html).

In this experiment, the sample has been prepared from the kaolinite powder by flocculating the sample with sodium chloride, using a similar procedure to that used in Pane and Schiffman (1997). The samples were prepared for four different water contents: 100%, 500%, 1000% and 2000% using deionized water. The material was prepared in a 20 liters bucket and was then mixed in smaller batches for each water content.

The dry kaolinite powder was weighed and mixed with the flocculating agent. The flocculating agent used is sodium chlorite at a concentration of 23g/l, the samples were mixed for 5 minutes using hand mixing. Each sample with it's corresponding water content was deposited into a column as a single batch. The samples were then allowed to settle overnight, at the start of the test the jar was inverted 20 times and the settlement rate was recorded every hour for the first 24 hours then every 12 hours thereafter.

3.6 Methods

In this study, the samples were collected after flocculation using 5cm columns, then using a syringe the subsamples were placed on the optical microscope slide. Using a high powered optical microscope, "Nikon model eclipse Ti: NIS Elements AR3.2" the images were captured (200X magnification). As a comparison, Lapointe and Barbeau (2016) sample collection was performed during flocculation using a micropipette with a large opening, the samples were then

placed in a modified Sedgewick Rafter to count flocs. Lapointe and Barbeau (2016) used a camera connected to an optical microscope (Olympus BX51) to capture images (100X magnification). In this study, floc dimensions and other characterizations were assessed by image processing software ImageJ while in Lapointe and Barbeau (2016) the image processing was done using DraftSight. In both studies three different locations were captured to ensure an adequate representation of floc distribution, the samples were not diluted and were used in their original wet state.

This methodology used in this study investigated the influence of polymer flocculation on FFT characteristics over time. A combination of tests and analyses included using: oscillatory rheometry, optical microscopy, capillary suction time (CST) test and graduated column settling tests were carried out to determine the optimum polymer dosage and evaluate the flocculation performance.

3.6.1 Optical Microscope Digital Image processing Methods:

The samples used are all imaged in their original state using a a high powered optical microscope, "Nikon model eclipse Ti: NIS Elements AR3.2". Samples were taken immediately after flocculation and placed in 5 cm PVC columns. The polymer amended FFT were sampled from the surface of the columns (using a small needle) placing them on the optical microscope slides. The samples were not modified or disturbed, rather they were taken in their original state. The position of the slide under the optical microscope was changed, different samples were taken from various locations (from the surface of the replicate columns) to ensure the images obtained were representative in terms of the variability in the column. The positions of the slides were changed frequently to obtain at least three (3) different images from 3 different locations of the same sample. The FFT samples used for optical microscopy were all in their wet state, which would

tend to dehydrate under atmospheric conditions, therefore the time between sampling and the image capturing was kept at maximum of 5 minutes. This is to ensure the samples were in their original natural state while being imaged. In cases where an immediate water release occurs (bleed water), a syringe is used to remove the water from the top of the column while ensuring the samples are not disturbed.

The magnification at which the optical microscope images were obtained was kept constant at 200x with a view field of 650 µm. Through trial and error this magnification showed the floc development best which is crucial in this study.

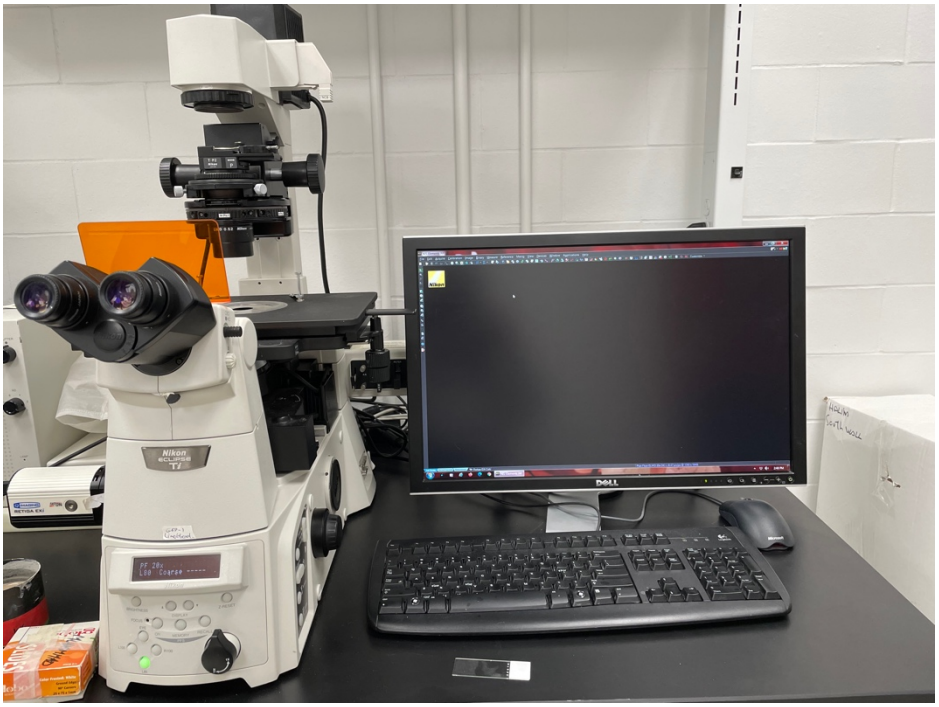

Figure 3.3: Optical microscope (Nikon model eclipse Ti: NIS Elements AR3.2)

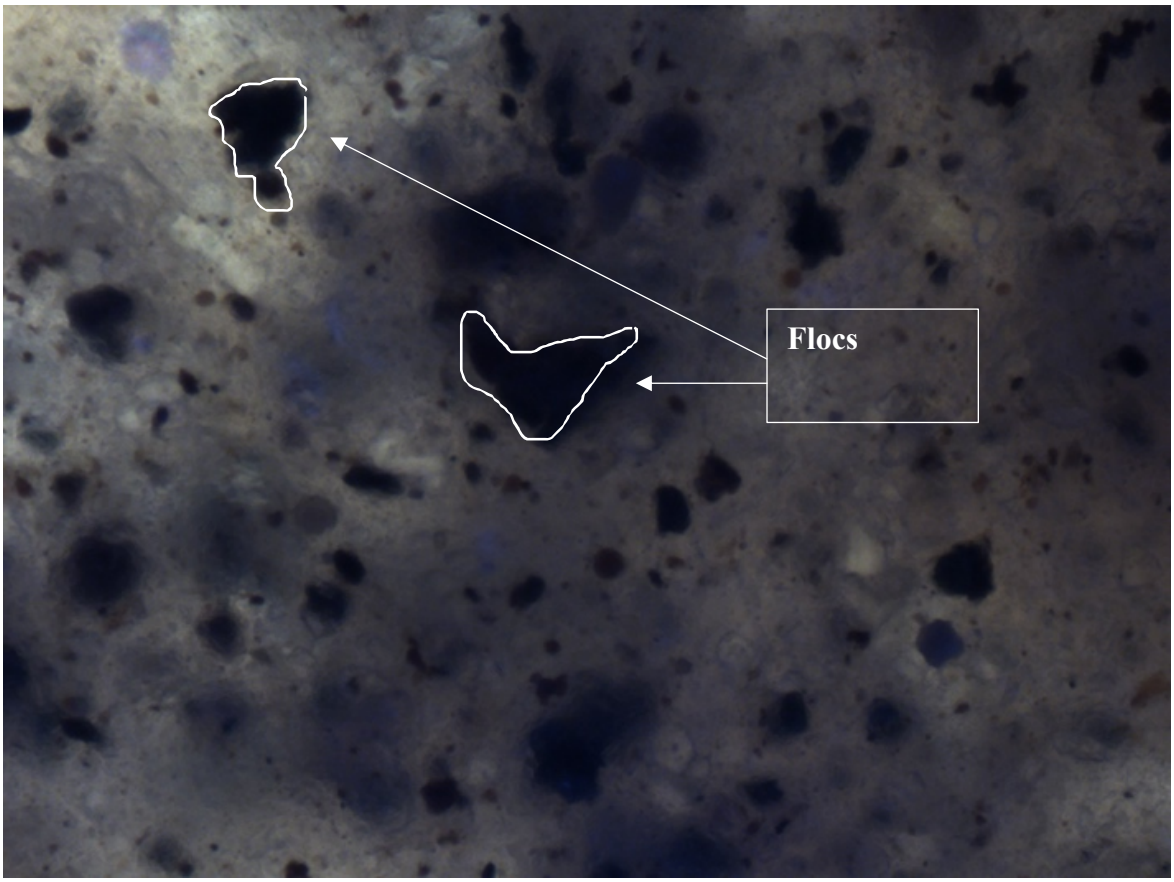

Figure 3.4: Optical microscope image for fFFT – Magnification 200x

3.6.2 Image Enhancement & Analysis

All optical microscope images are treated for better visualization, digital image processing is carried out using Fiji-ImageJ software. After many trial & error, the techniques used in this study allowed to produce repeatable trends from the information extracted after processing the raw optical microscope images. This technique investigates the microstructure and the morphology of the flocculated FFTs as well as the relationship between the pipeline shear and the particle-void area. However, the raw images are quite challenging to analyze, to differentiate between the particles and the voids in the presence of blurry regions and the variability in the floc sizes; an image enhancement technique is applied.

The following methodology was carried out in Fiji-ImageJ to enhance the optical microscope image while allowing to quantitively look at the microstructure of the samples.

Scaling: Raw Images obtained from the optical microscope were converted to 8 bit images (grey-scale). The dimensions of each image in pixels were 1040 pixels by 1392 pixels wide. The images are scaled by converting the pixel-based images into a real-world scale in "µm". The following procedure was adopted from Khattak (2018), Ferreira and Rasband (2012).

From the toolbox in the Fiji-ImageJ software, select "*Analyze* > *Set scale*". The straight-line tool is selected (as shown below in Figure 3.5), to draw a horizontal line across the image to know the "Distance in pixels". From the optical microscope used in the lab, the field view is known to be 650 µm which is entered as the "Known distance". This process converts the scaling of the image from pixel units to the measurement unit, in this case, µm. The scaling process was kept consistent throughout all the sample images presented in this research.

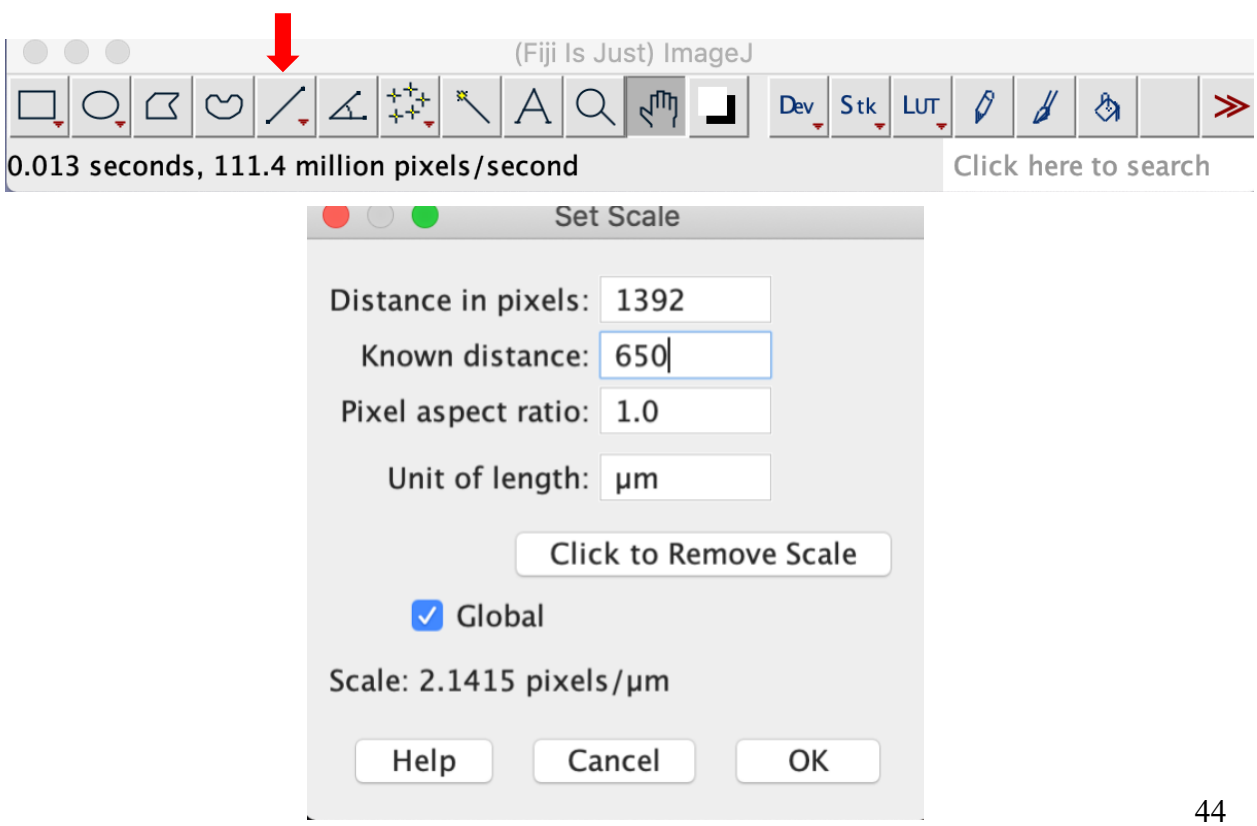

Figure 3.5: Scaling raw optical microscope images in Fiji-ImageJ

Brightness & Contrast: The image brightness and contrast were adjusted to have a clear differentiation between particles and voids. Using the toolbox in Fiji-ImageJ: *Image >Adjust > enhance brightness & contrast > Auto*. The *Auto* feature would automatically optimize brightness and contrast based on the histogram representing the pixel values associated with an image. In certain images the sliding bar was manually adjusted to produce the most optimal results. This process creates a more balanced image which allows for better visualization which is a key goal to achieve accurate results.

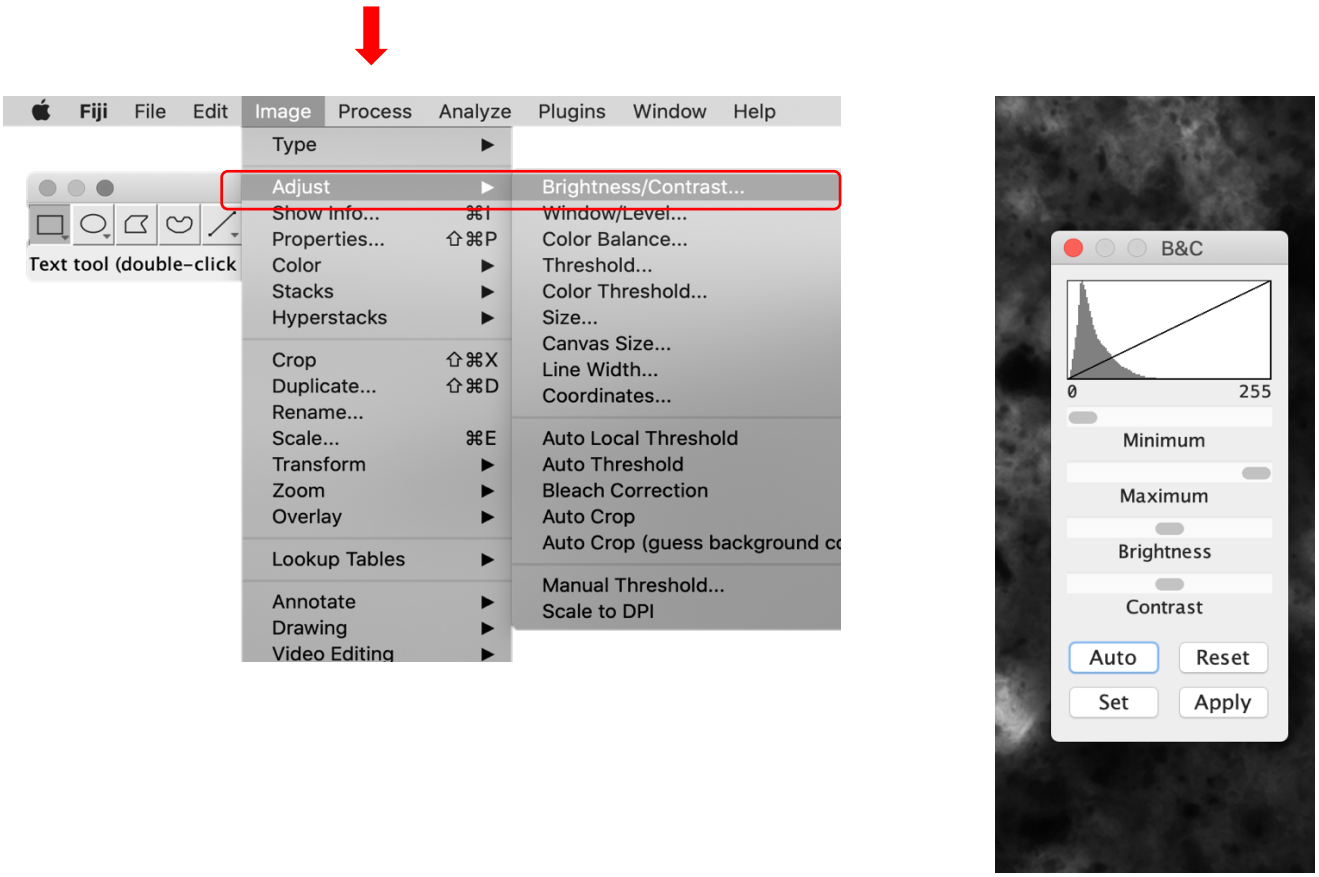

Figure 3.6: Enhancing the contrast and brightness on the raw images for better visualizations

Maxima function: "Find Maxima" function determines the local maxima in an image by creating a binary image where maximum point represents one segmented particle. This tool is used through "*Process* > *Find maxima*" to help identifying the floc regions via the assigned pixel units (dark regions vs light regions). Preview point selection tool is used to locate the maximum functions within an image, for this analysis the output type is selected as segmented particles (saved as Mask1). Note: *the prominence level* is selected based on the assigned point selection tool, using trial and error, when most of the particles are captured that's the optimal prominence level.

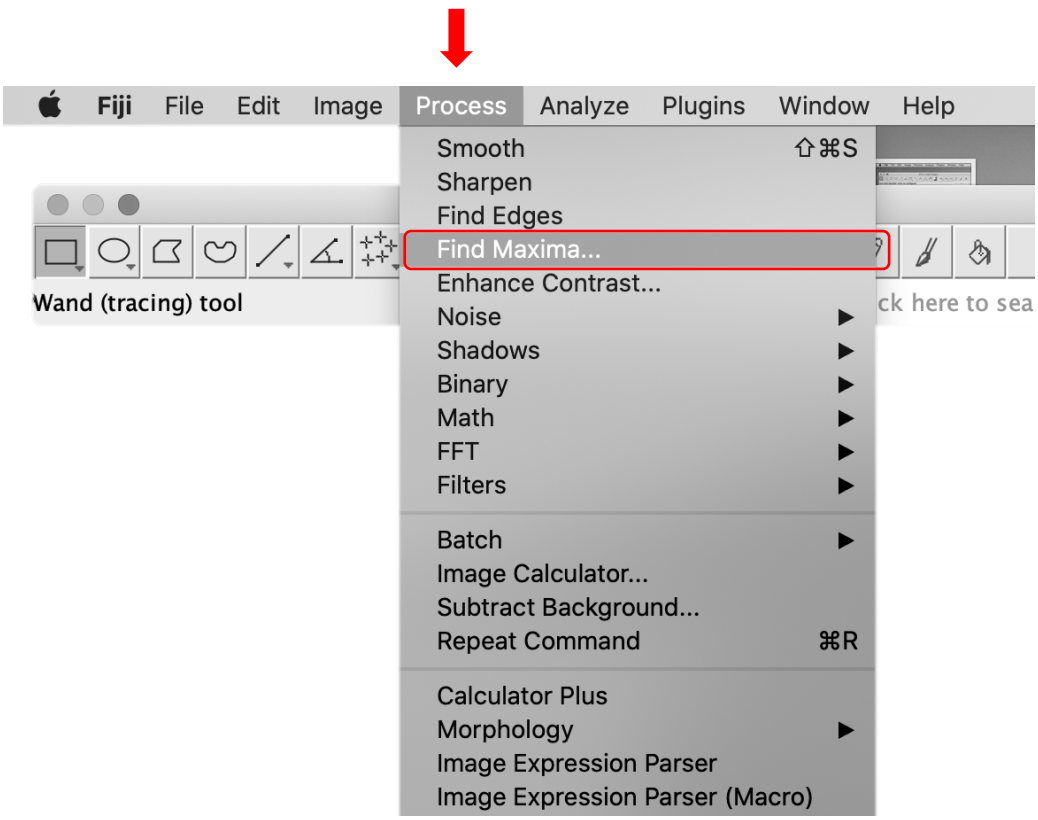

(A)

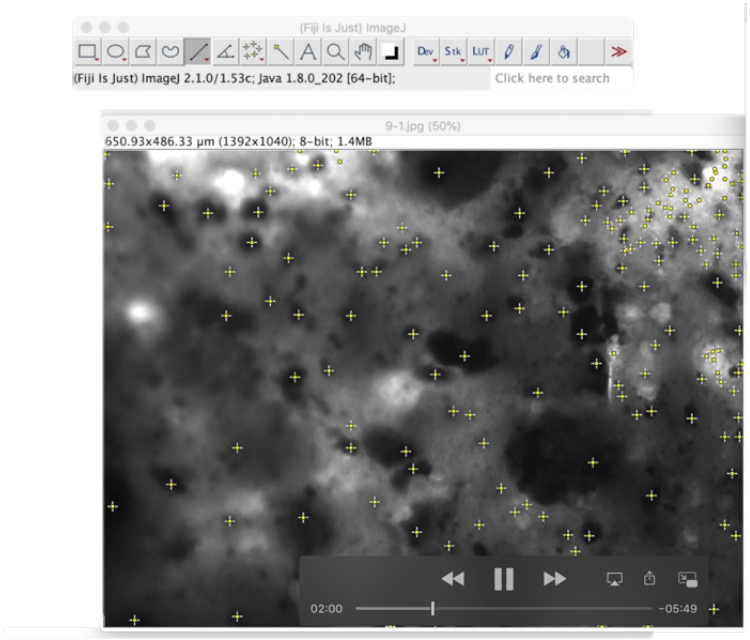
(Fiji Is Just) ImageJ
(Fiji Is Just) ImageJ 2.1.0/1.53c; Java 1.8.0_202 [64-bit];
Click here to search
9-1.jpg (50%)
650.93x486.33 µm (1392x1040); 8-bit; 1.4MB
02:00
-05:49

(B)

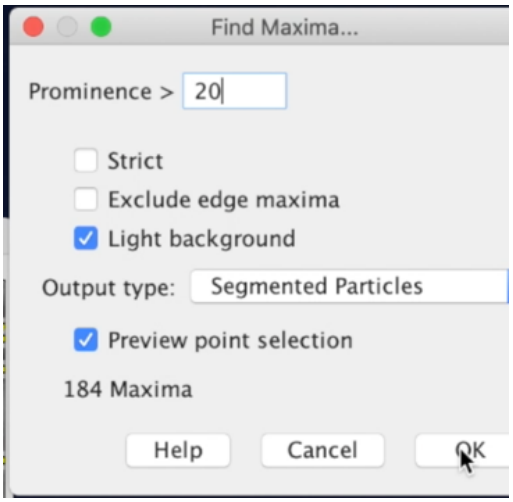
Find Maxima...
Prominence > 20
Strict
Exclude edge maxima
Light background
Output type: Segmented Particles
Preview point selection
184 Maxima
Help
Cancel
OK

(C)

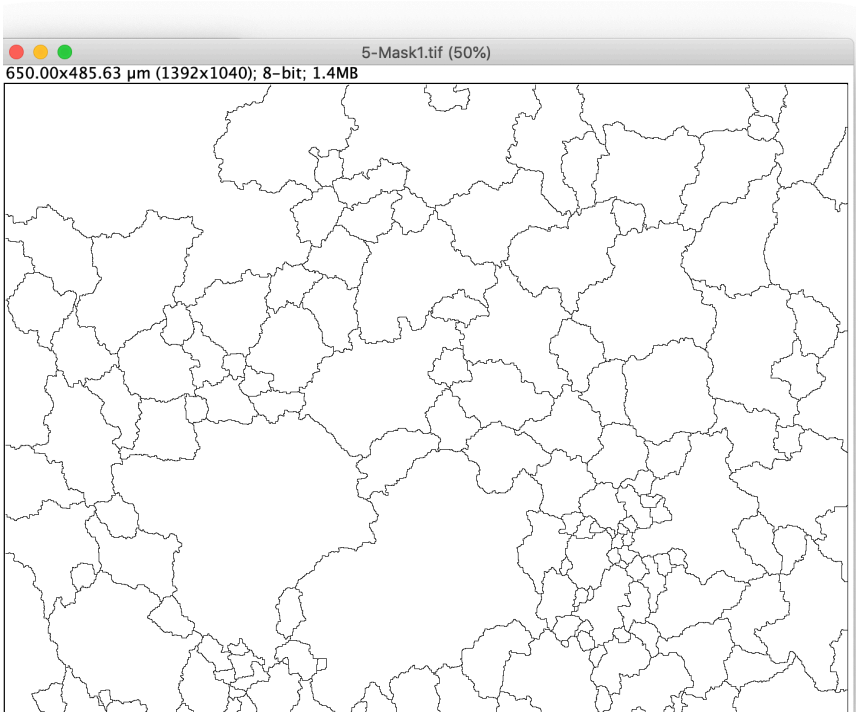
5-Mask1.tif (50%)
650.00x485.63 µm (1392x1040); 8-bit; 1.4MB

(D)

Figure 3.7 (A-D): Maxima function for particle segmentation

Trainable Weka Segmentation: Trainable Weka segmentation is a Fiji-ImageJ plugin where "a collection of machine leaning algorithms are combined with a set of chosen features producing pixel-based segmentations". *Trainable:* this plugin is trained to apply the input (train) data and apply it to the test data. *Weka:* makes use of all the classifier and tools. *Segmentation:* provides output results based on the training from the classifier provided. The ultimate objective of this plugin is to enhance the image processing field with the technological advances from the machine learning world. The flocs and backgrounds are outlined using different tracing tools (free-hand, circle, rectangle etc), then they are classified accordingly. The labels for particles vs Background/Voids are created under the *load classifier* tab. The software is then trained accordingly to perform the image segmentation based on the user's inputs (Ferreira and Rasband, 2012). In Figure 3.8 (A&B), the red areas represent the particles/flocs while the green areas are the voids/background. The toggle overlay feature enables to apply or remove the overlay image produced through the training process. This overlay image represents the probable areas of particles vs voids. The classifier is trained for an average of four times to obtain sufficient results. The trainable weka tool allows the user to save their data and classifiers and apply them on other "test data" or in this case other raw optical microscope images. In return, different images obtained from the same sample (for example, at the same time and the same polymer dose) can be analyzed in a time efficient manner by re-applying the same training data. At the end of the segmentation process, a probability map is created (Mask 2) where each pixel belongs to either a particle or a void.

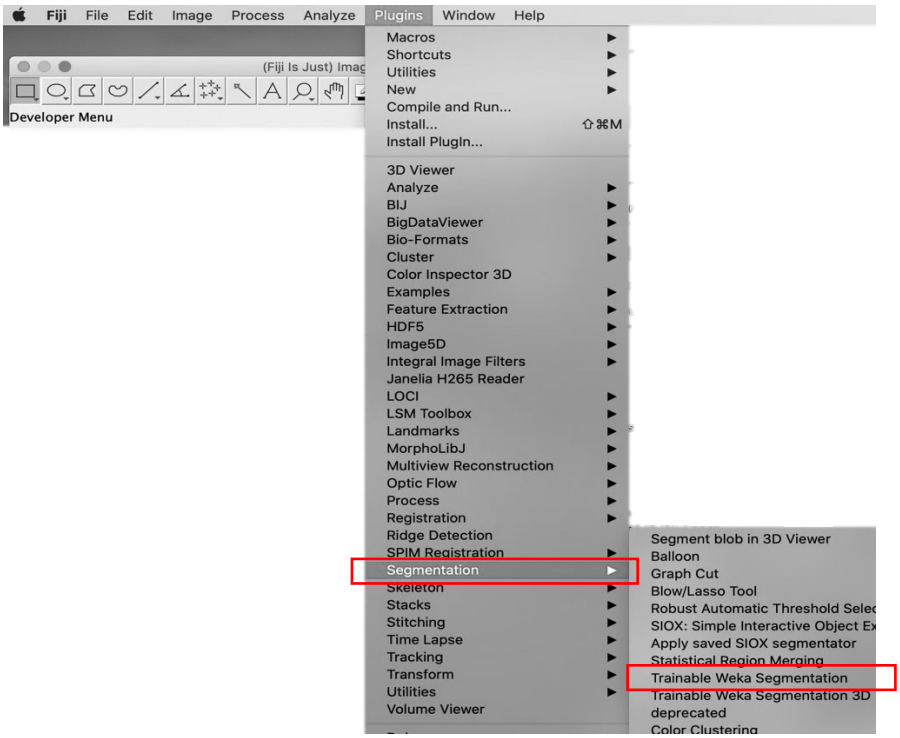
Fiji File Edit Image Process Analyze Plugins Window Help
Developer Menu
Macros
Shortcuts
Utilities
New
Compile and Run...
Install...
Install PlugIn...
3D Viewer
Analyze
BIJ
BigDataViewer
Bio-Formats
Cluster
Color Inspector 3D
Examples
Feature Extraction
HDF5
Image5D
Integral Image Filters
Janelia H265 Reader
LOCI
LSM Toolbox
Landmarks
MorphoLibJ
Multiview Reconstruction
Optic Flow
Process
Registration
Ridge Detection
SPIM Registration
Segmentation
Skeleton
Stacks
Stitching
Time Lapse
Tracking
Transform
Utilities
Volume Viewer
Segment blob in 3D Viewer
Balloon
Graph Cut
Blow/Lasso Tool
Robust Automatic Threshold Selec
SIOX: Simple Interactive Object Ex
Apply saved SIOX segmentator
Statistical Region Merging
Trainable Weka Segmentation
Trainable Weka Segmentation 3D
deprecated
Color Clustering

(A)

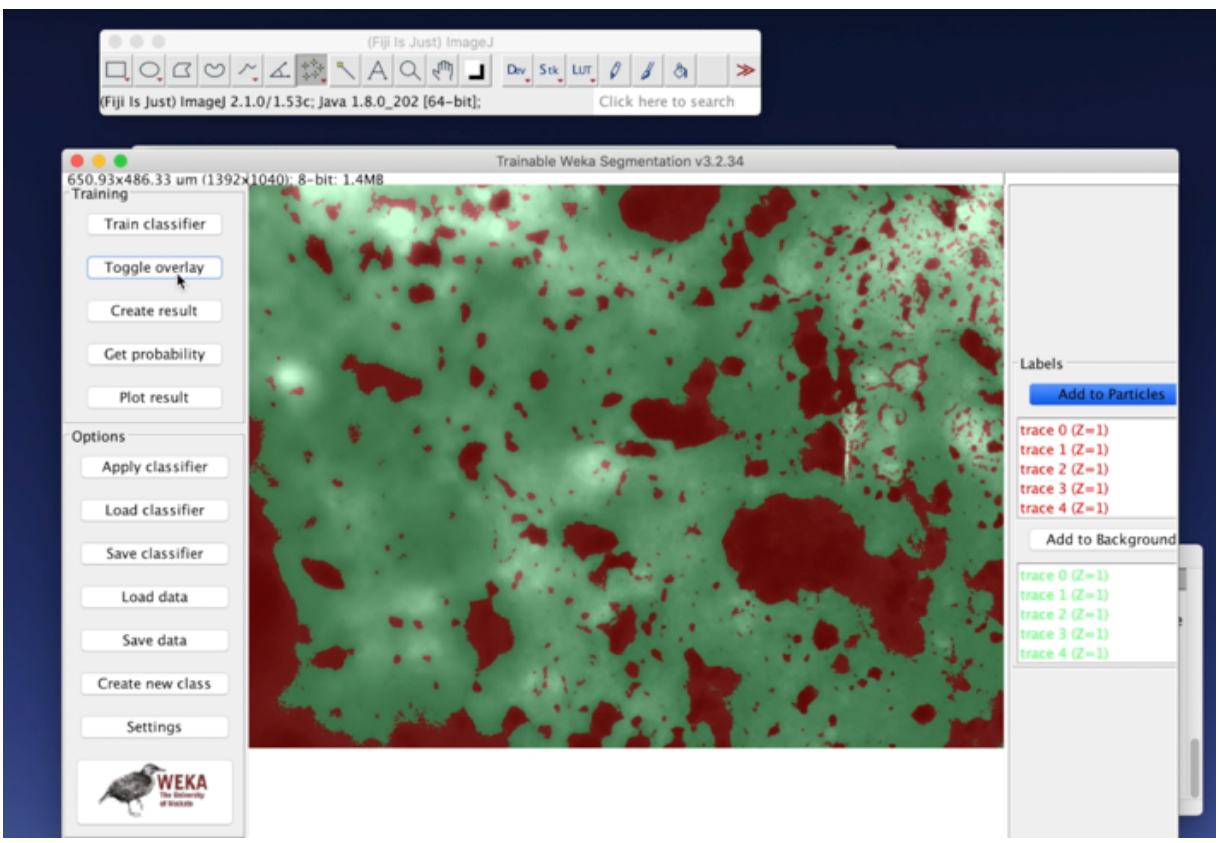
(Fiji Is Just) ImageJ
(Fiji Is Just) ImageJ 2.1.0/1.53c; Java 1.8.0_202 [64-bit];
Click here to search
Trainable Weka Segmentation v3.2.34
650.93x486.33 um (1392x1040); 8-bit; 1.4MB
Training
Train classifier
Toggle overlay
Create result
Get probability
Plot result
Options
Apply classifier
Load classifier
Save classifier
Load data
Save data
Create new class
Settings
WEKA
Labels
Add to Particles
trace 0 (Z=1)
trace 1 (Z=1)
trace 2 (Z=1)
trace 3 (Z=1)
trace 4 (Z=1)
Add to Background
trace 0 (Z=1)
trace 1 (Z=1)
trace 2 (Z=1)
trace 3 (Z=1)
trace 4 (Z=1)

(B)

Figure 3.8 (A&B): Trainable Weka segmentation – Particles vs Void Classification

Thresholding: After segmentation a probability map is created. A probability maps contains some blurry regions that are then removed using thresholding technique. The thresholding tool is accessed from the toolbox through *Image* > *Adjust* > *Thresholding.* It also enables segmenting 8-bit images into features of interest and background by setting the thresholding value. This in return removes the unwanted low frequency regions by ignoring them and converting them into nan values. After thresholding, the regions are converted to either black (pixel value of 0) or white (pixel value of 255). Increasing or decreasing the threshold values can skew the results since it affects the size/ region of the particles. However, there are different algorithms included and Fiji-ImageJ allows to try all methods which then produces a montage with the results from all of them.

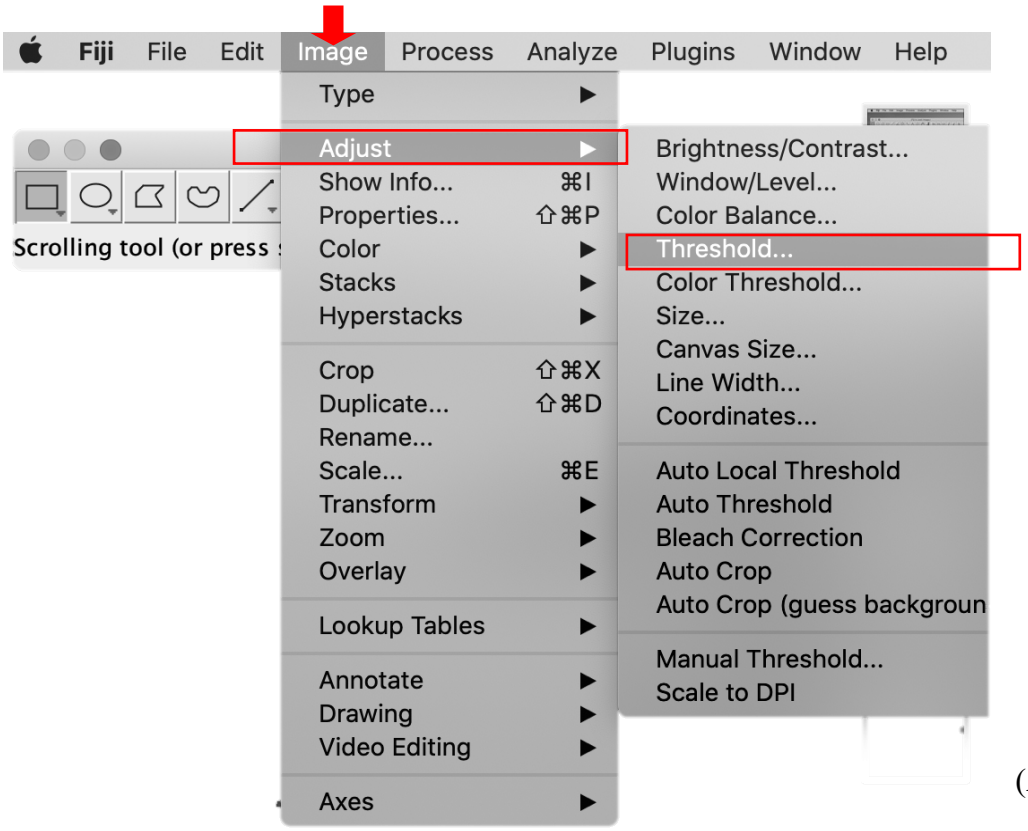

(A)

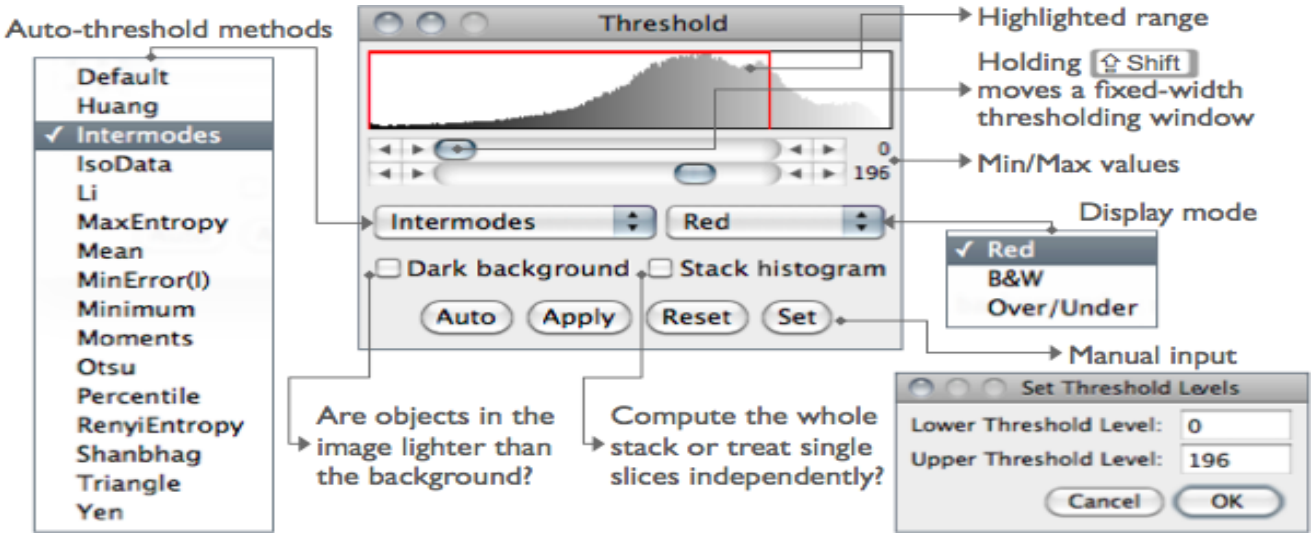
Auto-threshold methods
Default
Huang
Intermodes
IsoData
Li
MaxEntropy
Mean
MinError(I)
Minimum
Moments
Otsu
Percentile
RenyiEntropy
Shanbhag
Triangle
Yen
Threshold
Highlighted range
Holding ⇧ Shift moves a fixed-width thresholding window
0
196
Min/Max values
Intermodes
Red
Display mode
Red
B&W
Over/Under
Dark background
Stack histogram
Auto
Apply
Reset
Set
Manual input
Are objects in the image lighter than the background?
Compute the whole stack or treat single slices independently?
Set Threshold Levels
Lower Threshold Level: 0
Upper Threshold Level: 196
Cancel
OK

(B)

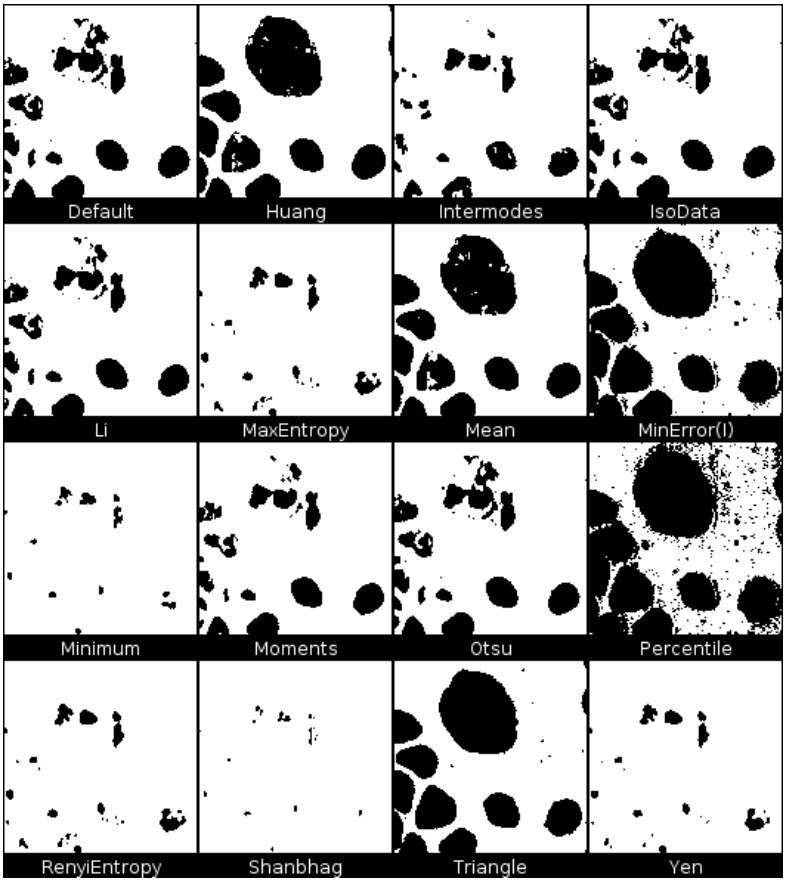
Default
Huang
Intermodes
IsoData
Li
MaxEntropy
Mean
MinError(I)
Minimum
Moments
Otsu
Percentile
RenyiEntropy
Shanbhag
Triangle
Yen

(C)

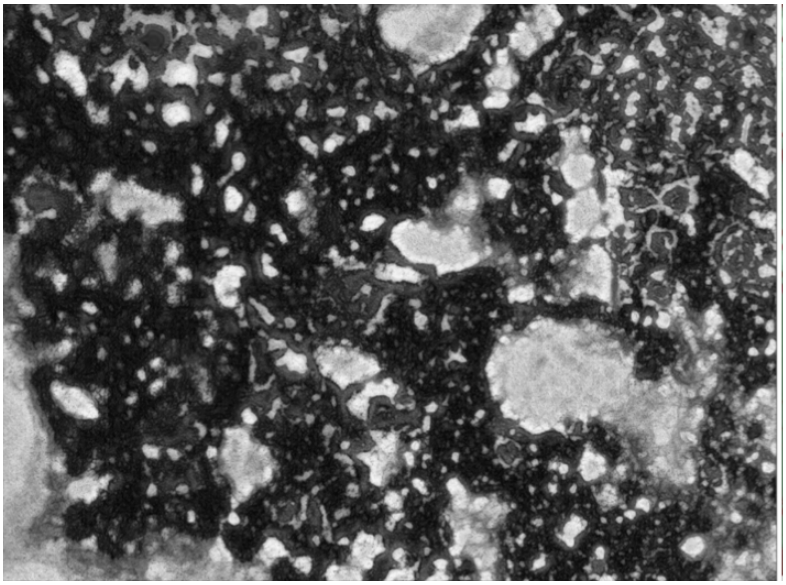

(D)

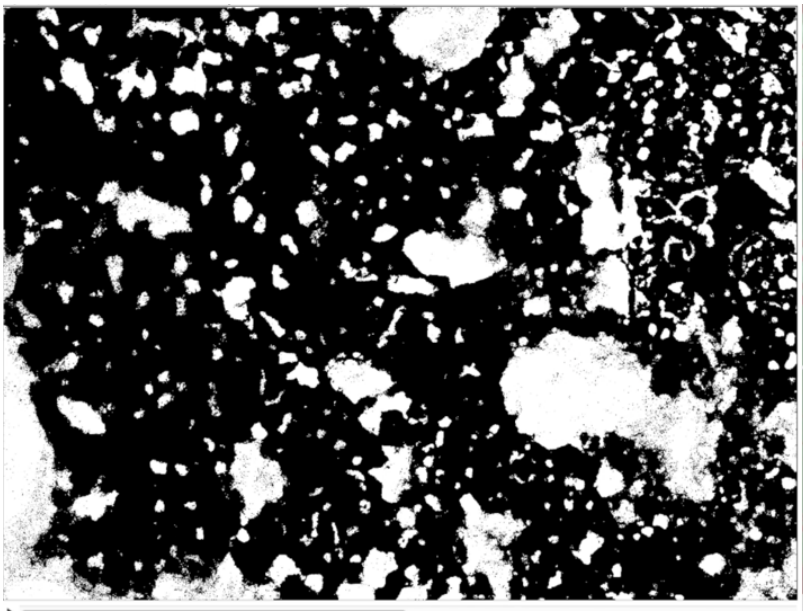

(E)

Figure 3.9: Generated Probability map & Thresholded Image

Binary Image -Mask1& Mask 2: Using the image calculator tool, the binary mask-like image from the maxima function (Mask1) is then combined with the binary image from the Weka segmentation (after thresholding- Mask2). This enables the software to combine and validate the regions assumed to be flocs/ voids by combining both techniques.

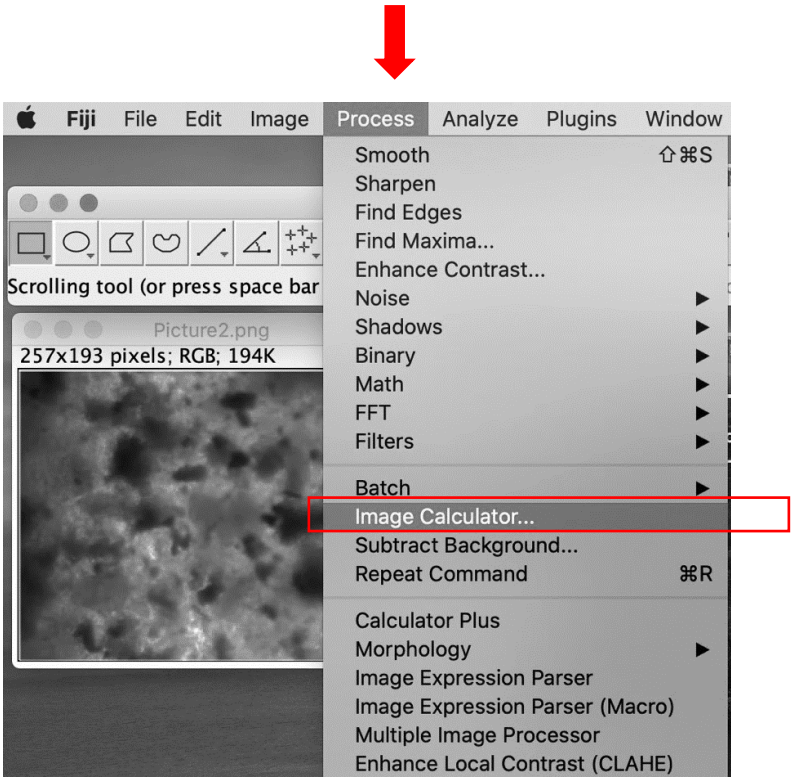

(A)

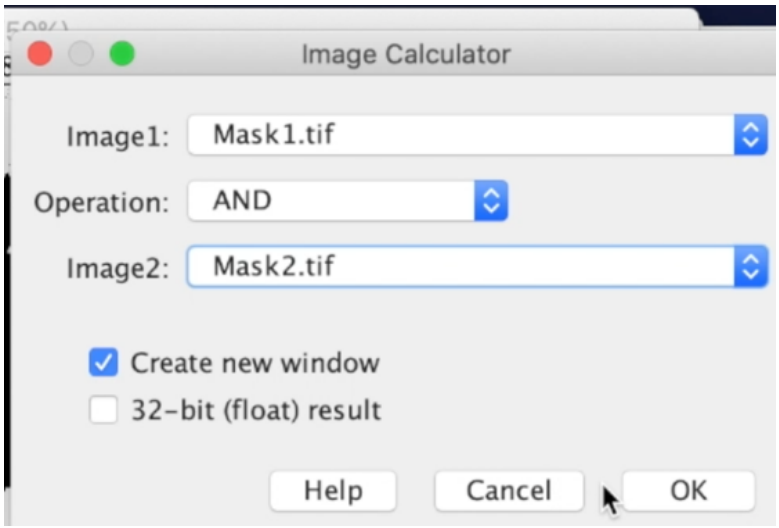

(B)

Figure 3.9: Combining two segmentation techniques to produce a final binary image

Analyze particles: Finally, the binary image produced can be analyzed quantitively. This command counts and measures objects in the binary image created. The software can provide the total particles area, particle count, total background/voids area, % particle area occupied, perimeter as well as a particle size distribution breakdown. Finally, the outlines of the measured particles can be produced for better visualization

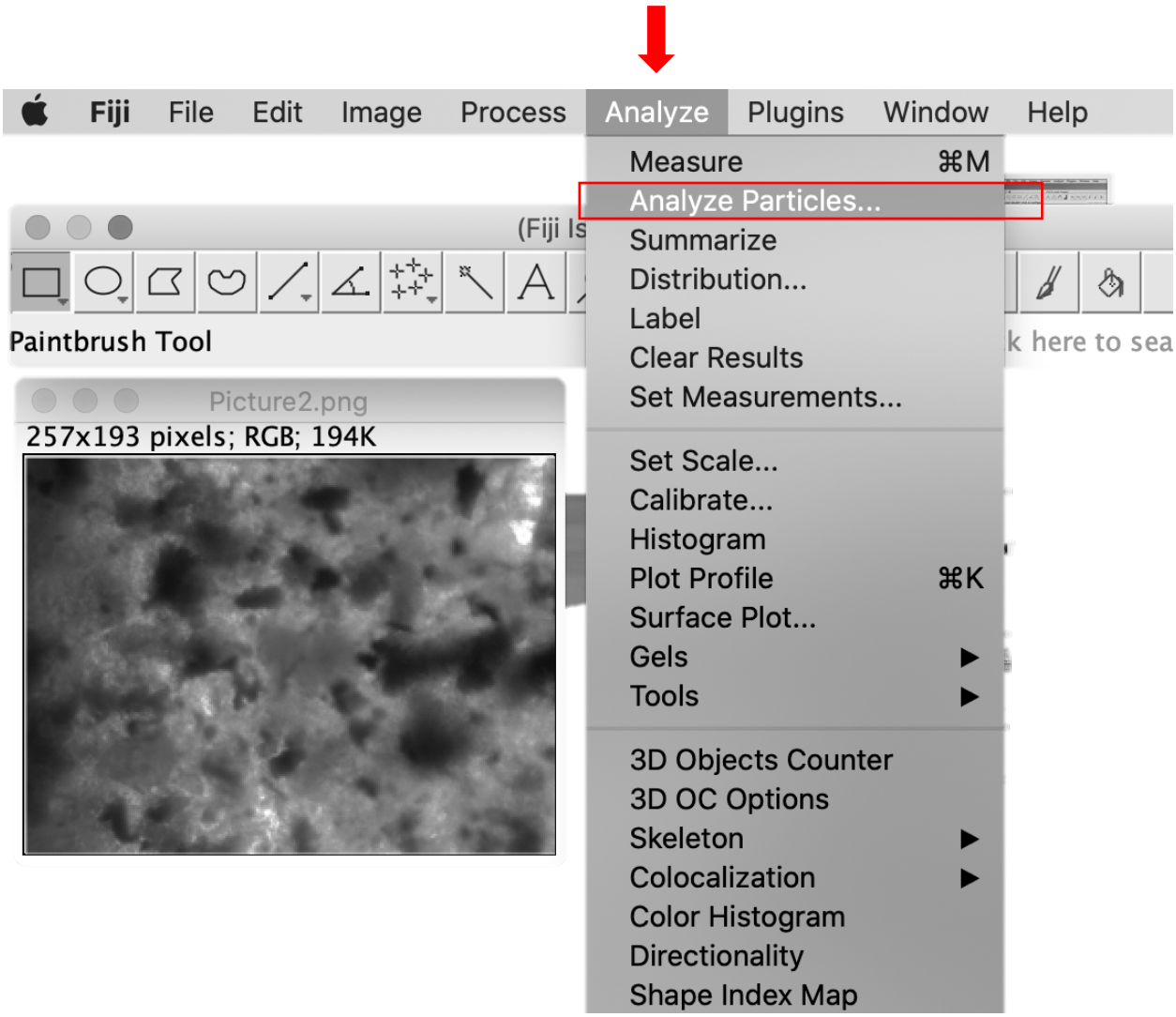

(A)

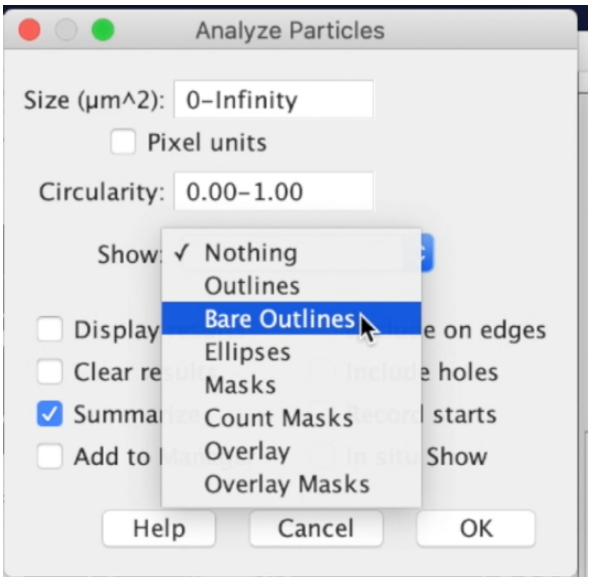

(B)

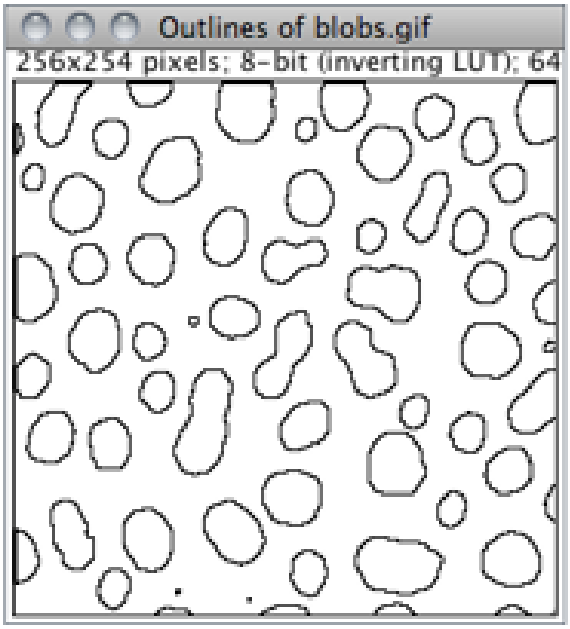

(C)

Figure 3.10 (A-C): Quantitative Image Analysis of particles using “Analyze Particle” tool

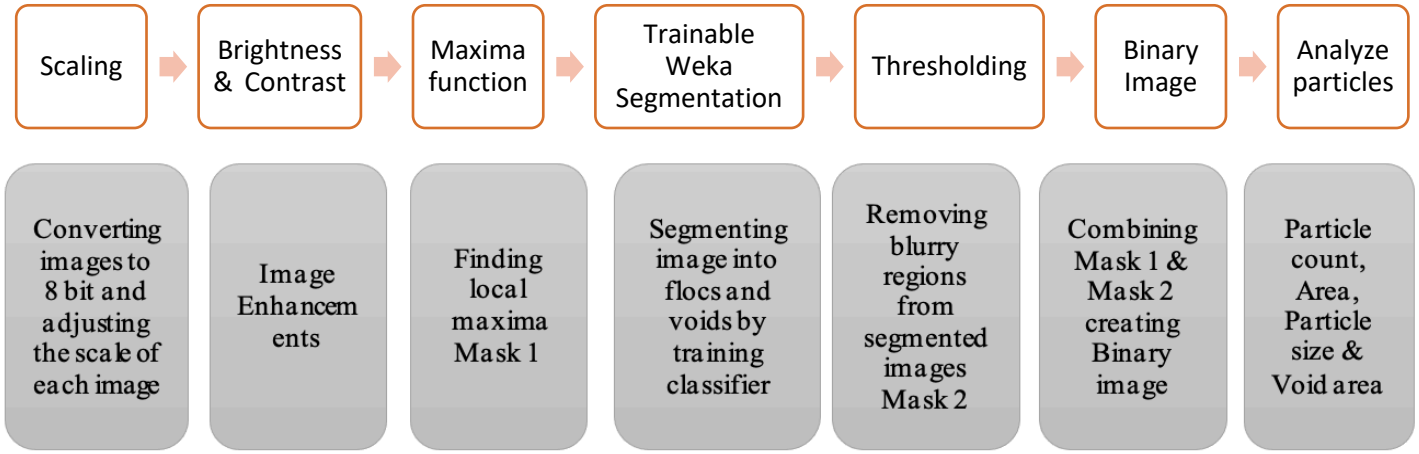

Figure 3.11: Workflow chart for Image processing and Quantitative analysis of Optical microscope images

3.6.3 Oscillatory Rheometer

The oscillatory rheometer tests were conducted using the HAAKE Viscotester iQ Air-bearing Measuring Head from Spectra Research Corporation (SRC). The testing fixture was a FL22 4/SS vane model with 4 blades, diameter of 22 mm, and height of 16 mm.

The oscillatory rheometry tests are used to examine the rheological parameters including the elastic modulus (G') and viscous modulus (G") of the flocculated polymer amended FFTs. The G' and G'' are recorded at a controlled increasing shear stress amplitude. The oscillation stress was applied at a constant frequency of 10 rad/sec (1.6 Hz) was selected based on Mizani et al. (2017). The elastic response of the flocculated FFT is independent of the frequency over a wide range of frequencies (between 0.1 to 10 hz). The oscillatory stress sweep was initially at 0.1 Pa and logarithmically increased over 25 steps (Aldaeef et al. 2019). From these tests, the elastic

range is determined (where the modulus of elasticity is relatively constant). In addition, the value of the elastic shear modulus and finally the yield stress which is represented at the point where G' decreases and G" becomes dominant. During measurement of G' over time, the range of shear stresses is limited to the elastic range determined by the original oscillatory sweep test.

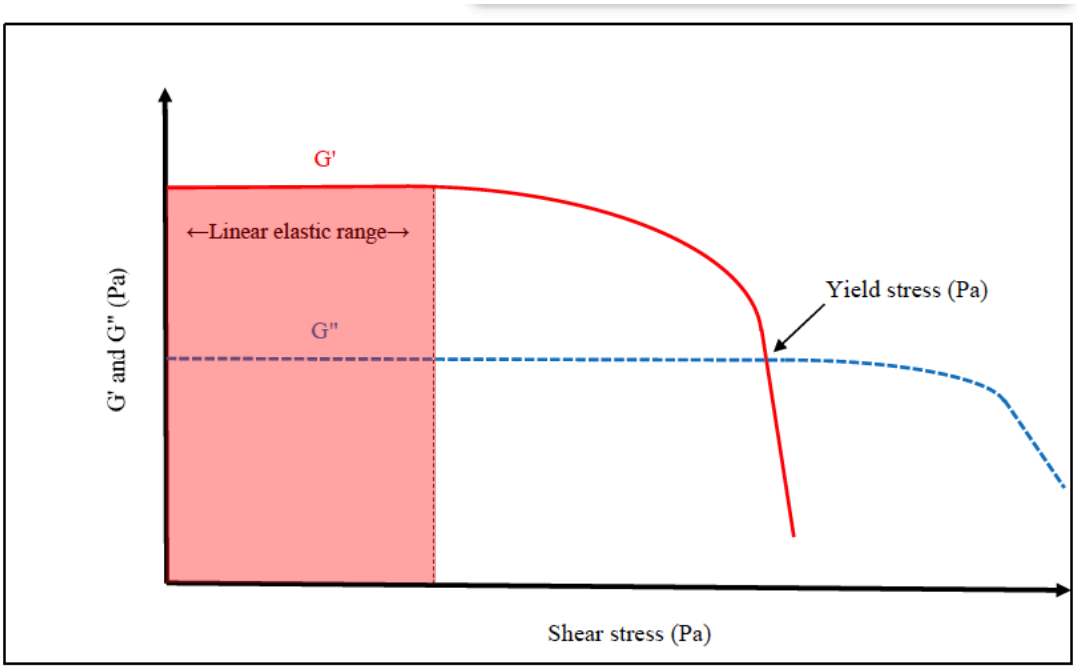

Figure 3.12: Oscillatory sweep test illustrating increasing shear stress with each oscillation at a constant oscillation frequency (Modified from Muhammad (2020)).

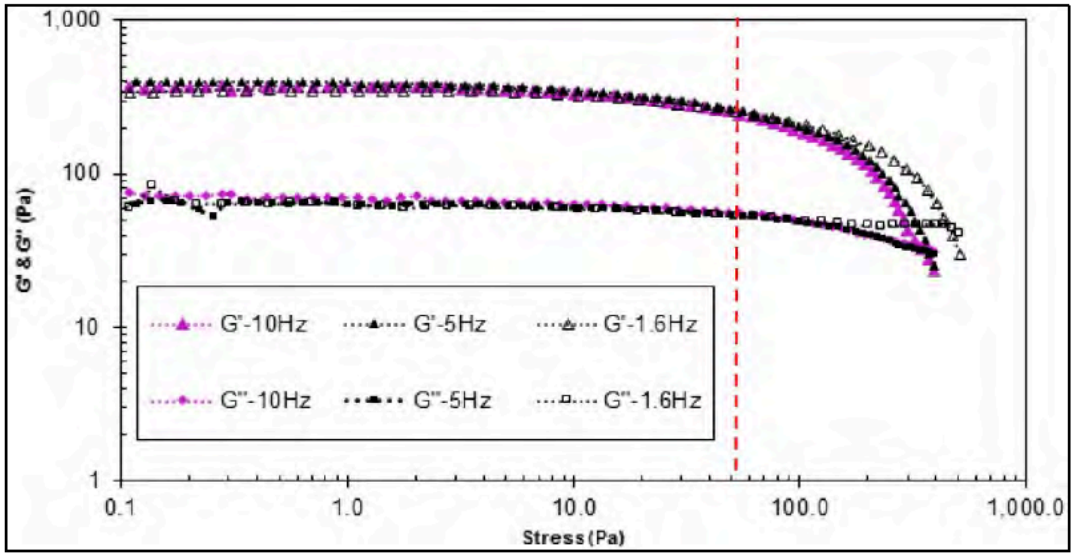

Figure 3.13: Amplitude sweep tests performed on fFFT showing the linear viscoelastic regions for three different frequencies (-10 Hz, -5 Hz, amd -1.6 Hz). (from Mizani et al. 2017)

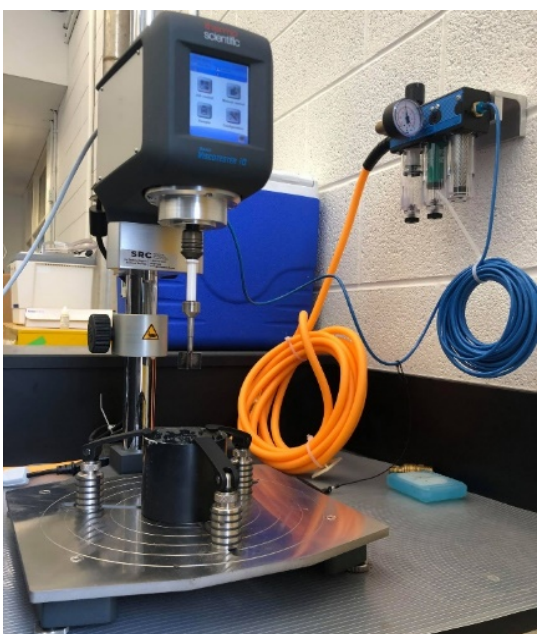

Figure 3.14: Oscillatory rheometer HAAKE Viscotester iQ

3.6.4 Capillary Suction Time (CST) test:

The CST test is a type of static filtration test that uses a filter paper as a medium and measures the rate the material passes through. Hence, it is used to assess the dewatering properties of the material. The CST used is the Triton Type 319 Multi-purpose CST, the filter paper is a special CST Paper, Chromatography Grade, Whatman 17 with dimension of 70mm x 90mm. The CST test measures the water release, in return it is used to assess the quality of flocculation and dewatering performance of the polymer-amended FFT samples. The CST values are inversely proportional to the water released. Higher CST values indicate poor flocculation and low dewaterability. Hence, the CST test is an important performance indicator where a low CST value refers to optimum conditions.

Figure 3.15: Triton Type 319 Multi-purpose CST machine

3.6.5 Estimating Consolidation Properties:

The estimation of consolidation properties using various predictors for oil sands and kaolinite are used in this thesis. The prediction of the compressibility curve method is relatively simple if the maximum depth of the deposition area, the initial solids content, and the specific gravity of the tailings are known. Changes in compressibility with time may have an influence on the dewatering and consolidation behavior of tailing deposits. This technique was suggested by Carrier and Freeman (2018), where a spreadsheet based numerical solution is used to estimate the final height of the fluid fine tailings without the use of large strain non-linear modelling solutions. This method splits the total deposition depth into small layers and estimates the final effective stress at the surface of each layer. The final void ratio is then calculated using the compressibility relationship ($e=a\sigma v'^{b}$). Finally, the hydraulic conductivity at the surface is calculated and the final height is determined based on the initial and final void ratios and initial height. (Carrier and Freeman, 2018). The analysis does not account for sedimentation and assumes that the single drainage boundary condition.

The samples were deposited in 100ml graduated cylinders for approximately 3 weeks, after which there was no significant settlement behavior observed. Figure 3.16(A-F), presents the sample after settling. First, the graduated cylinder containing the sample is weighed, then the bleed water is extracted using a syringe and the water removed is weighed. Second, the extraction process takes place by using a spatula to extract approximately 1 cm of tailings. To remove any excess bleed water, a mesh is used in the top layers. The extracted 1cm layer is then weighed and placed in an oven at a temperature of 105 ^{0}C for 24 hours to remove the water and subsequently, the water content is then estimated.

(A) **(B)**

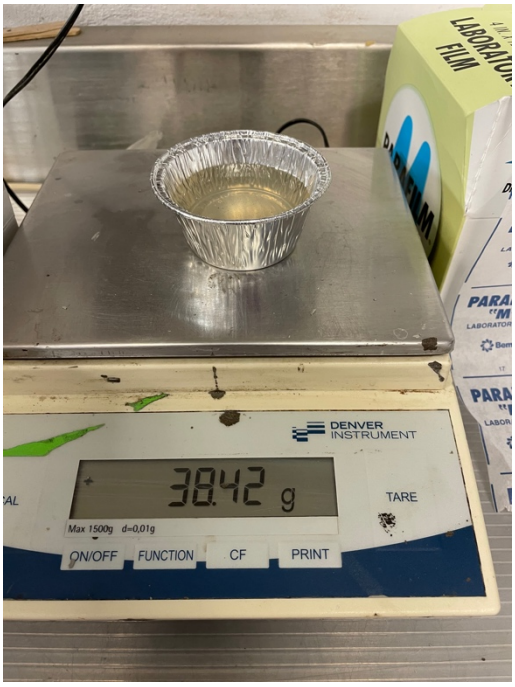
DENVER INSTRUMENT
38.42 g
TARE
Max 1500g d=0.01g
ON/OFF
FUNCTION
CF
PRINT

(C) **(D)**

(E)

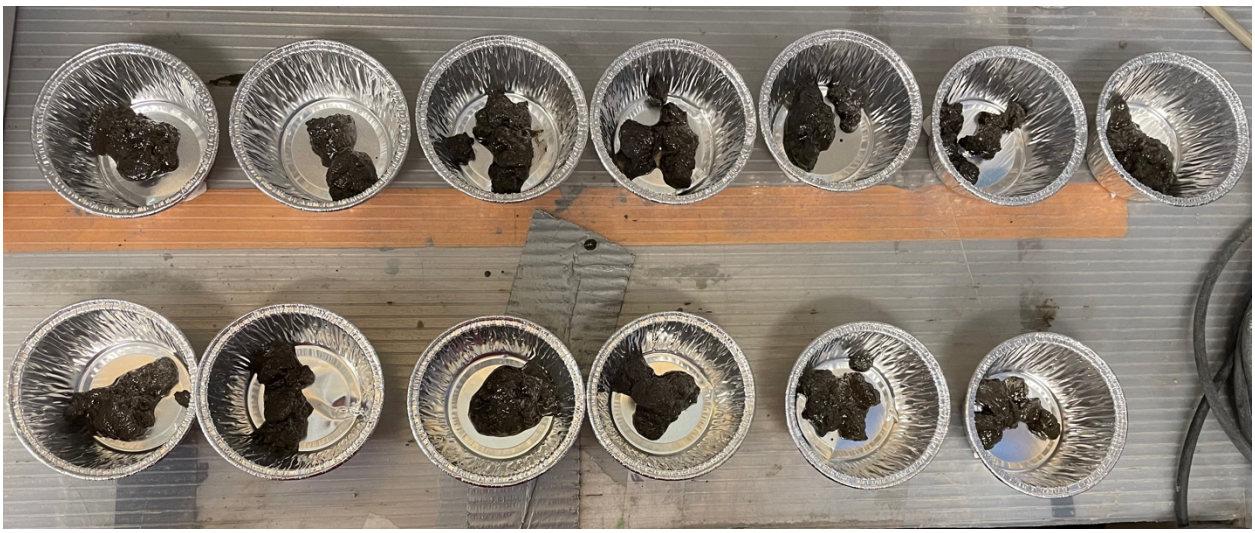

(F)

Figure 3.16 (A-F): Methodology for estimating consolidation properties

Pane and Schiffman (1997) technique is used calculate the initial hydraulic at the initial void ratio using the following equation:

$$k(e) = \frac{vsi\ (1+e)}{\gamma *} \qquad (\ldots 3.5)$$

where v_{si} is the initial settling velocity and k is hydraulic conductivity, e is the void ratio, γs is the unit weight of soil and γw is the unit weight of water.

$$\gamma * = \frac{\gamma s - \gamma w}{\gamma w} \qquad (\ldots 3.6)$$

This equation is only valid if the settling velocity is constant or if there is a suspension at the initial void ratio at the sediment-water interface.

Chapter 4: Results and Discussions

In this chapter, the image processing methodology presented in chapter 3 is implemented using Fiji-ImageJ software in order to process the Optical microscope images. Through which quantitative metrics such as the floc size, floc count, and void area are obtained and validated with tailings performance indicators. Four (4) different data sets are presented and analyzed in this chapter, a summary is shown in Table 6. Quantitative metrics of the optical microscope images are compared with quantitative metrics from the other tests across all these samples.

Table 6: Summarized tests, tailing type, mixing method and tests performed in each test.

Test	**Tailings type**	**Mixing method**	**Tests performed**
Assessing the effects of different mixing durations	Syncrude tailings	Torque-based feedback in Couette Rheometer	CST Optical microscopy Settlement & Consolidation properties from graduated cylinders Oscillatory Rheometer
Polymer Optimization of flocculated FFT	Shell tailings	Torque-based feedback in 5 Litre bucket	CST Optical microscopy Settlement from graduated cylinders Oscillatory Rheometer

Pipeline transport shear modelling on flocculated tailings	Shell tailings	Torque-based feedback in Couette rheometer	CST Optical microscopy Settlement & Consolidation properties from graduated cylinders
Optical microscopy applications in quantifying the microstructure of Kaolinite	Kaolinite	Hand-mixing with flocculant	Optical microscopy Settlement & Consolidation properties from graduated cylinders

4.1 Assessing the effects of different mixing durations on Syncrude tailings

The raw FFT was flocculated with PAM A3338 polymer with a dosage of 600 ppm at a rotational speed of 250 rpm in the Couette rheometer. The mixing was stopped when the torque applied reached its peak as a baseline reference to the shearing protocol. The developed torque showed a sharp increase after 3-4 seconds of polymer injection. The optimum mixing duration was determined based on the time that corresponded to the maximum developed torque during flocculation. To simulate and evaluate the effect of shearing on the flocculated samples, the samples were mixed for additional 3 seconds and 10 seconds after the peak torque is reached. Images from both samples obtained at 0 hour and 24 hour post flocculation, raw images were obtained from the optical microscope and studied for the same shear time. This is to ensure the

results and trends represent the whole material despite the slight variations within the same sample.

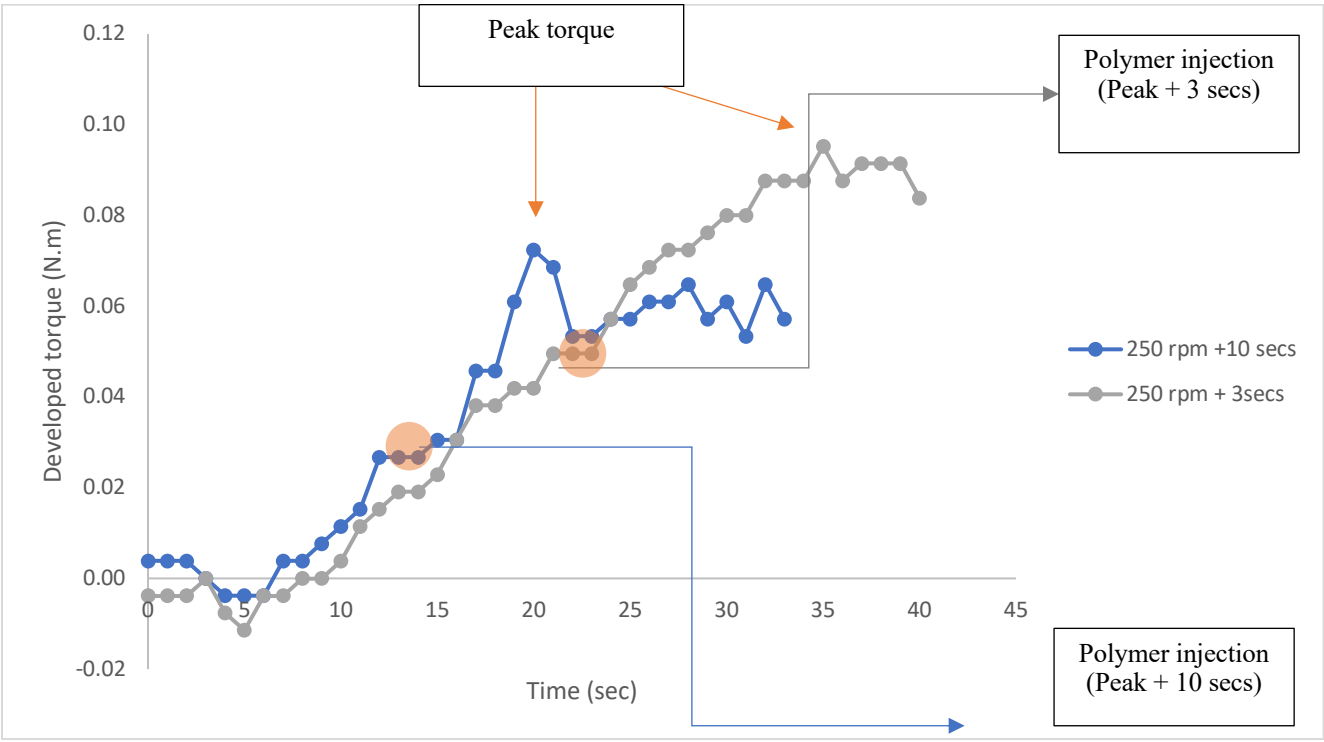

Figure 4.1: Developed Torque over time during flocculation

The development of torque during flocculation is plotted in Figure 4.1 for shearing time of 3 seconds and 10 seconds. The peak torque corresponds to the optimum mixing duration with optimum flocculation conditions.

To evaluate the short-term dewatering behavior and the microstructure of the flocculated FFT samples, several key performance indicator tests were conducted. This includes: Capillary Suction Time (CST) test, Oscillatory Rheometry tests, and Optical microscopy.

Table 7: Performance indicator tests

Performance Indicators	
Developed Torque	Flocs formation
CST	Immediate dewaterability
Optical Microscope	Floc Size & morphology
Graduated cylinders	Settlement
Oscillatory Rheometry	Elasticity (G'&G'')

The optical microscope image analysis showed that the sheared samples at 3 seconds showed the same trends and followed the same behavior as the non-sheared (peak torque) sample. Figures 4.2-4.4 show the raw images obtained from the optical microscope and the final binary images after using Fiji-ImageJ (Method explained in Chapter 3). From each sample, the optical microscope images were obtained from different locations from the surface of the sample, avoiding disrupting the sample, so that the images give a good representation of the sample. The variability within a given sample was observed to be minimal. Images from the same sample are shown in Appendix A.

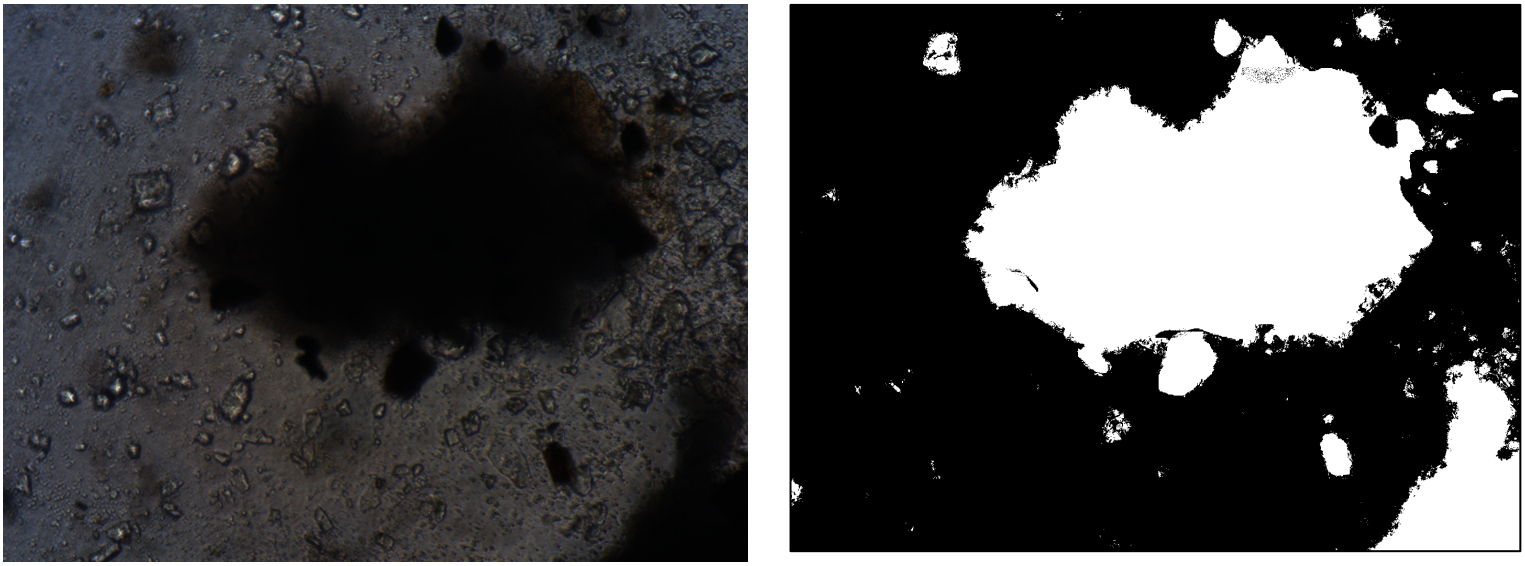

(A) (B)

Figure 4.2 (A&B): Raw Optical microscope image & Binary Image after processing using ImageJ - Trial 1 for “Peak torque + 3 secs”

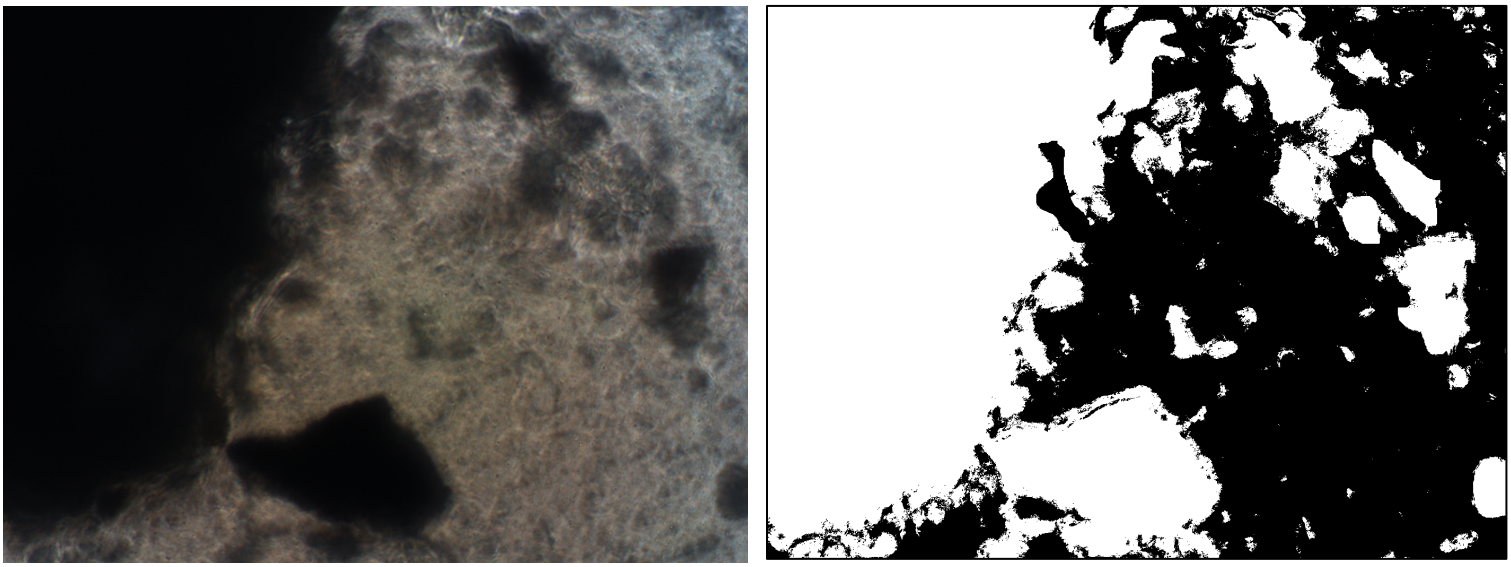

(A) (B)

Figure 4.3 (A&B): Raw Optical microscope image and Binary Image after processing using ImageJ - Trial 2 for “Peak torque + 3 secs”

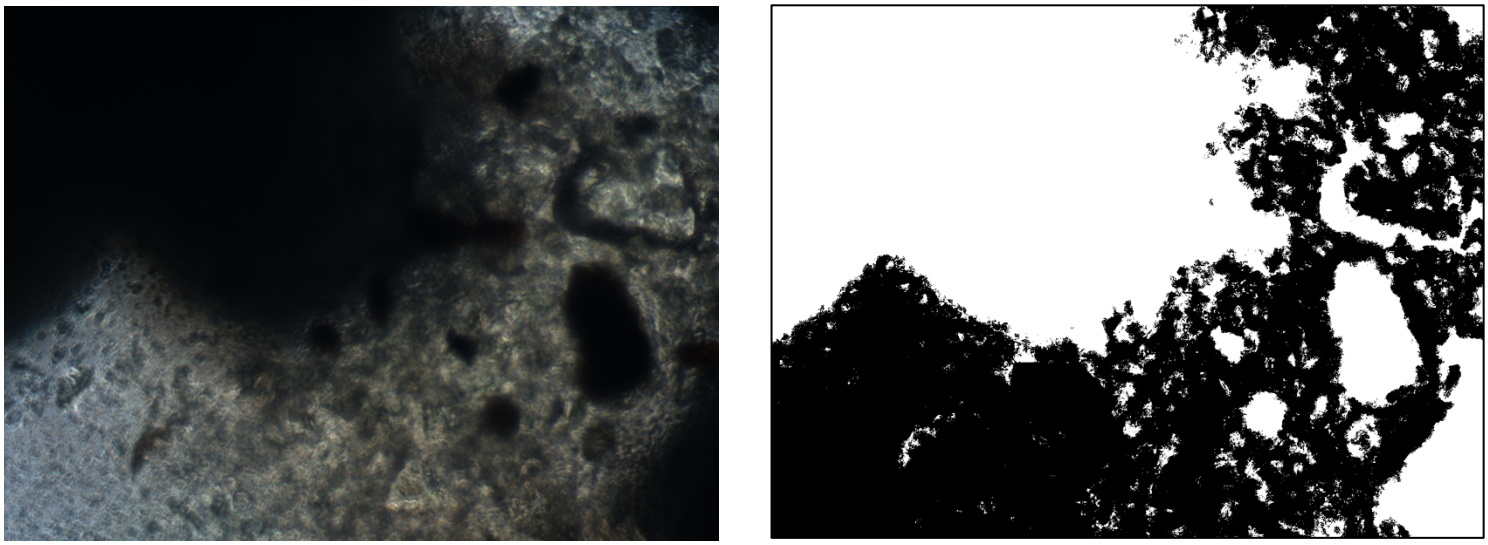

(A) (B)

Figure 4.4 (A&B): Raw Optical microscope image and Binary Image after processing using ImageJ - Trial 3 for “Peak torque + 3 secs”

Through Fiji-ImageJ, using the analyze particle feature, the number of particles are extracted and then plotted on the graph shown above. Comparing the images for the same sample, the Fiji-ImageJ analysis is shown to produce repeatable trends. The variability between the three images is very minimal, despite the relatively small size ranges plotted in Figure 4.5 (A). Overall, the particle size distribution bin (> 5000 μm^2) for larger particle is more dominant in the “peak torque + 3 secs” samples.

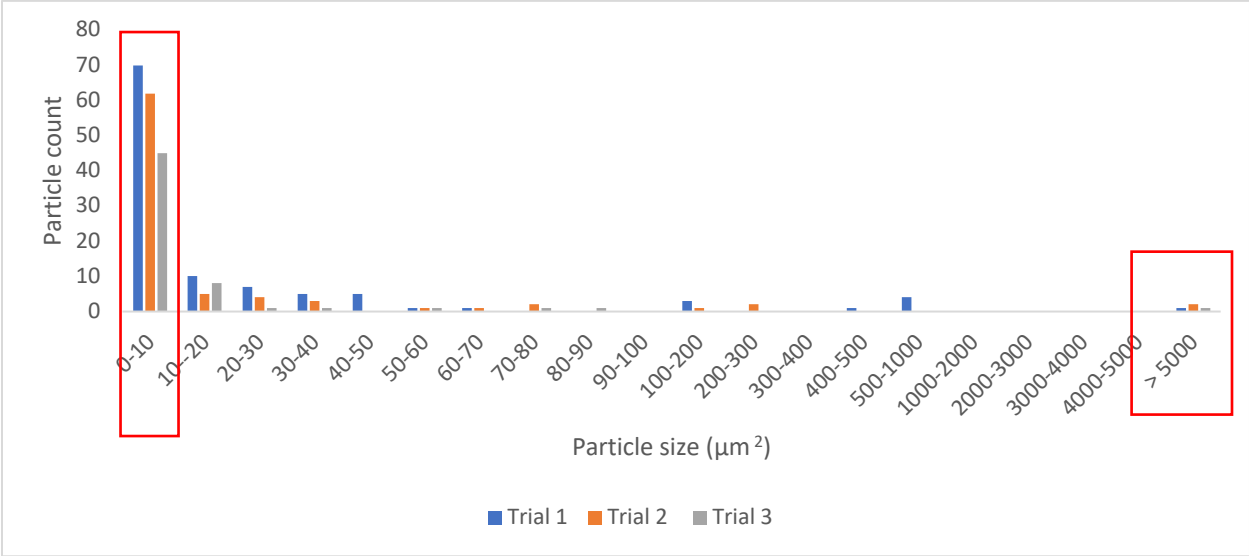

(A)

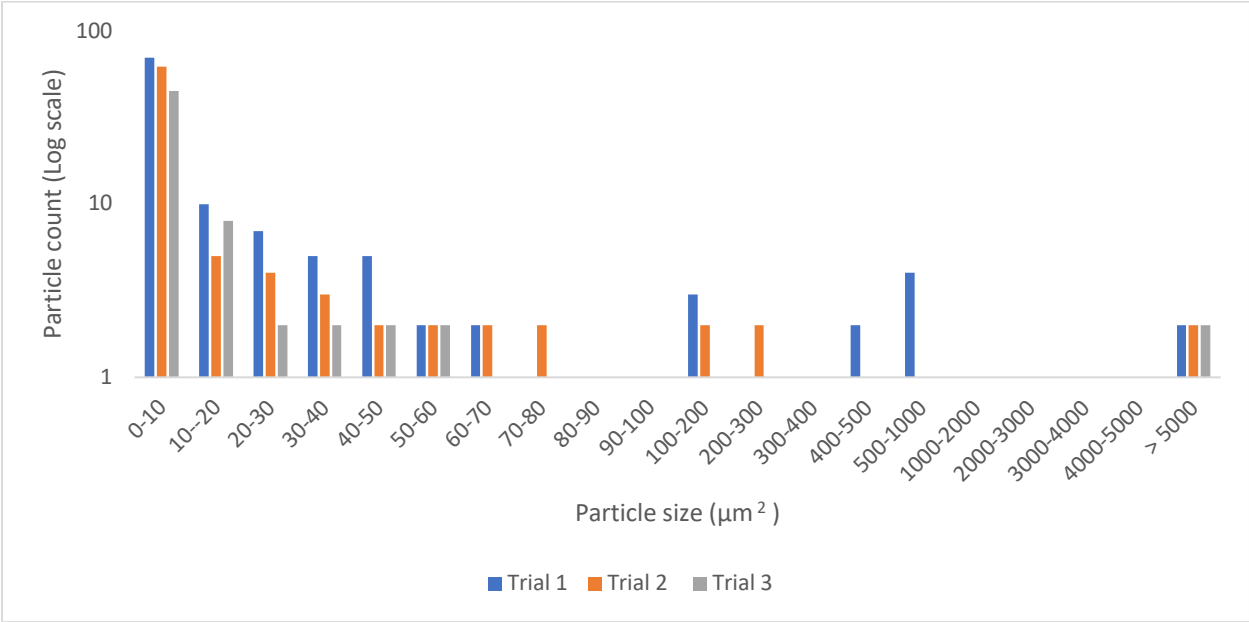

(B)

Figure 4.5 (A&B): Particle size distribution for "Peak torque + 3 secs" normal & log scales.

On the other hand, the "peak torque + 10 secs" sample was flocculated using the same polymer dosage but the shearing time is 10 seconds after the peak torque is reached. The polymer

amended FFT shows de-flocculation which led to a higher number of smaller flocs in comparison with the “peak torque + 3 seconds” samples, consistent with the longer shearing time and de-flocculation of larger flocs as shown in Figures 4.6 and 4.7.

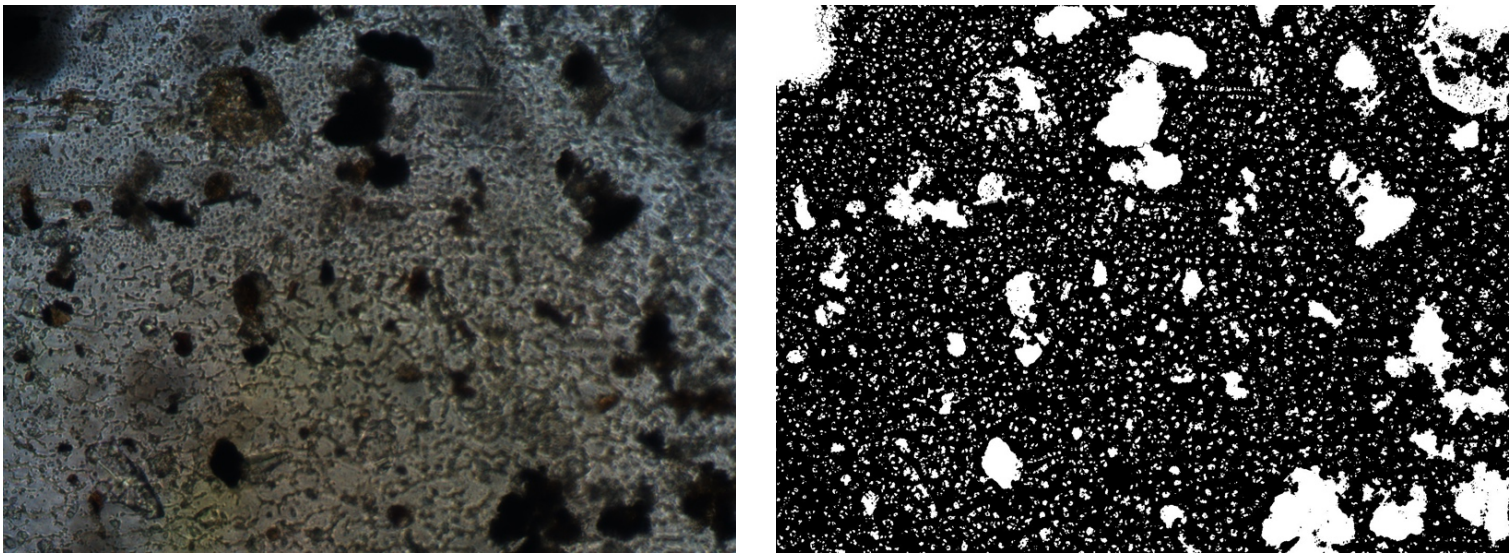

(A) (B)

Figure 4.6 (A&B): Raw Optical microscope image and Binary Image trial 1 for “Peak torque + 10 secs”

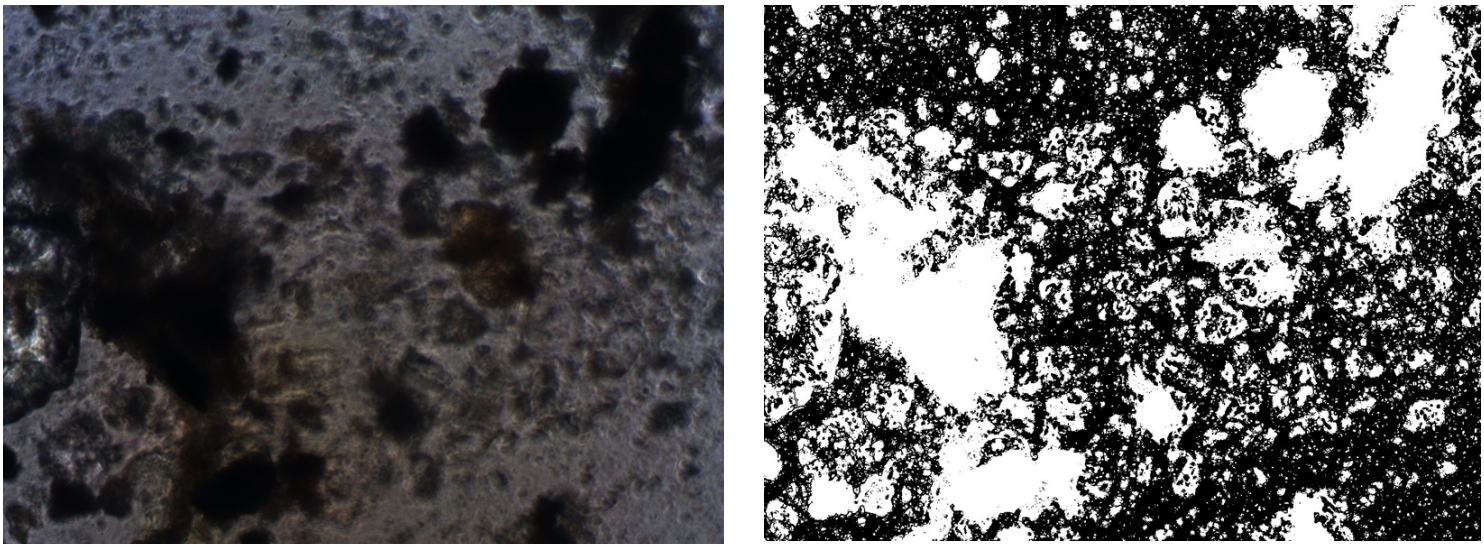

(A) (B)

Figure 4.7 (A&B): Raw optical microscope image and Binary Image - Trial 2 for "Peak torque + 10 secs"

Using the analyze particles tool from Fiji-ImageJ, the floc size distribution for the peak torque + 10 seconds is shown in Figure 4.8 (A&B). There's a clear correlation between the shearing time and the particle size. As the shearing time increases, the floc size decreases. The large flocs are clearly seen in the binary images and the particle size distribution curves presented in the "peak torque + 3 seconds" data.

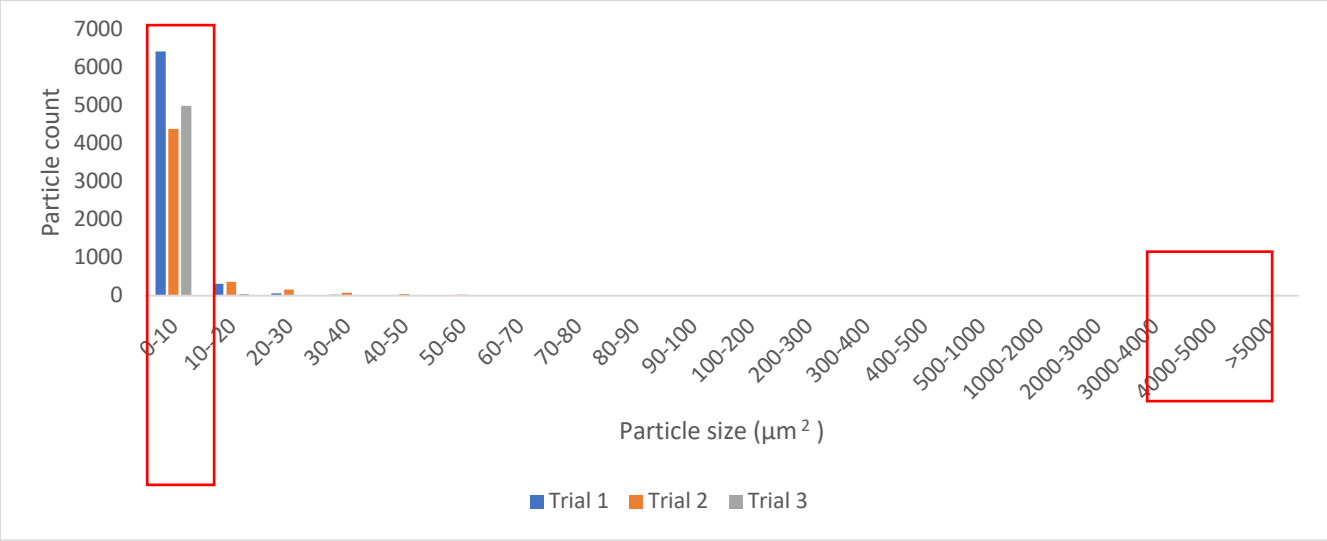

(A)

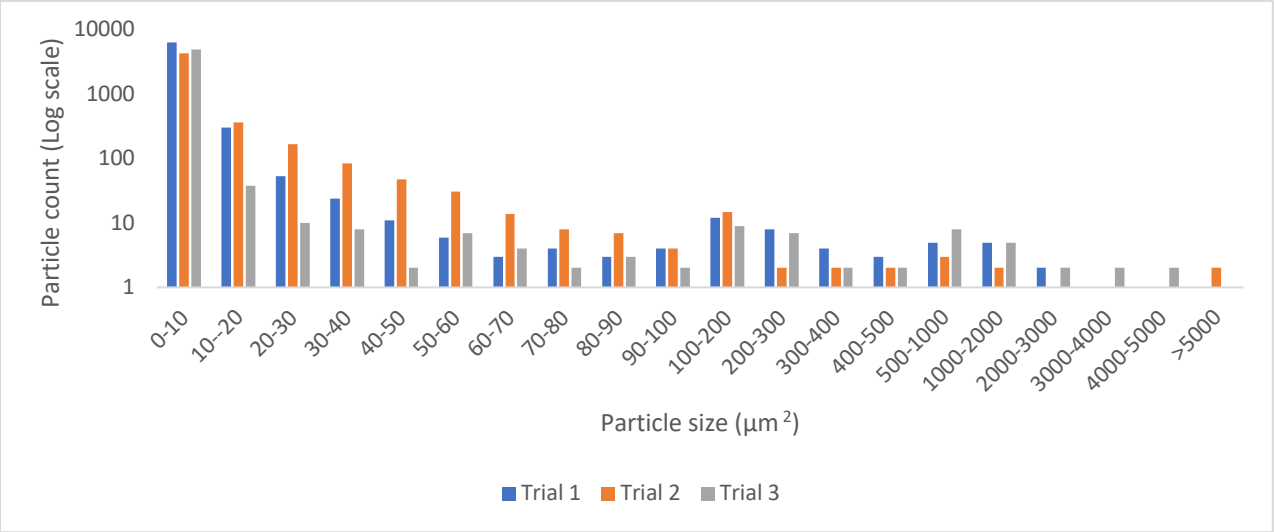

(B)

Figure 4.8 (A&B): Particle size distribution for "Peak torque + 10 secs"

The increase in the size of flocs is clearly seen in the binary images produced through image processing where the average total particle area for the "peak torque + 3 sec" sample is found to be significantly higher than the "peak torque + 10 seconds" (Figure 4.10). This can be directly correlated with the surface area those particles occupy since larger flocs are observed in the "peak torque + 3 sec" samples. Moreover, the maximum size flocs are found to in the size bin (> 5000 μm^2) for the peak torque + 3 sec samples while the maximum size flocs associated with the "peak torque + 10 sec" samples are in the 1000-3000 μm^2 size bin. Thus, as the total particle area and size increases, the maximum developed torque also increases.

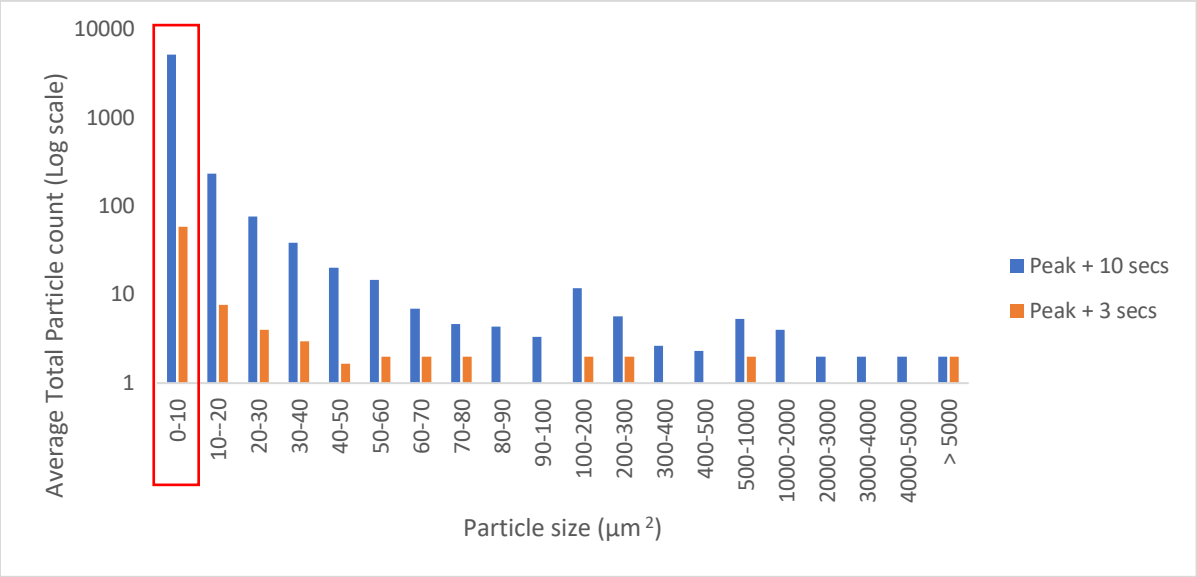

Figure 4.9: Particle size distribution curve comparing "Peak torque + 3 secs" with "Peak torque + 10 secs" samples on the same scale.

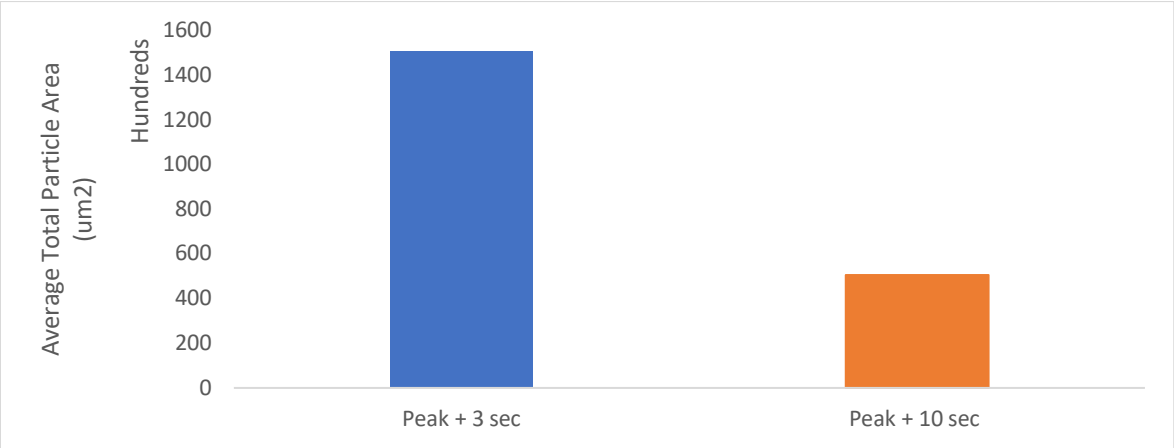

Figure 4.10: The average total particle area for "Peak torque + 3 secs" in comparison with "Peak torque + 10 secs".

All raw digital images to processed binary images demonstrate the capabilities of the methodology implemented by the author giving an accurate representation when comparing the

raw images with the binary images produced by Fiji-ImageJ. This is key specially when comparing metric quantitative results from Fiji-ImageJ with tailing's performance indicators.

4.1.1 Characterization tests

The CST was determined for sample at the end of the mixing process and plotted in Figure 4.11 to assess the shearing effect on the immediate dewatering behavior of the fFFTs. Lower CST values indicate better immediate dewaterability, therefore, "peak torque + 3 secs" is considered favorable condition. The "peak torque + 3 sec" sample experiences less shearing which in return accounts for larger flocs with better dewaterability and settlement behaviors.

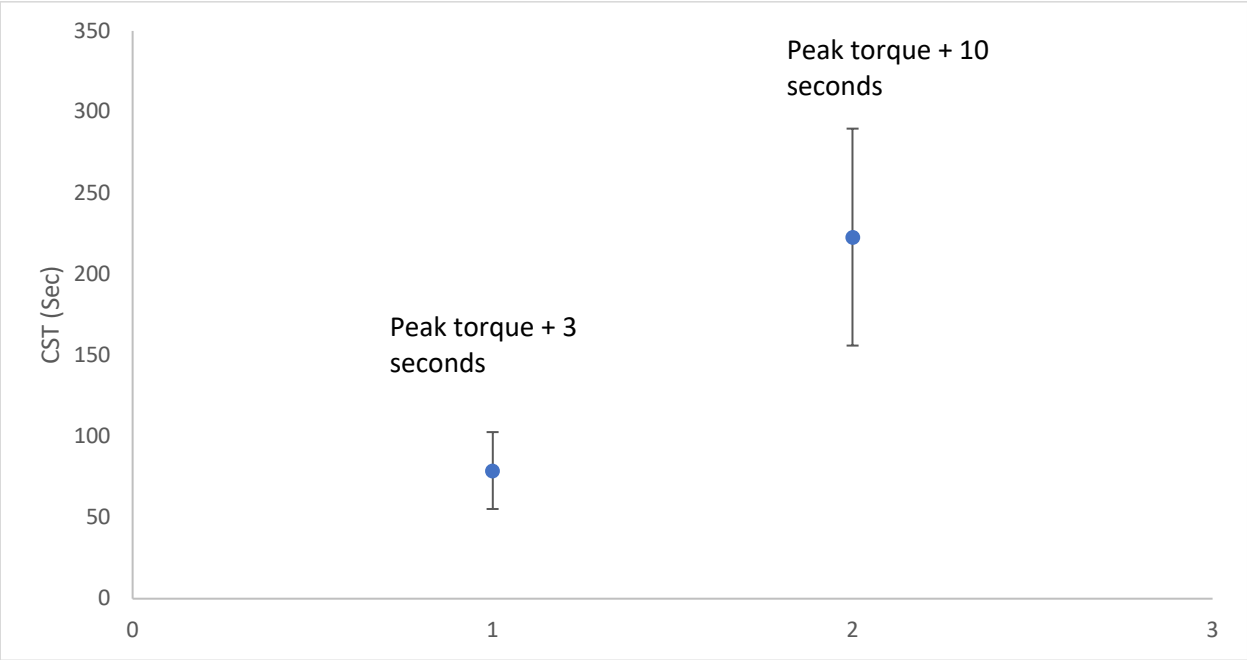

Figure 4.11: Shearing effect on the CST values

The oscillatory rheometry tests were performed on the samples after flocculation and shearing. Oscillatory rheometry test was performed right after flocculation (0 hour), 24 hours and 48 hours post flocculation on the sheared polymer amended FFT. Figures 4.12 (A&B) illustrate the results of the oscillatory rheometry tests performed. Oscillatory rheometry tests demonstrate the changes

in the linear elastic range as the stresses are applied. The elastic region is represented where the modulus of elasticity is relatively constant. While the point at which G' reduces and G" becomes more dominant represents the yield stress. The highest elastic shear modulus G' and yield stress recorded was for the peak torque + 3 seconds which supports the observations drawn, from the CST, Settlement, Optical microscopy data, of optimum conditions.

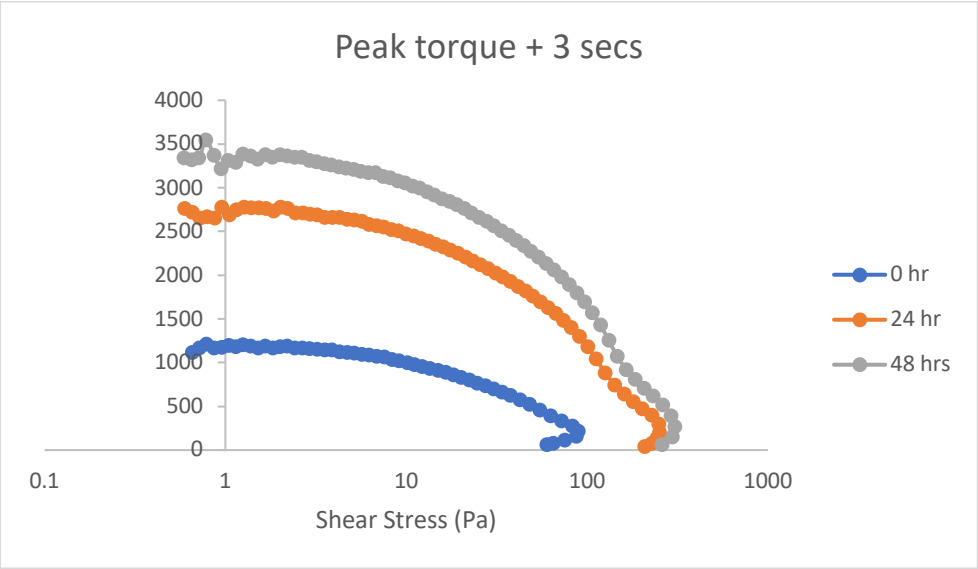

(A)

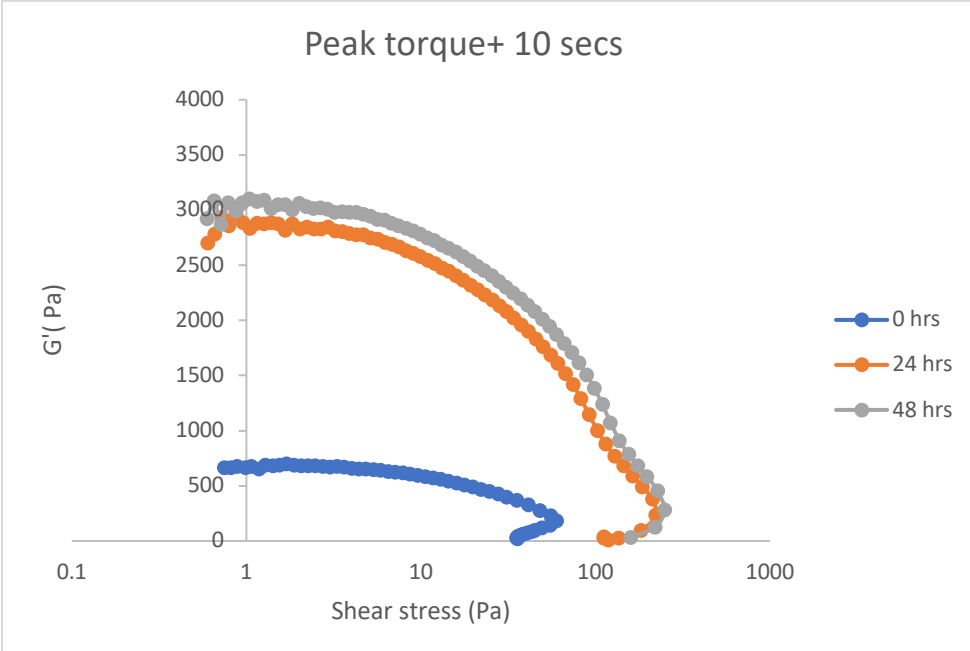

(B)

Figure 4.12 (A&B): Oscillatory Rheometer data for peak torque + 3 seconds , peak torque +10 seconds samples

In order to investigate the consolidation properties of the tailings, the final effective stress at the top of each layer and the final void ratio are calculated and plotted in Figure 4.13 (A&B). Using the compressibility relationship (e = $a\sigma_v{}^{'b}$), a and b are estimated based on fitting the compressibility curve with the power function where e is the void ratio and $\sigma_v{}^{'}$ is the vertical effective stress.

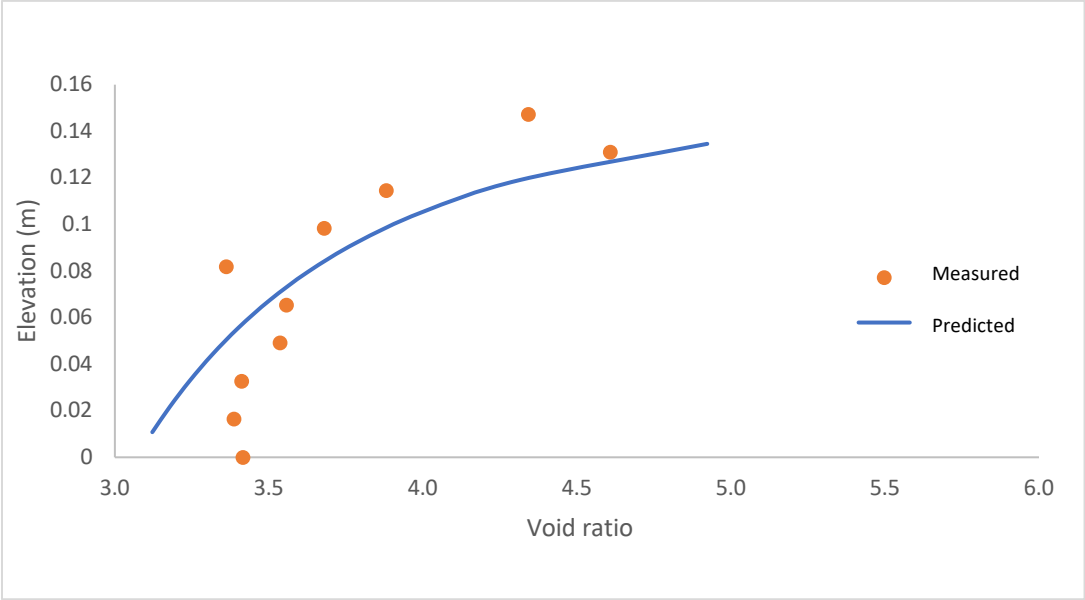

(A)

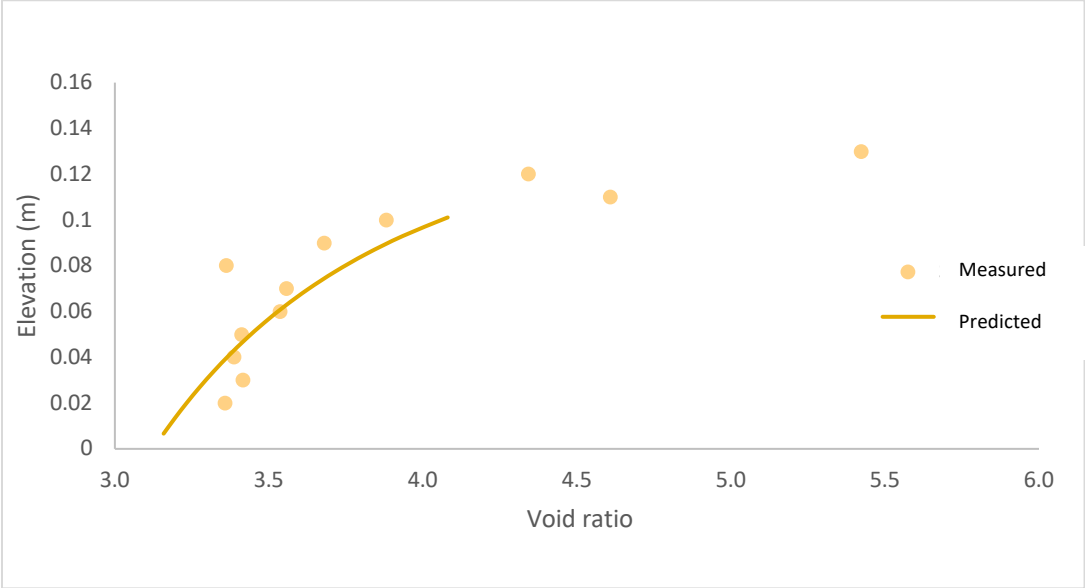

(B)

Figure 4.13: Void ratio vs Elevation for (A) “Peak torque + 3 secs” and (B) “Peak torque + 10 secs”

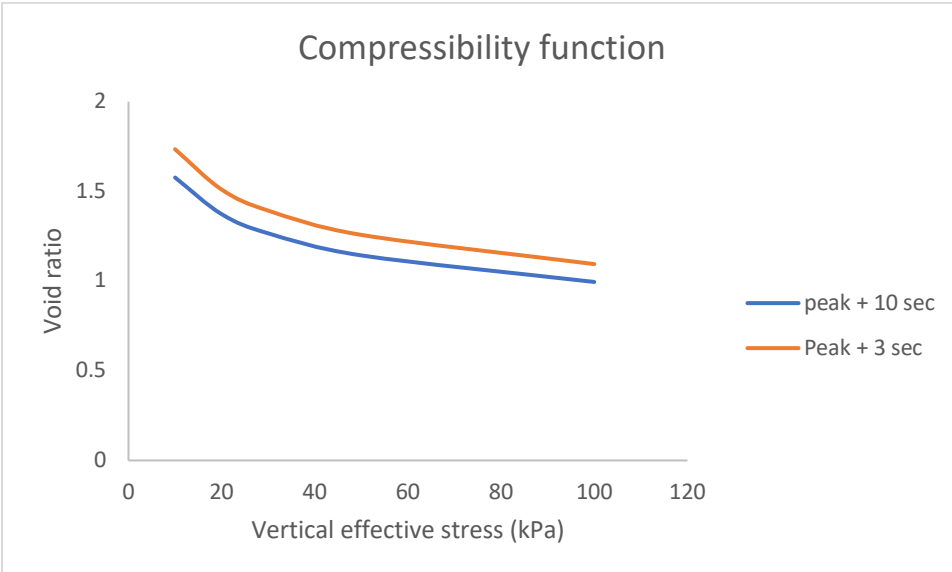

Figure 4.14: Compressibility function for "Peak torque + 3 secs" and "Peak torque + 10 secs"

The compressibility function and consolidation properties of the fFFT was calculated, using the compressibility relationship (e = $a\sigma v'^{b}$), a and b are estimated based on fitting the compressibility curve and were found to be the following:

Peak torque + 3 seconds: e = 2.75 $\sigma v'^{-0.2}$

Peak torque + 10 seconds: e = 2.5 $\sigma v'^{-0.2}$

To describe the variation of k with void ratio, the power function used was introduced by (Pane and Schiffman, 1997):

$$k = C\, e^{D} \qquad (\ldots 4.1)$$

where k is the hydraulic conductivity, e is the void ratio, C and D are constants. Using the general k-e relationship for polymer amended FFT presented by Babaoglu (2020), the D value is kept as a constant value of 7.5. Following the Pane and Schiffman (1997) technique, the initial hydraulic conductivity is calculated at the initial void ratio using the following equation:

$$k(e) = \frac{vsi(1+e)}{\gamma *} \qquad (\ldots 4.2)$$

where v_{si} is the initial settling velocity and $\gamma^* = \frac{(\gamma s - \gamma w)}{\gamma w}$

Subsequently, the C value is calculated using the initial void ratio and hydraulic conductivity to then calculate k at different void ratios.

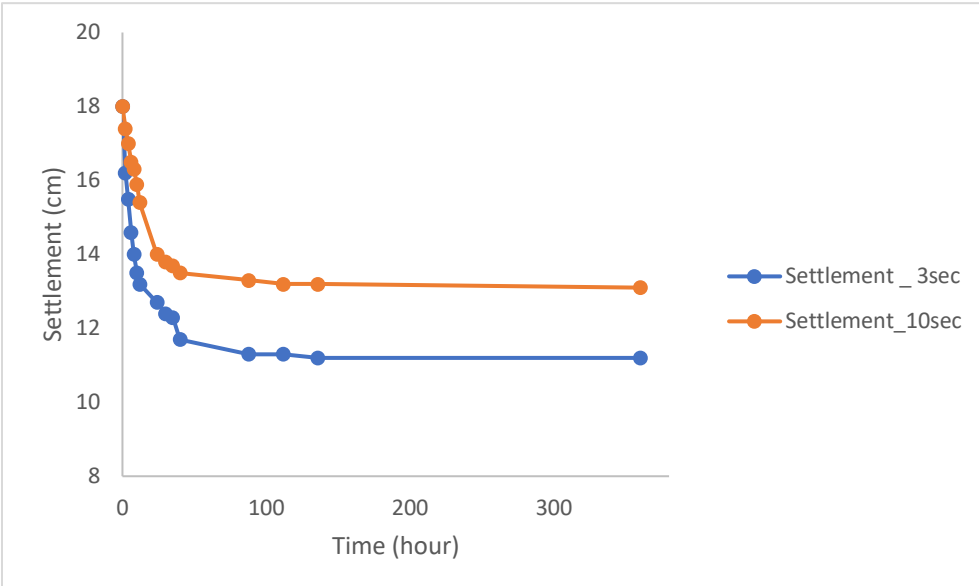

Figure 4.15: Settlement over time comparing "Peak torque + 3 seconds" vs "Peak torque + 10 seconds"

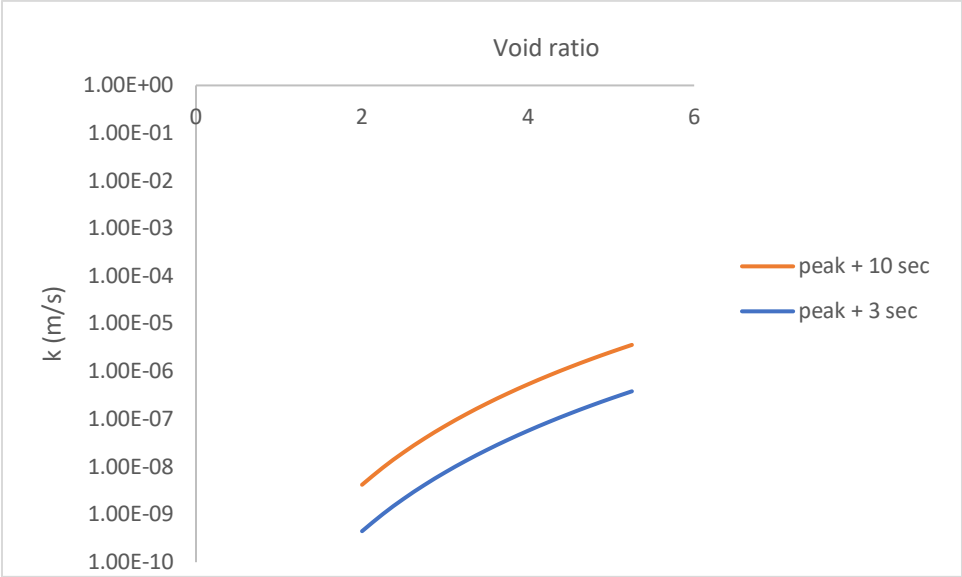

Figure 4.16: The k-e relationship comparing "Peak torque + 3 seconds" with "Peak torque + 10 seconds".

The k-e relationships presented in Figure 4.16 are represented by the following equation:

"Peak torque + 3 seconds": $k\ (m/s) = 3.29 \times 10^{-11}\ e^{7.5}$

"Peak torque + 10 seconds": $k\ (m/s) = 3.49 \times 10^{-12}\ e^{7.5}$

Lower CST values indicate better dewatering properties, in Figure 4.11 the CST values validated the results obtained from the optical microscopy images. The correlation between dewaterability and the peak torque values have also been validated with the study conducted by Aldaeef and Simms (2019).

Raw FFTs naturally have very low consolidation rate as well as poor settling behaviour. This behaviour is governed by the low hydraulic conductivity because the clay particles distribution is very sparse. Comparing the k-e relationships for the "peak torque + 3seconds" and the "peak torque + 10 seconds", the hydraulic conductivity is lower for the peak torque + 3 seconds. Comparing the k-e relationships for the "peak torque + 3seconds" and the "peak torque + 10 seconds", the hydraulic conductivity is higher for the peak torque + 3 seconds. This can be

correlated to the optical microscope image analysis, since the "peak torque + 3 seconds" had larger particles with a higher void area & high porosity, the hydraulic conductivity is expected to be higher than the peak torque + 10 seconds.

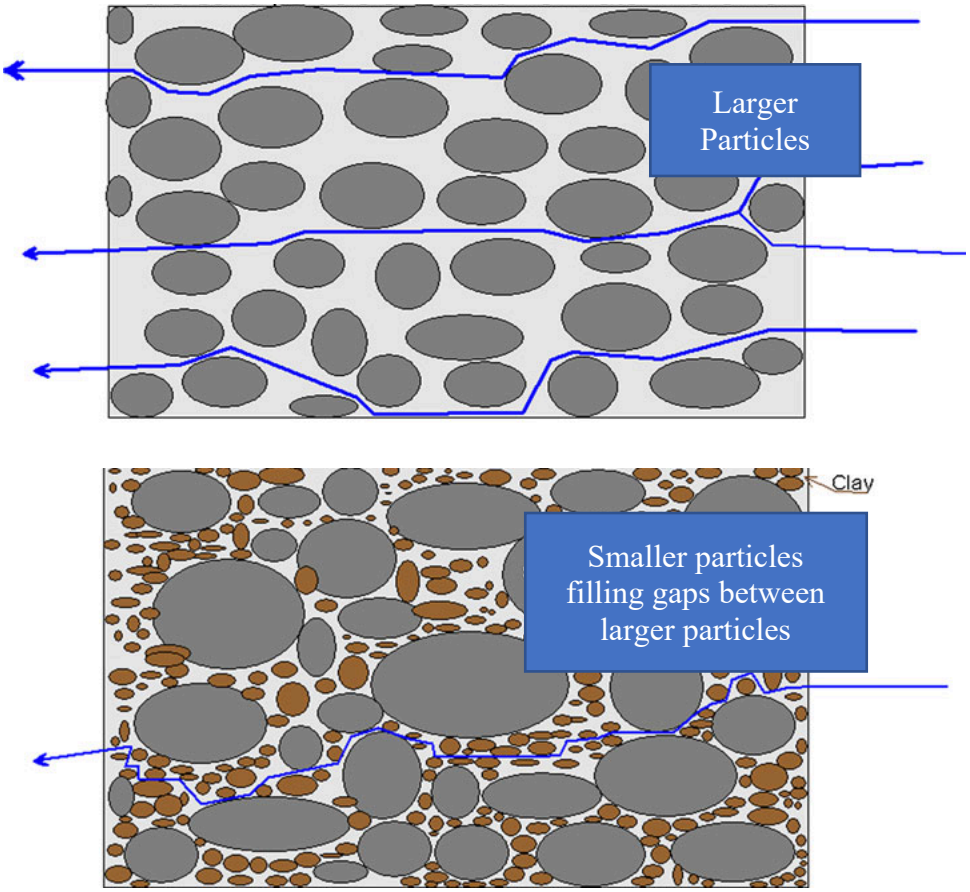

Figure 4.17: Effect of particle size distribution on the hydraulic conductivity (Sikandar, P., & Christen, E. W. (2012))

4.2 Polymer Optimization of flocculated FFT:

In this test, the mixing protocol for the flocculation process is based on the torque force developed as presented in Aldaeef and Simms (2019). The raw Shell FFT samples are flocculated in a 5 Litre bucket using PAM A3338 polymer with different dosages. A four-blade impleller with a radius of 8.5 cm is attached to an overhead mixer (EUROSTAR 60 control) .

The torque force is observed, once the peak torque is achieved, the mixing is stopped. The 800 ppm samples had the highest developed torque which is an indicator of the strength of the material.

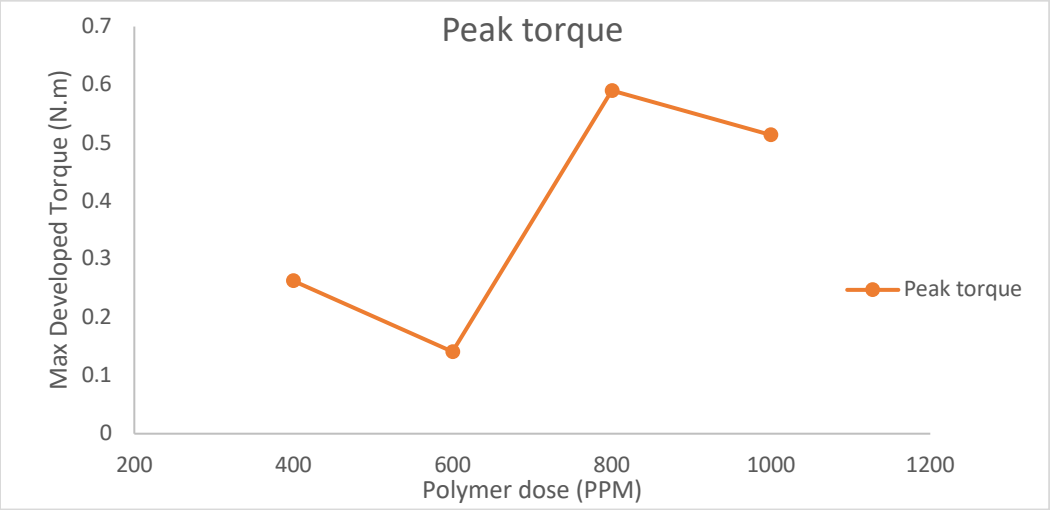

Figure 4.18: Maximum developed torque corresponding to various polymer dosages.

To assess the optimum polymer dosage, the flocculated FFT were assessed based on CST, torque feedback, Settlement, Optical microscopy and Oscillatory Rheometer. Despite the 1000 ppm dosed samples having better settlement (Figure 4.35), other performance indicators show that overall, the 800 ppm dose had a better immediate dewaterability and higher torque value. Both indicators show that the largest floc sizes are linked to this polymer dose. Therefore, 800 ppm polymer dosage is considered the optimum dose and from an economic perspective, the 800 ppm is also more feasible.

Looking at the raw optical microscope images and their processed images, the 400 ppm polymer dose had the smallest floc size particles in comparison with 600ppm, 800ppm and 1000ppm. For

the 0-10 μm^2 size bin, the 400ppm polymer dosed samples had the highest number of particles within this size range (Figure 4.21).

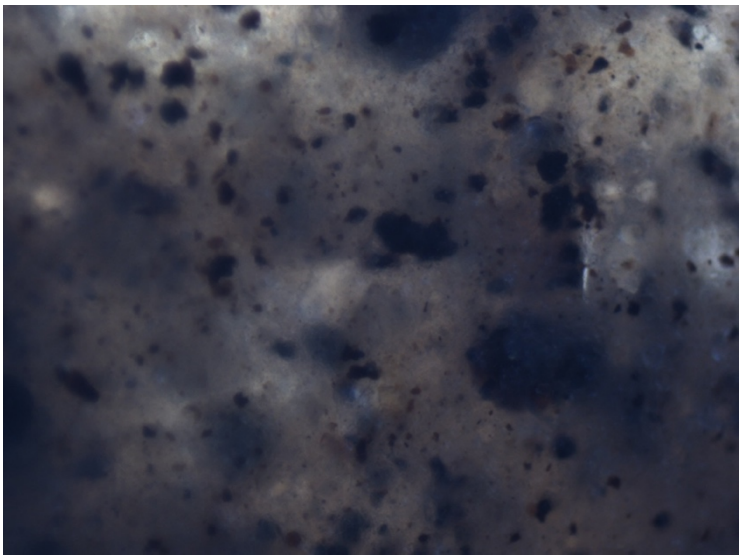

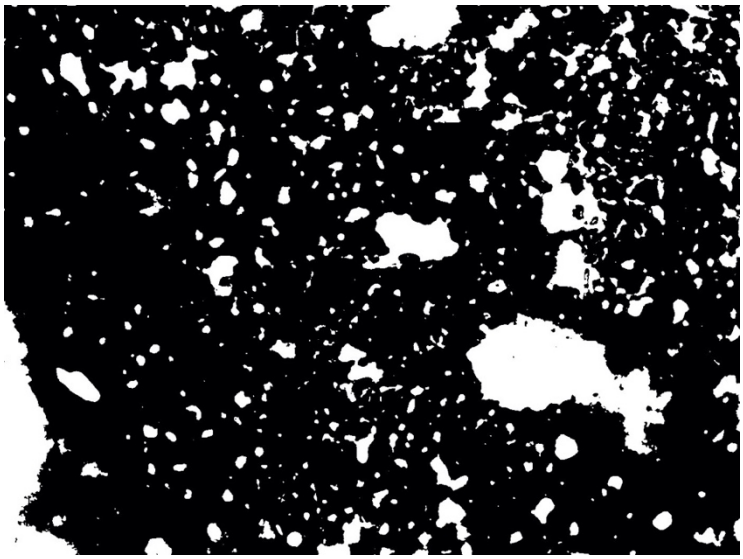

(A) (B)

Figure 4.19 (A&B): Raw optical microscope image and Binary Image - Trial 1 for 400 ppm polymer dosage

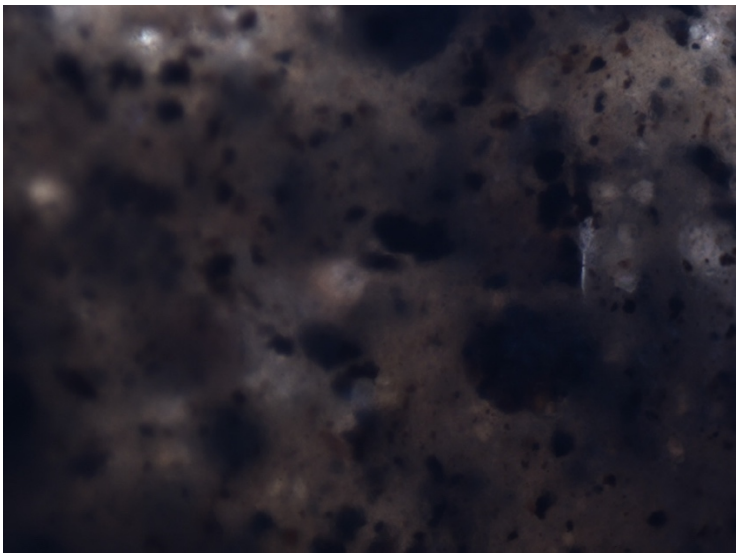

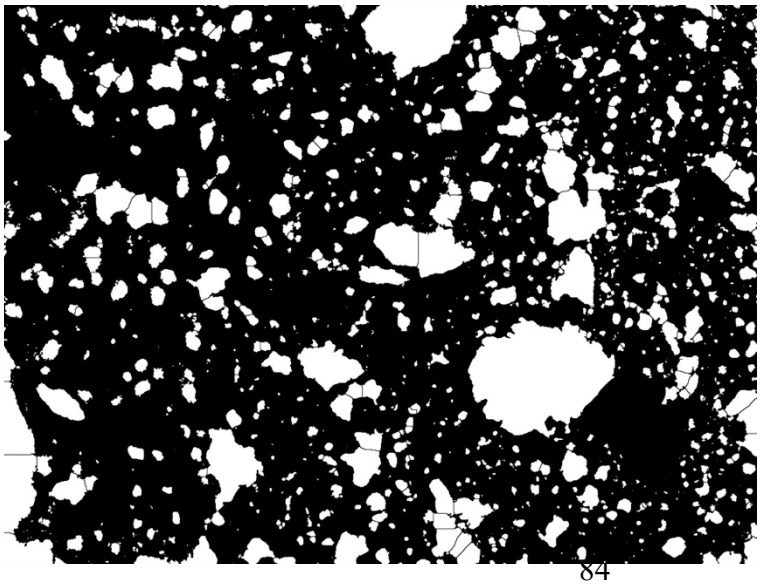

(A) (B)

Figure 4.20 (A&B): Raw optical microscope image and Binary Image - Trial 2 for 400 ppm polymer dosage

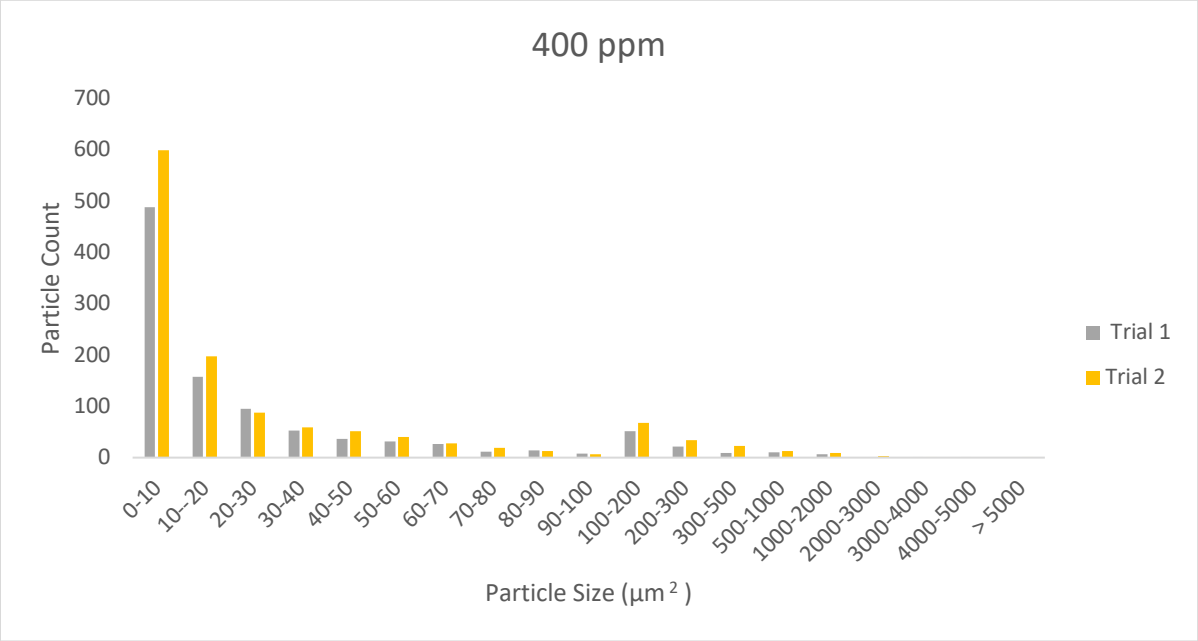

(A)

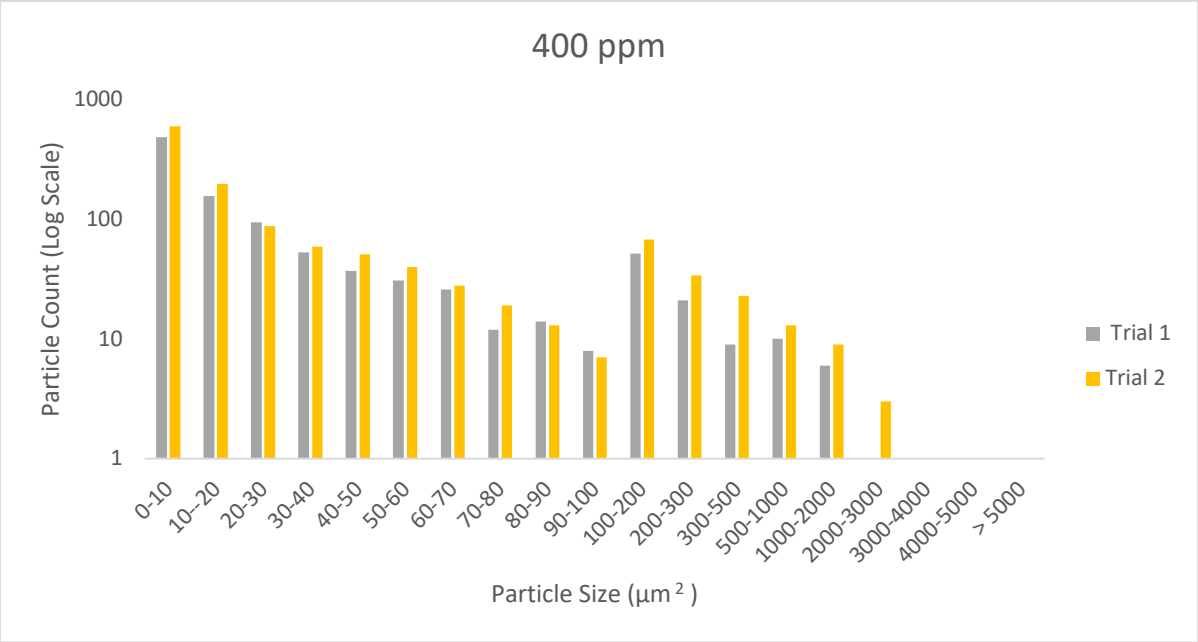

(B)

Figure 4.21 (A&B): Particle size distribution for 400 ppm polymer dosage

The 600 ppm polymer dosed samples showed similar behaviour and trends to the 400 ppm, although a few larger flocs can be observed; the smaller flocs have a big impact on the behaviour of the sample. Therefore, neither the 400 ppm nor the 600 ppm polymer dosages are considered favourable conditions.

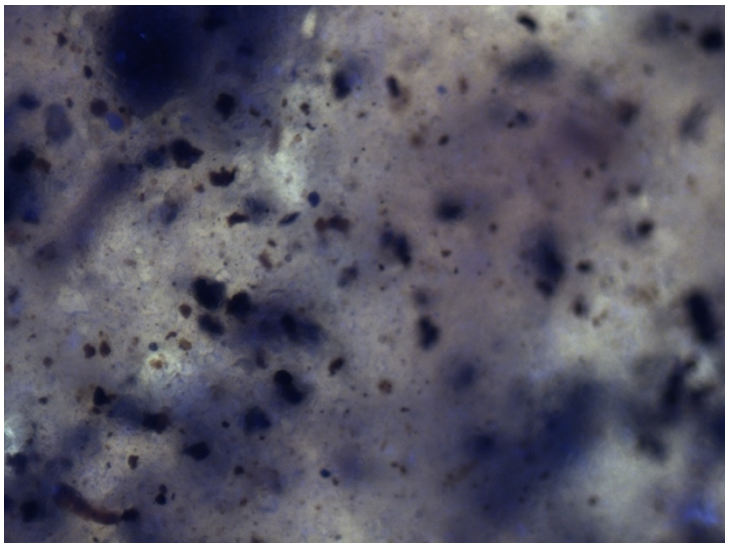

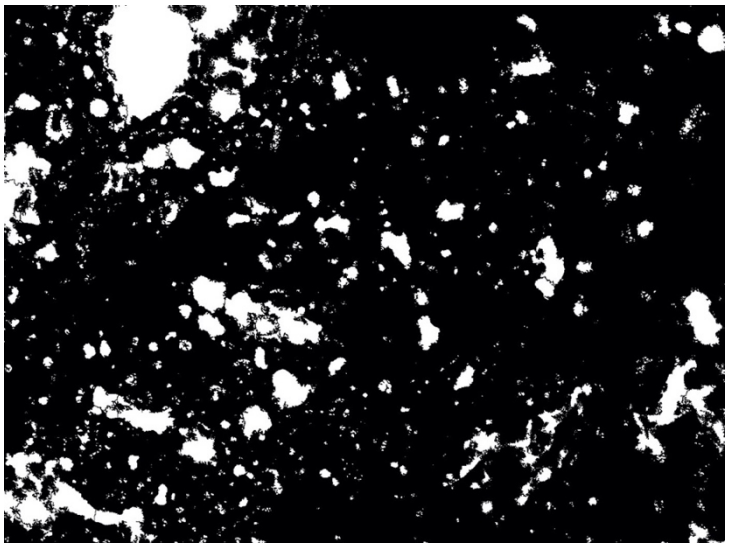

(A) (B)

Figure 4.22 (A&B): Raw optical microscope image and Binary Image - Trial 1 for 600 ppm polymer dosage

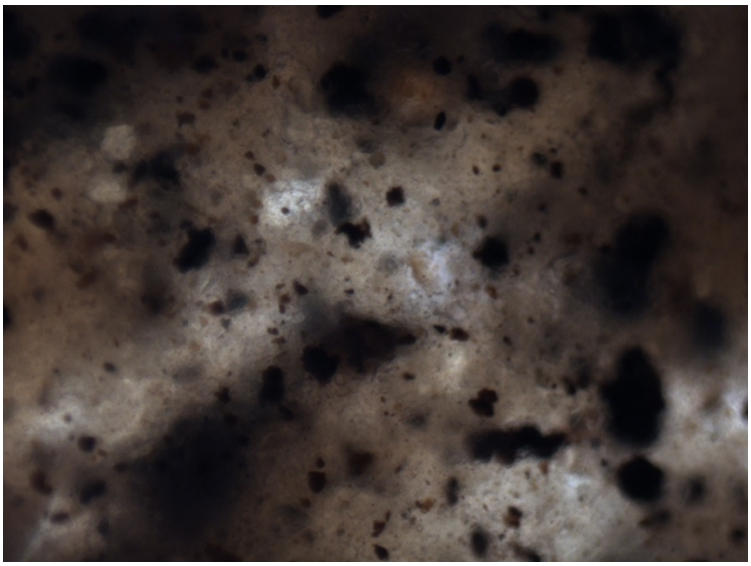

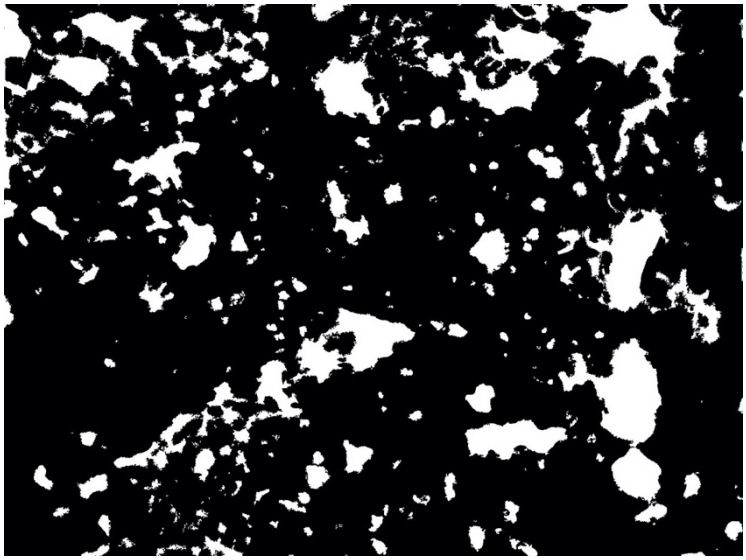

(A) (B)

Figure 4.23 (A&B): Raw optical microscope image and Binary Image - Trial 2 for 600 ppm polymer dosage

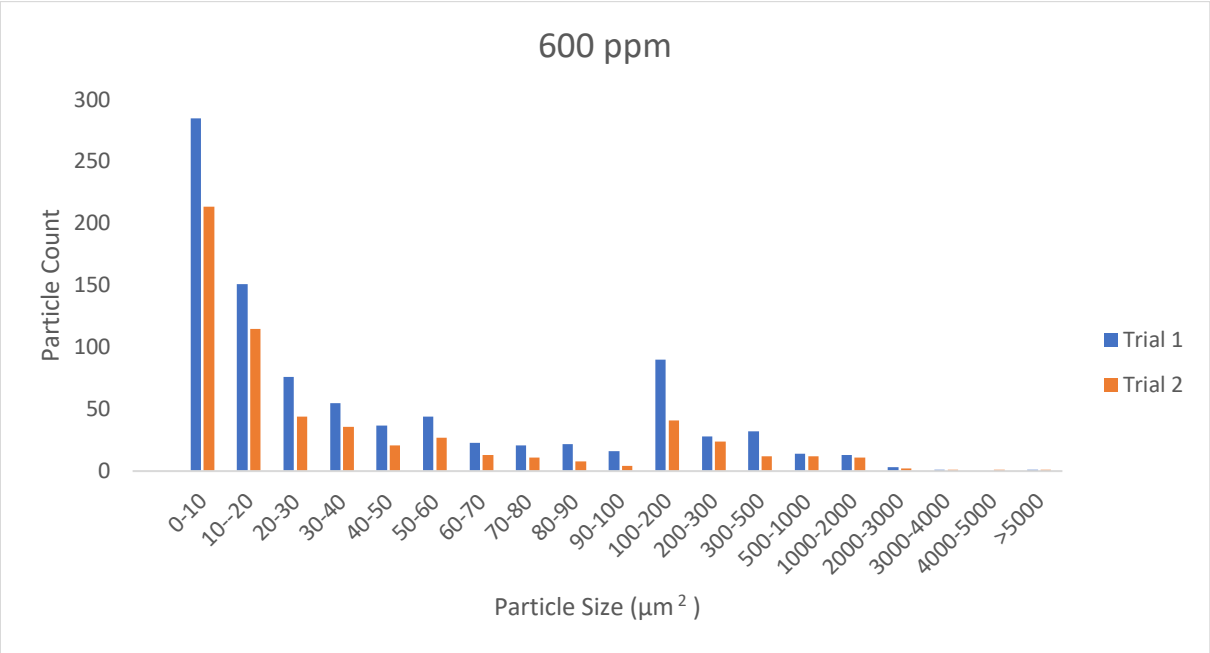

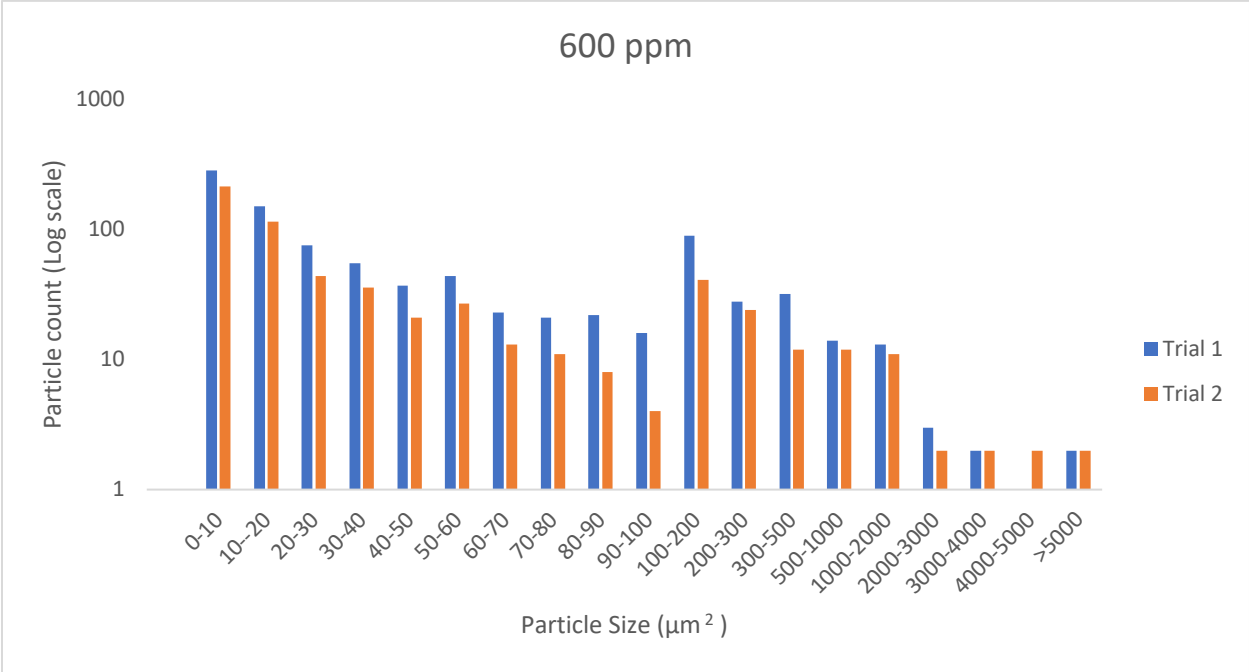

Figure 4.24 (A&B): Particle size distribution for 600 ppm polymer dosage.

Optical microscopy images (Raw & Processed Binary Images) of the 800 ppm samples both qualitatively and quantitatively show relatively larger maximum floc sizes. Based on the quantitative fabric analysis of the optical microscope images, 800 ppm appeared to be the optimum dosage. This was then validated with other key performance indicators such as CST, Settlement and developed torque.

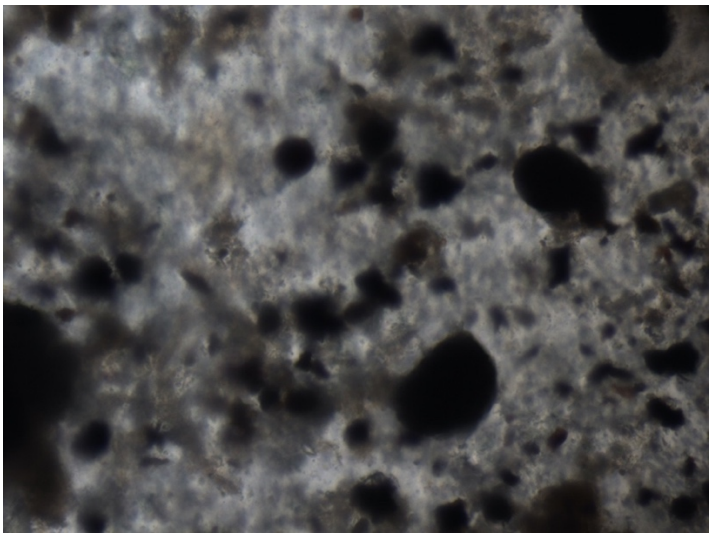

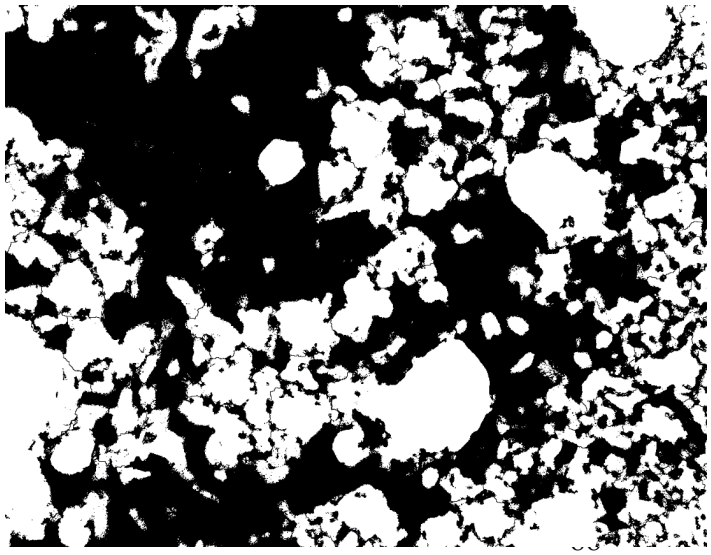

(A) (B)

Figure 4.25 (A&B): Raw optical microscope image and Binary Image - Trial 1 for 800 ppm polymer dosage

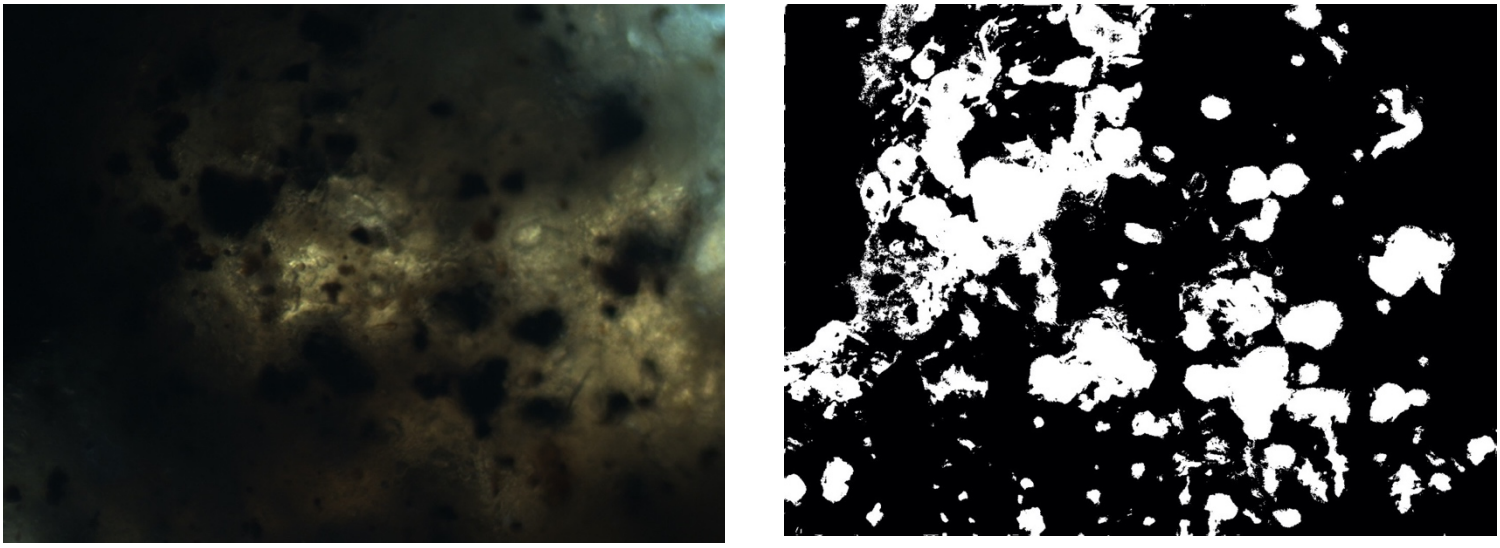

(A) (B)

Figure 4.26 (A&B): Raw optical microscope image and Binary Image - Trial 2 for 800 ppm polymer dosage

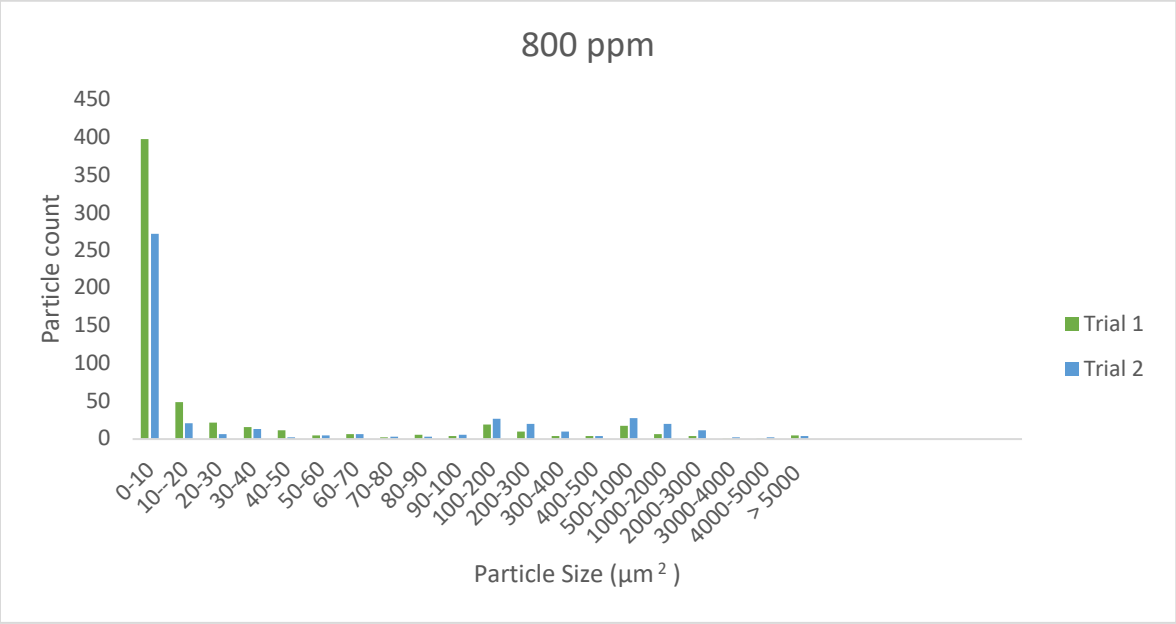

(A)

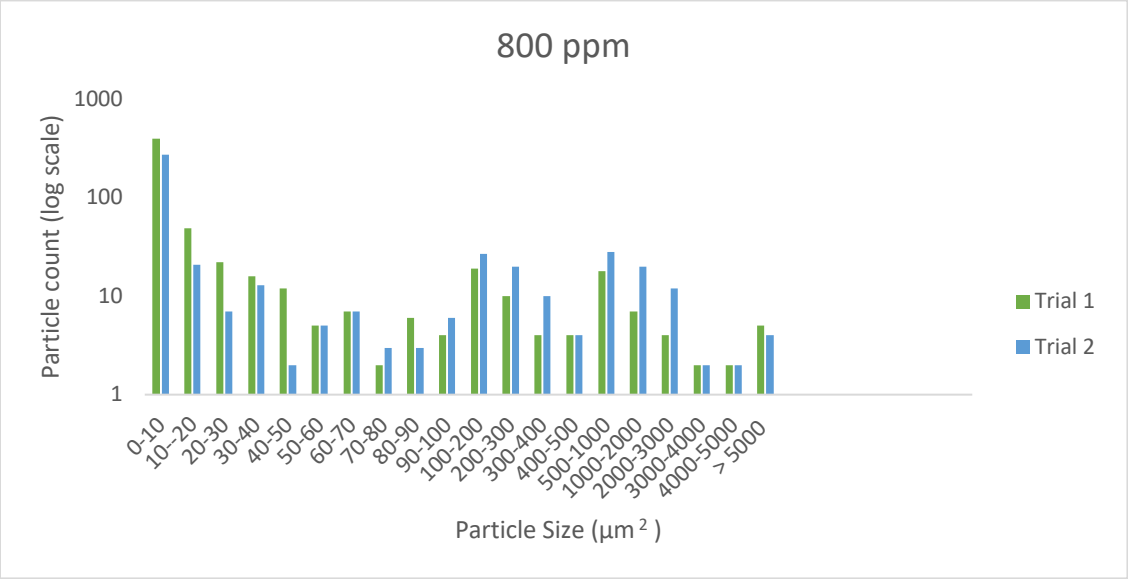

(B)

Figure 4.27 (A&B): Particle size distribution for 800 ppm polymer dosage

Finally, for the 1000 ppm polymer dosed samples, the optical microscope images were opaque (Figure 4.28) and challenging to analyze using Fiji-ImageJ, which could be attributed to either denser flocs or as a result of the high polymer dose the sample became non-homogenous (not enough particle surface to adhere to).

(A) (B)

Figure 4.28 (A&B): Raw optical microscope images for 1000 ppm polymer dosage

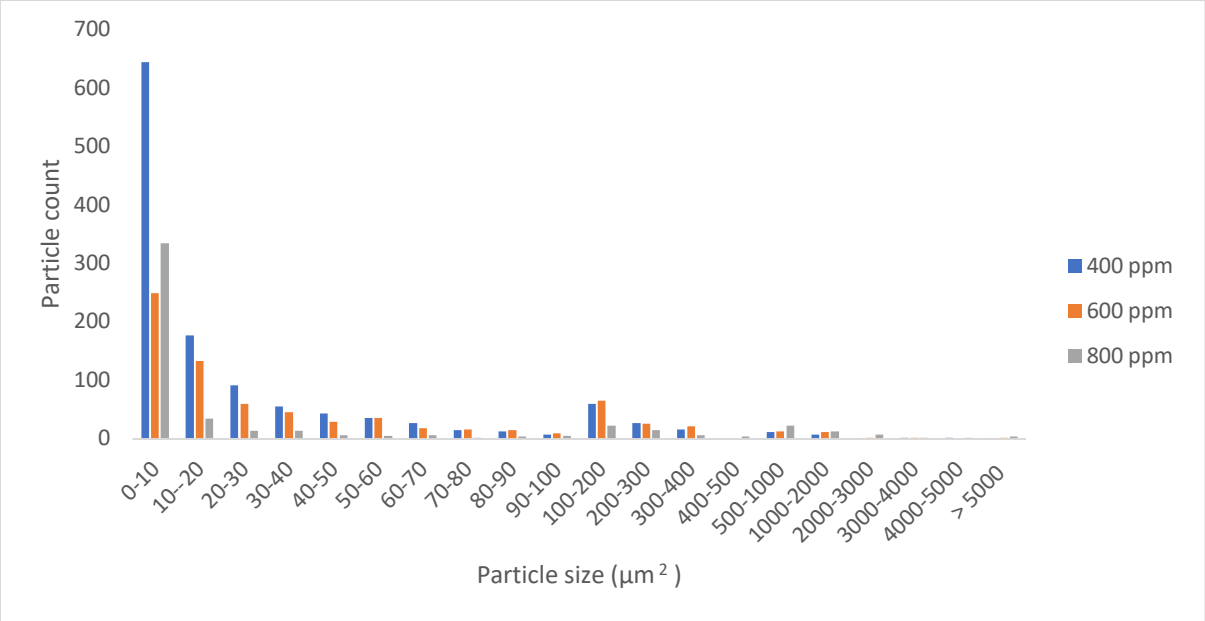

(A)

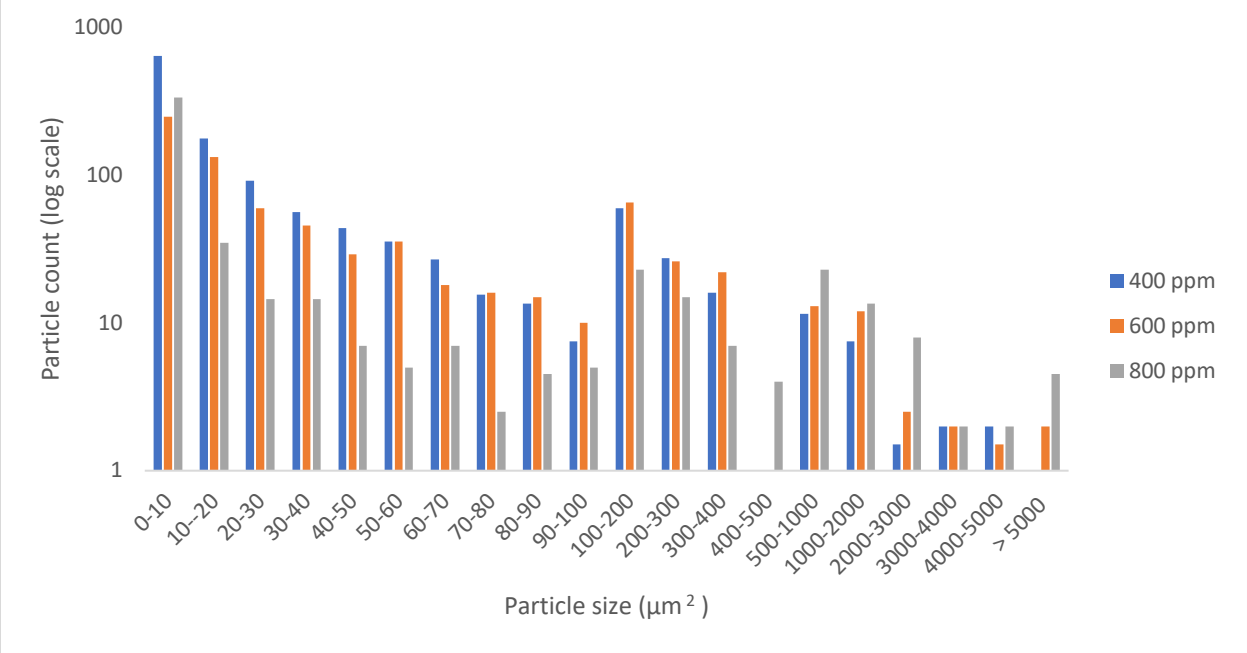

(B)

Figure 4.29 (A&B): The average total particle area for all polymer dosages (400ppm, 600ppm, 800ppm).

To assess the short term/ immediate dewatering behaviour, the CST test was used. Lower CST values indicate better immediate dewaterability, therefore, 800 ppm dosage samples were considered as favorable conditions. This indicates larger flocs with better settling and dewatering behaviours.

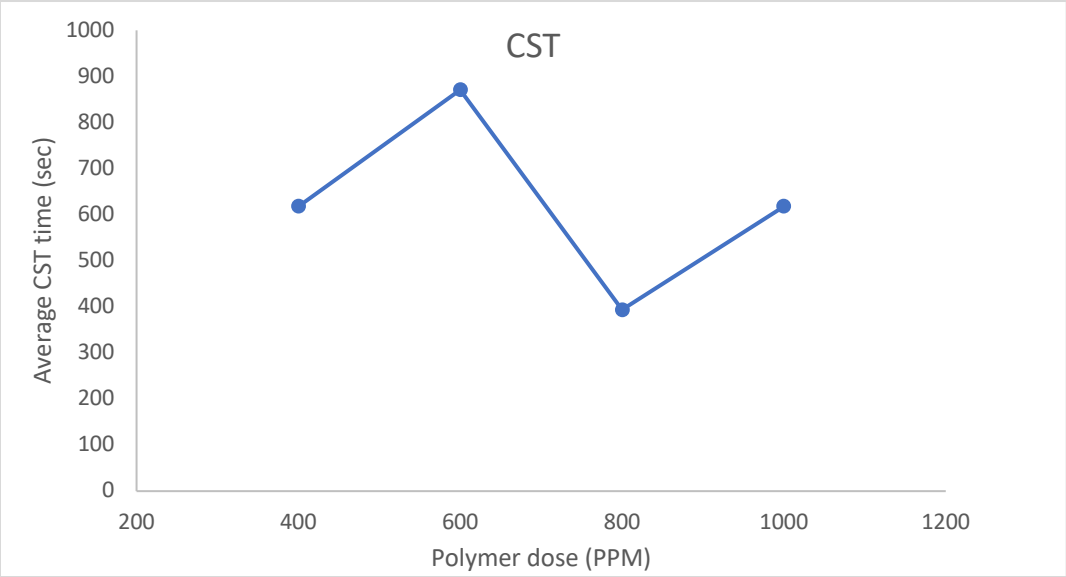

Figure 4.30: The Capillary Suction time for the different polymer dosages.

Both the elastic modulus (G') and the viscous modulus (G'') are determined from the oscillatory rheometer stress test. G' represents the elastic behaviour the material exhibits when there's a small strain shear and the elastic deformation is within the material's elastic limit. This deformation is reversible, and the material should regain its original shape. However, after a certain stress level, the deformation becomes irreversible. In all polymer dosages shown in Figures 4.31 – 4.34, the G' starts higher than G" where the elastic behaviour dominating. The yielding stress is then shown to increase as the G' and G'' increased for each polymer dose. The

corresponding G' in the linear elastic region and the yield stress was the highest in the 800 ppm and 1000 ppm dosed samples which agreed with the CST, Settlement and Optical microscope results.

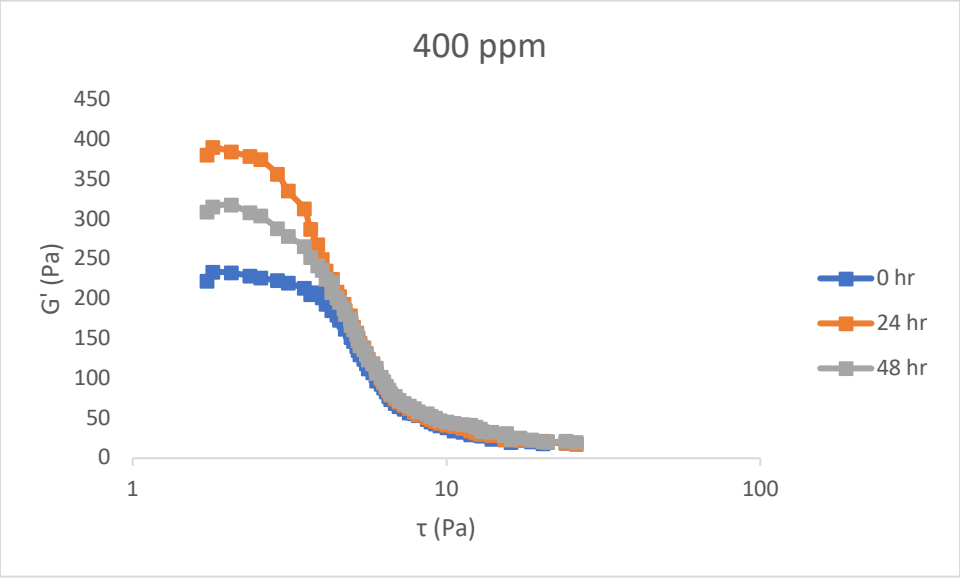

(A)

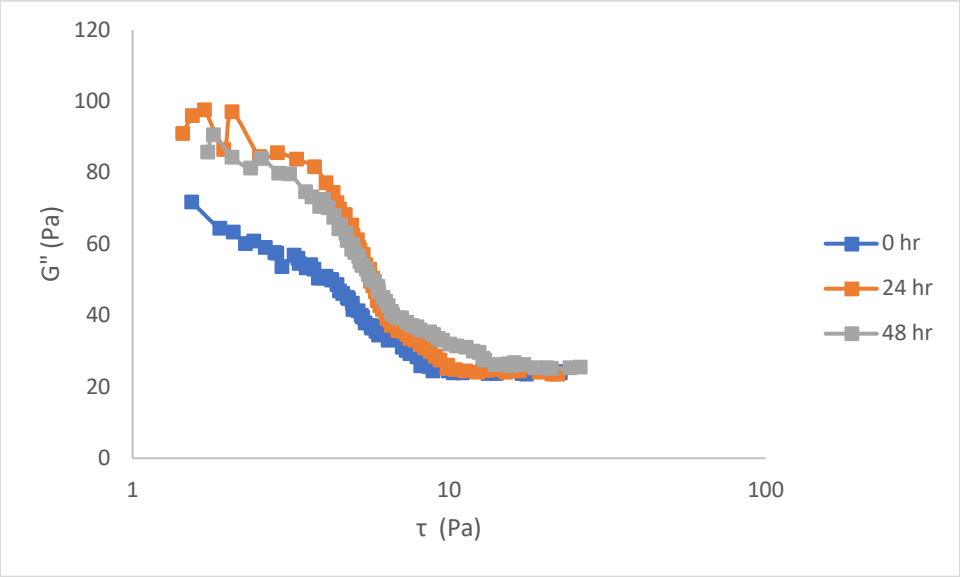

(B)

Figure 4.31 (A&B): Oscillatory Rheometer data for 400ppm polymer dosed samples.

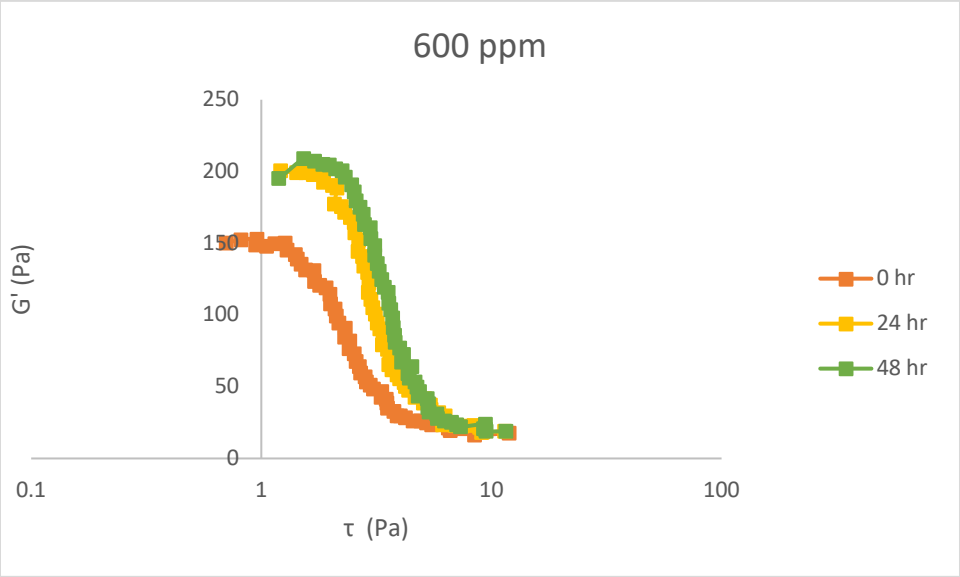

(A)

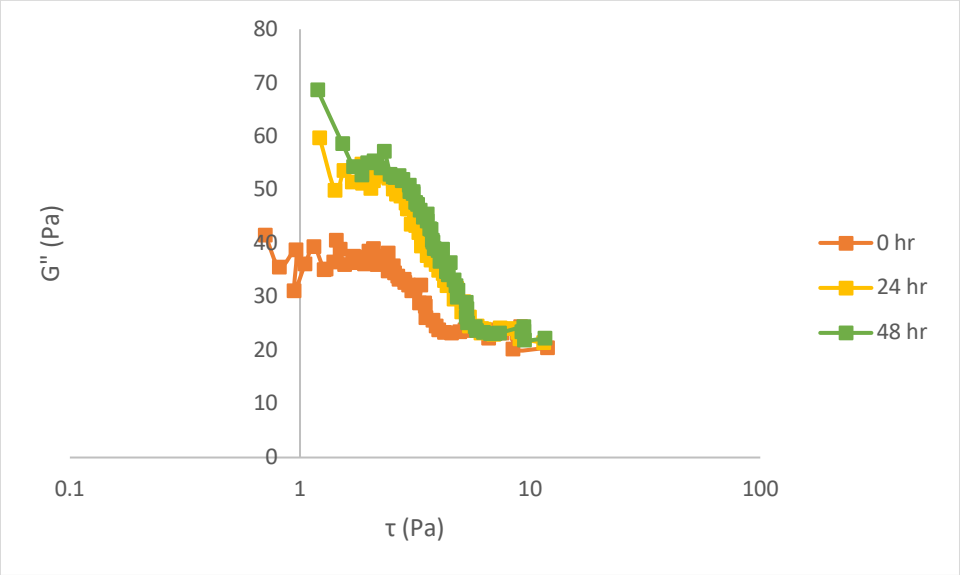

(B)

Figure 4.32 (A&B): Oscillatory Rheometer data for 600ppm polymer dosed samples.

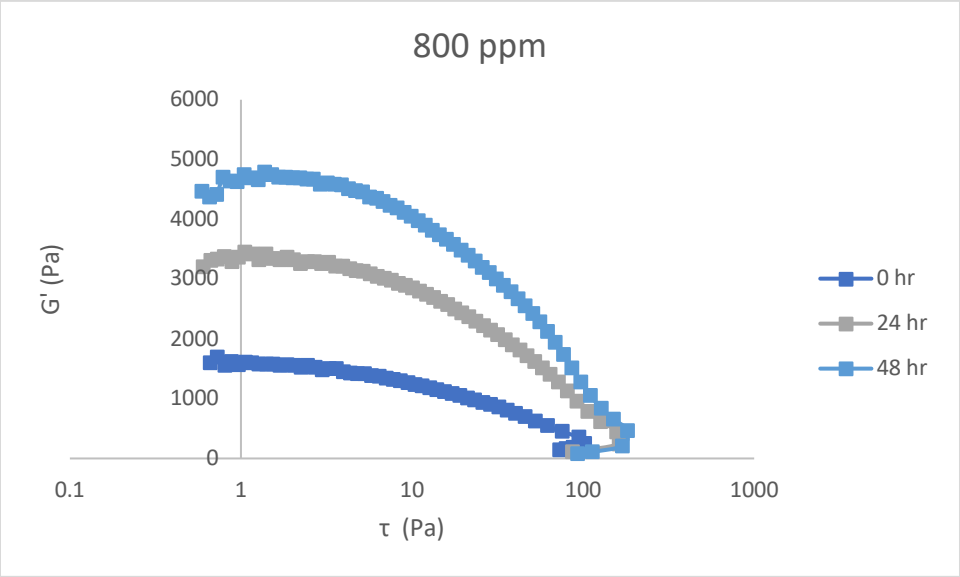

(A)

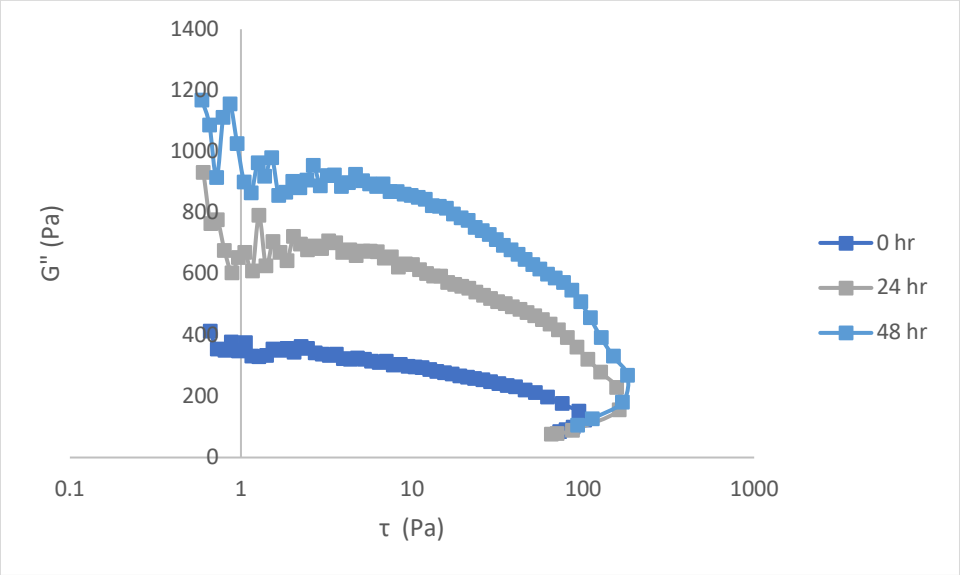

(B)

Figure 4.33(A&B): Oscillatory Rheometer data for 800ppm polymer dosed samples.

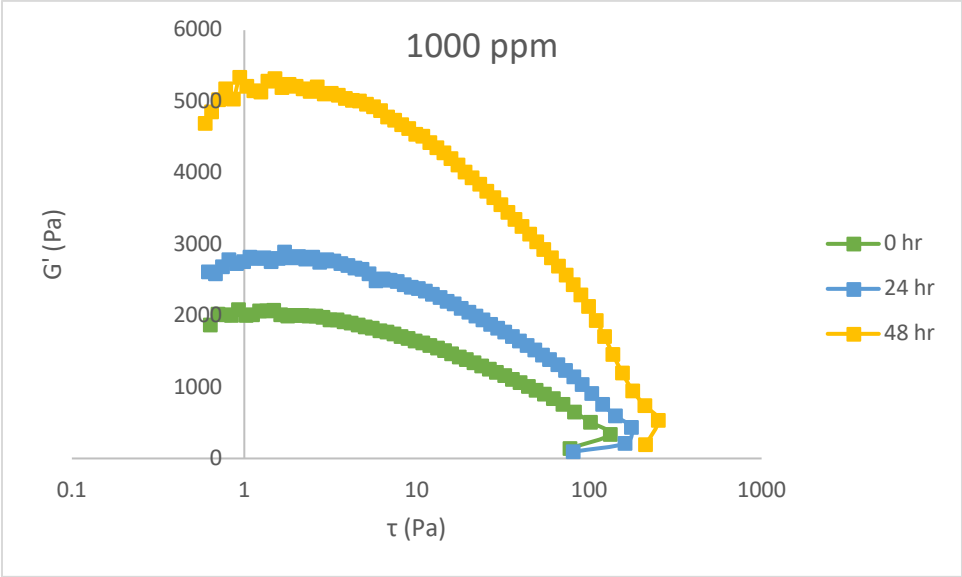

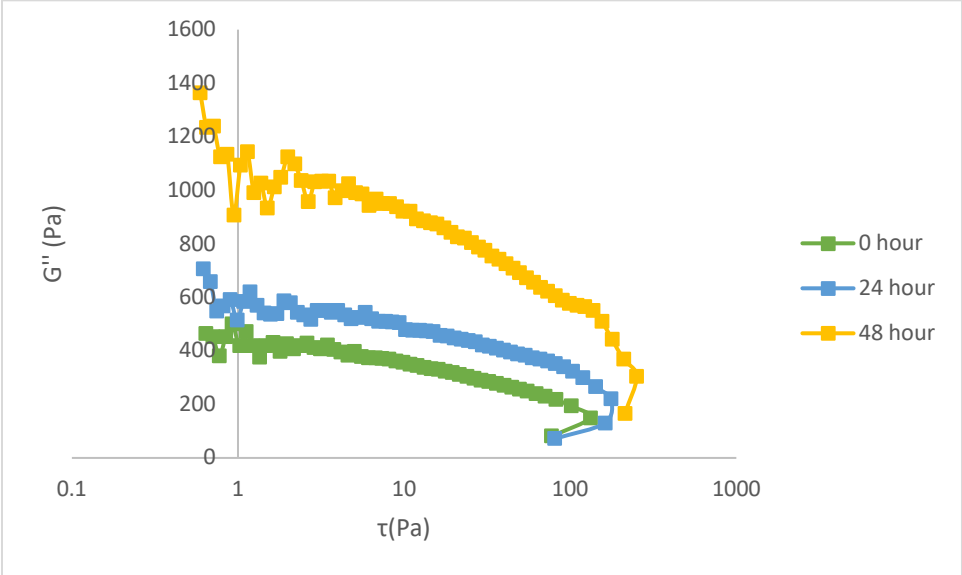

Figure 4.34 (A&B): Oscillatory Rheometer data for 1000ppm polymer dosed samples.

Therefore, using both qualitative and quantitative metrics, it was observed that the large particles seen in the 800 ppm polymer dosed samples (in the raw & processed optical microscope images) have a huge effect on the dewatering and overall performance of the tailings.

The settlement data also verified these observations where the 800 ppm and 1000 ppm dosed samples had the highest settlement indicating better immediate dewaterability.

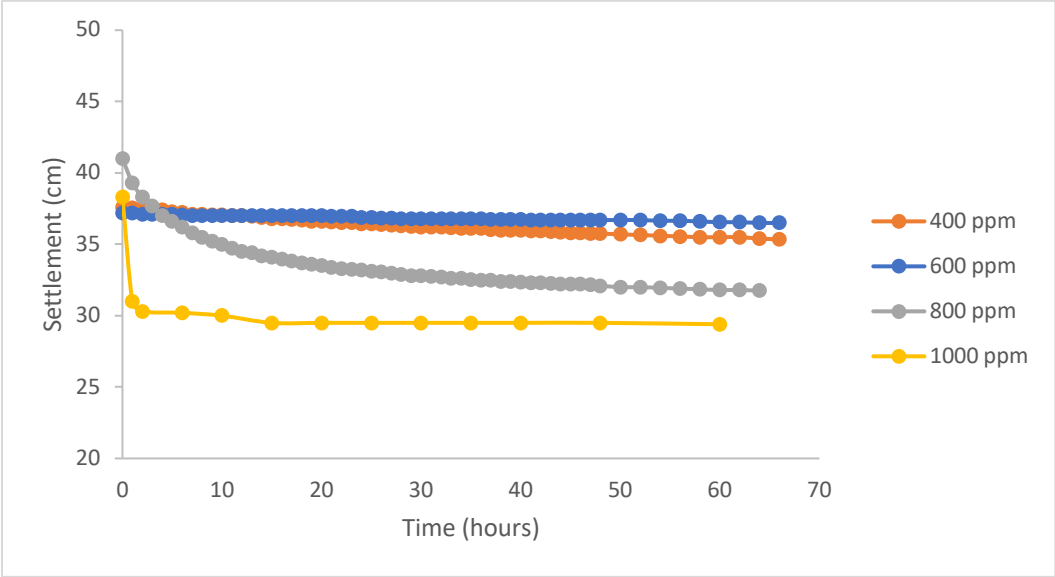

Figure 4.35: Settlement rate over time comparing different polymer dosages (400 ppm, 600 ppm, 800 ppm & 1000 ppm).

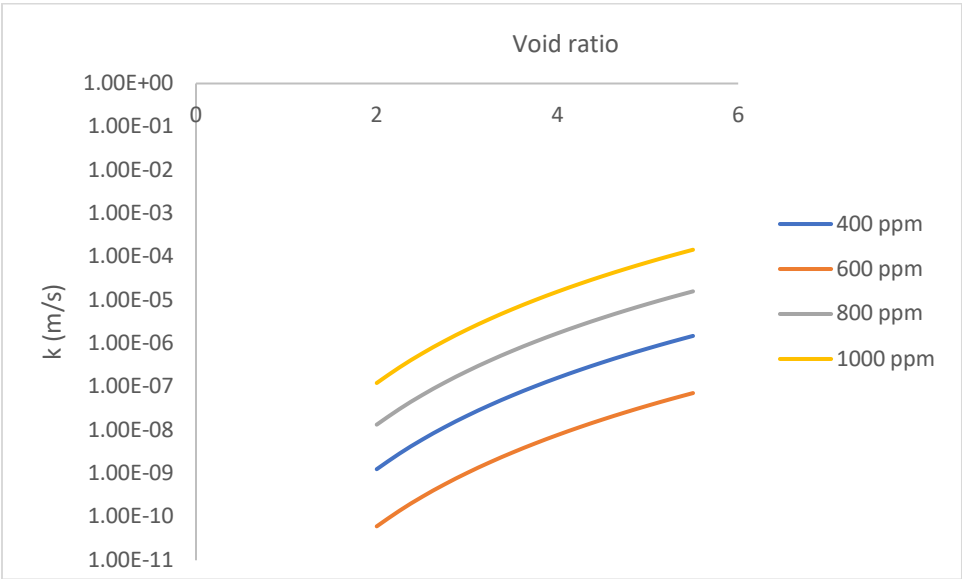

Figure 4.36: The k-e relationship between all polymer dosages

The k-e relationships plotted on Figure 4.36 are represented by the following equations using Pane and Schiffman (1997) power function ($k = C\ e^{D}$) :

400 ppm : $k\ (m/s) = 9.87 \times 10^{-12}\ e^{7.5}$

600 ppm: $k\ (m/s) = 9.34 \times 10^{-13}\ e^{7.5}$

800 ppm: $k\ (m/s) = 1.05 \times 10^{-10}\ e^{7.5}$

1000 ppm: $k\ (m/s) = 9.06 \times 10^{-10}\ e^{7.5}$

The polymer dose and hydraulic conductivity show a directly proportional relationship. As the particle sizes, it creates larger gaps/ voids between particles which in return increases the hydraulic conductivity.

4.3 Pipeline transport shear modelling on flocculated tailings

This experiment is used to assess the effects of shearing due to pipeline transport. Four scenarios were modelled and examined in the Couette rheometer using the torque based technique. The shearing duration was simulated for a pipeline transport distance of 1000m. To study the effects of the pipeline transport, the flocculated samples were exposed to the calculated shear rates of 4.23 s^{-1} , 8.27 s^{-1} , 16.93 s^{-1} and 33.1 s^{-1} by applying the corresponding rational speeds in the Couette. Several key performance indicator tests on the sheared flocculated FFT to evaluate the microstructure, short-term dewaterability and rheology aspect of the flocculated FFT samples.

The optical microscope image analysis showed that the sheared samples at different share rates have experienced de-flocculation which led to higher smaller flocs in comparison with the non-sheared samples. It also shows that as the shear rate increases, the number of smaller flocs also increases. To simulate the pipeline shear transport time for a distance of 1000m, each shear rate had it's corresponding transport time and rotational speed. The lowest shear rate, 4.23 s^{-1} , experienced the longest transport time while the highest shear rate, 33.1 s^{-1} , had the fastest transport time. This is qualitatively illustrated in the optical microscope images, the highest shear rate has the highest number of small particles, however, larger flocs still do exist. This can be due to the fact that, at the highest shear rate the FFT spend 6 minutes in the pipeline transport

simulation, whereas in the lowest shear rate, the FFT spend significantly longer time of 41 minutes (Table 5).

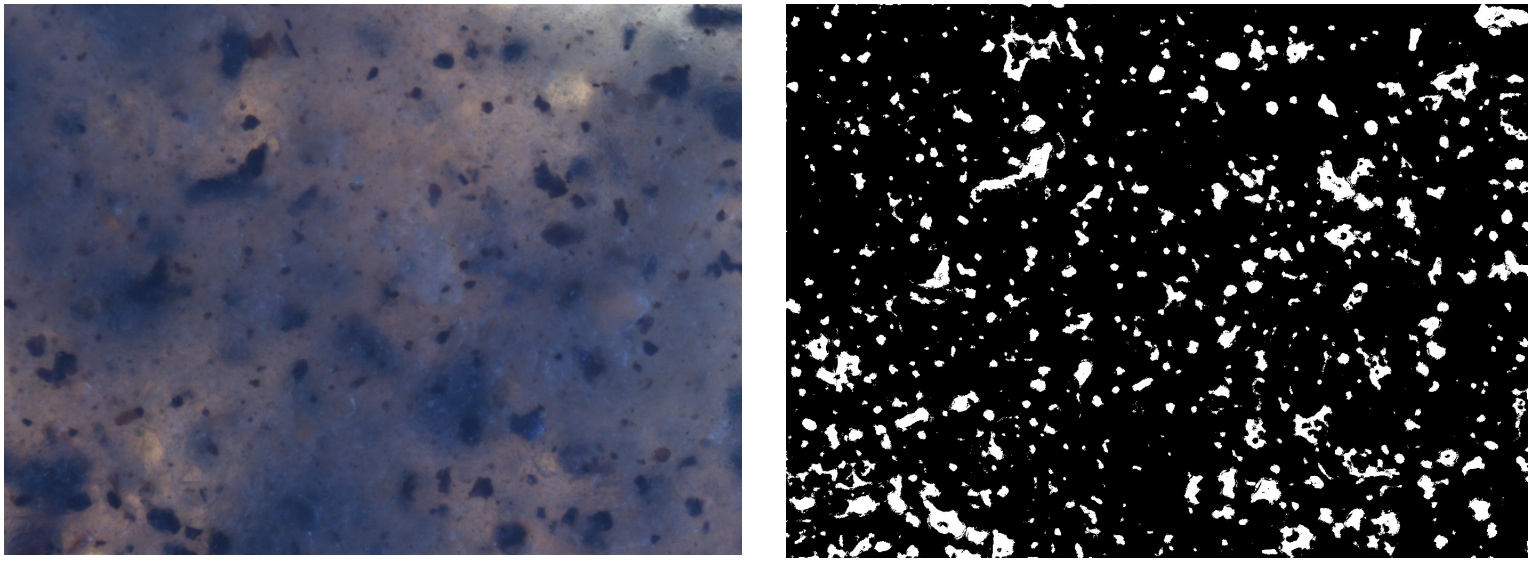

(A) (B)

Figure 4.37 (A&B): Raw optical microscope image and Binary Image - Trial 1 for 4.23 s^{-1} shearing rate

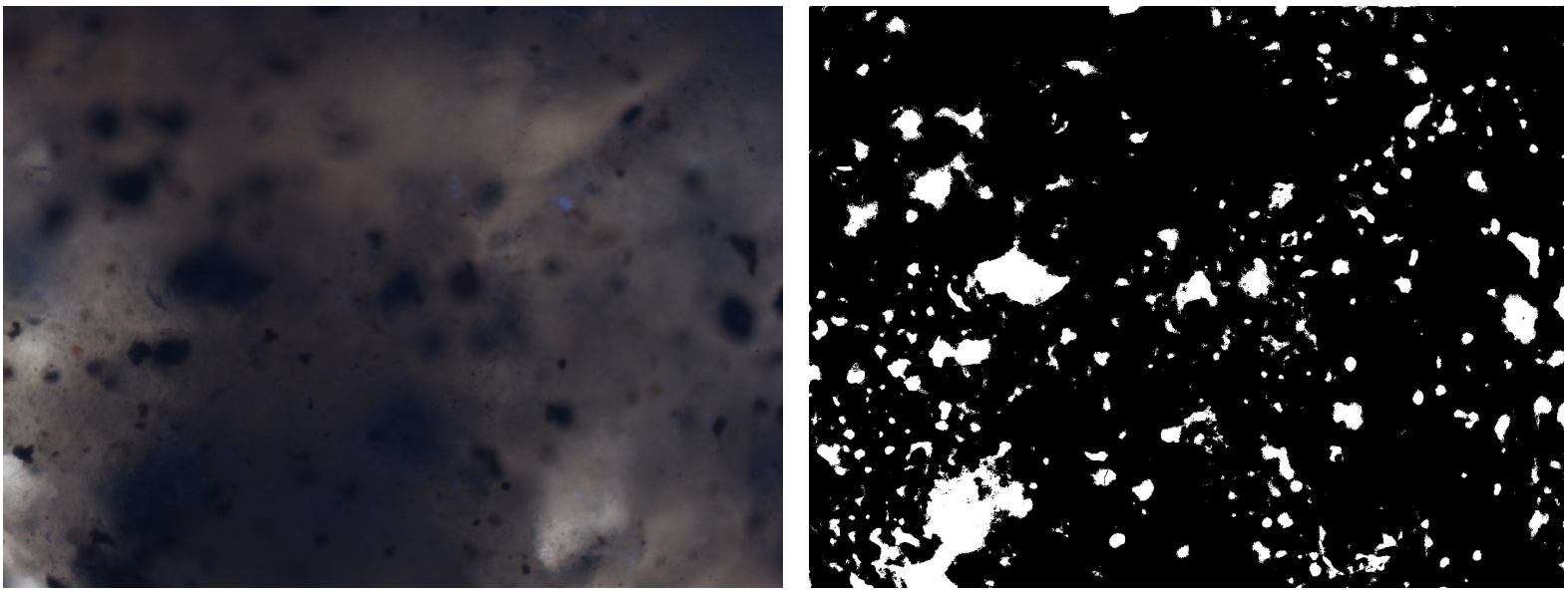

(A) (B)

Figure 4.38 (A&B): Raw optical microscope image and Binary Image - Trial 2 for 4.23 s^{-1} shearing rate

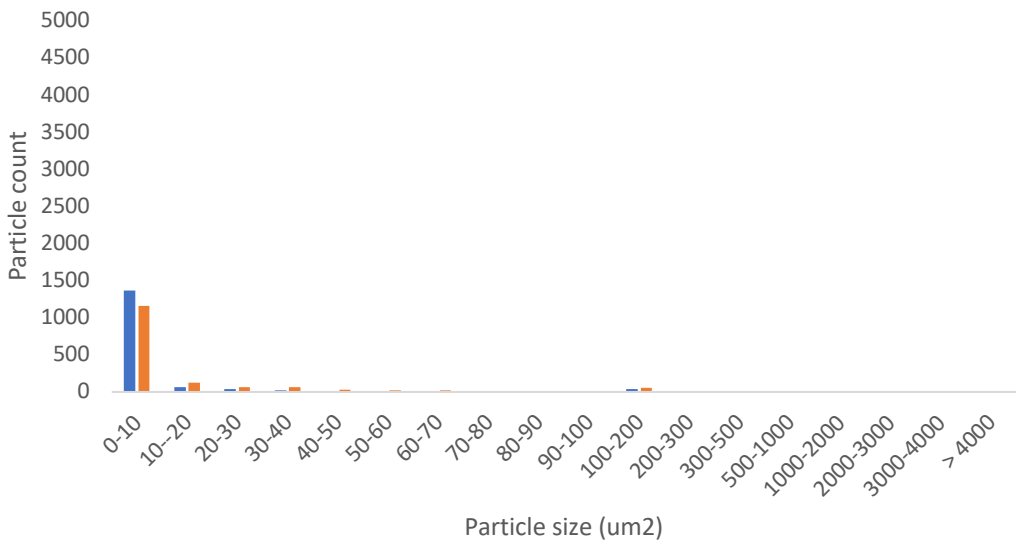

(A)

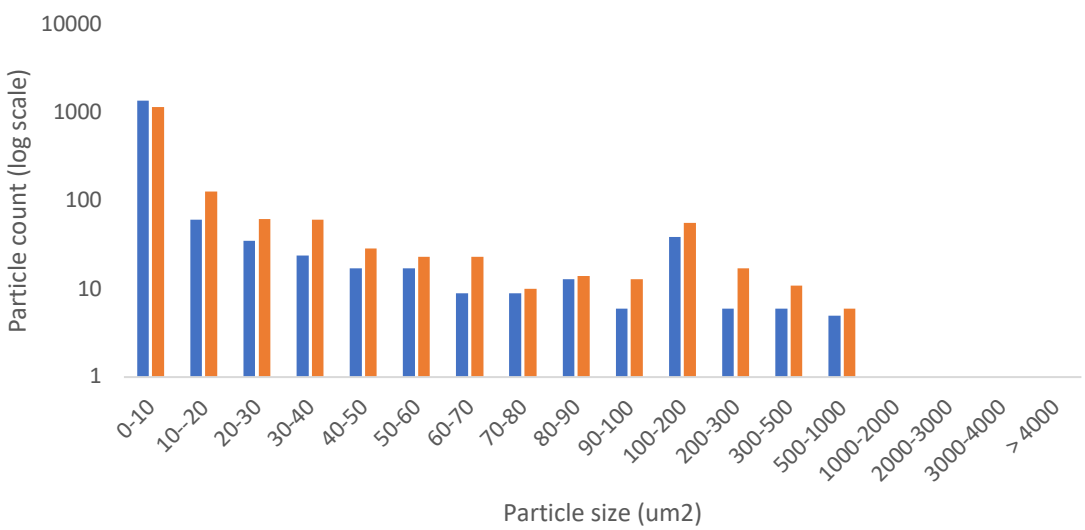

(B)

Figure 4.39 (A&B): Particle size distribution for 4.23 s^{-1} shearing rate

The raw optical microscope images and processed binary images for shear rate 8.27 s^{-1} show repeatable results for the same given sample. Since the rotational speed is higher than the 4.23 s^{-1} shear rate, it is expected to have overall a larger distribution of small floc particles.

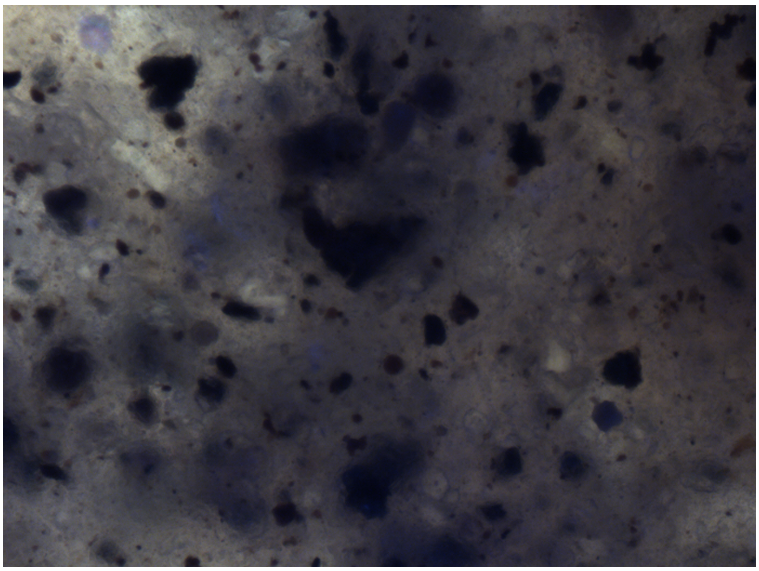

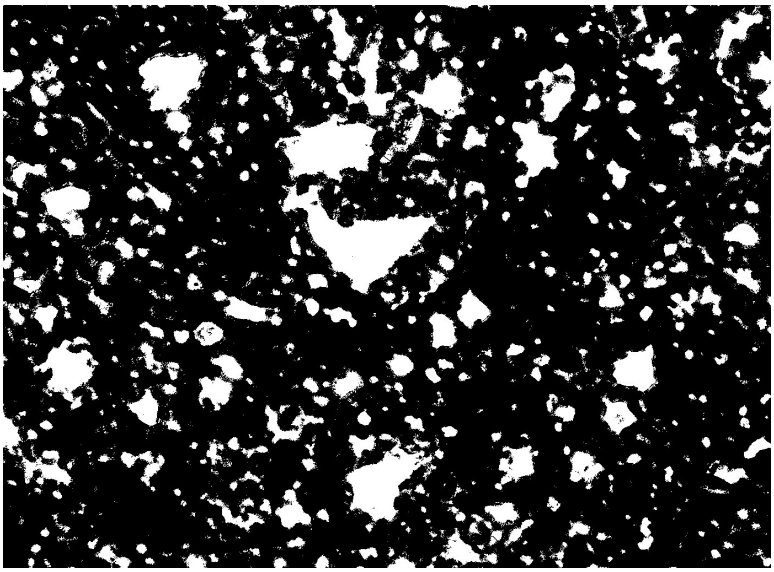

(A) **(B)**

Figure 4.40 (A&B): Raw optical microscope image and Binary Image - Trial 1 for 8.27 s^{-1}

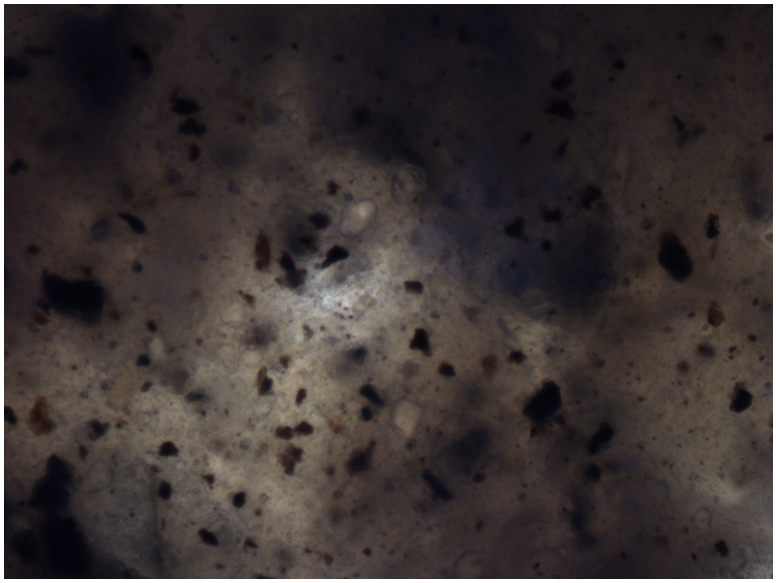

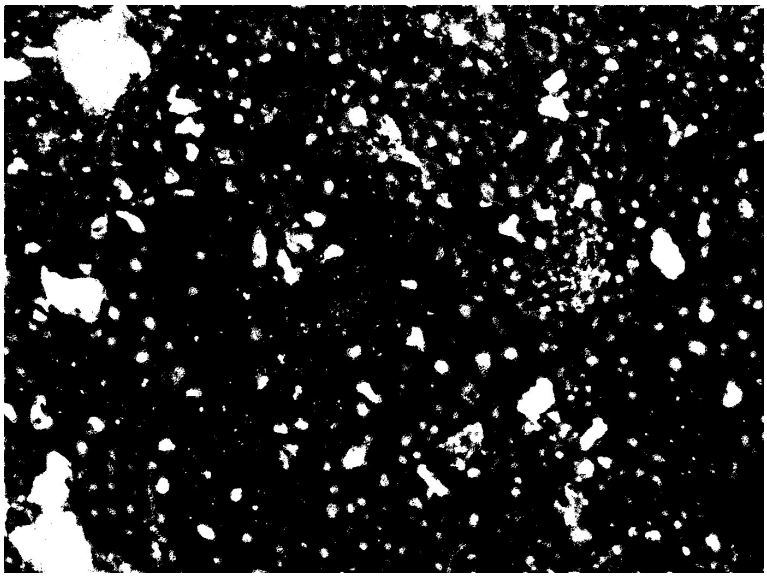

(A) **(B)**

Figure 4.41 (A&B): Raw optical microscope image and Binary Image - Trial 2 for 8.27 s^{-1} shearing rate

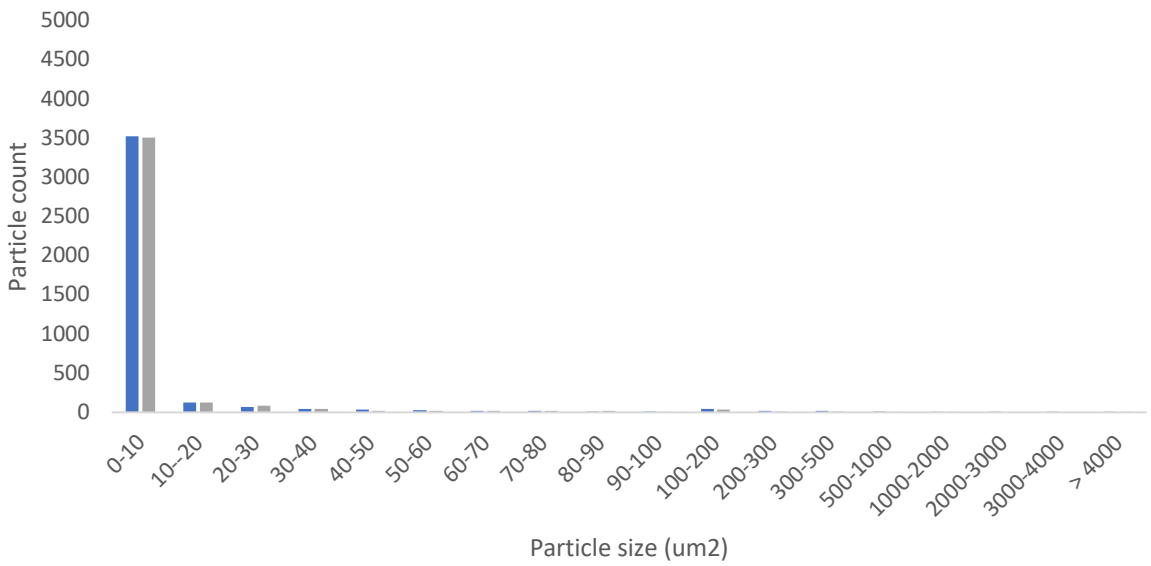

(A)

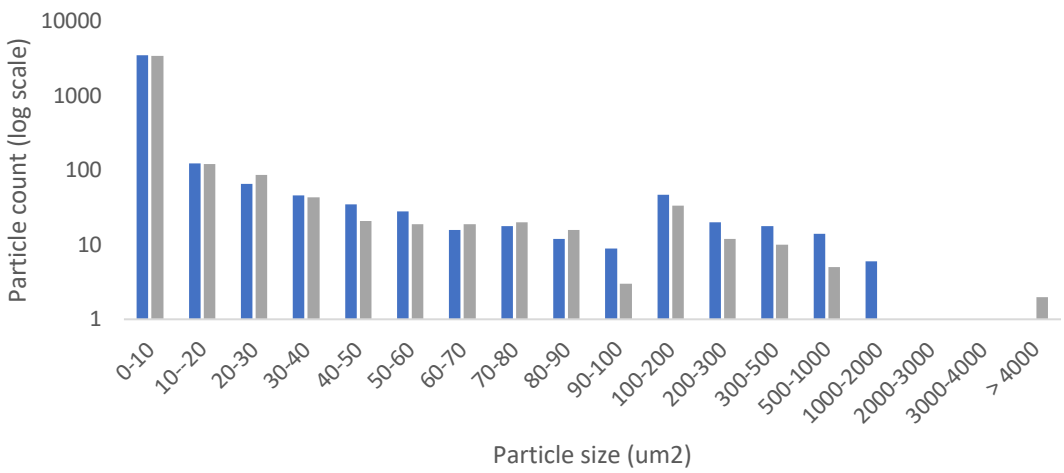

(B)

Figure 4.42 (A&B): Particle size distribution for 8.27 s^{-1} shearing rate

As the shearing rate increases to 16.93 s^{-1} , the population of smaller particles also increases significantly. However, since those samples (16.93 s^{-1}) spend more time in the pipeline transport simulation than the 33.09 s^{-1} shearing rate, they are considered the least favourable condition. Exposing the FFT to higher rotational speed but for shorter period has shown to have less impact on deflocculation in comparison with a slightly lower rotational speed but for longer period (Table 5), (Figures 4.43-4.46).

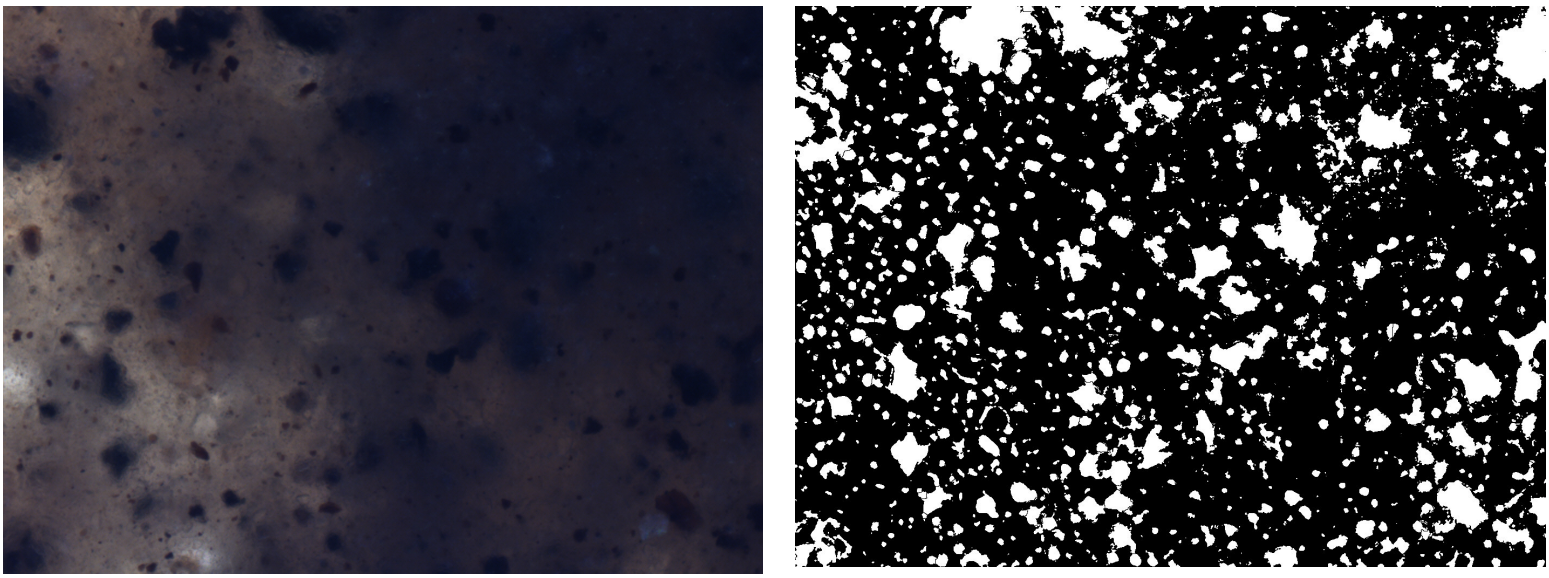

(A) **(B)**

Figure 4.43 (A&B): Raw optical microscope image and Binary Image - Trial 1 for 16.93 s^{-1} shearing rate

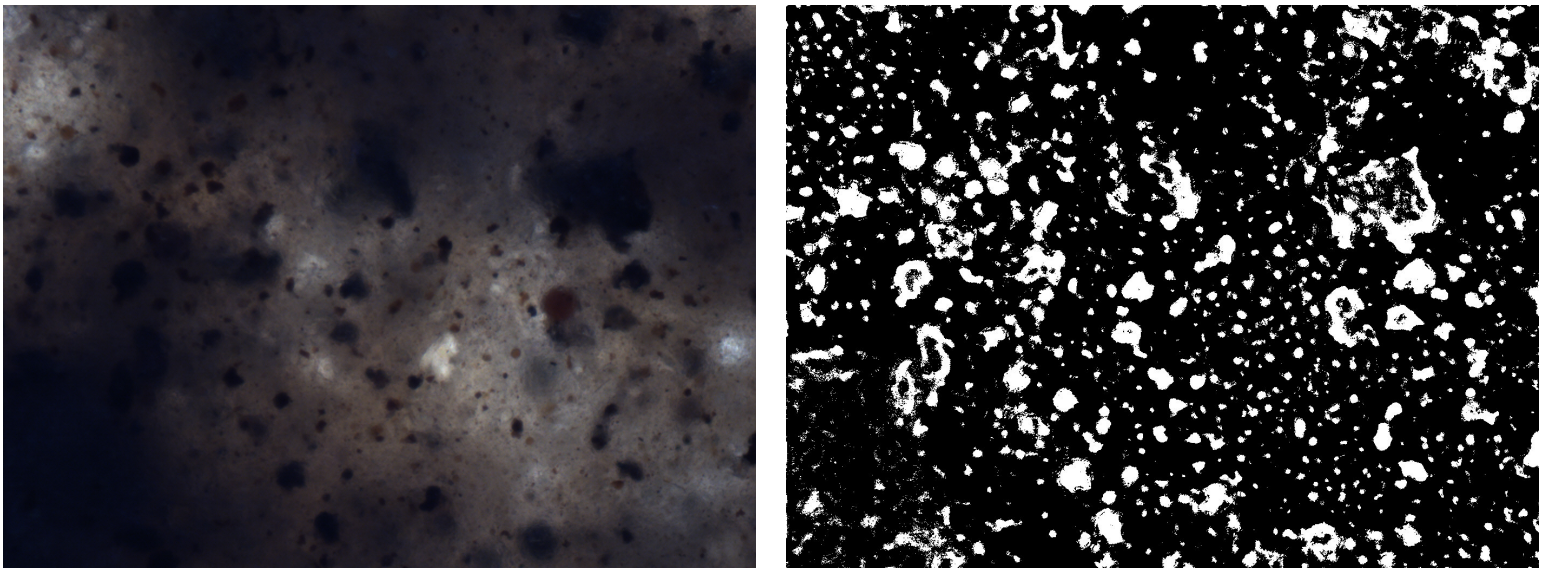

(A) **(B)**

Figure 4.44 (A&B): Raw optical microscope image and Binary Image - Trial 2 for 16.93 s^{-1} shearing rate

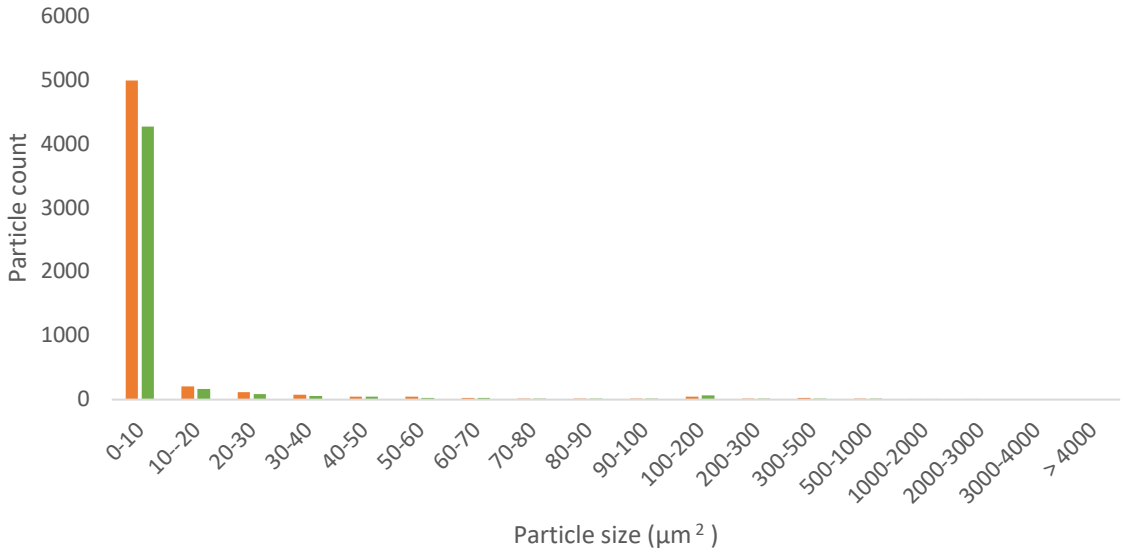

(A)

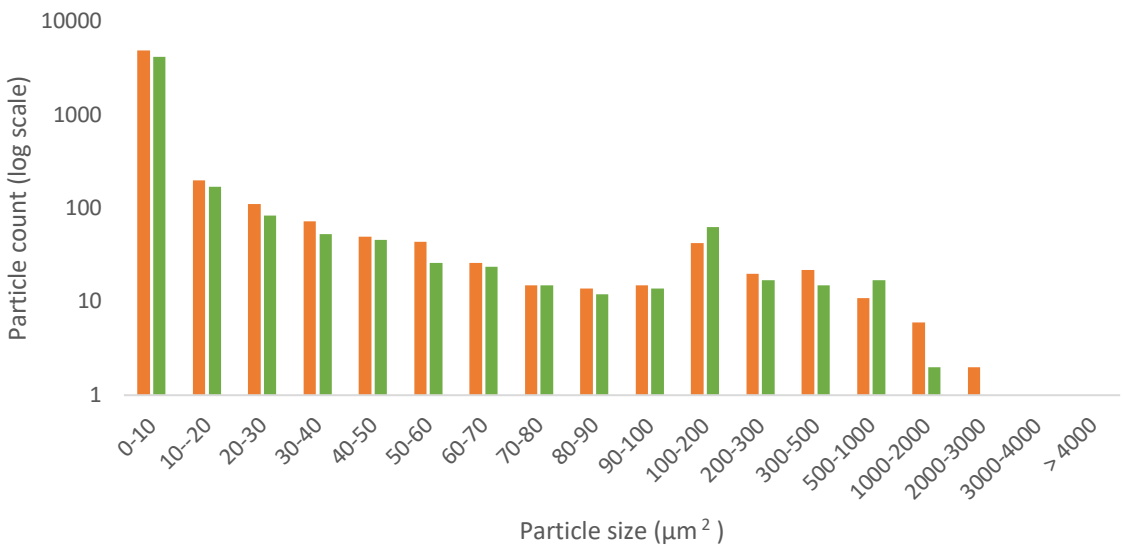

(B)

Figure 4.45 (A&B): Particle size distribution for 16.93 s^{-1} shearing rate

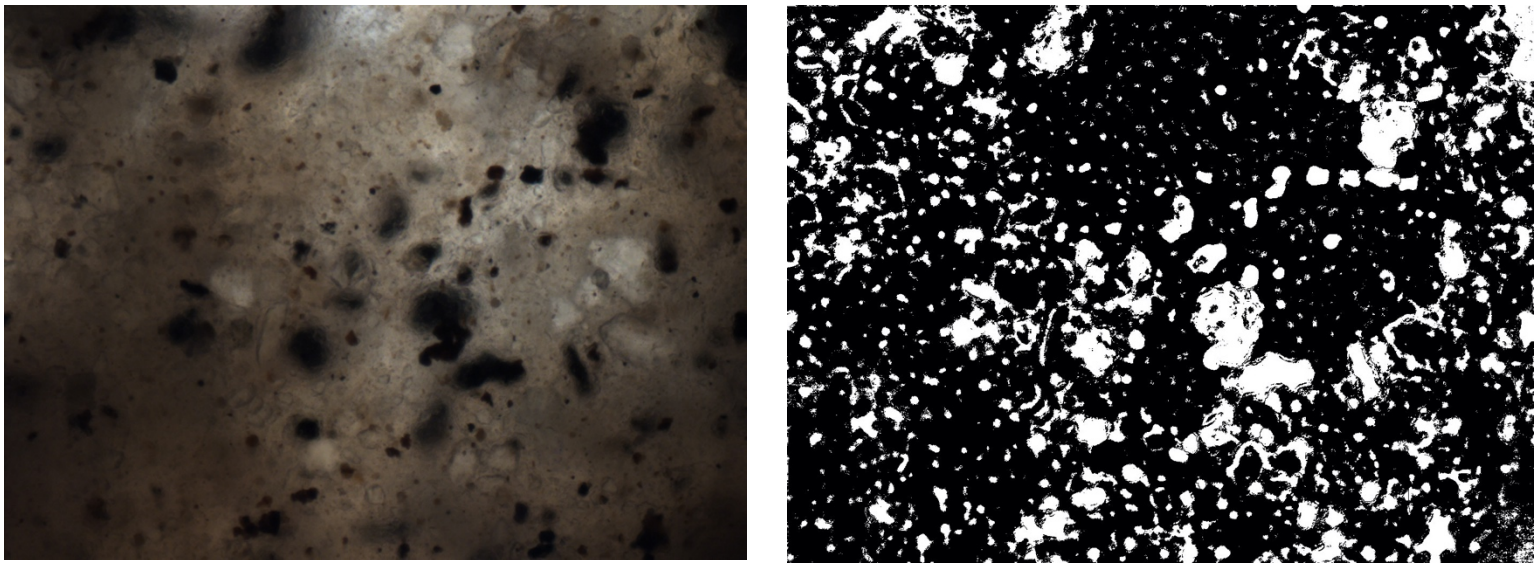

(A) **(B)**

Figure 4.46 (A&B): Raw optical microscope image and Binary Image - Trial 1 for 33.1 s^{-1} shearing rate

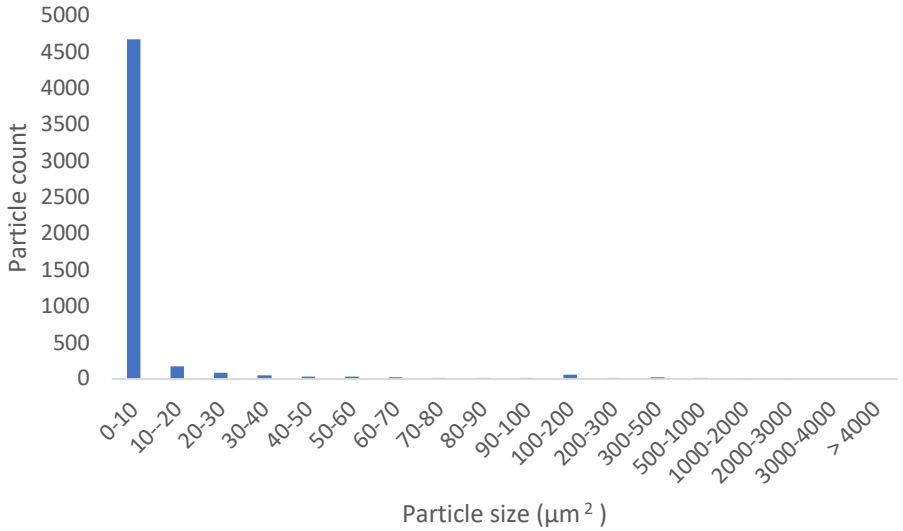

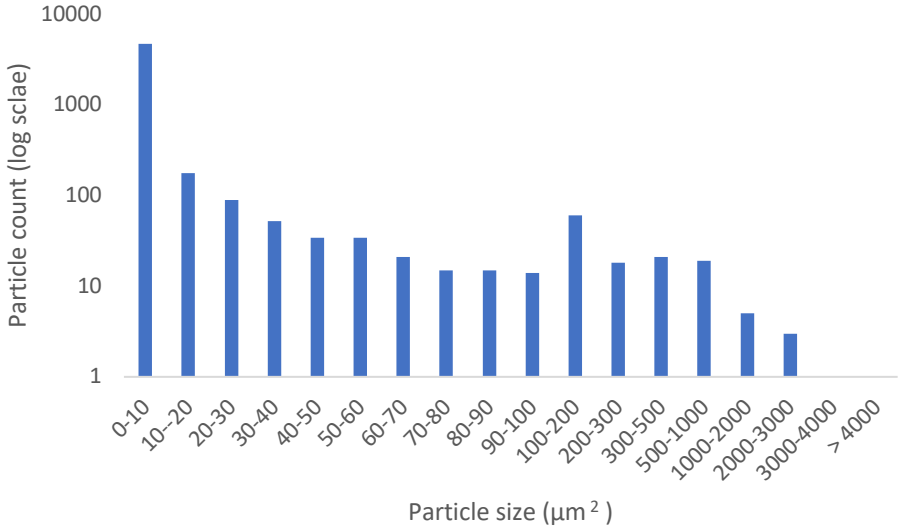

Figure 4.47 (A&B): Particle size distribution for 33.1 s^{-1} shearing rate

Oscillatory rheometry results shows a decrease of G' and yield stress (Figure 4.48-4.50). The maximum elastic shear modulus is reported to be 300 Pa for the samples sheared at 4.23 s^{-1} and 200 Pa for the samples sheared at 8.27 s^{-1} and 16.93 s^{-1}. The yield stress is also substantially low (10.5 Pa) for the sheared samples.

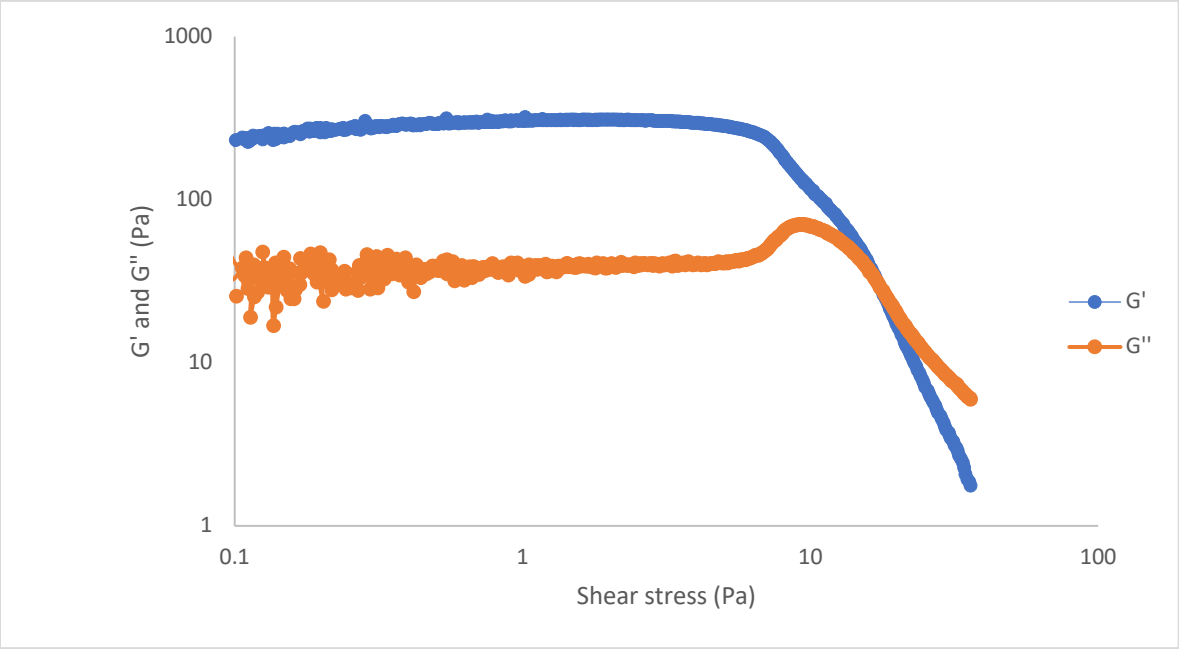

Figure 4.48: Oscillatory Rheometer data for 4.23 s^{-1} sheared samples

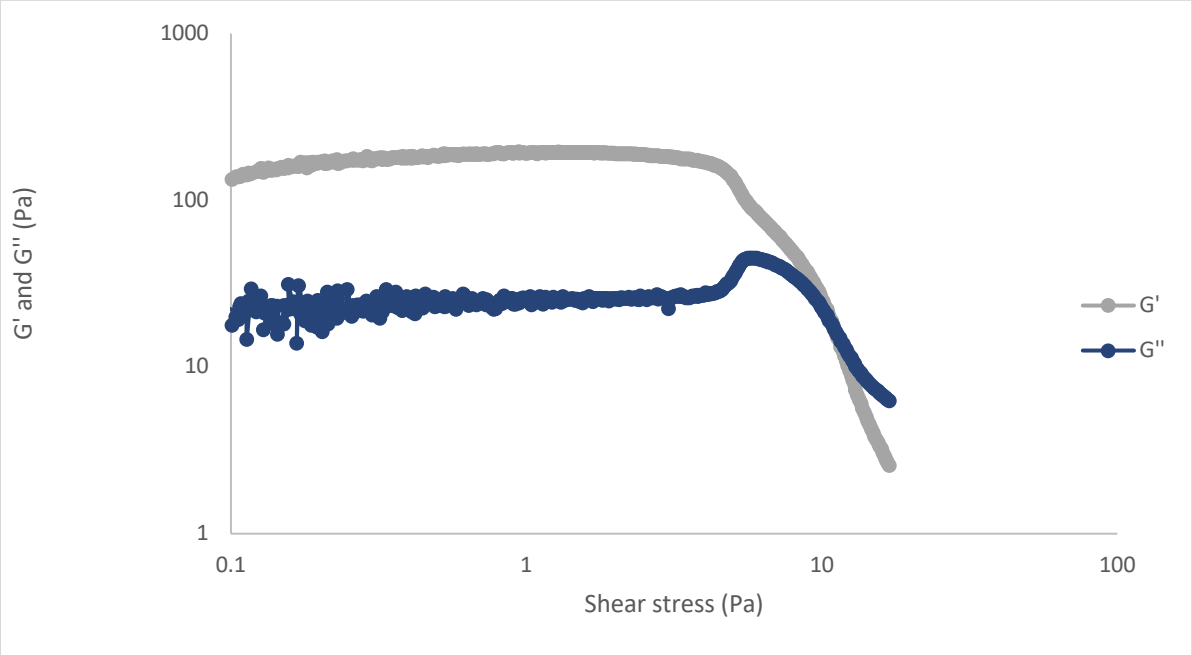

Figure 4.49: Oscillatory Rheometer data for 8.27 s^{-1} sheared samples

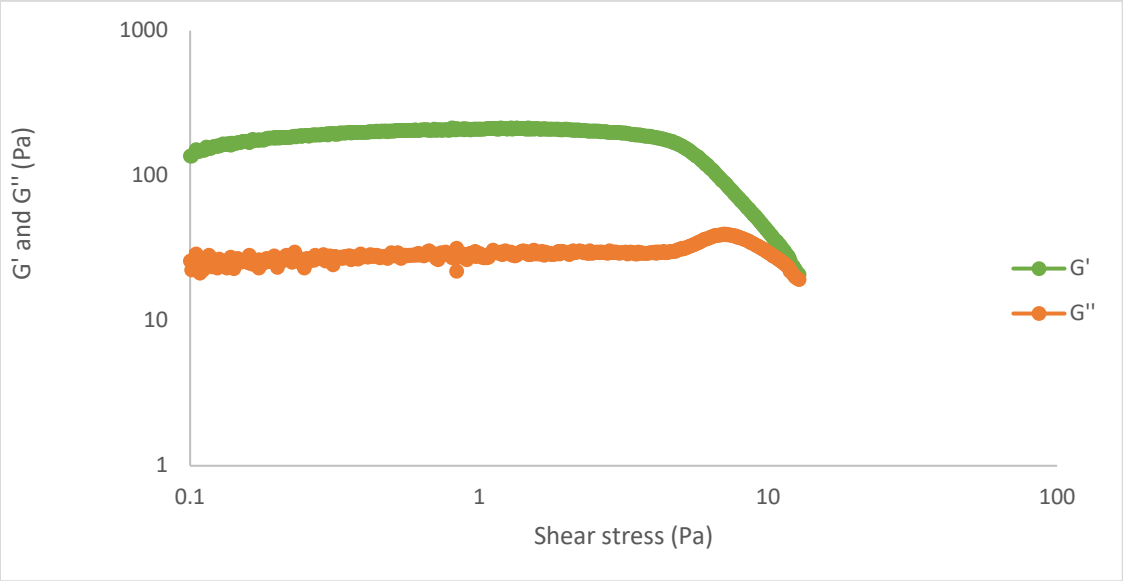

Figure 4.50: Oscillatory Rheometer data for 16.93 s^{-1} sheared samples

Validating some of the observations drawn from the optical microscopy, the settlement data shows that the 16.93 s^{-1} and the 33 s^{-1} sheared samples have a higher immediate dewaterability and overall settlement. Although smaller flocs were present in these samples, the larger flocs that were observed in the optical images seem to govern the overall settlement behaviour since larger particles are more dense and settle fast. This behaviour is opposite to what we expect in general terms, the higher shear rate is expected to cause more deflocculation, however, a potential factor could be the amount of time spent by each sample as part of the pipeline simulation.

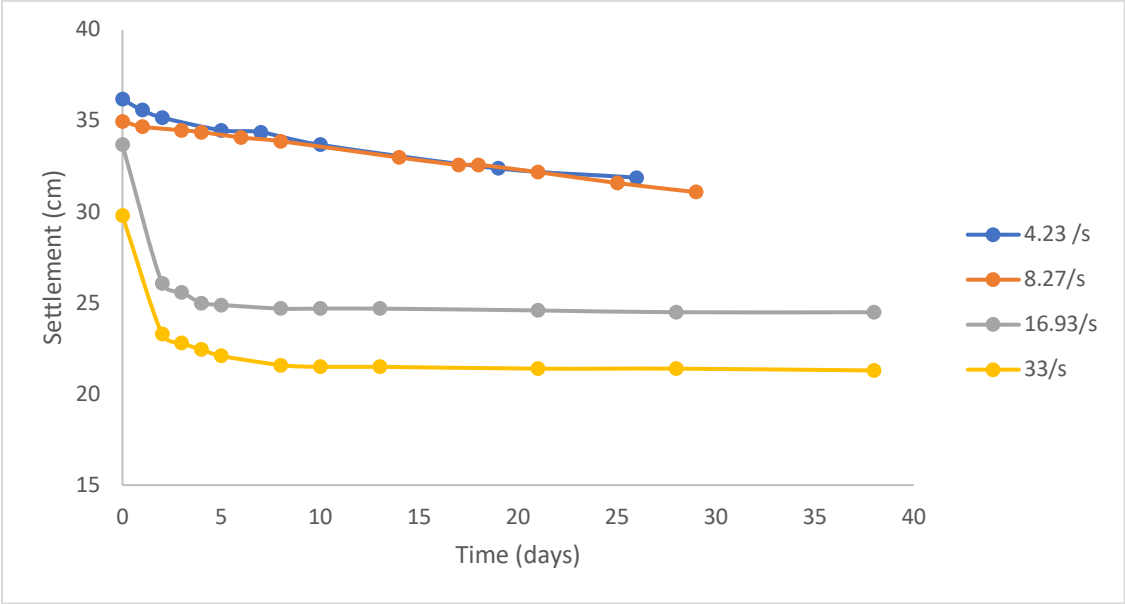

Figure 4.51: Settlement rate over time comparing the different shear rates

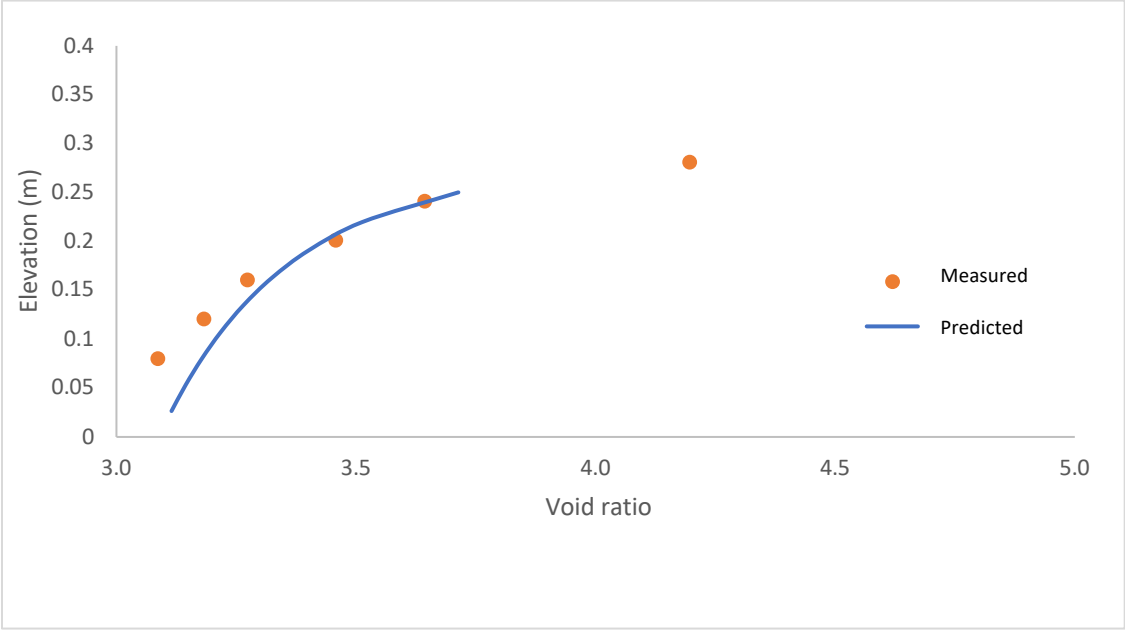

(A)

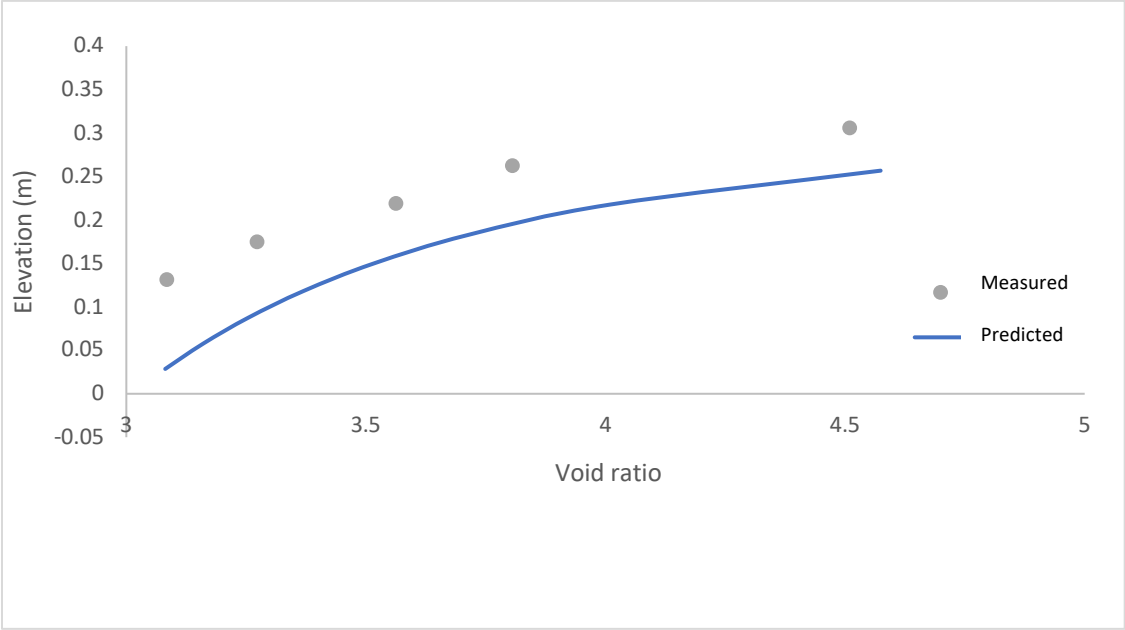
0.4
0.35
0.3
0.25
0.2
0.15
0.1
0.05
0
-0.05
Elevation (m)
3
3.5
4
4.5
5
Void ratio
Measured
Predicted

(B)

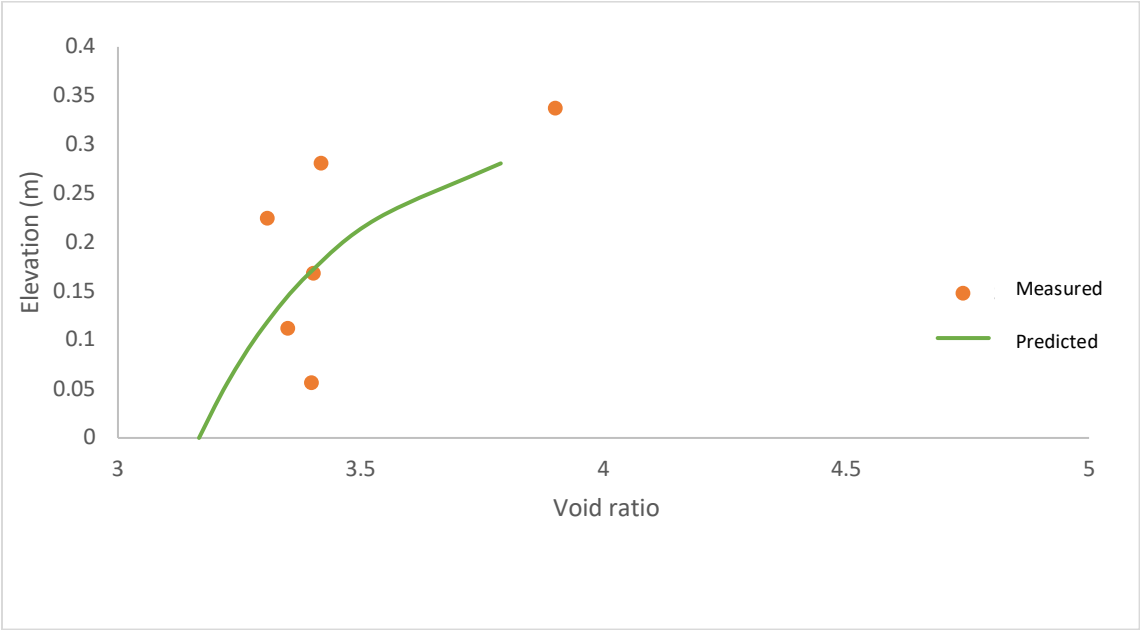
0.4
0.35
0.3
0.25
0.2
0.15
0.1
0.05
0
Elevation (m)
3
3.5
4
4.5
5
Void ratio
Measured
Predicted

(C)

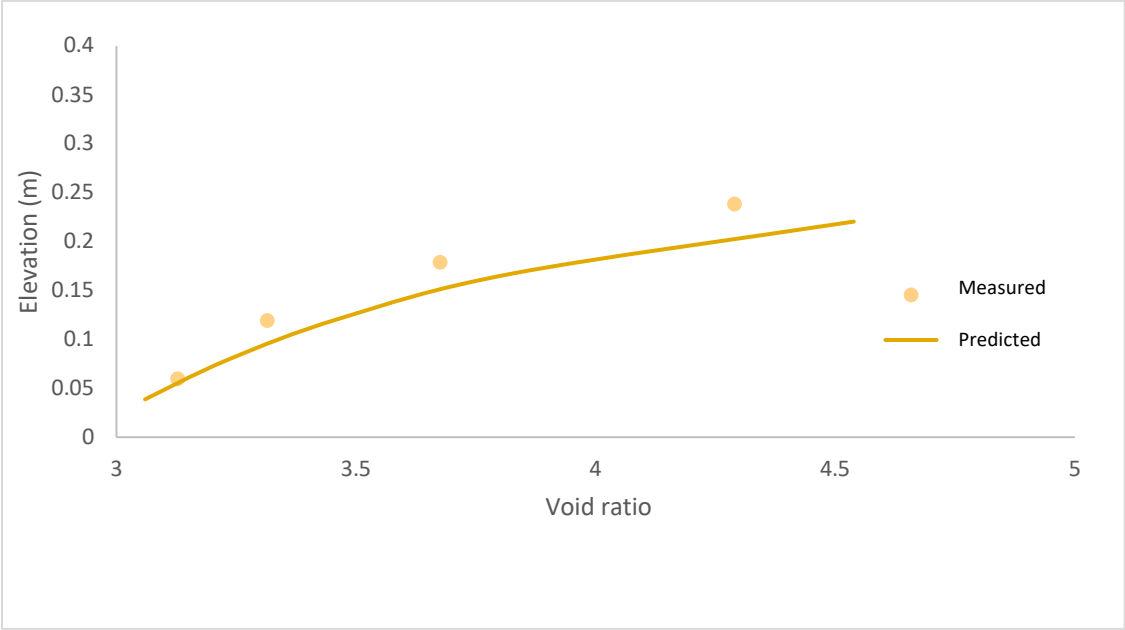

(D)

Figure 4.52 (A-D): Void ratio vs Elevation for shear rates: (A) 4.23 s^{-1} (B) 8.27 s^{-1} (C) 16.93 s^{-1} (D) 33 s^{-1}

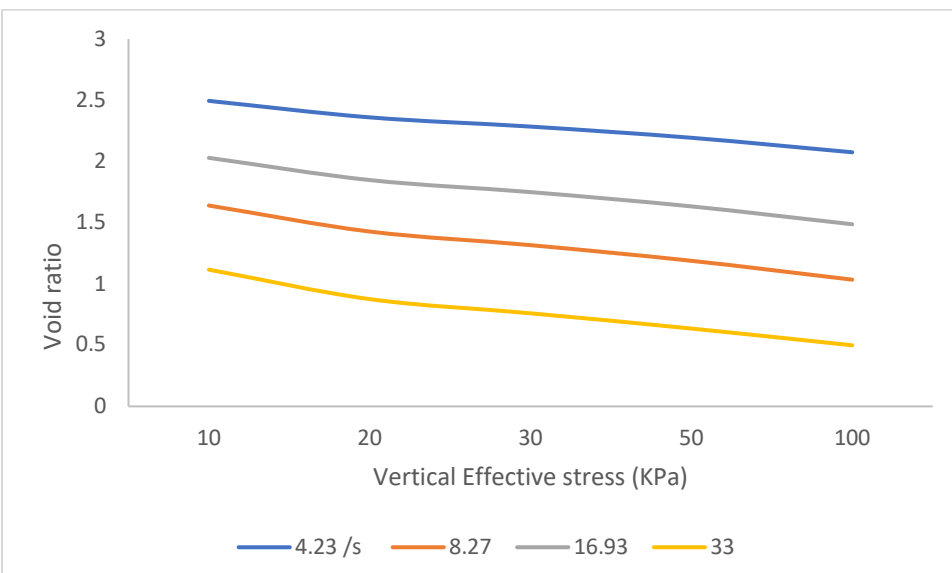

Figure 4.53: Compressibility function for all shear rates

The compressibility function and consolidation properties of the sheared fFFT are as follows:

(compressibility relationship ($e = A\sigma v'^{B}$)

Shear rate 4.23 s^{-1}: $e = 3.0\ \sigma v'^{-0.08}$

Shear rate 8.27 s^{-1}: $e = 2.6\ \sigma v'^{-0.2}$

Shear rate 16.93 s^{-1}: $e = 2.77\ \sigma v'^{-0.135}$

Shear rate 33 s^{-1}: $e = 2.5\ \sigma v'^{-0.35}$

The k-e relationship follows the same trend as the settlement behaviour. Overall, the higher shear rates have higher hydraulic conductivity which could be as a result of the larger flocs observed (as discussed earlier).

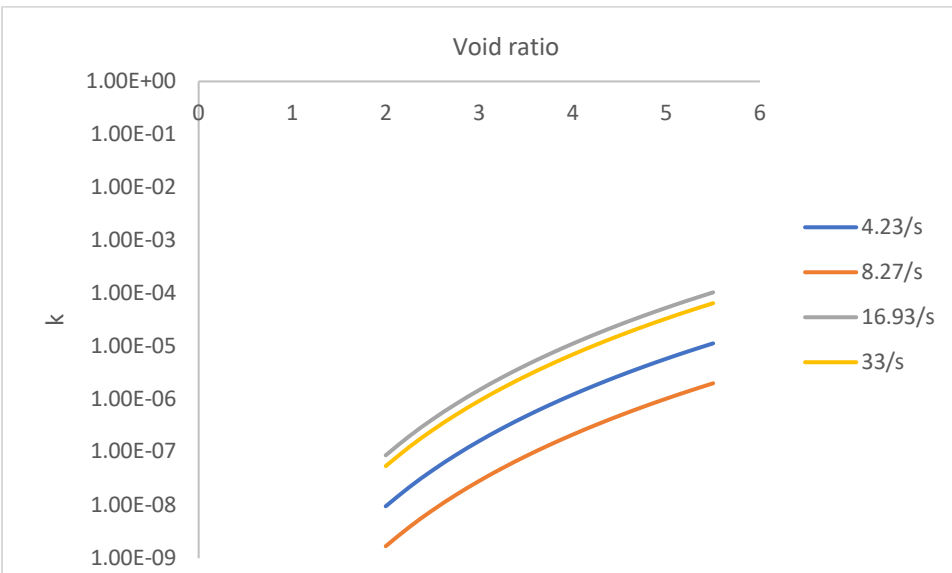

Figure 4.54: k-e relationships all shear rates

4.23s^{-1} : $k\ (m/s) = 9.87 \times 10^{-12}\ e^{7.5}$

8.27 s^{-1} : $k\ (m/s) = 9.34 \times 10^{-13}\ e^{7.5}$

16.93 s^{-1} : $k\ (m/s) = 1.05 \times 10^{-10}\ e^{7.5}$

33 s^{-1}: $k\ (m/s) = 9.06 \times 10^{-10}\ e^{7.5}$

4.5 Optical microscopy applications in quantifying the microstructure of Kaolinite

The goal of this test is to demonstrate the capabilities of optical microscopy applications in quantifying the fabric of other clays, Kaolinite. The optical microscope images were obtained for the flocculated Kaolinite samples at different water contents. The compressibility function and consolidation properties of the flocculated Kaolinite were calculated, using the compressibility relationship (e = $a\sigma v'^{b}$), a and b are estimated based on fitting the compressibility curve where e is the void ratio and $\sigma v'$ is the vertical effective stress. The hydraulic conductivity at the initial void ratio of 3.44 was calculated to be 3.6 x 10^{-6} m/s using the Pane and Schiffman's method:

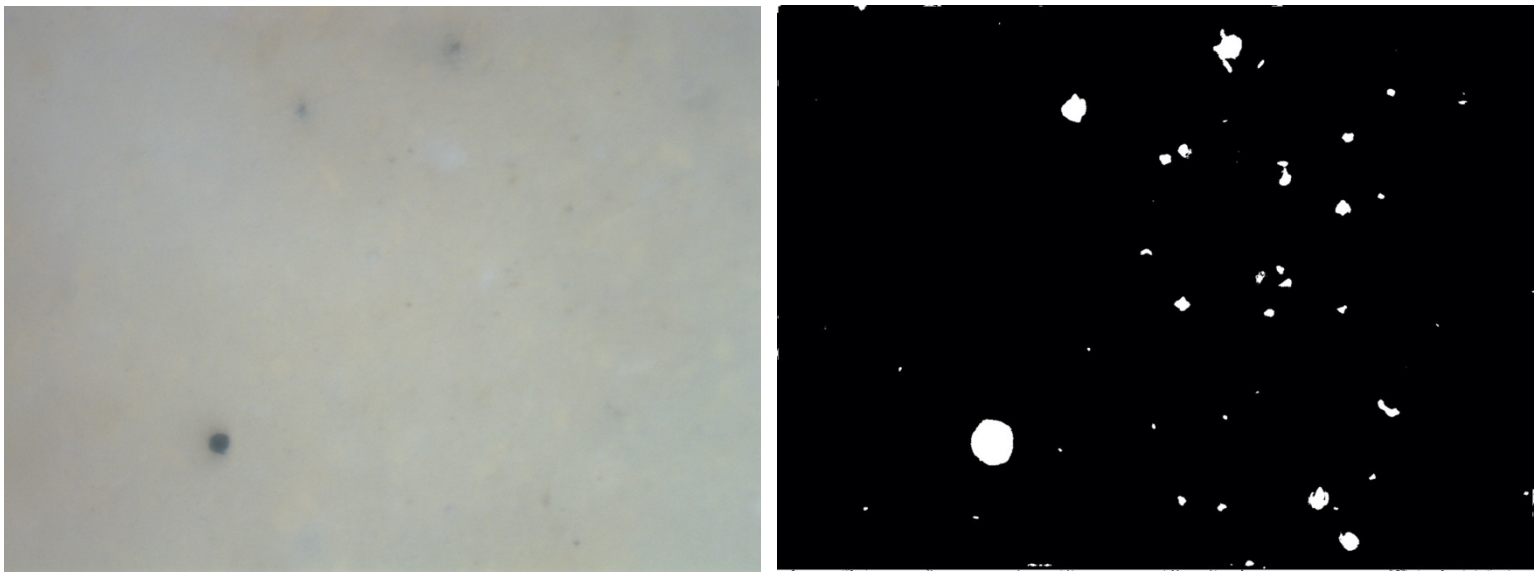

(A) **(B)**

Figure 4.55 (A&B): Raw optical microscope image and Binary Image for flocculated Kaolinite at 100% - Trial 1

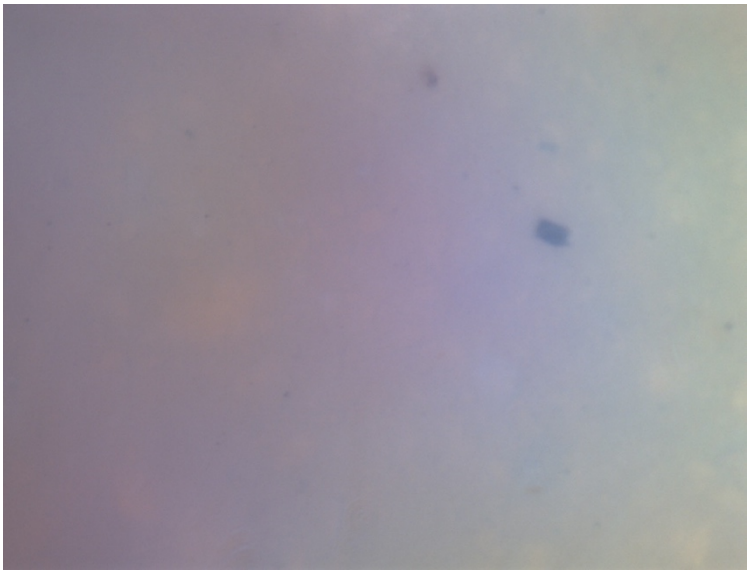

(A) **(B)**

Figure 4.56 (A&B): Raw optical microscope image and Binary Image for flocculated Kaolinite at 100% - Trial 2

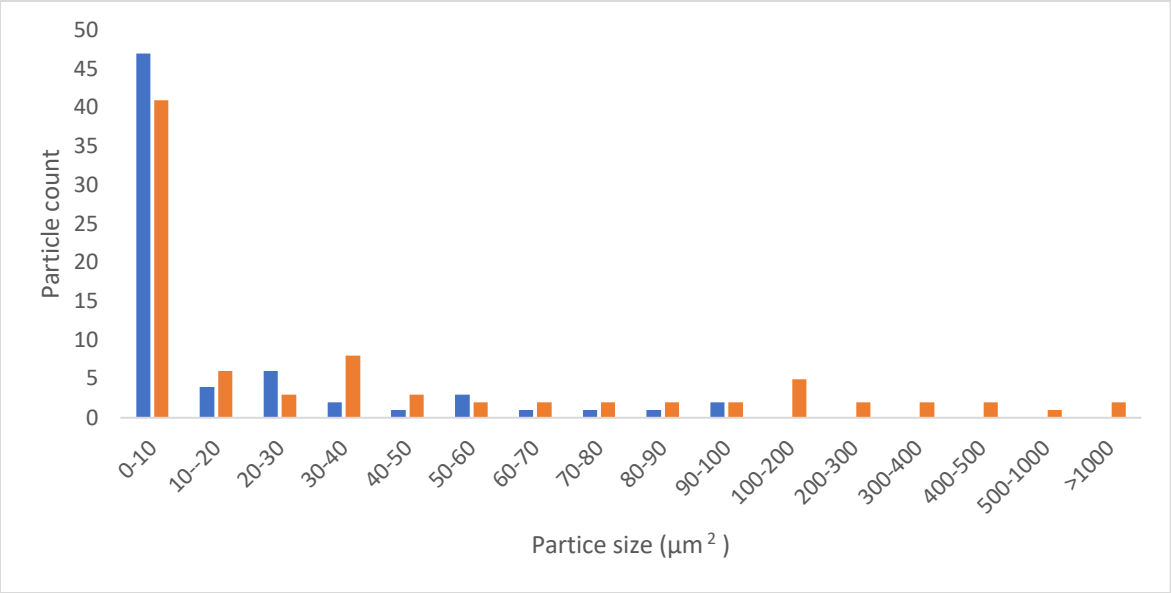

(A)

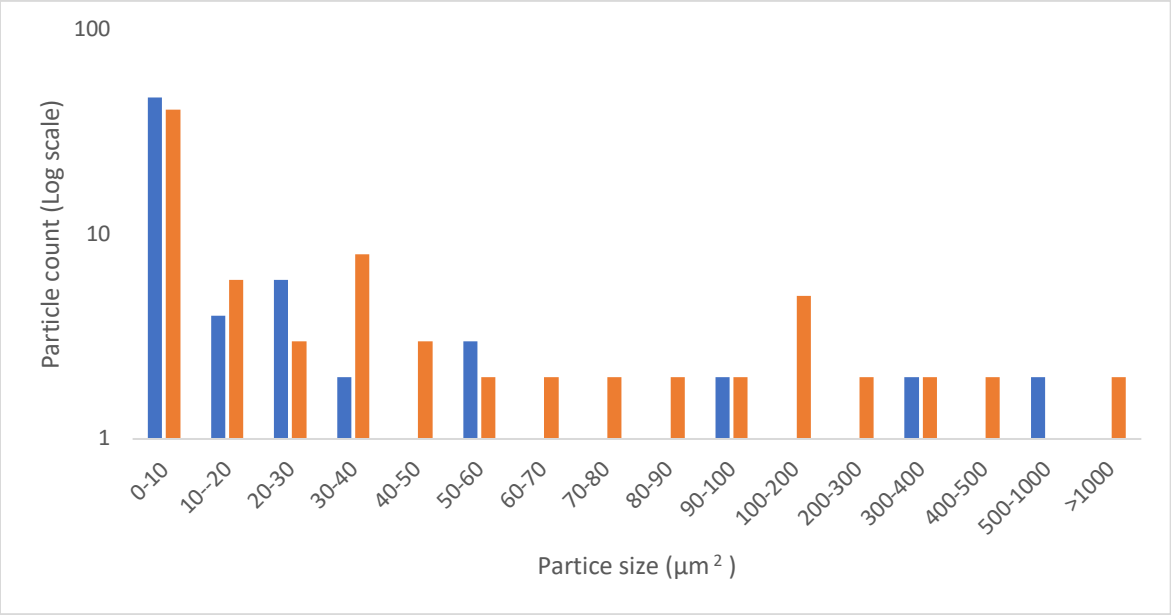

(B)

Figure 4.57 (A&B): Particle size distribution for flocculated Kaolinite at 100%

The goal of flocculating the kaolinite samples at different water contents is to obtain the ideal water content percentage for this type of clays. It was crucial for this experiment to showcase the capabilities of the Image analysis technique developed being used on different types of materials.

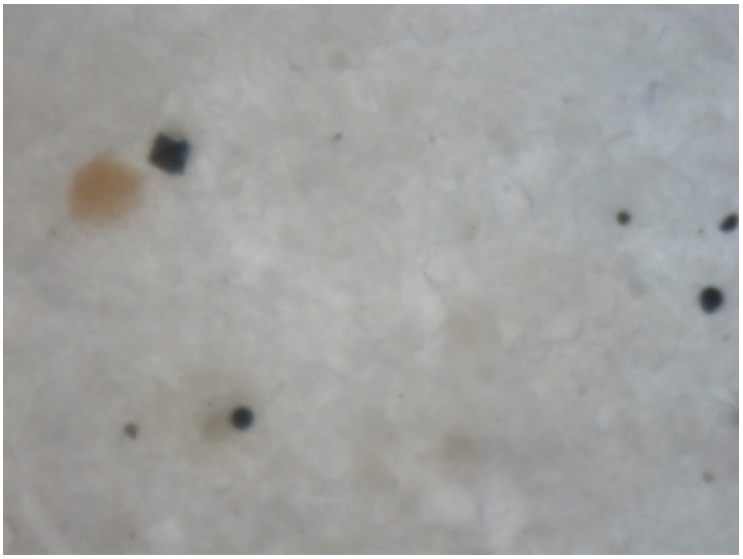

(A)

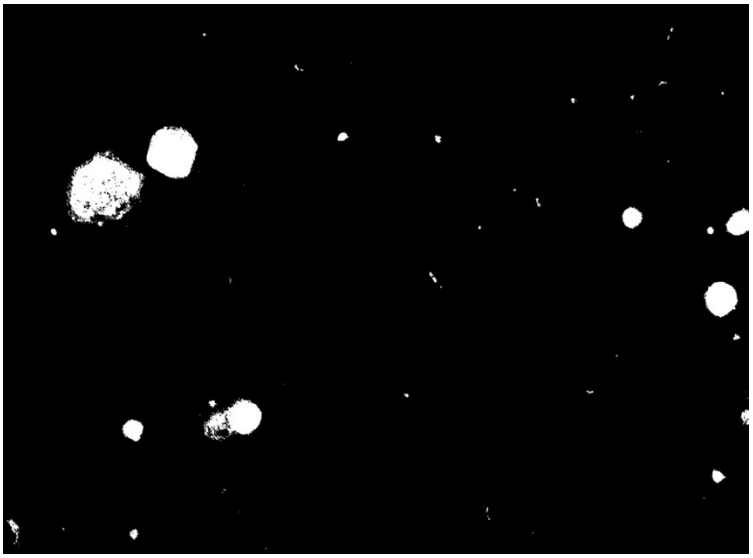

(B)

Figure 4.58(A&B): Raw optical microscope image and Binary Image for flocculated Kaolinite at 500% - Trial 1

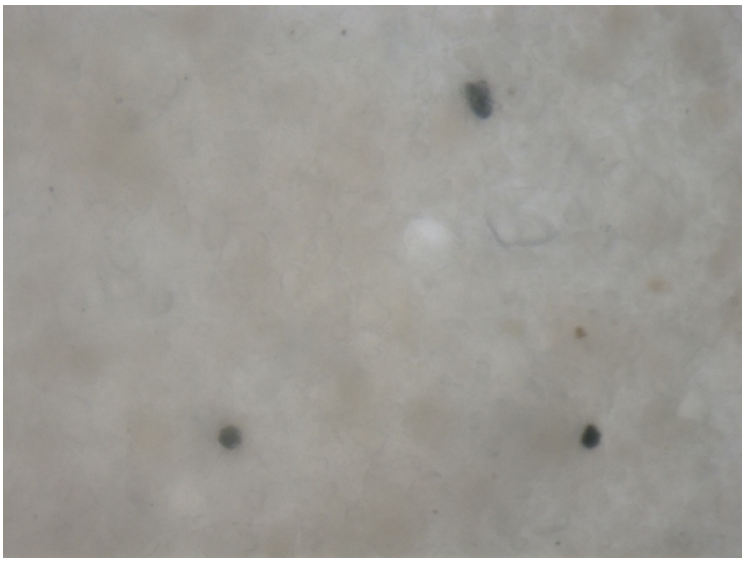

(A)

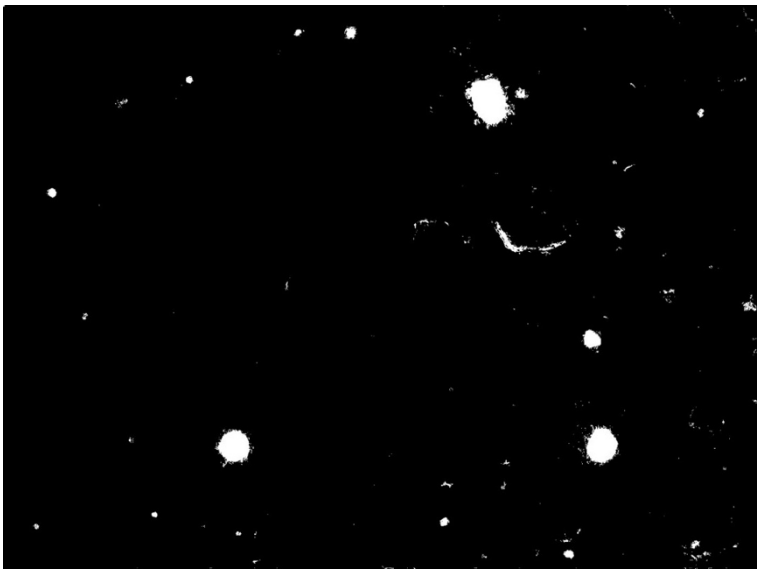

(B)

Figure 4.59 (A&B): Raw optical microscope image and Binary Image for flocculated Kaolinite at 500% - Trial 2

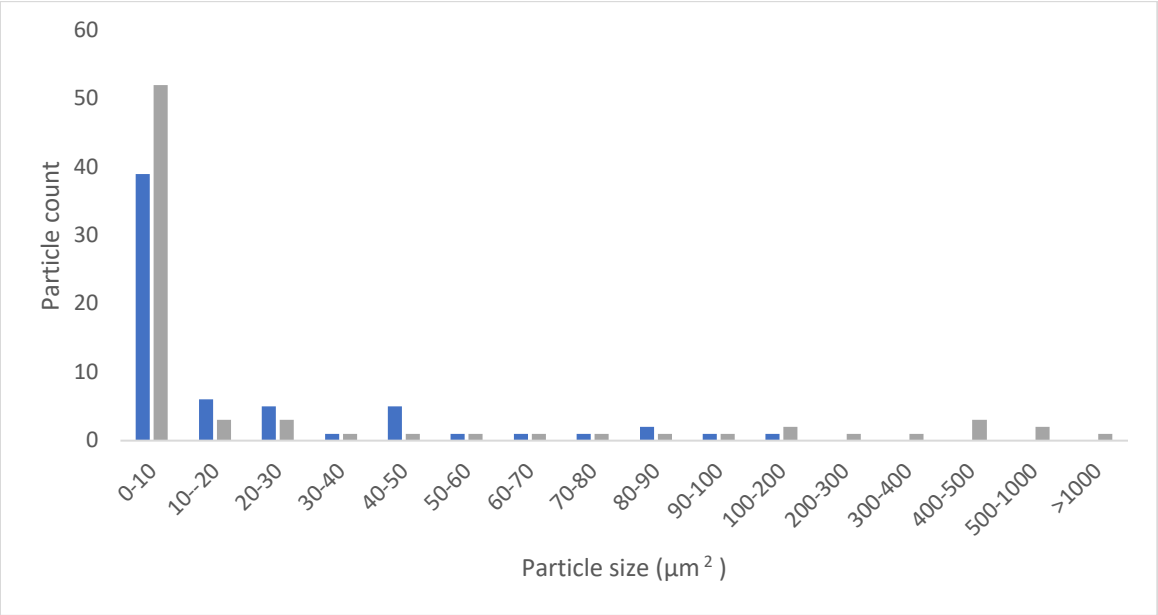

(A)

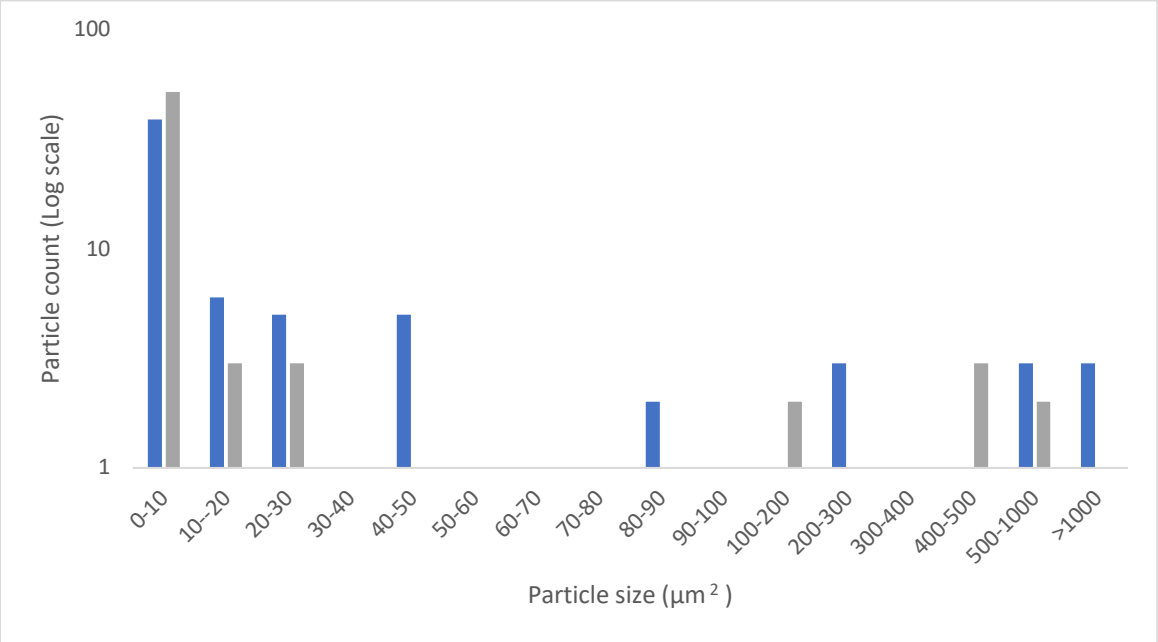

(B)

Figure 4.60 (A&B): Particle size distribution for flocculated Kaolinite at 500%

Through the settlement data and the optical microscope image analysis, it was observed that the samples with 500% water content and 1000% water content had the highest immediate dewaterability and largest floc sizes. On the other hand, the 100% water content samples had the least favourable conditions which is directly correlated to being flocculated with the lowest flocculant dosage.

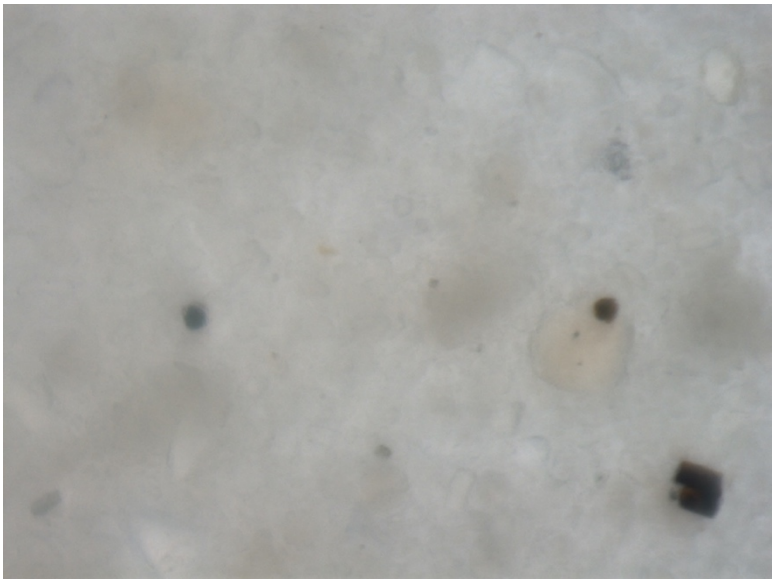

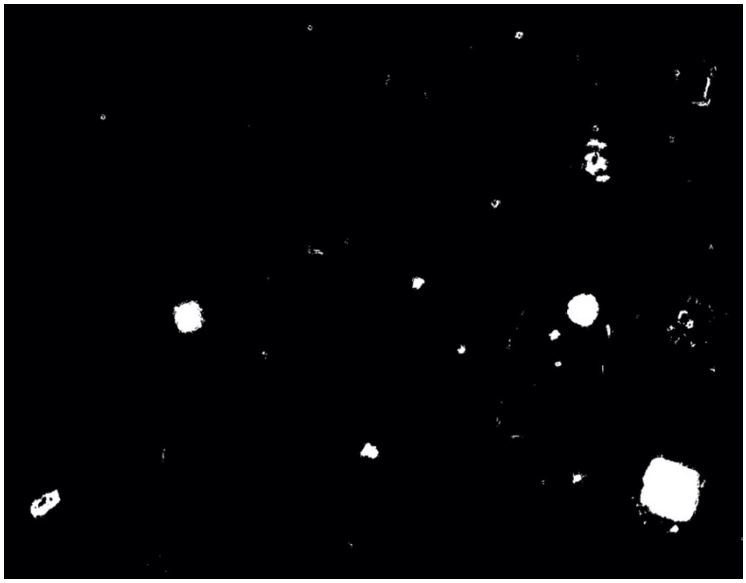

(A) **(B)**

Figure 4.61 (A&B): Raw optical microscope image and Binary Image for flocculated Kaolinite at 1000% - Trial 1

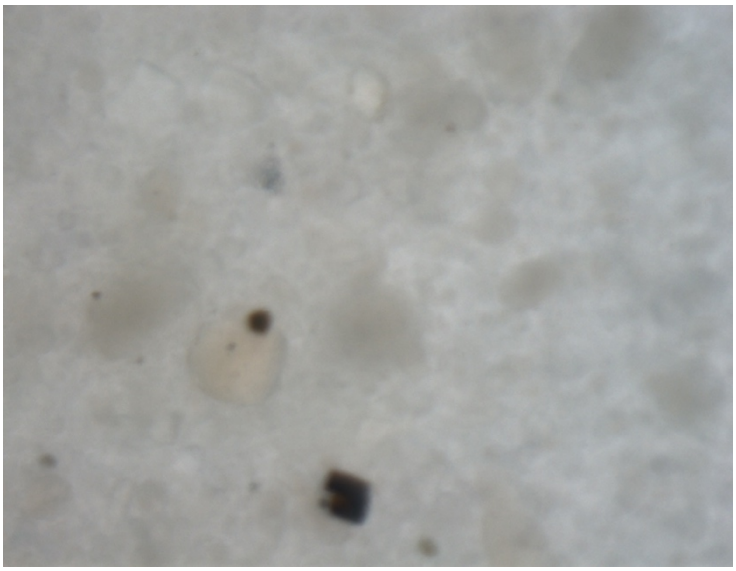

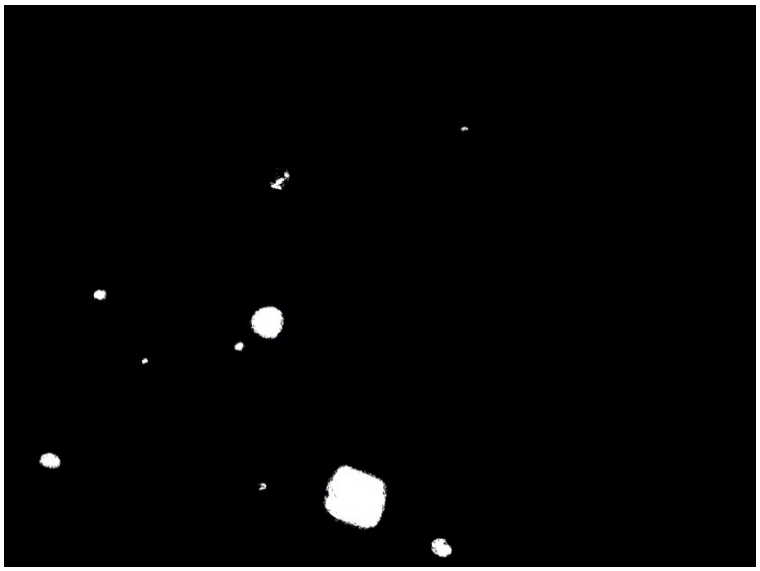

(A) **(B)**

Figure 4.62 (A&B): Raw optical microscope image and Binary Image for flocculated Kaolinite at 1000% - Trial 2

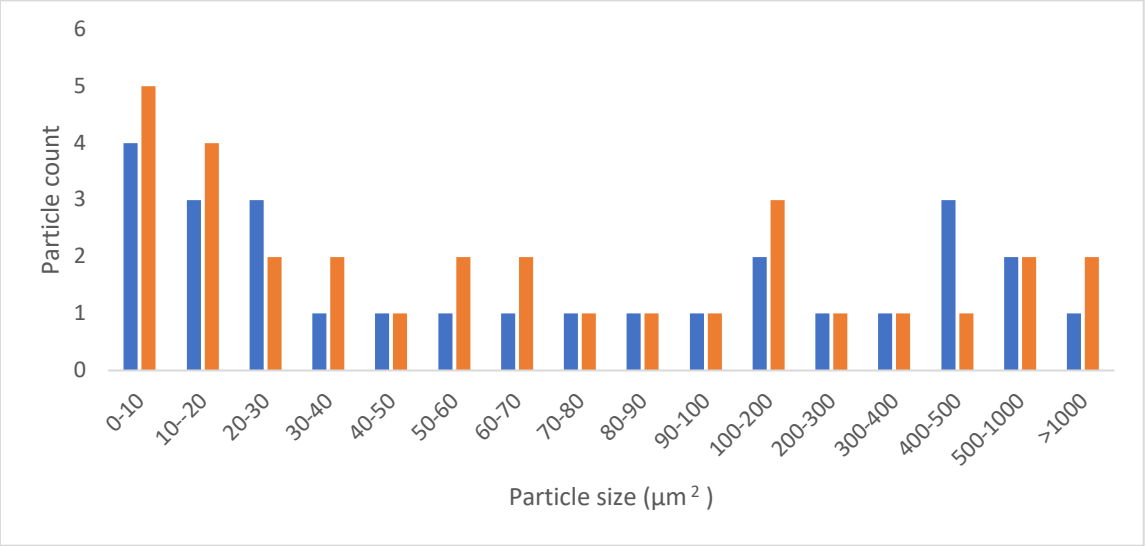

(A)

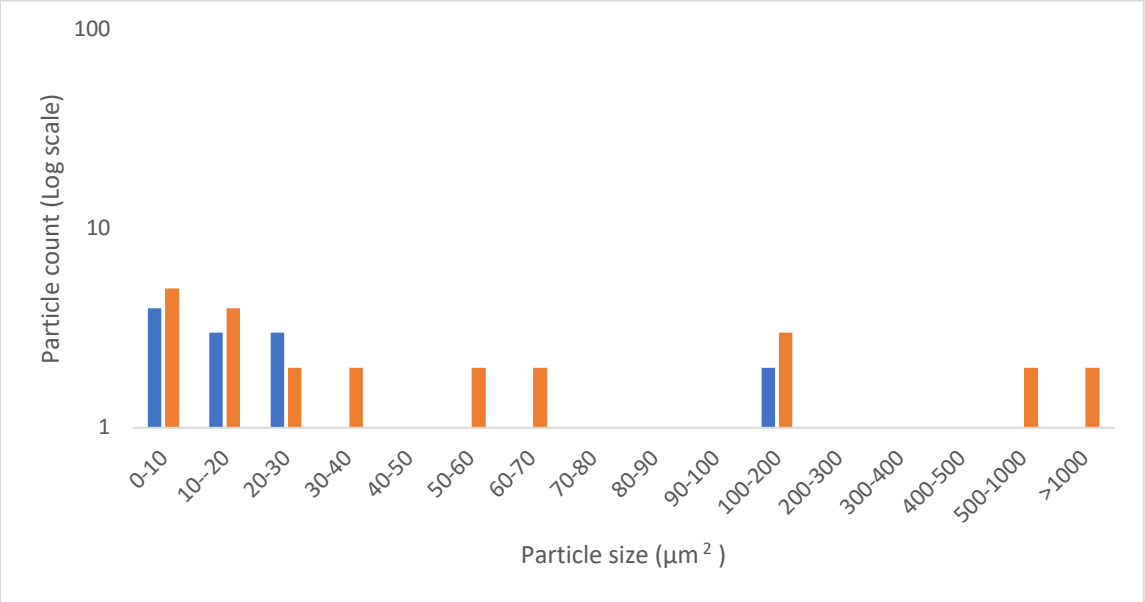

(B)

Figure 4.63 (A&B): Particle size distribution for flocculated Kaolinite at 1000%

The particle size distribution graphs show that > 1000 um^2 size bin representing the large floc particles are directly proportional to the rate of settlement. It's worth noting, even though the 2000% water content samples did not have a quick immediate dewaterability, the samples experienced the highest overall settlement over time (after two weeks final height is 2 cm). This behaviour can be explained since the sample had the highest water content in comparison with the 500% and 1000% water content samples.

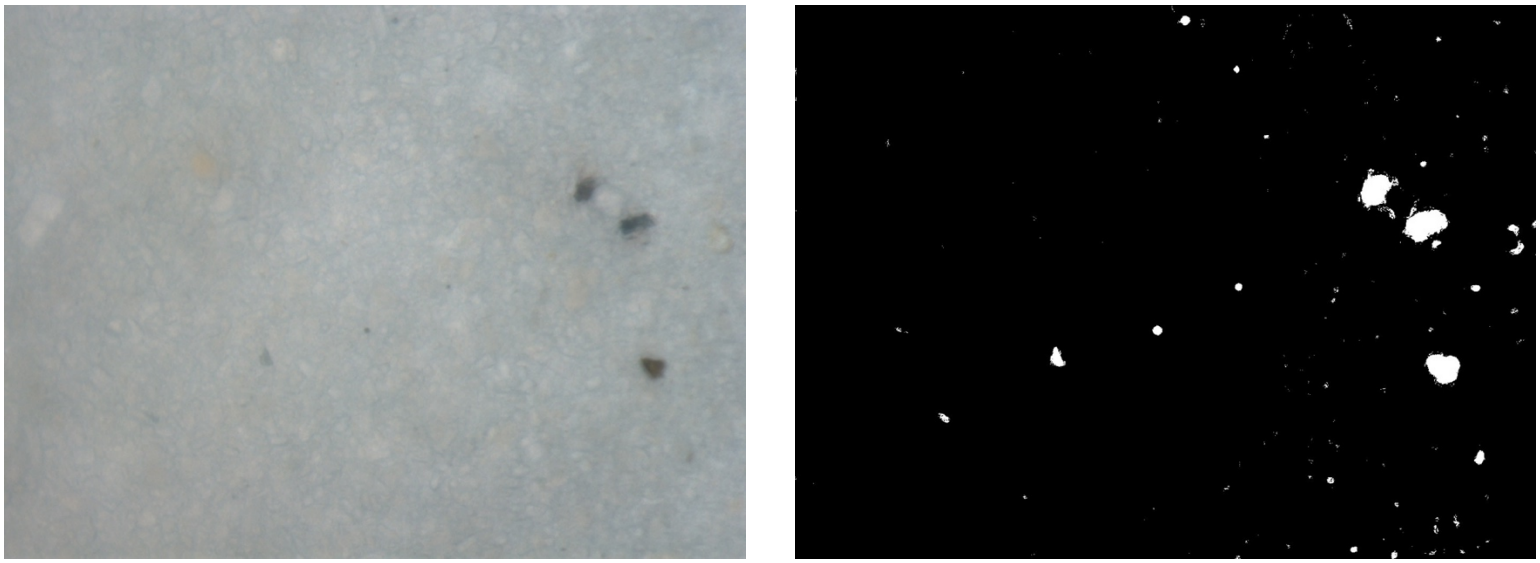

(A) **(B)**

Figure 4.64 (A&B): Raw optical microscope image and Binary Image for flocculated Kaolinite

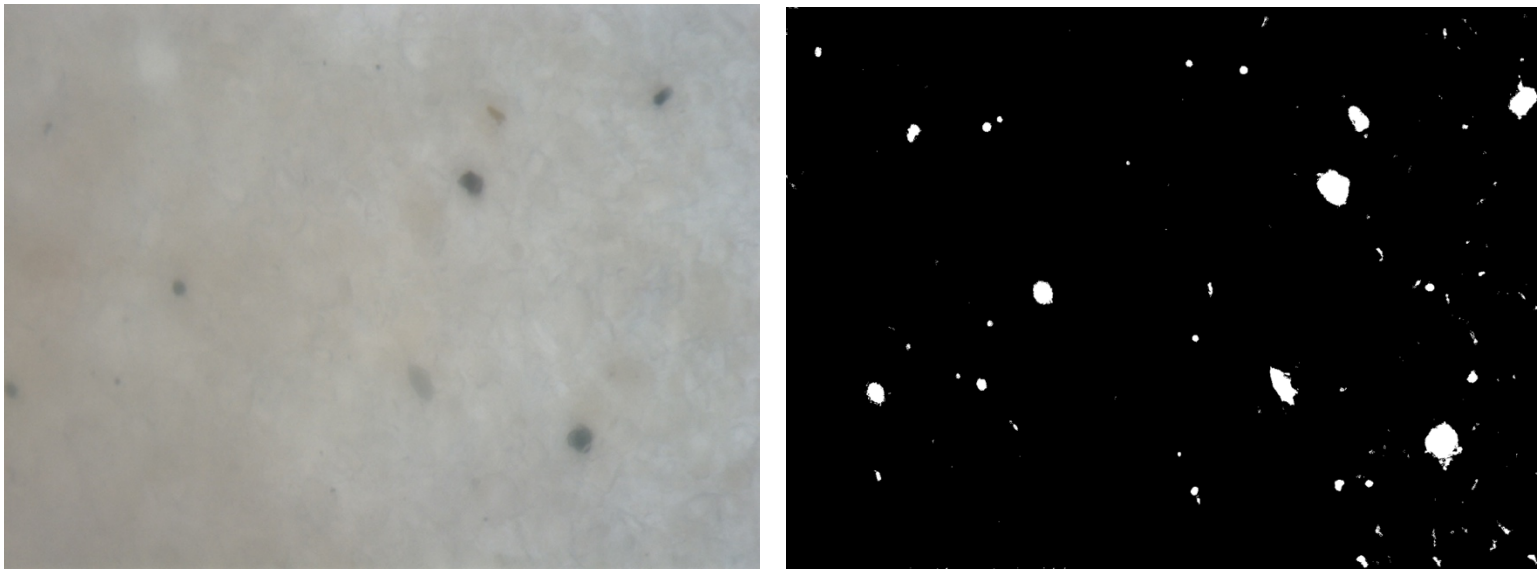

(A) **(B)**

Figure 4.65 (A&B): Raw optical microscope image and Binary Image for flocculated Kaolinite at 2000% - Trial 2

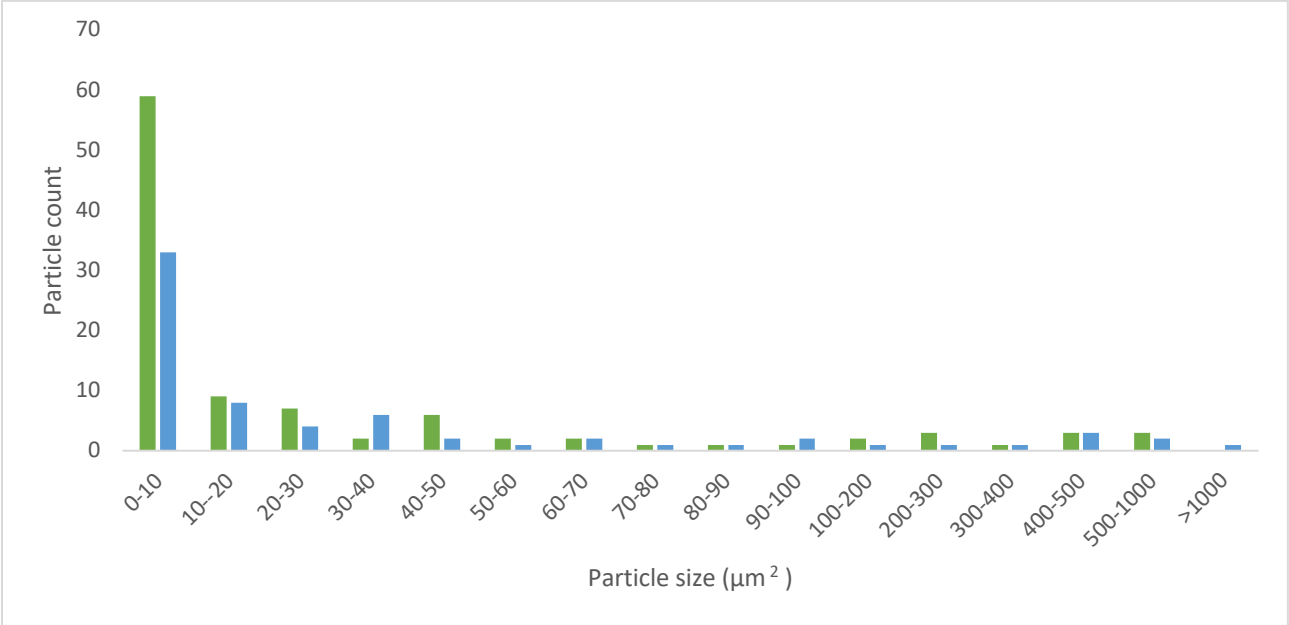

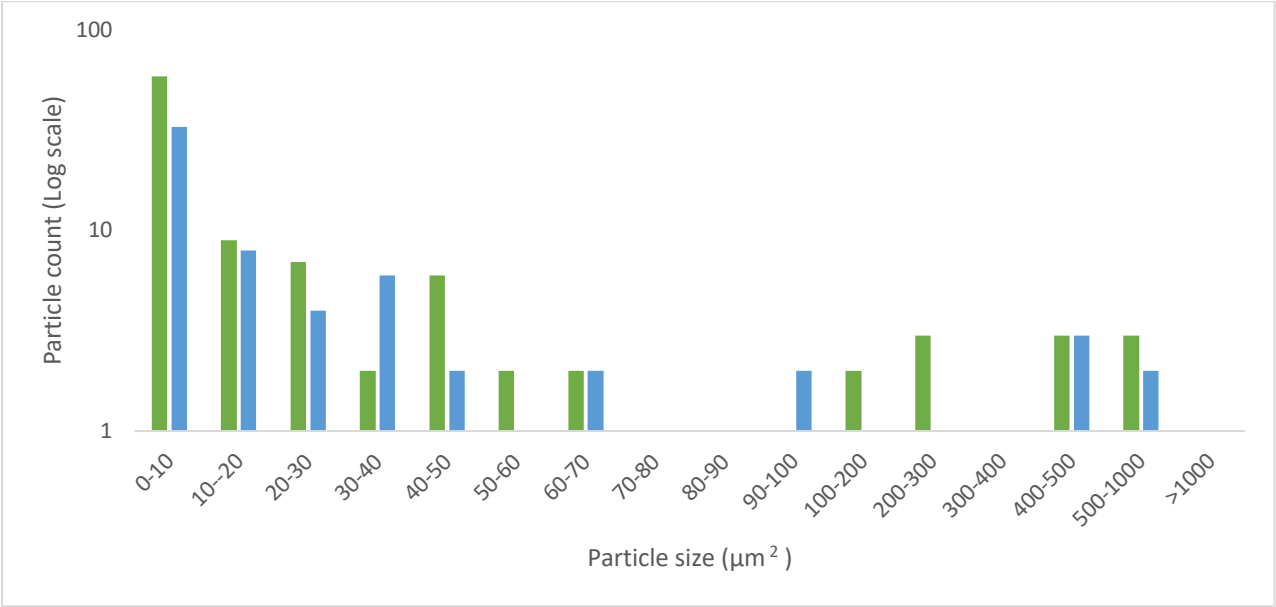

Figure 4.66: Particle size distribution for flocculated Kaolinite at 2000%

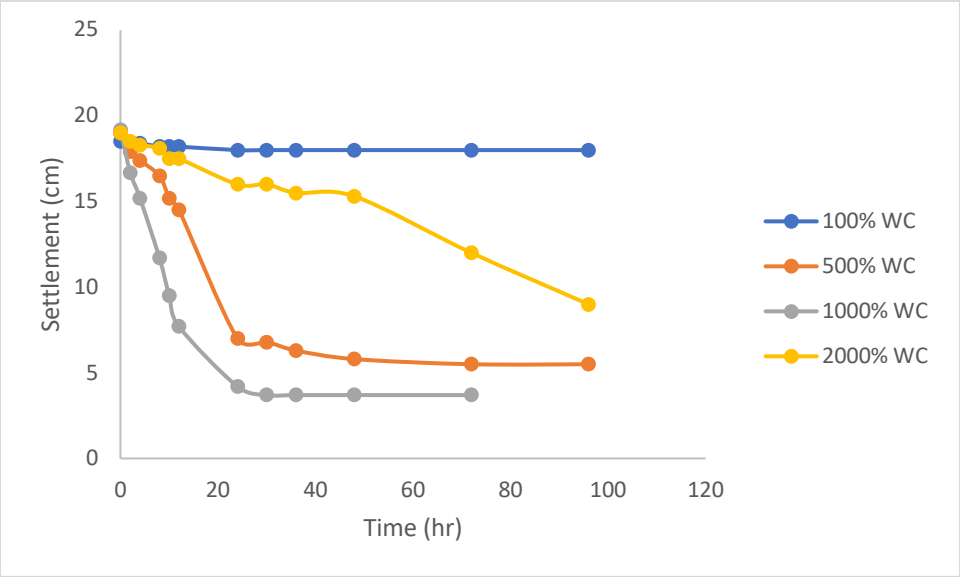

Figure 4.67: Settlement over time for flocculated Kaolinite at different water contents

The k-e relationships presented in Figures 4.69 , shows that the flocculated kaolinite samples at 1000% WC has a higher hydraulic conductivity than 500% WC. This validates the results observed from the optical microscopy images where the largest number of flocs where observed and hence higher porosity and hydraulic conductivity. The flocculated kaolinite samples at 2000% water content were observed to have lower immediate dewaterability, and settlement. Through the image analysis of the optical microscope images, the largest particles observed were observed at the 1000% WC and then 500% WC. The 2000% WC samples didn't have a quick dewatering behaviour which was confirmed through both settlement data and the optical microscope results (0 hours post flocculation). However, after 2 weeks the 2000% WC settled further and had the highest overall settlement. The calculated hydraulic conductivity values using Pane and Schiffman (1987) demonstrated that in fact the 2000% WC samples had a lower k in comparison with 1000% WC. Overall, through the various performance indicator tests, the optical microscope analysis has shown to be a valuable parameter that validates and is directly correlated with tailings performance observed.

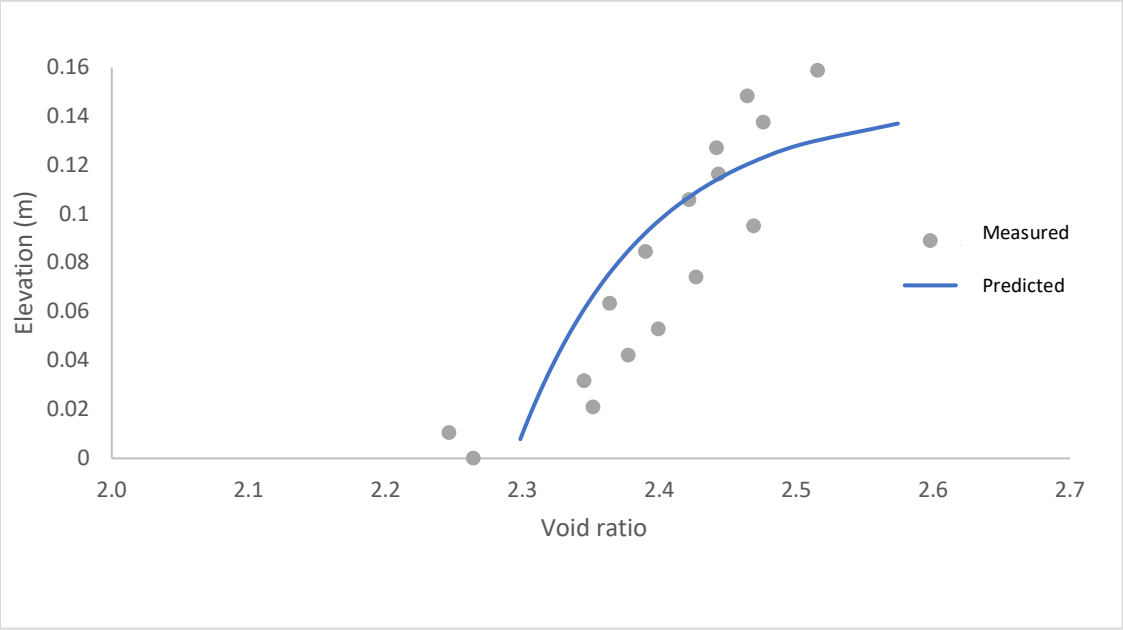
0.16
0.14
0.12
0.1
0.08
0.06
0.04
0.02
0
Elevation (m)
2.0
2.1
2.2
2.3
2.4
2.5
2.6
2.7
Void ratio
Measured
Predicted

(A)

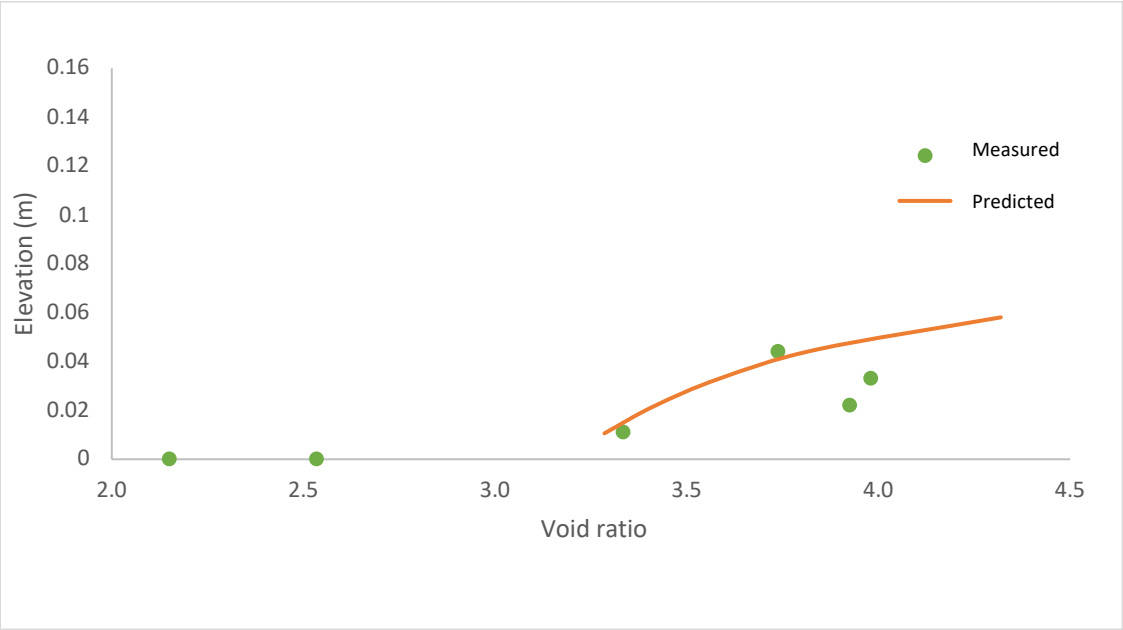
0.16
0.14
0.12
0.1
0.08
0.06
0.04
0.02
0
Elevation (m)
2.0
2.5
3.0
3.5
4.0
4.5
Void ratio
Measured
Predicted

(B)

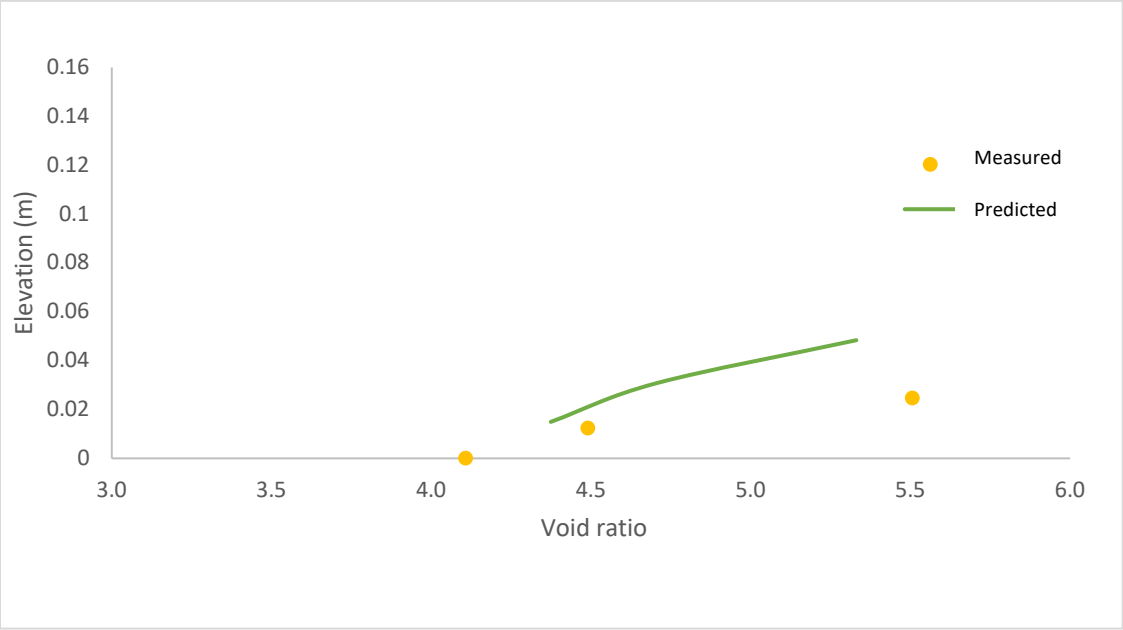

(C)

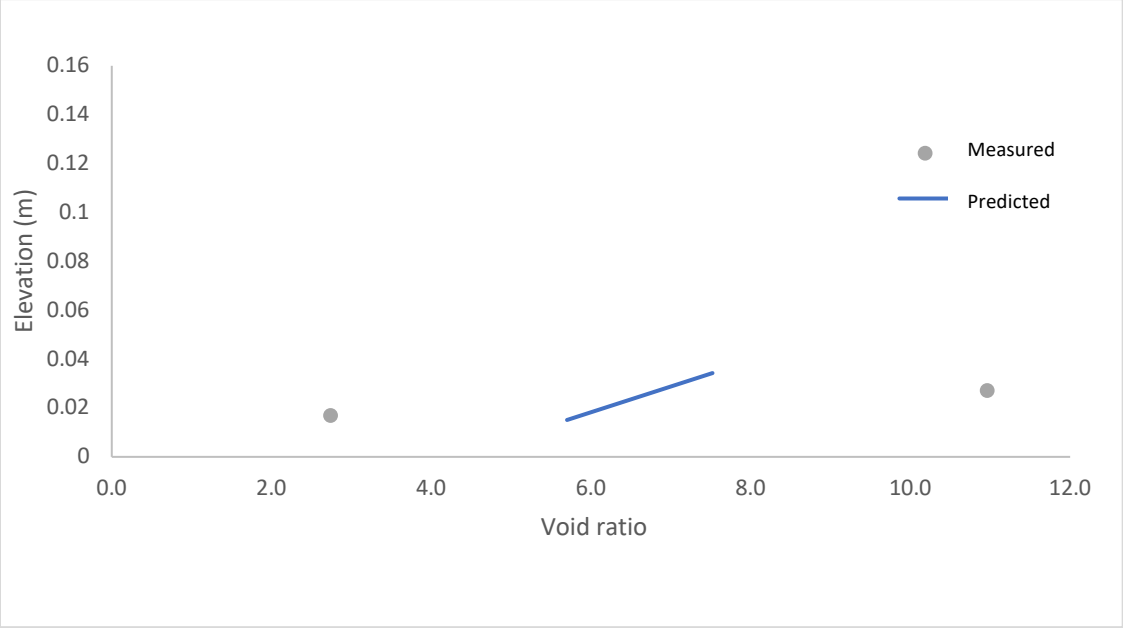

(D)

Figure 4.68 (A-D): Void ratio vs Elevation for water contents 100%, 500%, 1000% and 2000%

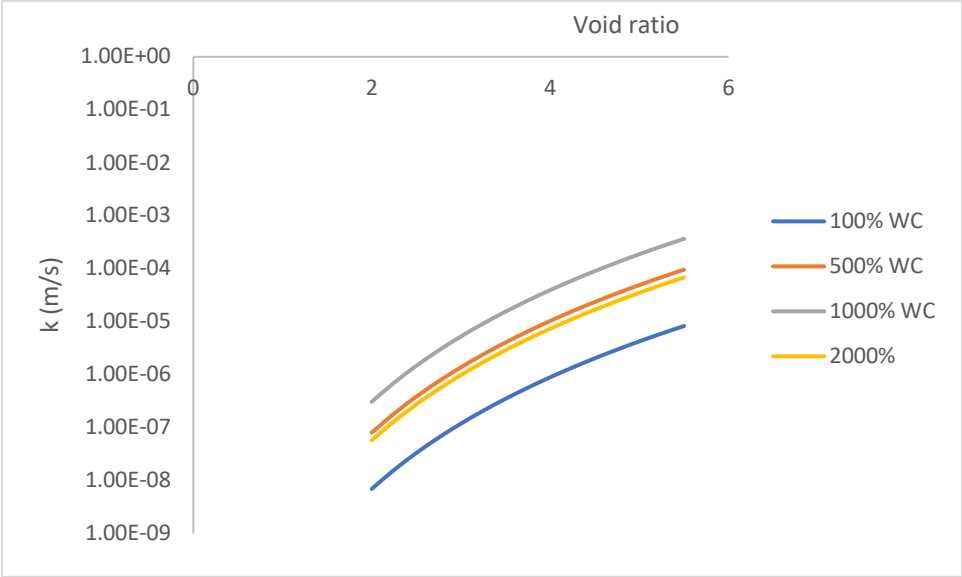

Figure 4.69: The k-e relationship between all flocculated Kaolinite samples at different water contents

The k-e relationships plotted on Figure 4.69 are represented by the following equations using Pane and Schiffman (1997) power function ($k = C\ e^{D}$) :

100% WC: $k = 5.46 \times 10^{-11}\ e^{7.5}$

500% WC: $k = 6.31 \times 10^{-10}\ e^{7.5}$

1000% WC: $k = 2.41 \times 10^{-9}\ e^{7.5}$

2000% WC: $k = 4.51 \times 10^{-10}\ e^{7.5}$

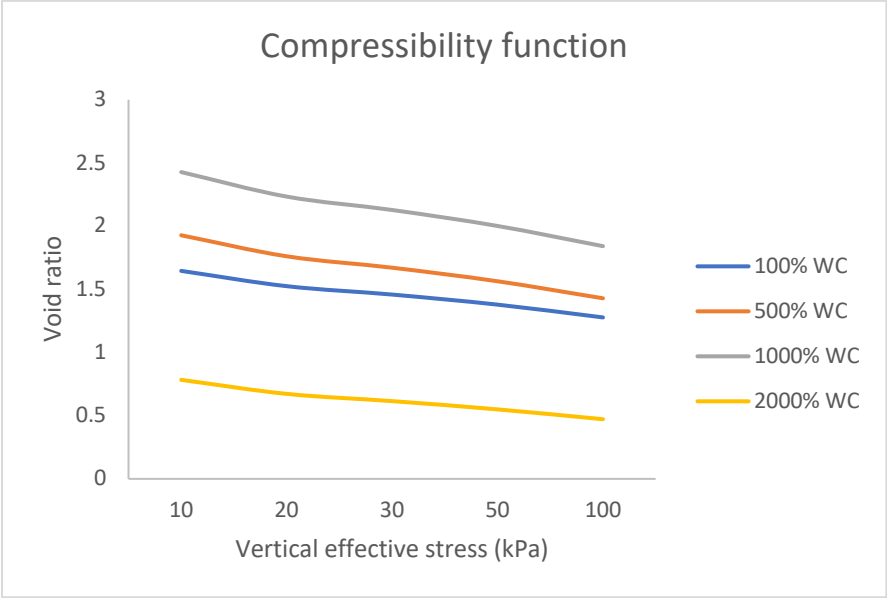

Figure 4.70: The compressibility function all flocculated Kaolinite samples at different water contents

The compressibility function and consolidation properties of the flocculated Kaolinite was calculated, using the compressibility relationship (e = $a\sigma v'^{b}$), a and b are estimated based on fitting the compressibility curve and were found to be the following:

100% WC: e = 2.23 $\sigma v'^{-0.05}$

500% WC: e = 2.6 $\sigma v'^{-0.13}$

1000% WC: e = 3.1 $\sigma v'^{-0.16}$

2000% WC: e = 2.0 $\sigma v'^{-0.4}$

4.6 Quantitative correlations of microscope image metrics to consolidation properties

This section attempts to investigate comparisons of quantitative metrics from the optical microscope images with consolidation parameters. The microscope metrics are associated, with two particle modes, when present. In the tailings, the two groups are from 0 to 20 μm^2 (small particles) and from 3000 to greater than 5000 μm^2 (large particles). The metrics are average

particle diameter, as well as the total area of particles. The consolidation parameters are the A and B parameters of the compressibility function, and the C parameter from the *k-e* curves. The D parameter is assumed to be constant at 7.5 for this analysis**.**

To remind the reader, The materials parameters that control consolidation are the compressibility function and the *k-e* function given by the following:

$$e = A\ \sigma v'^{B}$$

$$k = C\ e^{D}$$

Correlations are presented as the combination of all flocculated fluid fine tailing data sets, and then for the kaolinite tests.

4.6.1 All flocculated FFT samples

Comparing the average particle diameter for the flocculated FFT from the different experiments presented, it is clear that the peak torque + 3 sec samples have the largest particle diameters followed by the 800 ppm samples from the optimization test. It's worth noting that the peak torque + 3 sec samples were flocculated with a polymer dose of 600ppm in the Couette. Comparing this with the 800ppm samples (in the bucket), it is believed that even though 800ppm is considered the optimum dose (determined in the optimization test), the Couette provides better mixing than the bucket. Another factor that could have an impact, these two tests were done using different tailings materials: Syncrude FFT ("Peak + 3 second" sample) and Shell FFT (800ppm – Optimization test). On the other hand, the sheared samples at 4.23 s^{-1} , 8.27 s^{-1} , 16.93

s^{-1} and 33 s^{-1} all had an overall smaller particle diameter size in comparison with the non-sheared samples from the other tests.

The strongest correlations are obtained between the A and C parameters and the small and large particle area and diameters. Interesting, and against expectations, the C parameter shows inverse correlations with the average particle diameter of both ranges, most strongest with large particle size. This may point to increased hinderance of settling as floc sizes become very large. A high population of large particles inhibit hindered settlement and consolidation. Initially, rapid dewatering with larger particles but they quickly come in contact with one another causing a lower hydraulic conductivity. It could be that the permeability is governed by the voids in between the larger particles, the smaller flocs will end up having more void space in between particles. This may also explain the slight negative correlation of the A parameter with large particle size – larger flocs interlock and stop consolidating at higher void ratios.

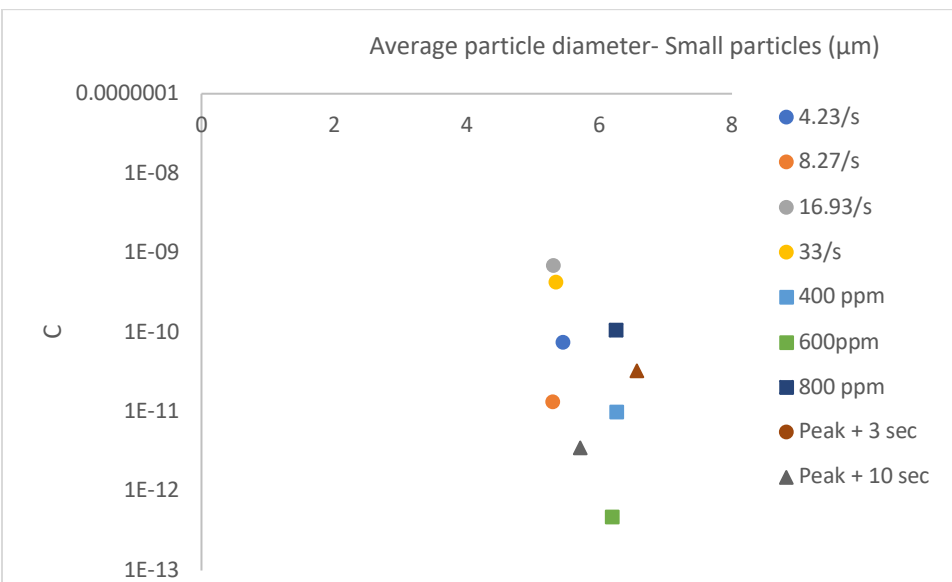

Figure 4.71: Average particle diameter for all flocculated FFT correlations with C parameter – Small particles 0-20 μm^2

The "peak + 3 seconds" sample seems to be an outlier when compared with the other samples from 600ppm & 800ppm samples. This could be since in this sample specifically, it was observed that there are very large cluster flocs which could be dominating these results, however, this result bears further investigation.

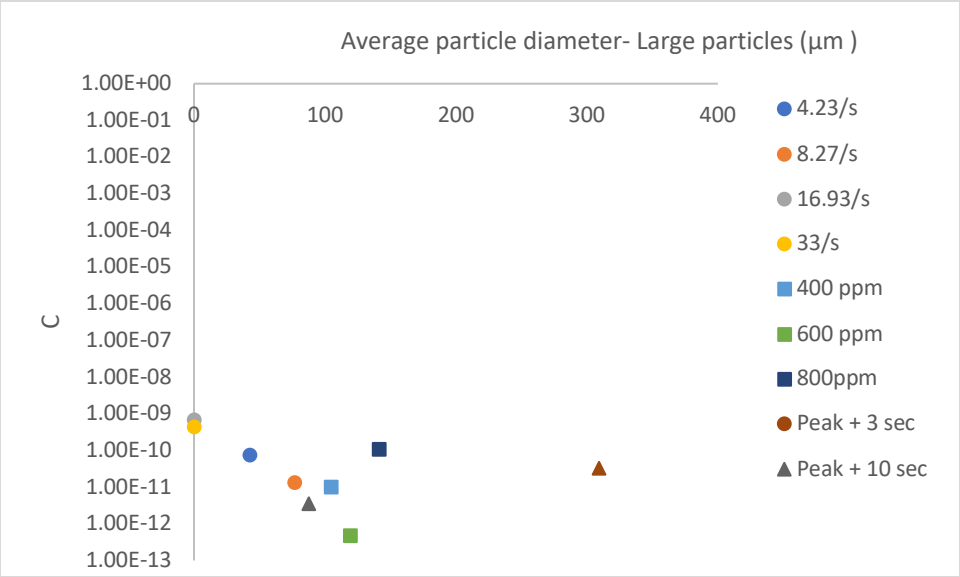

Figure 4.72: Average particle diameter for all flocculated FFT correlations with C parameter – Large particles 3000 to > 5000 μm^2

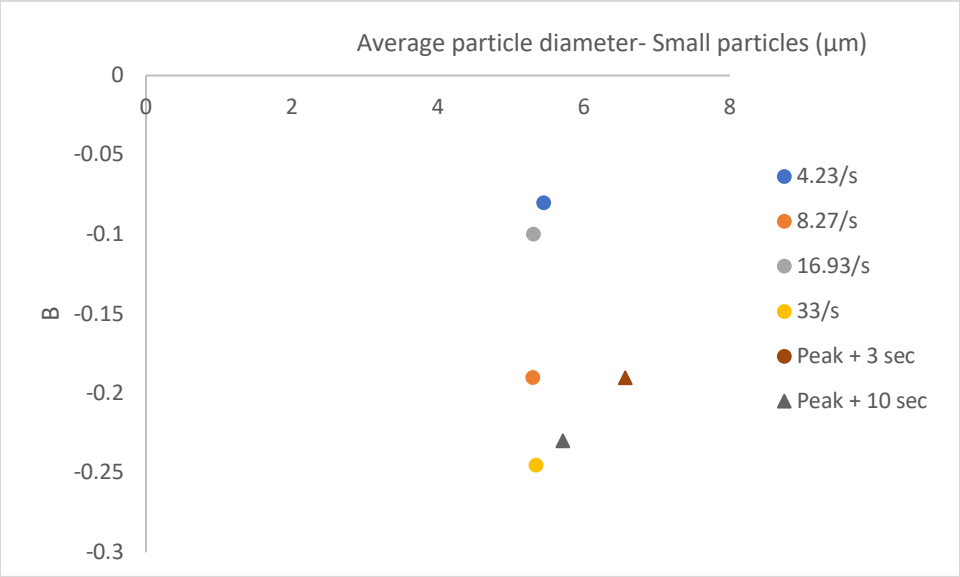

Figure 4.73: Average particle diameter for all flocculated FFT correlations with B parameter – Small particles 0-20 µm^2

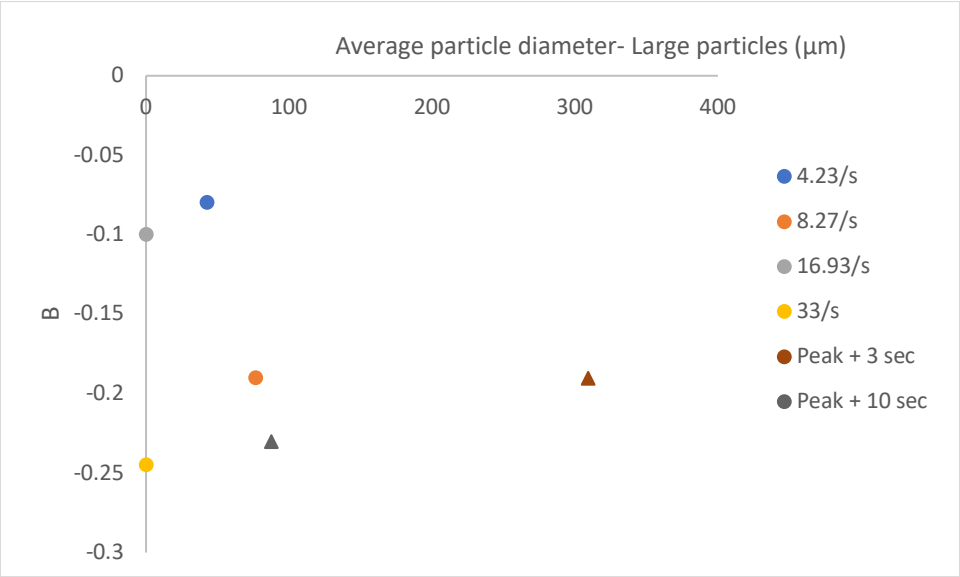

Figure 4.74: Average particle diameter for all flocculated FFT correlations with B parameter – Large particles 3000 to > 5000 µm^2

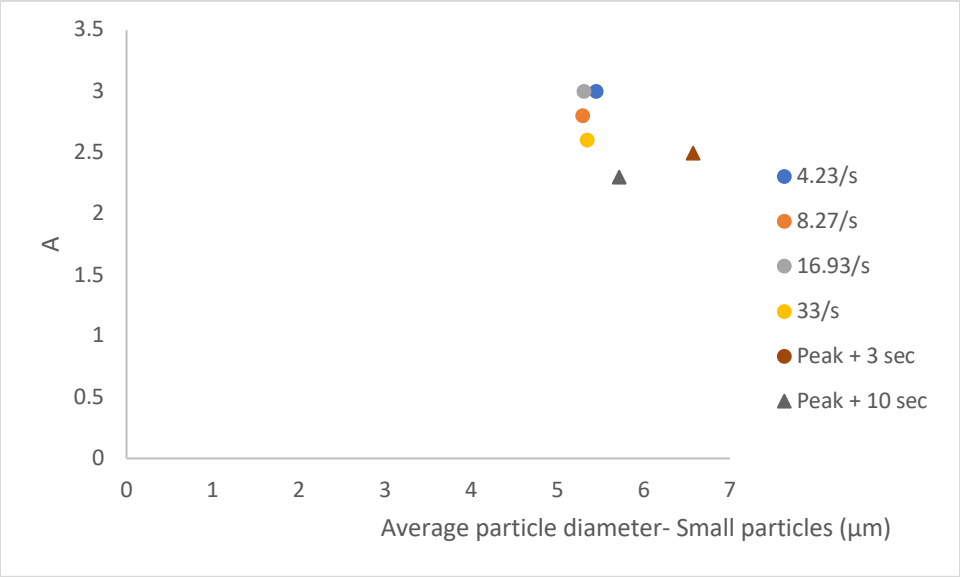

Figure 4.75: Average particle diameter for all flocculated FFT correlations with A parameter – Small particles 0-20 μm^2

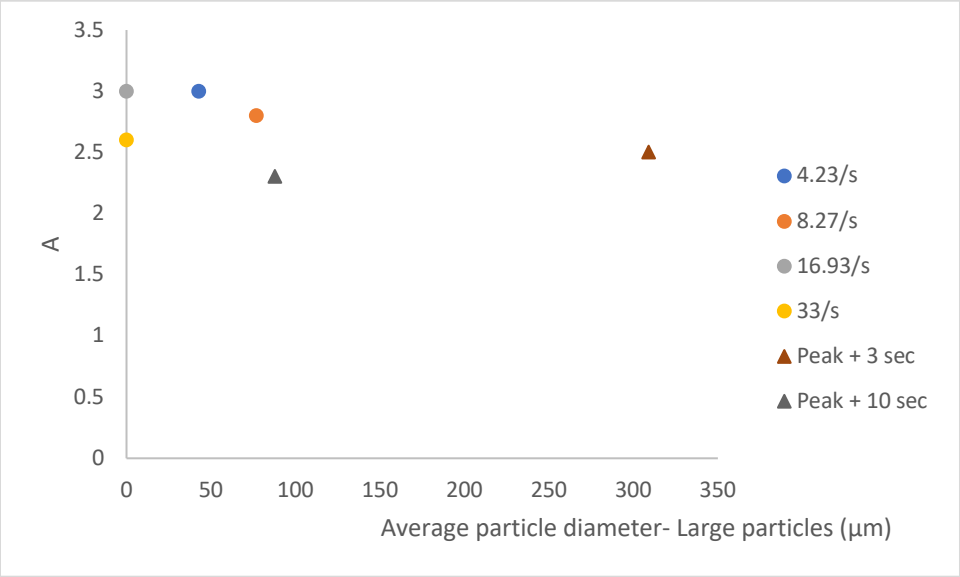

Figure 4.76: Average particle diameter for all flocculated FFT correlations with A parameter – Large particles 3000 to > 5000 μm^2

4.6.2 Kaolinite

The flocculated Kaolinite samples at 500% and 1000% water contents were shown to have the largest average particle diameter in comparison with 100% and 2000%. This is validated by the optical microscopy images that show the same behaviour. The A parameter in compressibility function ($e = A\ \sigma v'^{B}$) has a range of 2.5-3.05, unlike in the tailings tests, the A parameter shows a strong positive correlation with both the average diameter of the large and small particle population. Similar trends are observed for the C parameter, which are more consistent with expected trends of hydraulic conductivity with average pore-size or particle size observed in the literature (for example, Romero and Simms 2008). It should be noted that the average diameter of the large floc population in the kaolinite is smaller (20 to 80 microns) compared to the large floc population in the tailings (~50 to 400 microns).

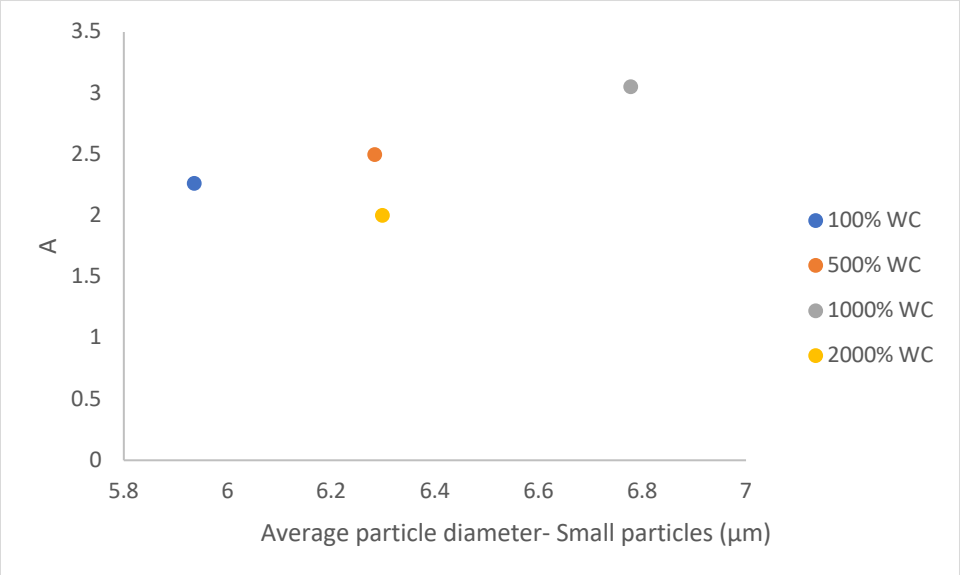

Figure 4.77: Average particle diameter for all flocculated FFT correlations with A parameter – Small particles 0-20 µm^2

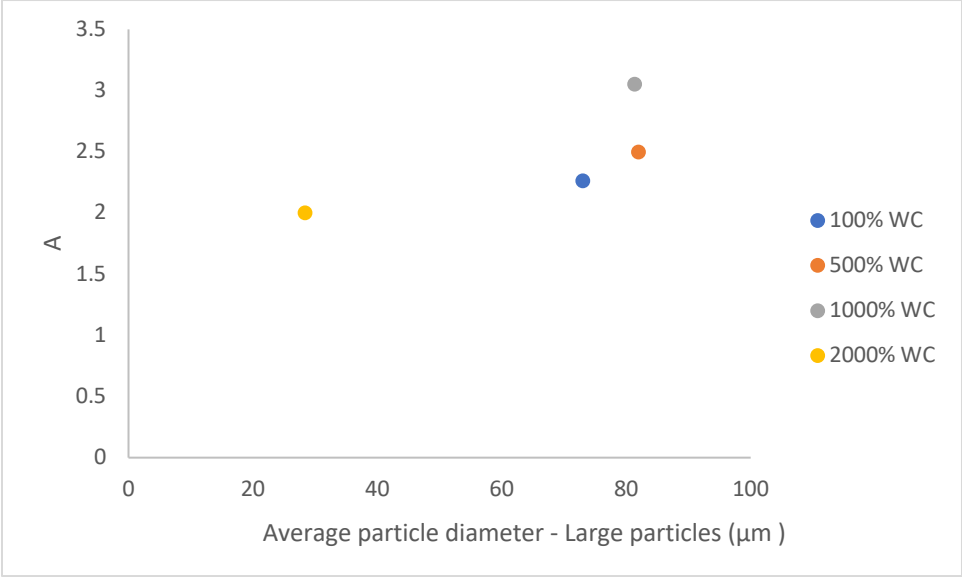

Figure 4.78: Average particle diameter for all flocculated FFT correlations with A parameter – Large particles 3000 to > 5000 μm^2

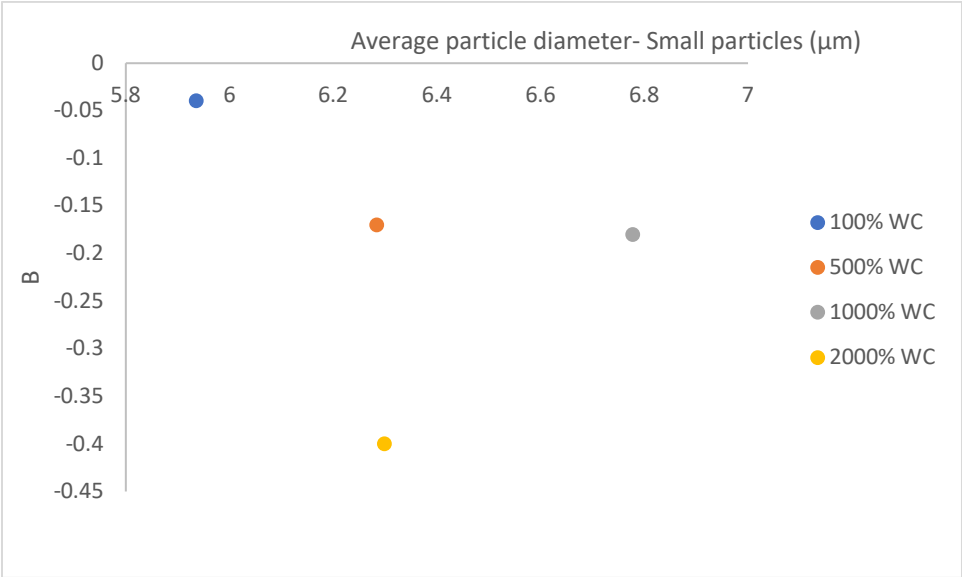

Figure 4.79: Average particle diameter for all flocculated FFT correlations with B parameter – Small particles 0-20 μm^2

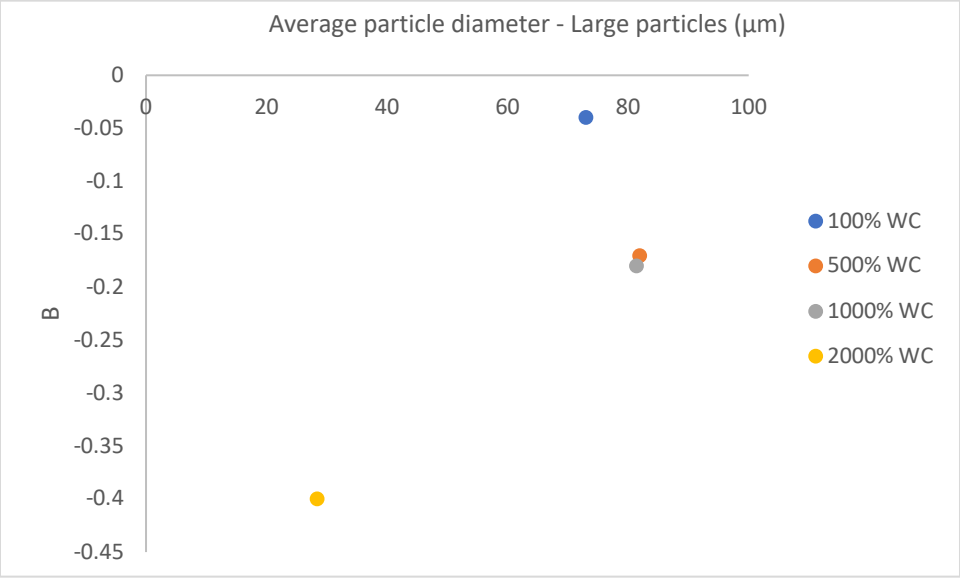

Figure 4.80: Average particle diameter for all flocculated FFT correlations with B parameter – Large particles 3000 to > 5000 μm^2

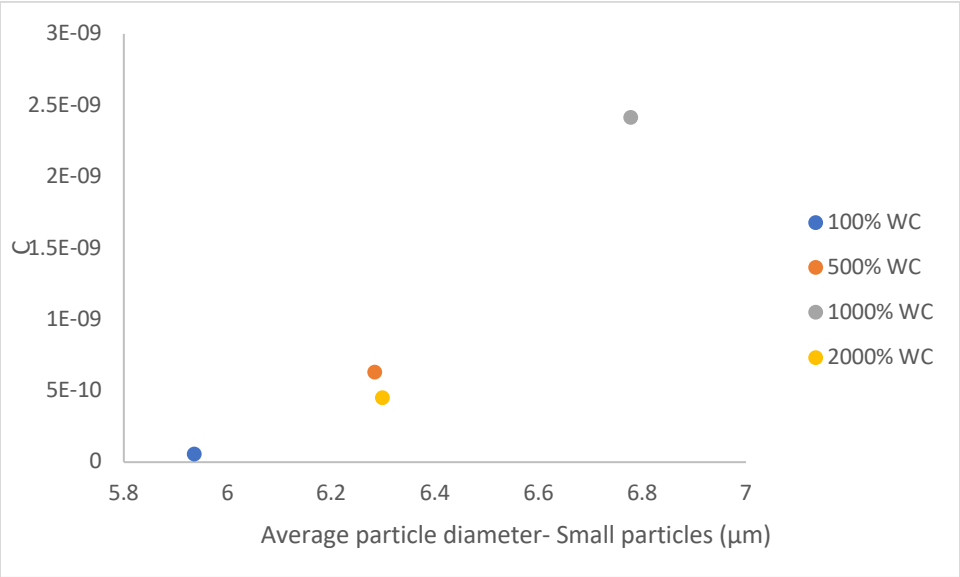

Figure 4.81: Average particle diameter for all flocculated FFT correlations with C parameter – Small particles 0-20 μm^2

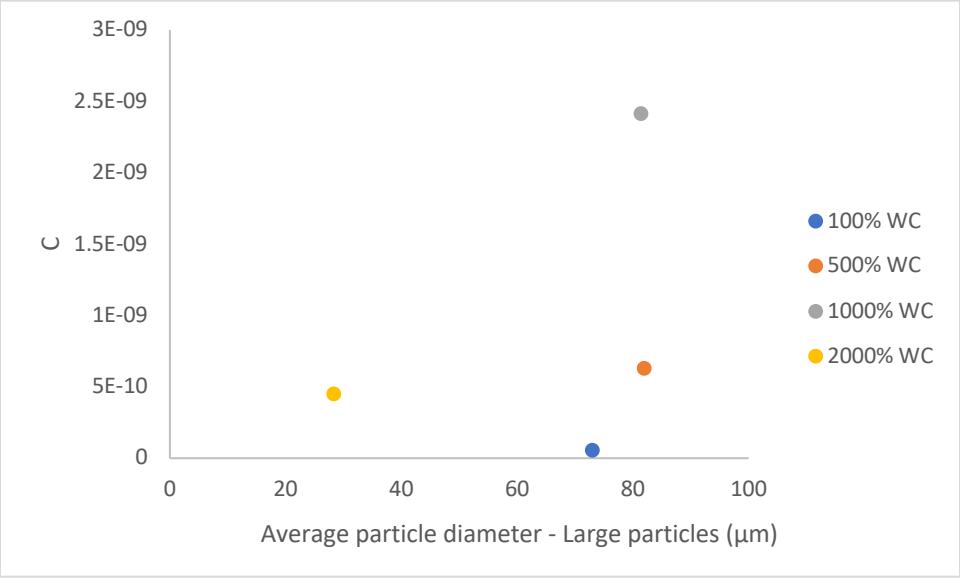

Figure 4.82: Average particle diameter for all flocculated FFT correlations with C parameter – Large particles 3000 to > 5000 μm^2

Chapter 5: Conclusion and Recommendations

This work evaluates the morphology and fabric in oil sands flocculated fluid fine tailings and other clays such as Kaolinite using optical microscope images in conjunction with Fiji-ImageJ software. Quantitative metrics extracted from these images were qualitatively and quantitatively compared with other sample characteristics, such as rheology, CST, and consolidation parameters.

5.1 Conclusions

Throughout this research, optical microscopy was used to evaluate the behaviour of the tailings. Determining how much tailings would settle using conventional methods requires a very long time, and hence the objective of this research is to assess these characteristics rapidly and examine some of the key governing properties such as the k-e relationship which dictates the rate and magnitude of settlement and consolidation. This work studied the evolution of fabric in flocculated fluid fine tailings using optical microscope images. Different polymer dosages, shearing rates, optimization methods were used to investigate quantitative metrics from the optical microscope images compared with consolidation properties of the tailings.
Repeatable metrics from different images (particle diameter, particle distribution) showed that consistent information could be obtained from different images of the same sample under the same experimental conditions. The analysis of three images from one given sample showed very small difference and hence repeatable trends were observed.

The optical microscope images are helpful in illustrating both visually and quantitively differences in macroscopic behaviour between different samples: for example, the role of small

particle populations in the differences in hydraulic conductivity due to different mixing durations.

Comparing the average particle diameter for the flocculated FFT from the different experiments presented, it is clear that the "peak torque + 3 sec" samples (polymer dosage 600ppm) have the largest particle diameters followed by the 800 ppm samples from the optimization test. This validates the hypothesis that samples flocculated using the Couette (peak torque + 3 seconds) have better flocculation than samples flocculated using a bucket (800ppm- Optimization test). Preliminary general correlations indicated some surprising trends: the magnitude of hydraulic conductivity in the fFFT samples was inversely correlated with the size of the larger particles. However, for the kaolinite samples, this was reversed. In this study, the "Different mixing durations" test (Torque-based feedback in Couette Rheometer) was studied using 600ppm polymer dosage. In order to investigate some of the surprising trends, this test should be repeated assessing different polymer dosages at different mixing durations (peak + 3 seconds & peak + 10 seconds). In addition, differences between Syncrude FFT and Shell FFT should be examined further, using optical microscopy to ensure that at a microstructure level the raw FFT is comparable in behaviour and characteristics. This will ensure that the comparisons done between the different tests on either material are accurate and valid. Furthermore, in previous studies the impact of small particles is often overlooked, however in cases where there's significantly large population of small particles (sheared materials); optical microscopy can provide insights on the void area & porosity which governs the k-e relationships. Evaluating the impact of large population of small flocs vs small population of large flocs on different key performance indicators should be further studied using optical microscope imaging analysis.

Polymer dosages greater than the optimum could result in excess polymer that can not bind to flocs (surface area occupied) leading to high viscosity samples. Higher viscosity indicates that the sample has a low permeability. This needs further consideration in future work.

Finally, samples flocculated in the bucket should have a constant gap ratio between the radius of the spindle and the vessel. Larger gap ratios usually reduce slip at the wall of the mixing vessel and hence it increases the shear stress. On the other hand, if the rotating blade has slip, flocculation and torque development will not be representative. Therefore, optimum flocculation protocol should be selected carefully after examining these considerations as it has an influence on both short and long term performance.

5.2 Recommendations for future work

The objective of this research was to develop a reliable methodology that produces repeatable results to measure the floc sizes and assess some of the parameters that influence the quality of flocculation. Though future studies may include:

- Applying the methodology developed for different types of soils and clays – including Leda clays.
- Optical microscopy images are only available in 2-D which is sometimes challenging as flocs can overlap and may affect the analysis. Hence, exploring new technologies that allow to look at the optical microscope slides from multiple different angles will provide a sense of 3D space occupied by the flocs and voids. This can be used to give a complete visual and conceptual understanding of the microstructure of the material.
- Investigating the possibility of applying this technique beyond the 48 hour limit without disturbing the samples to assess the long term behaviour.
- Applying more advanced statistical and Artificial Intelligence analysis of the images.

References

Asante , S. (2015). *Alternate methods to determine the microstructure of potentially collapsible soils.* doi: 10.13140/RG.2.1.1768.2328

Alberta energy regulatory board 2005. *http://www.aer.ca/about-aer*.

Alberta Energy Regulator (AER) (2019). *Directive 085. Retrieved from https://www.aer.ca/regulating-development/rules-anddirectives/directives/directive-085*.

Alberta.ca (n.d). Capping oil sands emissions. Retrieved May 8, 2022, from https://www.alberta.ca/climate-oilsands-emissions.aspx

Aldaeef, A., & Simms, P. (2019). *Influence of pipeline transport on sedimentation and consolidation of flocculated fluid fine tailings* Paper presented at the Geo St.John's - 72nd Canadian Geotechnical Conference, St. John, NL Canada.

Aldaeef, A. A., & Simms, P. H. 2020. Evaluation of Polymer Feed Rate, Polymer Dose, and Mixing Duration for Flocculation Optimization of Clayey Tailings with Various Solid Contents. *Geovirtual 2020*, Calgary, CA.

Babaoglu, Y., & Simms, P. (2020). Improving Hydraulic Conductivity Estimation for Soft Clayey Soils, Sediments, or Tailings Using Predictors Measured at High-Void Ratio. *Journal of geotechnical and geoenvironmental engineering*, 146(10), 06020016.

Bara, B., Yuan, S., Siman, R., & Gomez, C. 2013. Oil sands fine tailings flocculation using dynamic mixing. *U.S. Patent Application 13/620*,121.

Been, K. (1980). *Stress strain behaviour of a cohesive soil deposited under water.*

Been, K., & Sills, G. (1981). Self-weight consolidation of soft soils: an experimental and theoretical study. *Geotechnique, 31*(4), 519-535.

Beier, N., Wilson, W., Dunmola, A., & Sego, D. (2013). Impact of flocculation-based dewatering on the shear strength of oil sands fine tailings. Canadian Geotechnical Journal, 50(9), 1001-1007.

Berry, P., & Poshitt, T. (1972). The consolidation of peat. Geotechnique, 22(1). BGC Engineering, B. E. (2010). *Oil Sands Tailings Technology Review*. Retrieved from Edmonton, AB:

Canadian Association of Petroleum Producers. (2019). *Oil sands*. Retrieved from https://www.capp.ca/canadian-oil-and-natural-gas/oil-sands

Carrier III, W. D., Bromwell, L. G., & Somogyi, F. (1983). Design capacity of slurried mineral waste ponds. *Journal of Geotechnical Engineering*, 109(5), 699-716. doi:10.1061/(ASCE)0733-9410(1983)109:5(699)

Carrier, D., and Freeman, G. (2018). *Soft soil settlement and strength as applied to oil sand fine tailings.*

Chalaturnyk, R. J., Don Scott, J., & Özüm, B. (2002). Management of oil sands tailings. *Petroleum Science and Technology, 20*(9-10), 1025-1046.

Chryss, A. G., Monch, A., & Constanti-Carey, K. 2019. Online rheology monitoring of a thickener underflow. *In Proceedings of the 22nd International Conference on Paste, Thickened and Filtered Tailings (pp. 495-504)*. Australian Centre for Geomechanics.

Delage, P., & Pellerin, F. M. (1984). Influence de la lyophilisation sur la structure d'une argile sensible du Québec. *Clay minerals*, 19(2), 151-160.

Demoz, A., & Mikula, R. J. (2011). Role of mixing energy in the flocculation of mature fine tailings. *Journal of Environmental Engineering,* 138(1), 129-136.

Deng, R., Arifin, D. Y., Chyn, M. Y., & Wang, C. H. (2010). Taylor vortex flow in presence of internal baffles. *Chemical Engineering Science, 65(16)*, 4598-4605.

Derakhshandeh, B., Junaid A., and Freeman G. (2016). Effects of shearing and shearing time on dewatering and yield characteristics of oil sands flocculated fine tailings. *International Oil Sands Tailings Conference (IOSTC)*, Lake Louise, AB, Canada.

Elliot, T. R., & Heck, R. J. (2007). A comparison of optical and X-ray CT technique for void analysis in soil thin section. *Geoderma*, 141(1-2), 60-70.

Feng, T. W. (2000). Fall-cone penetration and water content relationship of clays. *Geotechnique*, 50(2), 181–187.

Feng, T. W. (2001). A linear log d - log w model for the determination of consistency limits of soils. *Can. Geotech. J.*, 38, 1335–1342.

Feng, T. W. (2004). Using a small ring and a fall-cone to determine the plastic limit. *Journal of Geotechnical and Geoenvironmental engineering*, 130(6), 630- 635.

Ferreira, T., and Rasband, W. (2012). Image J/Fiji 1.46 User Guide, available from (http://imagej.nih.gov/ij/docs/guide/user-guide.pdf)

Fine Tailings Fundamentals Consortium (FTFC). (1995). Advances in oil sands tailings research. Department of Energy, *Oil Sands and Research Division*

Fox, P. J., & Berles, J. D. (1997). CS2: a piecewise-linear model for large strain consolidation.

International Journal for Numerical and Analytical Methods in Geomechanics*, 21*(7), 453-475.

FTFC. (1995). Clark hot water extraction for fine tailings. *In Advances in oil sands tailings*

research. Fine Tailings Fundamentals Consortium (FTFC), Oil Sands and Research Division, Alberta Department of Energy, Edmonton, Alberta. 1:79–84.

Gibson, R. E., England, G. L., & Hussey, M. J. L. (1967). The Theory of one-dimensional consolidation of saturated clays: 1. finite non-Linear consolidation of thin homogeneous layers. *Geotechnique, 17*(3), 261-273.

Hogg, R. (1999). The role of polymer adsorption kinetics in flocculation. *Colloids and Surfaces A: Physicochemical and Engineering Aspects*, 146(1-3), 253-263.

Hong Doan Dinh, Pierre Delage, Jean-François Nauroy, Anh Minh Tang, Youssef Souhail. *Microstructural characterization of a Canadian oil sand. Canadian GeotechnicalJournal,* NRC Research Press, 2012, 49 (10), pp.1212-1220. 10.1139/T2012-072. Hal-00773092

Houlsby, G. T. (1982). Theoretical analysis of the fall-cone test. *Can. Geotech. J.*, 32(2), 111–118.

Hyndman, A., & Sobkowicz, J. (2010). Oil sands tailings: reclamation goals and the state of technology. *In Proceedings of the 63rd Canadian Geotechnical Conference, Calgary, Alta* (pp. 12-16).

Jeeravipoolvarn, S., Chalaturnyk, R.J., & Scott, J. D. (2009). Sedimentation–consolidation modeling with an interaction coefficient. *Computers and Geotechnics, 36*, 751-761.

Jeeravipoolvarn, S., Scott, J. D., & Chalaturnyk, R. J. (2009). 10 m standpipe tests on oil sands tailings: long-term experimental results and prediction. *Canadian Geotechnical Journal*, 46(8), 875-888.

Khattak, M. H. (2018). *Microstructural Quantitative Analysis of Polymer amended Fluid Fine Tailing's Using Digital Image Processing Techniques* (Master's Thesis, Carleton University).

Koppula, S. D. (1970). *Consolidation of Soil in Two Dimensions and Moving Boundaries*. Univ Alberta.

Koppula, S., & Morgenstern, N. (1982). On the consolidation of sedimenting clays. *Canadian Geotechnical Journal, 19*(3), 260-268.

Krieger, I. M., and Maron, S. H. (1952) Direct Determination of the Flow Curves of Non-Newtonian Fluids. Journal of Applied Physics 23(12),1412-1412.

Krieger, I. M., and Maron, S. H. (1954). Direct determination of the flow curves of non-Newtonian fluids. III. Standardized treatment of viscometric data. Journal of applied physics, 25(1), 72-75.

Lapointe, M., & Barbeau, B. (2016). Characterization of ballasted flocs in water treatment using microscopy. *Water Research*, *90*, 119–127. https://doi.org/10.1016/j.watres.2015.12.018

Lawson, K. (2020). Analysis of 3D Printed Prosthetics Using Xrd & Sem Techniques (thesis).

Lyn, D. A., Stamou, A. I., & Rodi, W. (1992). Density currents and shear-induced flocculation in sedimentation tanks. *Journal of hydraulic Engineering, 118(6)*, 849- 867.

Macedo, A., Vaz, C. M. P., Naime, J. M., Cruvinel, P. E., & Crestana, S. (1999). Xray microtomography to characterize the physical properties of soil and particulate systems. *Powder technology*, 101(2), 178-182.

Masliyah, J., Zhou, Z. J., Xu, Z., Czarnecki, J., & Hamza, H. (2008). Understanding water-based bitumen extraction from Athabasca Oil Sands. The Canadian Journal of Chemical Engineering, 82(4), 628–654. https://doi.org/10.1002/cjce.5450820403

Miller, W. G. (2010). *Comparison of geoenvironmental properties of caustic and noncaustic oil sand fine tailings.* (PhD Thesis, the University of Alberta).

Mizani, S., Simms, P., & Wilson, W. (2017). Rheology for deposition control of polymer-amended oil sands tailings. *Rheologica Acta, 56(7-8)*, 623-634.

Nielsen, B. D. (2004). *Non-destructive soil testing using X-ray computed tomography*. Bozeman, Montana.

Oil Sands Pathways (n.d). *Oil sands pathways to net zero*. Retrieved May 8, 2022, from https://www.oilsandspathways.ca/

Pane, V., & Schiffman, R. L. (1997). The permeability of clay suspensions. *Geotechnique, 47*(2), 273-288.

Qi, S., Chen, X., Simms, P., Zhou, J., & Yang, X. (2020). New method for determining the permeability function parameters of soft soils considering synchronous sedimentation and consolidation. *Computers and Geotechnics, 127*, 103781.

Qi, S., Salam, M., & Simms, P. (2017). *Modelling thixotropy at short and long time scales in dewatering analyses for soft soil or tailings*. Paper presented at the Proceedings the 70th Canadian Geotechnical Conference.

Qi, S., Salam, M., & Simms, P. (2018). *Creep and Structuration in Tailings and Natural Clays.* Paper presented at the Proceedings of IOSTC, Edmonton, Alberta.

Qi, S., & Simms, P. (2020). Robust methods to estimate large-strain consolidation parameters from column experiments. *Canadian Geotechnical Journal*, 57(5), 683- 705.

Qi, S., Simms, P., & Vanapalli, S. (2017). Piecewise-linear formulation of coupled large strain consolidation and unsaturated flow. I: Model development and implementation. *Journal of geotechnical and geoenvironmental engineering*, 143(7), 04017018.

Qi, S., Simms, P., Vanapalli, S., & Soleimani, S. (2017). Piecewise-Linear Formulation of Coupled Large-Strain Consolidation and Unsaturated Flow. II: Testing and Performance. *Journal of geotechnical and geoenvironmental engineering*, 143(7), 04017019. doi:10.1061/(ASCE)GT.1943-5606.0001658

Raymond, G. (1969). Consolidation of deep deposits of homogeneous clay. *Geotechnique, 19*(4), 478-494.

Salam, M.A., Simms, P.H., and Örmeci, B. (2017). Investigation of Creep in Polymer Amended Oil Sand Tailings. *Proceeding of GeoOttawa 2018*, Ottawa, Canada.

Salam, M.A., Simms, P.H., and Örmeci, B. (2018). Structuration in Polymer Amended Oil Sands Fine Tailings. *Proceeding of GeoEdmonton 2018*, Edmonton, Canada.

Salam, M.A. (2020). Effects of polymers on short- and long-term dewatering of oil sands tailings. (Doctoral dissertation). Carleton University, Ottawa, CA.

Sikandar, P., & Christen, E. W. (2012). Geoelectrical sounding for the estimation of hydraulic conductivity of alluvial aquifers. Water Resources Management, 26(5), 1201–1215. https://doi.org/10.1007/s11269-011-9954-3

Suthaker, N., & Scott, J. (1994). Large strain consolidation testing of oil sand fine tails in a wet landscape. *Paper presented at the Proceedings, 47th Canadian Geotechnical Conference*.

Terzaghi, K. (1943). Theory of consolidation. *Theoretical Soil Mechanics*, 265-296.

Tripathy, T., & De, B. R. (2006). Flocculation: a new way to treat the waste water. *Journal of Physical Sciences*, 10:93-127.

Vajihinejad, V., Gumfekar, S. P., Bazoubandi, B., Rostami Najafabadi, Z., & Soares, J. B.
(2019). Water Soluble Polymer Flocculants: Synthesis, Characterization, and Performance Assessment. *Macromolecular Materials and Engineering, 304*(2), 1800526

Webster, S. E., Brown, W. A., Derakhshandeh, B., Dubash. N., Gomez. C., Veenstra. C. N. and Junaid. A. (2016). A comprehensive control scheme for dynamic inline flocculation of oil sands tailings. Lake Louise, AB, Canada.

Wood, D. M. (1985). Some fall-cone tests. *Geotechnique 35*, No. 1, 64-68

Yang, Y., Wang, L., Wendroth, O., Liu, B., Cheng, C., Huang, T., & Shi, Y. (2019). Is the laser diffraction method reliable for soil particle size distribution analysis*? Soil Science Society of America Journal*, *83*(2), 276–287. https://doi.org/10.2136/sssaj2018.07.0252

Yudina, A., & Shishkov, V. (2018). Partitioning of primary and secondary soil particles by ultrasonic energy: consequences for microstructure organization. *Proceedings of 20th EGU General Assembly, 2018,* Vienna, Austria.

Appendix A

Peak torque + 3 second samples – Raw optical microscope images:

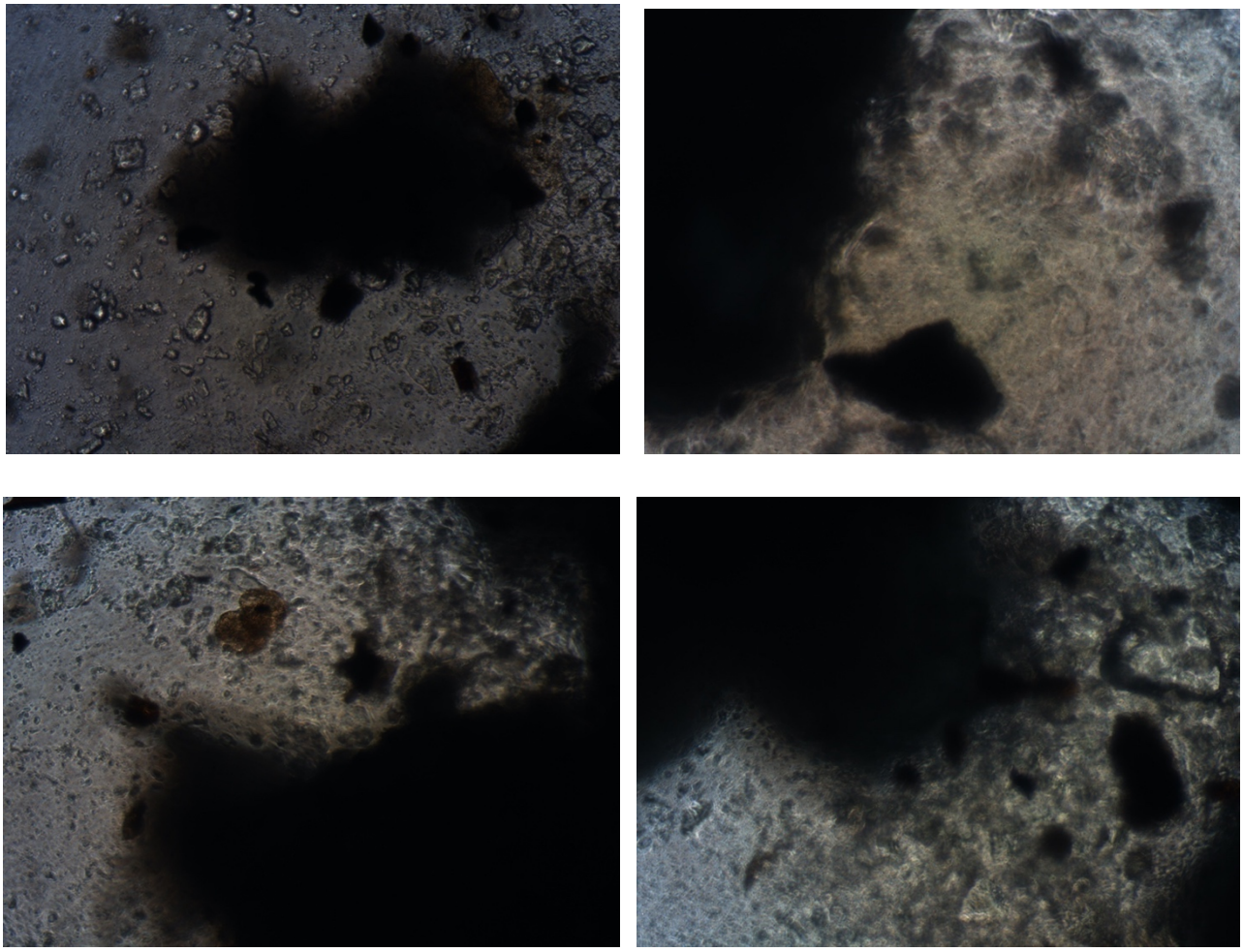

Peak torque + 10 second samples – Raw optical microscope images:

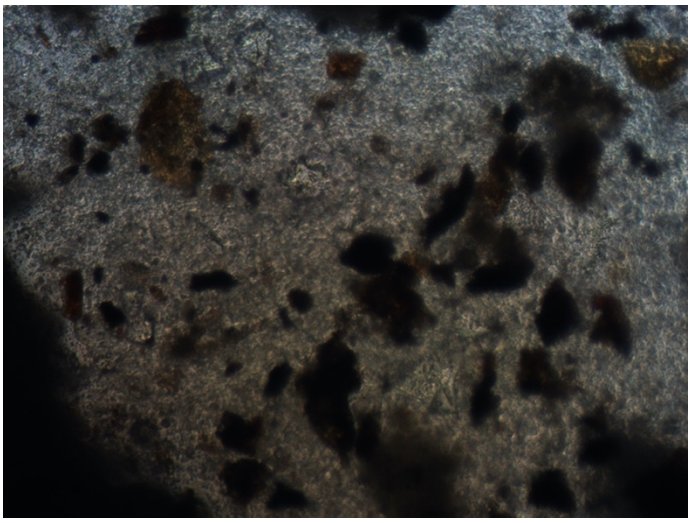

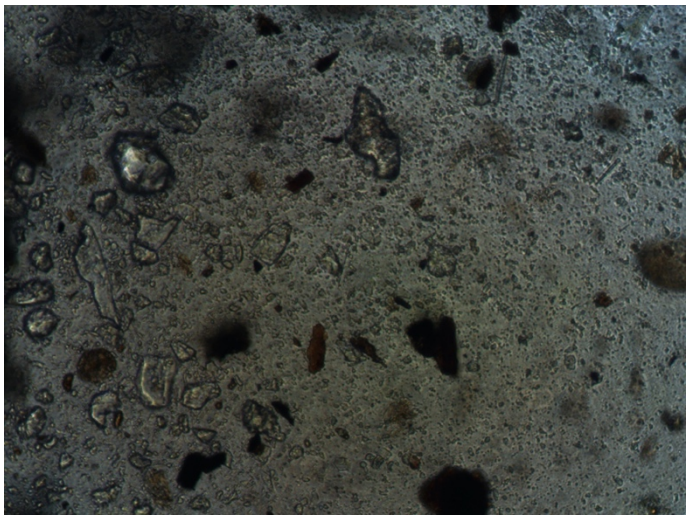

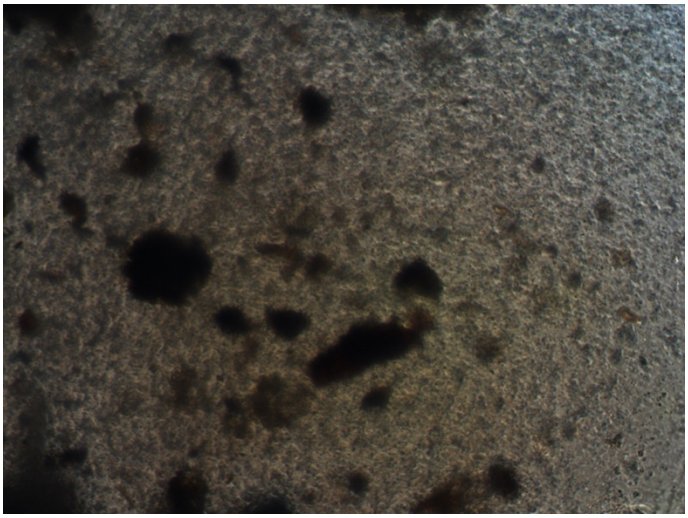

Optimization test:

400 ppm

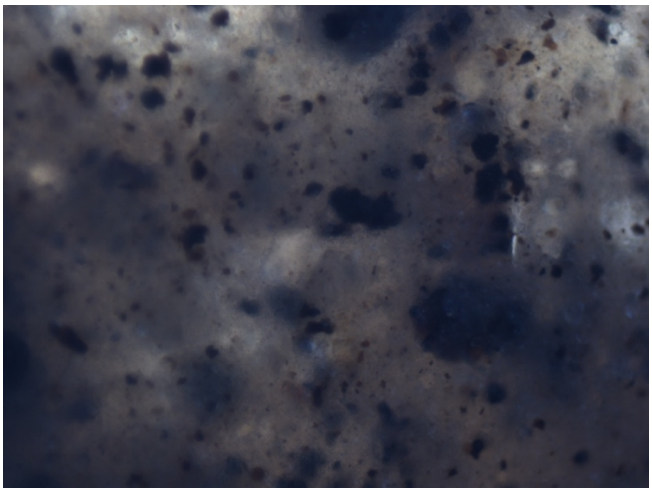

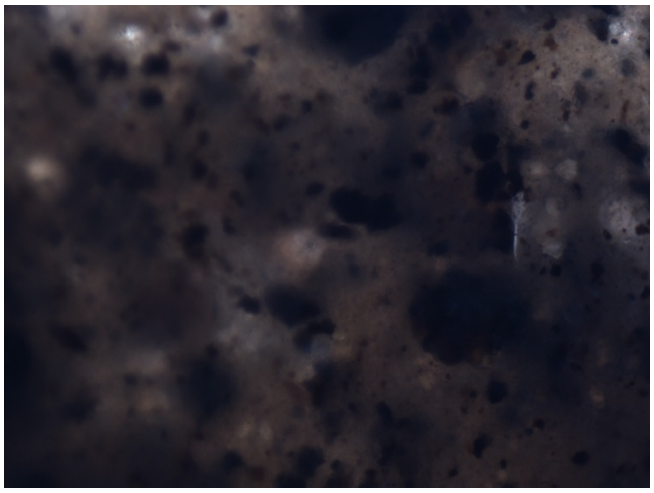

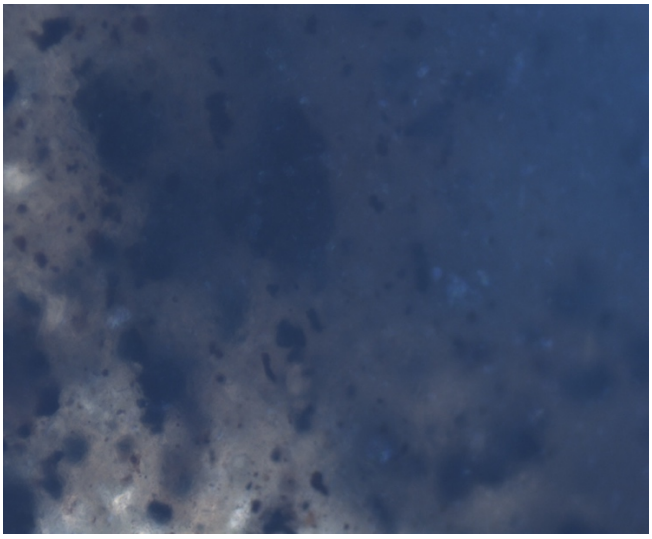

600ppm:

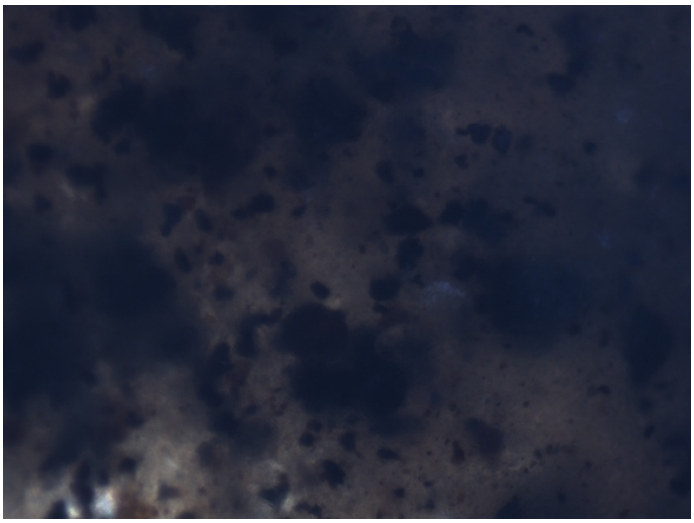

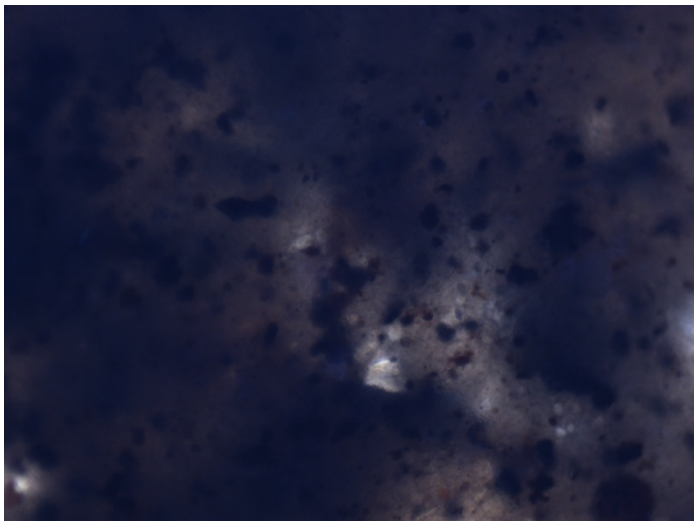

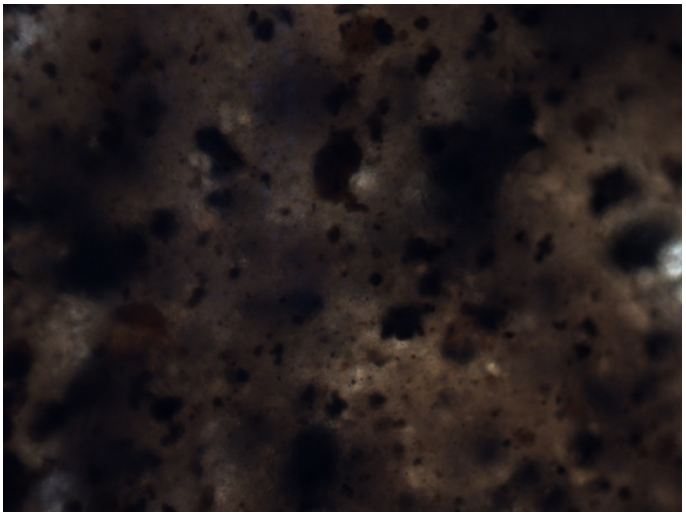

800ppm:

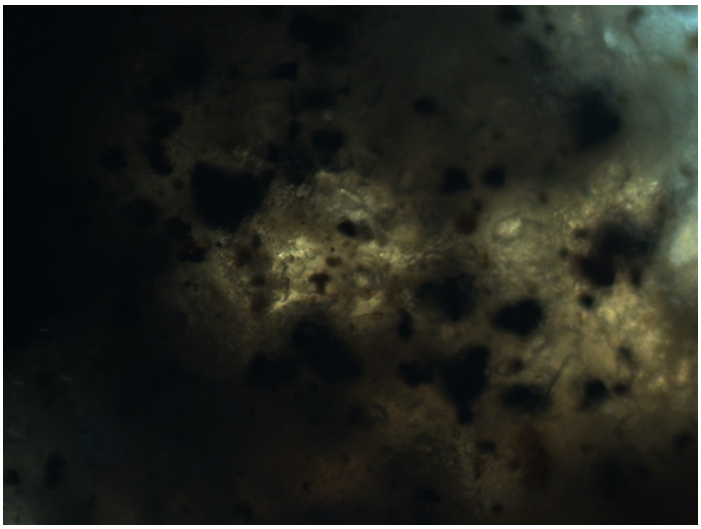

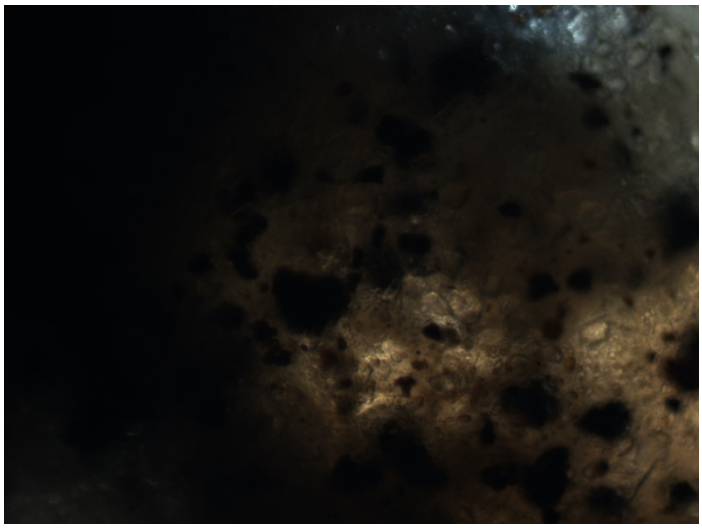

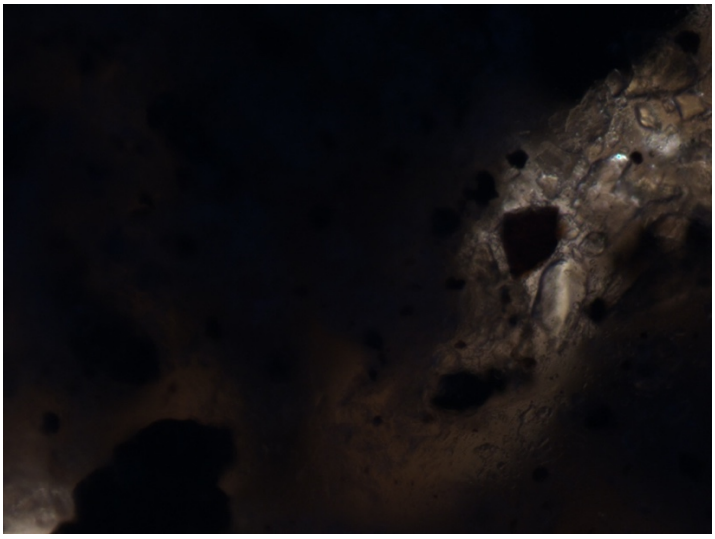

1000ppm:

Shearing test:

4.23 s^{-1}

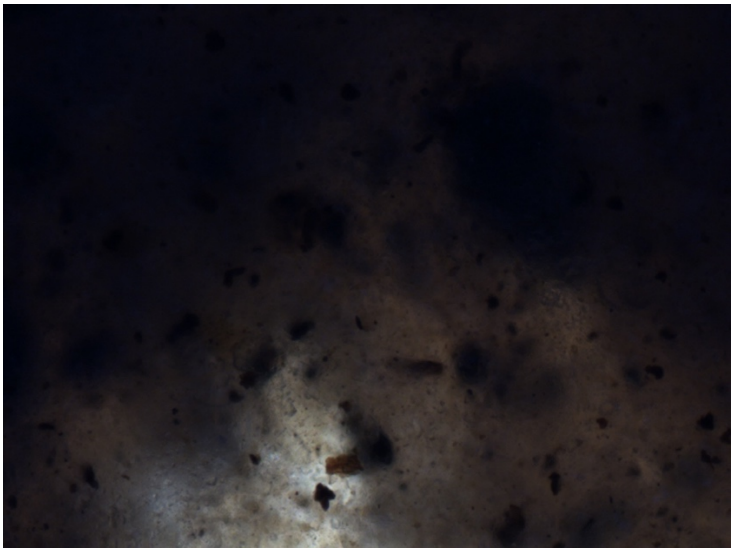

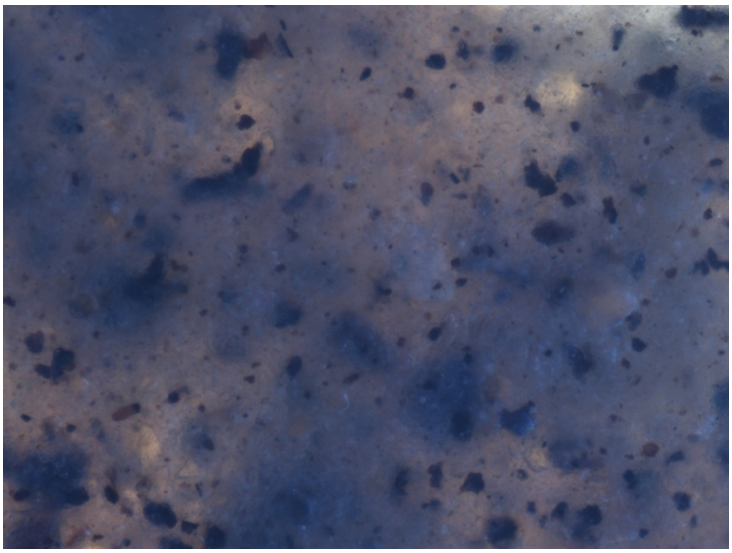

8.27 s^{-1}

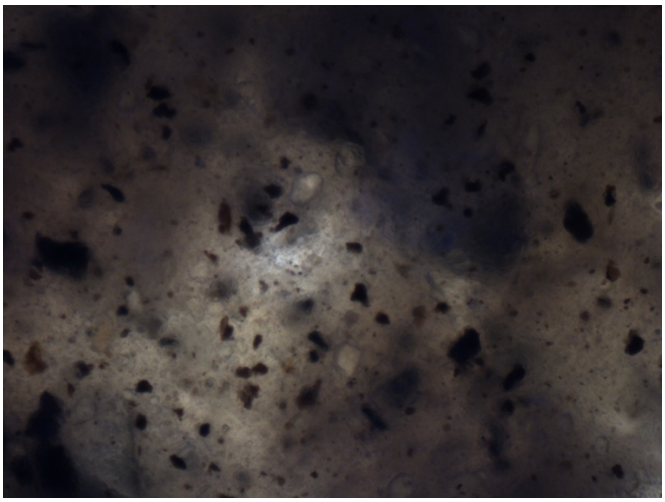

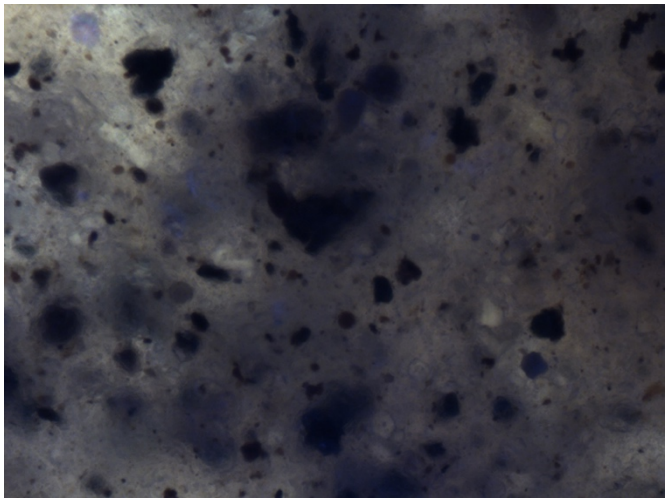

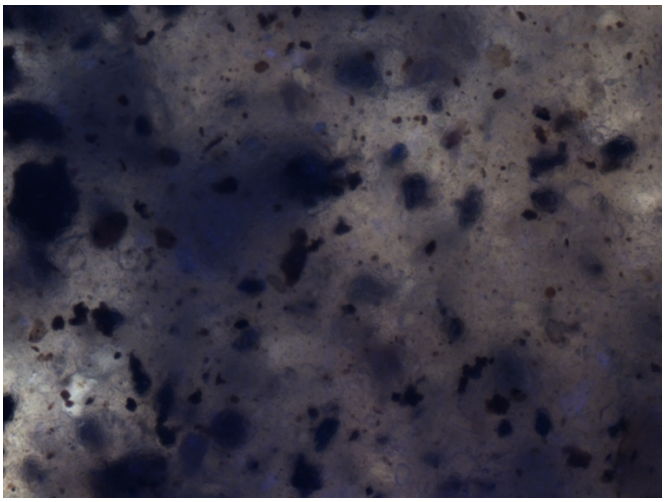

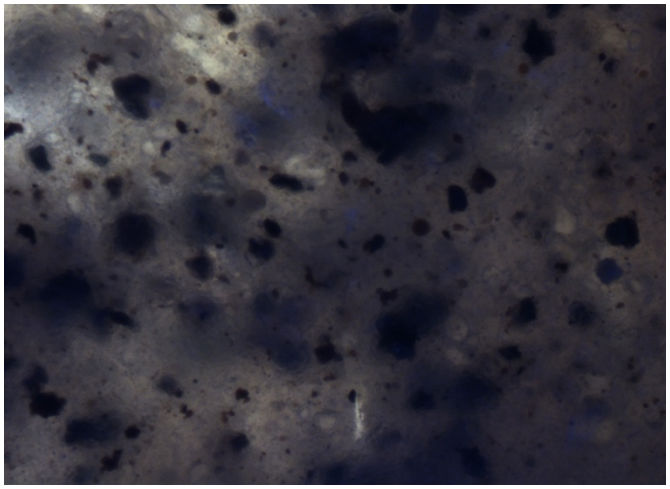

16.93 s^{-1}

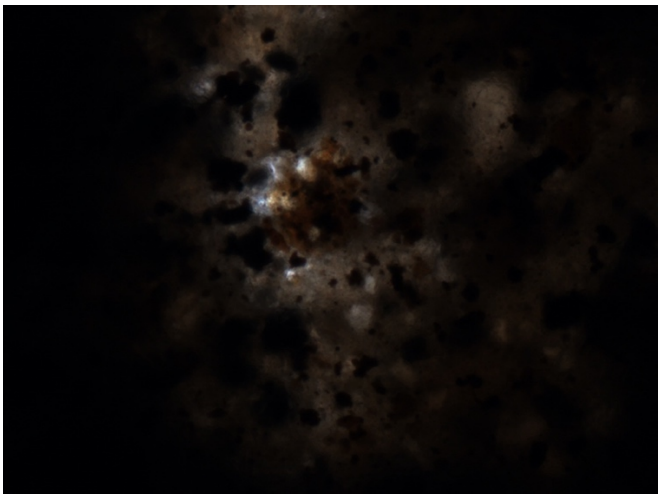

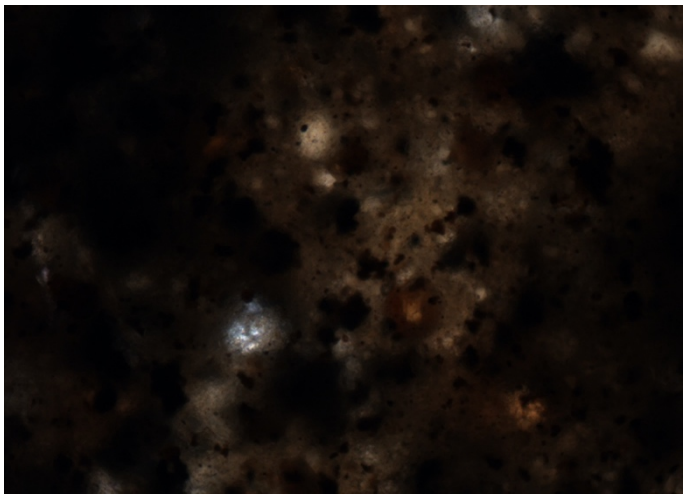

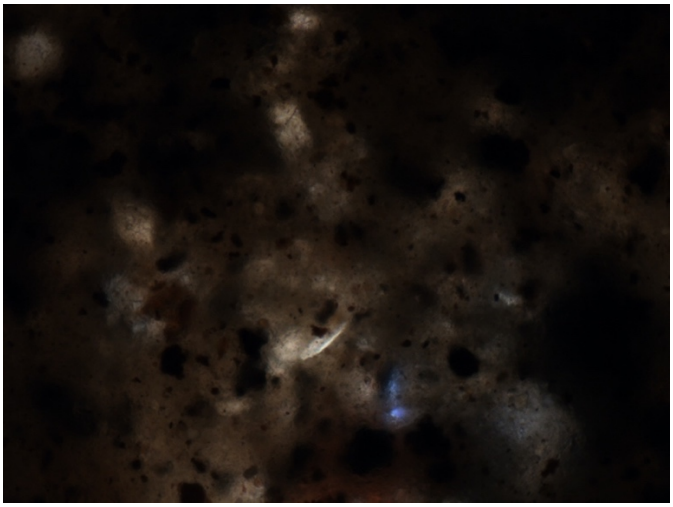

33 s^{-1}